University of Nottingham
UK | CHINA | MALAYSIA

ASSESSMENT OF DELAMINATION IN LAMINATED COMPOSITE STRUCTURES BASED ON THE PHASE SPACE TOPOLOGY OF STRUCTURAL DYNAMIC RESPONSES

A thesis submitted to The University of Nottingham for the degree of Doctor of Philosophy

Submitted by Xuan LI, MSc

2021-1-8

The University of Nottingham, Ningbo, China (UNNC)
199 Taikang East Road, Ningbo, 315100, China

Content

FIGURE LIST..... iv

TABLE INDEX..... xiv

ABSTRACT..... 16

ACKNOWLEDGEMENT..... 21

Chapter 1 INTRODUCTION..... 23

1.1 Background..... 23

1.1.1 Delamination in Composite Structure..... 23

1.1.2 Analysis of the Dynamic responses of Delamination Structures..... 24

1.1.3 Damage Detection Method for Composite Structures..... 28

1.2 Introduction of Proposed Methods..... 39

1.2.1 Green's Function Method..... 39

1.2.2 Phase Space Method for Dynamic responses Analysis and Damage Detection..... 41

1.2.3 Other Methods..... 46

1.3 Research Gaps..... 55

1.4 Aim and Objective..... 58

1.5 Research Novelty and Significance..... 59

1.6 The Structure of Thesis..... 62

Chapter 2 A THEORETICAL MODEL OF DELAMINATED BEAM STRUCTURES BASED ON THE GREEN'S FUNCTION METHOD..... 65

2.1 Analysis of Delaminated Beams..... 66

2.1.1 Model of Delaminated Beams..... 66

2.1.2 The Green's Function..... 71

2.2 Free Vibration Responses of a Delaminated Beam..... 73

2.3 Forced Vibration Analysis of a Delaminated Beam..... 83

2.3.1 Dimensionless Beam Displacement under Various Excitation Frequencies 85

2.3.2 Vibration Responses of Different Points with 1Hz Excitation..... 97

2.3.3 Vibration Responses of Different Points with 5Hz Excitation..... 111

2.4 Conclusions..... 124

Chapter 3 THE OPTIMIZATION FOR DYNAMIC RESPONSES MEASUREMENT FOR DELAMINATED BEAMS..... 127

3.1 The Effect of Delamination on the Dynamic responses of Different Location 129
3.2 Optimization for Signal Measurement....136
3.3 Result of the Constrained Mode Model....140
3.3.1 Different Delamination Sizes....140
3.3.2 Different Delamination Depths....146
3.3.3 Different Delamination Locations....152
3.3.4 Different Delamination Locations and Sizes....158
3.3.5 Different Delamination Depths and Sizes....164
3.4 Result of the Free Mode Model....169
3.4.1 Different Delamination Depths....170
3.4.2 Different Delamination Sizes....177
3.4.3 Different Delamination Locations....185
3.4.4 Different Delamination Locations and Sizes....191
3.5 Conclusions....196
Chapter 4 THE DELAMINATION DETECTION AND ASSESSMENT USING A VIBRATION-BASED PHASE SPACE RECONSTRUCTED METHOD....199
4.1 The Phase Space Topology Analysis of Structural Dynamic responses....200
4.1.1 The Phase Space Topology Analysis using Phase Space Reconstructed (PSR) Method....200
4.1.2 The Change of Phase Space Topology (CPST)....204
4.2 Delamination Assessment for Beam Sample....206
4.2.1 Delamination Size Assessment....208
4.2.2 Delamination Depth Assessment....212
4.3 Delamination Assessment for Laminated Panel....217
4.3.1 Simulation....218
4.3.2 Experiment....229
4.4 Conclusions....234
Chapter 5 THE DELAMINATION DETECTION AND ASSESSMENT BASED ON PHASE SPACE TOPOLOGY ANALYSIS COMBINED WITH WAVELET PACKET DECOMPOSITION....236
5.1 Methodology....237
5.1.1 Wavelet Packet Decomposition Method....237
5.1.2 Phase Space Topology Analysis of Sub-signals....241

5.2 Delamination Assessment for Beam Structures....243
5.2.1 Delamination Size Assessment....244
5.2.2 Delamination Depth Assessment....250
5.3 Delamination Assessment for Laminated Panel....256
5.3.1 Simulation....259
5.3.2 Experiment....271
5.4 Conclusions....277
Chapter 6 THE DELAMINATION ASSESSMENT IN COMPOSITE LAMINATE PANEL BASED ON THE ANN WITH DIFFERENT INPUT FACTORS....279
6.1 Artificial Neural Network (ANN) Design....280
6.2 Delamination Assessment Procedure....282
6.2.1 Fourier Transform Method....283
6.2.2 Phase Space Topology Analysis with ANN....283
6.2.3 Phase Space Topology Analysis with Wavelet Packet Decomposition and ANN....284
6.3 Simulation Result....285
6.3.1 The Delamination Assessment for Beams....285
6.3.2 The Delamination Assessment for Laminate Panel....290
6.4 Conclusions....311
Chapter 7 CONCLUSIONS....313
7.1 Conclusions....313
7.2 Future Work....317
APPENDIX....320
REFERENCE....327
PUBLICATION DURING PHD STUDY....346

FIGURE LIST

FIGURE 1-1 THE DYNAMIC RESPONSES OF THE DUFFING SYSTEM [111]......41

FIGURE 1-2 THE STRUCTURE OF NEURAL NETWORK [148]......50

FIGURE 2-1 THE MODEL OF A BEAM WITH DELAMINATION...... 67

FIGURE 2-2 THE CONTINUITY OF SHEAR FORCE AND BENDING MOMENT AT $X = L1$.
.....68

FIGURE 2-3 THE REDUCTION OF NATURAL FREQUENCY GENERATED BY DELAMINATION LOCATION AND SIZE FROM THE CONSTRAINED MODE MODEL.
.....78

FIGURE 2-4 THE MODE SHAPE OF THE DELAMINATED BEAM WITH DIFFERENT LENGTH BASED ON THE FREE MODE MODEL ($H2H = 0.25, L1 + A2 = 0.5L$*).*.....80

FIGURE 2-5 THE MODE SHAPE OF THE DELAMINATED BEAM WITH DIFFERENT DEPTH BASED ON THE FREE MODE ($AL = 0.3, L1 + A2 = 0.5L$*).*..... 82

FIGURE 2-6 THE MODEL OF A DELAMINATED BEAM WITH EXCITATION......84

FIGURE 2-7 THE DIMENSIONLESS DISPLACEMENT UNDER 4HZ EXCITATION WITH DIFFERENT DAMPING RATIOS FOR THE BEAM WITH DELAMINATION (DELAMINATION PARAMETERS: $H2 = 0.5H, A = 0.1L, B = 0.5L$*) FROM THE CONSTRAINED MODE MODEL.*.....86

FIGURE 2-8 THE DEFORMATION OF DELAMINATED BEAMS UNDER VARIOUS EXCITATION FREQUENCY OF THE CONSTRAINED MODE MODEL WITH DAMPING RATIO $Z = 0.01$ *(A-B),* $Z = 0.05$ *(C-D),* $Z = 0.1$ *(E-F) (DELAMINATION PARAMETERS:* $H2 = 0.5H, A = 0.1L, B = 0.5L$*)*.....87

FIGURE 2-9 THE DEFORMATION OF TWO BEAMS UNDER VARIOUS EXCITATION FREQUENCY OF THE CONSTRAINED MODE MODEL WITH DELAMINATION AT DIFFERENT LOCATIONS: 1) UNDAMAGED BEAM (A-B); 2) $H2 = 0.5H, A = 0.3L, L1 = 0.15L$ *(C-D); 3)* $H2 = 0.5H, A = 0.3L, L1 = 0.35L$ *(E-F).*..... 88

FIGURE 2-10 THE AXIAL LOAD OF SUB-BEAMS IN THE DELAMINATED REGION BASED ON THE CONSTRAINED MODE MODEL......90

FIGURE 2-11 THE DEFORMATION OF BEAMS UNDER VARIOUS EXCITATION FREQUENCY OF THE CONSTRAINED MODE MODEL WITH DIFFERENT DELAMINATION SIZES A: 1) UNDAMAGED (A-B); 2) $H2 = 0.5H$, $A = 0.1L$, $B = 0.5L$ *(C-D); 3)* $H2 = 0.5H$, $A = 0.3L$, $B = 0.5L$ *(E-F); 4)* $H2 = 0.5H$, $A = 0.5L$, $B = 0.5L$ *(G-H).*.....92

FIGURE 2-12 THE DEFORMATION OF TWO DELAMINATED BEAMS UNDER VARIOUS EXCITATION FREQUENCY OF THE CONSTRAINED MODE MODEL: 1) UNDAMAGED (A-B); 2) $H2 = 0.25H$, $A = 0.1L$, $B = 0.5L$ *(C-D); 3)* $H2 = 0.5H$, $A = 0.1L$, $B = 0.5L$ *(E-F).*.....94

FIGURE 2-13 THE DEFORMATION OF DELAMINATED BEAMS UNDER VARIOUS EXCITATION FREQUENCY OF SAMPLE ($H2 = 0.25H$, $A = 0.1L$, $B = 0.5L$*) FROM THE CONSTRAINED MODE MODEL (A-B) AND THE FREE MODE MODEL (C-D).* 96

FIGURE 2-14 THE VIBRATION RESPONSES OF DIFFERENT POINTS: (A) VIBRATION RESPONSES OF FOUR AXIAL POSITIONS LS *OF THE BEAM (*$LS = 0.10L$, $LS = 0.20L$, $LS = 0.85L$, $LS = 0.90L$*); (B) THE RELATIONSHIP BETWEEN MAX DISPLACEMENT AND MEASURE POINTS LOCATION.*..... 98

*FIGURE 2-15 THE MAX DISPLACEMENT OF DIFFERENT LOCATIONS IN THE BEAM.*100

FIGURE 2-16 THE SHAPE OF THE BEAM WITH 0.25L DELAMINATION AT DIFFERENT VALUES OF TIME...... 102

FIGURE 2-17 THE SHAPE OF THE BEAM WITH 0.5L DELAMINATION AT DIFFERENT VALUES OF TIME...... 103

FIGURE 2-18 THE RELATIONSHIP BETWEEN DELAMINATION SIZE AND MAX DISPLACEMENT...... 104

FIGURE 2-19 THE CHANGE RATIO OF MAX DISPLACEMENT WITH DIFFERENT DELAMINATION SIZE...... 104

*FIGURE 2-20 THE MAX DISPLACEMENT OF DIFFERENT LOCATIONS IN THE BEAM.*106

FIGURE 2-21 THE SHAPE OF THE BEAM WITH $0.25H$ *DELAMINATION AT DIFFERENT VALUES OF TIME.*..... 108

FIGURE 2-22 THE SHAPE OF THE BEAM WITH $0.5H$ *DELAMINATION AT DIFFERENT VALUES OF TIME.*..... 109

FIGURE 2-23 THE VIBRATION RESPONSES OF DELAMINATION IN DIFFERENT DEPTHS. 110
FIGURE 2-24 THE CHANGE RATIO OF MAX DISPLACEMENT WITH DIFFERENT DELAMINATION DEPTHS. 110
FIGURE 2-25 THE MAX DISPLACEMENT OF DIFFERENT LOCATIONS IN THE BEAM. 112
FIGURE 2-26 THE SHAPE OF THE BEAM WITH 0.25L *DELAMINATION AT DIFFERENT VALUES OF TIME.* 114
FIGURE 2-27 THE SHAPE OF THE BEAM WITH 0.5L *DELAMINATION AT DIFFERENT VALUES OF TIME.* 115
FIGURE 2-28 THE RELATIONSHIP BETWEEN DELAMINATION SIZE AND MAX DISPLACEMENT. 116
FIGURE 2-29 THE CHANGE RATIO OF MAX DISPLACEMENT WITH DIFFERENT DELAMINATION SIZES. 116
FIGURE 2-30 THE MAX DISPLACEMENT OF DIFFERENT LOCATIONS IN THE BEAM. 118
FIGURE 2-31 THE SHAPE OF THE BEAM WITH 0.25H *DELAMINATION AT DIFFERENT VALUES OF TIME.* 120
FIGURE 2-32 THE SHAPE OF THE BEAM WITH 0.5H *DELAMINATION AT DIFFERENT VALUES OF TIME.* 121
FIGURE 2-33 THE VIBRATION RESPONSES OF DELAMINATION IN DIFFERENT DEPTHS 122
FIGURE 2-34 THE CHANGE RATIO OF MAX DISPLACEMENT WITH DIFFERENT DELAMINATION DEPTHS. 122
FIGURE 3-1 THE MAX DISPLACEMENT OF DIFFERENT AXIAL POINTS BASED ON THE CONSTRAINED MODE MODEL WITH 1HZ EXCITATION (A-B) AND 10HZ EXCITATION (C-D) 130
FIGURE 3-2 THE MAX DISPLACEMENT OF DIFFERENT AXIAL POINTS WITH 5HZ EXCITATION BASED ON THE CONSTRAINED MODE MODEL 131
FIGURE 3-3 THE MAX DISPLACEMENT OF DIFFERENT AXIAL POINTS WITH 10HZ EXCITATION BASED ON THE CONSTRAINED MODE MODEL. 133
FIGURE 3-4 THE DISPLACEMENT OF MEASUREMENT LOCATIONS BASED ON THE

CONSTRAINED MODE MODEL WITH DELAMINATION AT DIFFERENT LOCATIONS: 1) $H2 = 0.5H, A = 0.1L$ *(A-B); 2)* $H2 = 0.5H, A = 0.15L$ *(C-D); 3)* $H2 = 0.5H, A = 0.2L$ *(E-F).* 134

FIGURE 3-5 THE NATURAL FREQUENCY OF THE BEAM WITH DIFFERENT DELAMINATION SIZES. 141

FIGURE 3-6 THE MODAL OBSERVABILITY (M_N) OF THE BEAM WITH DIFFERENT DELAMINATION SIZES. 142

FIGURE 3-7 THE SPATIAL OBSERVABILITY (S_O) OF THE FIRST THREE MODES. 143

FIGURE 3-8 THE RESPONSE OF OPTIMAL LOCATION X_0=0.73L. 144

FIGURE 3-9 THE FREQUENCY RESPONSE FUNCTION (FRF) OF OPTIMAL LOCATION X_0=0.73L. 145

FIGURE 3-10 THE FREQUENCY RESPONSE FUNCTION (FRF) OF LOCATION X_0=0.10L. 145

FIGURE 3-11 THE FREQUENCY RESPONSE FUNCTION (FRF) OF LOCATION X_0=0.50L. 145

FIGURE 3-12 THE NATURAL FREQUENCY OF THE BEAM WITH DIFFERENT DELAMINATION DEPTHS. 147

FIGURE 3-13 THE MODAL OBSERVABILITY (MN) OF THE BEAM WITH DIFFERENT DELAMINATION DEPTHS. 148

FIGURE 3-14 THE SPATIAL OBSERVABILITY (S_O) OF THE FIRST THREE MODES. 149

FIGURE 3-15 THE RESPONSE OF OPTIMAL LOCATION. 149

FIGURE 3-16 THE FREQUENCY RESPONSE FUNCTION (FRF) OF OPTIMAL LOCATION X_0=0.76L. 150

FIGURE 3-17 THE FREQUENCY RESPONSE FUNCTION (FRF) OF LOCATION X_0=0.10L. 151

FIGURE 3-18 THE FREQUENCY RESPONSE FUNCTION (FRF) OF LOCATION X_0=0.50L. 151

FIGURE 3-19 THE NATURAL FREQUENCY OF THE BEAM WITH DELAMINATION AT VARIOUS LOCATIONS. 152

FIGURE 3-20 THE MODAL OBSERVABILITY (M_N) OF THE BEAM WITH

DELAMINATION AT VARIOUS LOCATIONS. 154

FIGURE 3-21 THE SPATIAL OBSERVABILITY (S_O) OF THE FIRST THREE MODES. 155

FIGURE 3-22 THE RESPONSE OF OPTIMAL LOCATION. 156

FIGURE 3-23 THE FREQUENCY RESPONSE FUNCTION (FRF) OF OPTIMAL LOCATION X_0=0.76L 157

FIGURE 3-24 THE FREQUENCY RESPONSE FUNCTION (FRF) OF LOCATION X_0=0.10L. 157

FIGURE 3-25 THE FREQUENCY RESPONSE FUNCTION (FRF) OF LOCATION X_0=0.50L. 158

FIGURE 3-26 THE NATURAL FREQUENCY OF BEAMS WITH DIFFERENT DELAMINATION. 159

FIGURE 3-27 THE AVERAGE MODAL OBSERVABILITY (M_{NA}) OF BEAMS WITH DIFFERENT DELAMINATION. 161

FIGURE 3-28 THE SPATIAL OBSERVABILITY (S_{OA}) OF THE FIRST THREE MODES. 162

FIGURE 3-29 THE RESPONSE OF OPTIMAL LOCATION. 163

FIGURE 3-30 THE NATURAL FREQUENCY OF BEAMS WITH VARIOUS DELAMINATION SIZES AND DEPTHS. 164

FIGURE 3-31 THE AVERAGE MODAL OBSERVABILITY (M_{NH}) OF BEAMS WITH DIFFERENT DELAMINATION SIZES AND DEPTHS. 166

FIGURE 3-32 THE SPATIAL OBSERVABILITY (S_{OH}) OF THE FIRST THREE MODES. 167

FIGURE 3-33 THE RESPONSE OF OPTIMAL LOCATION. 168

FIGURE 3-34 THE NATURAL FREQUENCY OF THE BEAM WITH DIFFERENT DELAMINATION DEPTHS. 170

FIGURE 3-35 THE MODAL OBSERVABILITY (M_N) OF THE BEAM WITH DIFFERENT DELAMINATION DEPTHS. 172

FIGURE 3-36 THE SPATIAL OBSERVABILITY (S_O) OF THE FIRST THREE MODES. 173

FIGURE 3-37 THE RESPONSE OF OPTIMAL LOCATION. 174

FIGURE 3-38 THE FREQUENCY RESPONSE FUNCTION (FRF) OF OPTIMAL LOCATION. 175

FIGURE 3-39 THE FREQUENCY RESPONSE FUNCTION (FRF) OF LOCATION X_0=0.10L.

.....175

FIGURE 3-40 THE FREQUENCY RESPONSE FUNCTION (FRF) OF LOCATION X_0=0.50L.

.....176

FIGURE 3-41 THE NATURAL FREQUENCY OF THE BEAM WITH DIFFERENT DELAMINATION SIZES......178

FIGURE 3-42 THE MODAL OBSERVABILITY (M_N) OF THE BEAM WITH DIFFERENT DELAMINATION SIZES......179

FIGURE 3-43 THE SPATIAL OBSERVABILITY (S_O) OF THE FIRST THREE MODES...... 181

FIGURE 3-44 THE RESPONSE OF OPTIMAL LOCATION X_0=0.73L......182

FIGURE 3-45 THE FREQUENCY RESPONSE FUNCTION (FRF) OF OPTIMAL LOCATION X_0=0.73L......183

FIGURE 3-46 THE FREQUENCY RESPONSE FUNCTION (FRF) OF LOCATION X_0=0.10L.

.....183

FIGURE 3-47 THE FREQUENCY RESPONSE FUNCTION (FRF) OF LOCATION X_0=0.50L.

.....184

FIGURE 3-48 THE NATURAL FREQUENCY OF THE BEAM WITH DELAMINATION AT VARIOUS LOCATIONS......185

FIGURE 3-49 THE MODAL OBSERVABILITY (M_N) WITH DELAMINATION AT VARIOUS LOCATIONS......187

FIGURE 3-50 THE SPATIAL OBSERVABILITY (S_O) OF THE FIRST THREE MODES...... 188

FIGURE 3-51 THE RESPONSE OF OPTIMAL LOCATION...... 189

FIGURE 3-52 THE FREQUENCY RESPONSE FUNCTION (FRF) OF OPTIMAL LOCATION X_0=0.76L......190

*FIGURE 3-53 THE FREQUENCY RESPONSE FUNCTION (FRF) OF LOCATION X_0=0.10L*190

FIGURE 3-54 THE FREQUENCY RESPONSE FUNCTION (FRF) OF LOCATION X_0=0.50L.

.....190

FIGURE 3-55 THE NATURAL FREQUENCY OF BEAMS WITH DIFFERENT DELAMINATION SIZES AT VARIOUS LOCATIONS...... 192

FIGURE 3-56 THE AVERAGE MODAL OBSERVABILITY (M_{NA}) OF BEAMS WITH DIFFERENT DELAMINATION SIZES AT VARIOUS LOCATIONS...... 193

FIGURE 3-57 THE SPATIAL OBSERVABILITY (S_{OA}) OF THE FIRST THREE MODES......194

FIGURE 3-58 THE RESPONSE OF OPTIMAL LOCATION...... 195

FIGURE 4-1 THE PHASE SPACE RECONSTRUCTION OF TIME SERIES......202

*FIGURE 4-2 THE PHASE SPACE RECONSTRUCTED WITH DIFFERENT TIME DELAY T.*203

FIGURE 4-3 THE PHASE SPACE TOPOLOGY STRUCTURES OF POINTS......205

FIGURE 4-4 THE MODEL OF THE DELAMINATED BEAM......207

FIGURE 4-5 UNDAMAGED BEAM......209

FIGURE 4-6 BEAM WITH DELAMINATION SIZE $A/L = 0.1$..... 209

FIGURE 4-7 BEAM WITH DELAMINATION SIZE $A/L = 0.2$..... 210

FIGURE 4-8 BEAM WITH DELAMINATION SIZE $A/L = 0.3$..... 210

FIGURE 4-9 BEAM WITH DELAMINATION SIZE $A/L = 0.4$..... 210

FIGURE 4-10 THE RESULT OF DELAMINATION WITH DIFFERENT SIZES......211

FIGURE 4-11 THE CHANGE RATIO OF NATURAL FREQUENCY AND CPST......212

FIGURE 4-12 UNDAMAGED BEAM......214

FIGURE 4-13 BEAM WITH DELAMINATION DEPTH $H2 = 0.1H$..... 214

FIGURE 4-14 BEAM WITH DELAMINATION DEPTH $H2 = 0.2H$..... 215

FIGURE 4-15 BEAM WITH DELAMINATION DEPTH $H2 = 0.3H$..... 215

FIGURE 4-16 BEAM WITH DELAMINATION DEPTH $H2 = 0.4H$..... 215

FIGURE 4-17 THE RESULT OF DELAMINATION WITH DIFFERENT DEPTHS......216

FIGURE 4-18 THE CHANGE RATIO OF NATURAL FREQUENCY AND CPST...... 216

FIGURE 4-19 THE MODEL OF A COMPOSITE LAMINATE WITH DELAMINATION......219

FIGURE 4-20 THE UNDAMAGED RESULT...... 222

FIGURE 4-21 THE RESULT OF LAMINATE WITH DELAMINATION SIZE A=16MM...... 222

FIGURE 4-22 THE RESULT OF LAMINATE WITH DELAMINATION SIZE A=32MM...... 222

FIGURE 4-23 THE RESULT OF LAMINATE WITH DELAMINATION SIZE A=48MM...... 222

FIGURE 4-24 THE RESULT OF DELAMINATION WITH DIFFERENT SIZES......225

FIGURE 4-25 THE CHANGE RATIO OF TWO FEATURES OF DELAMINATION WITH VARIOUS SIZES......226

FIGURE 4-26 THE PHASE TOPOLOGY OF THE UNDAMAGED SAMPLE WITH DIFFERENT NOISE LEVELS......227

FIGURE 4-27 THE CHANGING TREND OF CPST WITH DIFFERENT NOISE LEVELS... 228

FIGURE 4-28 THE ARRANGEMENT OF THE EXPERIMENT......229

FIGURE 4-29 THE SAMPLES FOR EXPERIMENTS...... 230

FIGURE 4-30 SIMULATION RESULT (A-C) AND EXPERIMENT RESULT (D-F) OF NO.1 SAMPLE...... 232

FIGURE 4-31 SIMULATION RESULT (A-C) AND EXPERIMENT RESULT (D-F) OF NO.2 SAMPLE...... 232

FIGURE 4-32 SIMULATION RESULT (A-C) AND EXPERIMENT RESULT (D-F) OF NO.3 SAMPLE...... 233

FIGURE 4-33 THE CHANGING TREND OF EXPERIMENT AND SIMULATION...... 234

FIGURE 5-1 THE TREE-MAP OF 2 LEVEL WAVELET PACKET DECOMPOSITION......239

FIGURE 5-2 THE ORIGINAL SIGNAL AND THE SUB-SIGNALS AFTER WAVELET PACKET DECOMPOSITION......240

FIGURE 5-3 THE PROCEDURE OF THE PROPOSED METHOD BASED ON THE PHASE SPACE TOPOLOGY STRUCTURES AND WAVELET PACKET DECOMPOSITION.... 242

FIGURE 5-4 THE MODEL OF DELAMINATED BEAM...... 243

FIGURE 5-5 THE TIME DOMAIN SUB-SIGNAL (A-D) AND PHASE SPACE TOPOLOGY (E-H) OF EACH SUB-SIGNALS FROM THE UNDAMAGED BEAM...... 246

FIGURE 5-6 THE TIME DOMAIN SUB-SIGNAL (A-D) AND PHASE SPACE TOPOLOGY (E-H) OF EACH SUB-SIGNALS FROM THE BEAM WITH DELAMINATION SIZE $\mathrm{A}/\mathrm{L} = 0.1$..... 247

FIGURE 5-7 THE TIME DOMAIN SUB-SIGNAL (A-D) AND PHASE SPACE TOPOLOGY (E-H) OF EACH SUB-SIGNALS FROM THE BEAM WITH DELAMINATION SIZE $\mathrm{A}/\mathrm{L} = 0.2$..... 248

FIGURE 5-8 THE CHANGING TREND OF CPST RATIO FROM EACH SUB-SIGNAL FROM BEAMS WITH DIFFERENT SIZE DELAMINATION...... 249

FIGURE 5-9 THE TIME DOMAIN SUB-SIGNAL (A-D) AND PHASE SPACE TOPOLOGY (E-H) OF EACH SUB-SIGNALS FROM THE UNDAMAGED BEAM...... 252

FIGURE 5-10 THE TIME DOMAIN SUB-SIGNAL (A-D) AND PHASE SPACE TOPOLOGY (E-H) OF EACH SUB-SIGNALS FROM THE BEAM WITH DELAMINATION DEPTH

$H2/H = 0.1$.....253

FIGURE 5-11 THE TIME DOMAIN SUB-SIGNAL (A-D) AND PHASE SPACE TOPOLOGY (E-H) OF EACH SUB-SIGNALS FROM THE BEAM WITH DELAMINATION DEPTH $H2/H = 0.2$.....254

FIGURE 5-12 THE CHANGING TREND OF CPST RATIO FROM EACH SUB-SIGNALS FROM BEAMS WITH DIFFERENT DEPTH DELAMINATION......255

FIGURE 5-13 THE MODEL OF A COMPOSITE LAMINATE WITH DELAMINATION......257

FIGURE 5-14 THE TIME DOMAIN SUB-SIGNAL (A-D) AND PHASE SPACE TOPOLOGY (E-H) OF EACH SUB-SIGNAL FROM UNDAMAGED LAMINATE.....261

*FIGURE 5-15 THE TIME DOMAIN SUB-SIGNAL (A-D) AND PHASE SPACE TOPOLOGY (E-H) OF EACH SUB-SIGNAL FROM LAMINATE WITH A=16MM DELAMINATION.*262

*FIGURE 5-16 THE TIME DOMAIN SUB-SIGNAL (A-D) AND PHASE SPACE TOPOLOGY (E-H) OF EACH SUB-SIGNAL FROM LAMINATE WITH A=32MM DELAMINATION.*263

FIGURE 5-17 THE CHANGING TREND OF CPST RATIO FROM EACH SUB-SIGNALS FROM LAMINATE WITH DIFFERENT DELAMINATION SIZES...... 265

FIGURE 5-18 THE PHASE SPACE OF SUB-SIGNALS WITHOUT NOISE......267

FIGURE 5-19 THE PHASE SPACE OF SUB-SIGNALS WITH NOISE (SNR=10DB)......268

FIGURE 5-20 THE PHASE SPACE OF SUB-SIGNALS WITH NOISE (SNR=5DB)......268

FIGURE 5-21 THE CHANGING TREND OF CPST RATIO FROM EACH SUB-SIGNAL WITH DIFFERENT NOISE LEVELS......270

FIGURE 5-22 THE ARRANGEMENT OF THE EXPERIMENT......271

FIGURE 5-23 THE SAMPLE FOR EXPERIMENTS...... 272

FIGURE 5-24 THE PHASE SPACE TOPOLOGY OF EACH SUB-SIGNALS FROM SAMPLE NO.1 (SIMULATION (A-D) AND EXPERIMENT (E-H))......273

FIGURE 5-25 THE PHASE SPACE TOPOLOGY OF EACH SUB-SIGNALS FROM SAMPLE NO.2 (SIMULATION (A-D) AND EXPERIMENT (E-H))......274

FIGURE 5-26 THE PHASE SPACE TOPOLOGY OF EACH SUB-SIGNALS FROM SAMPLE NO.3 (SIMULATION (A-D) AND EXPERIMENT (E-H))......275

FIGURE 5-27 THE CHANGING TREND OF CPST RATIO FROM EACH SUB-SIGNALS

FROM LAMINATE WITH DIFFERENT DELAMINATION SIZES. 276

FIGURE 6-1 THE MODEL OF ANN. 281

FIGURE 6-2 THE PROCEDURE USING NATURAL FREQUENCY AND AMPLITUDE WITH ANN. 283

FIGURE 6-3 THE PROCEDURE OF THE PHASE SPACE METHOD WITH ANN. 284

FIGURE 6-4 THE PROCEDURE OF PHASE SPACE METHOD AND WAVELET PACKET DECOMPOSITION WITH ANN. 285

FIGURE 6-5 THE MODEL OF THE DELAMINATED BEAM. 286

FIGURE 6-6 THE MODEL OF A COMPOSITE LAMINATE WITH DELAMINATION. 291

FIGURE 6-7 THE TOP VIEW RESULT FOR SAMPLE NO.1. 293

FIGURE 6-8 THE TOP VIEW RESULT FOR SAMPLE NO.2. 294

FIGURE 6-9 THE SIDE VIEW RESULT FOR SAMPLE NO.1. 295

FIGURE 6-10 THE SIDE VIEW RESULT FOR SAMPLE NO.2. 296

FIGURE 6-11 THE TOP VIEW RESULT FOR SAMPLE NO.1. 298

FIGURE 6-12 THE TOP VIEW RESULT FOR SAMPLE NO.2. 299

FIGURE 6-13 THE SIDE VIEW RESULT FOR SAMPLE NO.1. 300

FIGURE 6-14 THE SIDE VIEW RESULT FOR SAMPLE NO.2. 301

FIGURE 6-15 THE TOP VIEW RESULT FOR SAMPLE NO.1. 303

FIGURE 6-16 THE TOP VIEW RESULT FOR SAMPLE NO.2. 304

FIGURE 6-17 THE SIDE VIEW RESULT FOR SAMPLE NO.1. 305

FIGURE 6-18 THE SIDE VIEW RESULT FOR SAMPLE NO.2. 306

TABLE INDEX

TABLE 2-1 THE 1ST MODE NATURAL FREQUENCY Ω (RAD/S) FOR DIFFERENT DELAMINATION SIZES..... 74

TABLE 2-2 THE 2ND MODE NATURAL FREQUENCY Ω (RAD/S) FOR DIFFERENT DELAMINATION SIZES..... 75

TABLE 2-3 THE 3RD MODE NATURAL FREQUENCY Ω (RAD/S) FOR DIFFERENT DELAMINATION SIZES..... 75

TABLE 2-4 THE 1ST MODE NATURAL FREQUENCY Ω (RAD/S) OF DIFFERENT DELAMINATION DEPTH..... 76

TABLE 4-1 THE PROPERTIES OF BEAM SAMPLES...... 207

TABLE 4-2 NATURAL FREQUENCY OF THE FIRST TWO MODES AND CPST FOR DIFFERENT DELAMINATION SIZES...... 208

TABLE 4-3 NATURAL FREQUENCY OF 1ST AND 2ND MODES AND CPST WITH DIFFERENT DELAMINATION DEPTHS...... 213

TABLE 4-4 THE PROPERTIES OF THE COMPOSITE LAMINATE..... 220

TABLE 4-5 NATURAL FREQUENCY OF 1ST AND 2ND MODES AND CPST WITH DIFFERENT DELAMINATION SIZES...... 221

TABLE 4-6 NATURAL FREQUENCY OF 1ST MODE AND CPST FOR CASES WITH DIFFERENT DELAMINATION...... 231

TABLE 5-1 THE PROPERTIES OF BEAM...... 244

TABLE 5-2 FREQUENCY RANGE OF COMPONENTS..... 244

TABLE 5-3 THE CPST OF SUB-SIGNALS WITH DIFFERENT DELAMINATION SIZES.... 245

*TABLE 5-4 THE CPST OF SUB-SIGNALS WITH DIFFERENT DELAMINATION DEPTHS.*251

TABLE 5-5 THE PROPERTIES OF THE COMPOSITE LAMINATE...... 258

TABLE 5-6 FREQUENCY RANGE OF COMPONENTS..... 258

TABLE 5-7 THE CPST OF SUB-SIGNAL FROM LAMINATE WITH DIFFERENT

DELAMINATION SIZE...... 259

TABLE 5-8 THE CPST OF SUB-SIGNAL FROM CASES WITH DIFFERENT DELAMINATION...... 272

TABLE 6-1 THE PARAMETERS OF SAMPLES...... 287

TABLE 6-2 THE RESULT OF SAMPLE NO.1...... 288

TABLE 6-3 THE RESULT OF SAMPLE NO.2...... 288

TABLE 6-4 THE RESULT OF SAMPLE NO.3...... 289

TABLE 6-5 THE PROPERTIES OF THE COMPOSITE LAMINATE...... 292

TABLE 6-6 THE ACCURACY FOR SAMPLE NO.1..... 309

TABLE 6-7 THE ACCURACY FOR SAMPLE NO.2..... 310

ABSTRACT

This research focuses on the investigation of delamination assessment in composite structures by using methods based on structural dynamic responses. Delamination is a common type of damages for composite structures in applications. It is necessary to detect and assess the delamination in composite structures to ensure the composite structures operating and maintaining. However, the dynamic responses of structures with delamination may be difficult to be analyzed due to the complexity of composite structures as the result of the different properties of materials in the composite structures. Therefore, it is necessary to develop effective methods for delamination analysis and assessment, which will be investigated in this research. To address these problems, this research aims to:

1. Develop new methodologies for dynamic analysis of delaminated composite structures to analyze the effect of delamination based on the evaluation of the vibration characteristics of composite structures with different delamination configuration;

2. Develop effective methodologies to detect and assess delamination in composite structures based on the dynamic responses by using the phase space topology analysis to improve the sensitivity and robustness of delamination assessment for composites structures;

To achieve these two aims, the research content and novelty are stated as:

1) Firstly, this study proposes a method based on the Green's function to develop analytical models of delaminated structures that can be used to investigate the effect generated by delamination on the vibration characteristics. The accuracy of this developed model to describe the vibration characteristics of delaminated beam structures especially under forced excitation is verified by the comparison with other types of models, including the numerical models. The result demonstrates the accuracy and advantages of the proposed analytical model to investigate the effect of delamination on the vibration characteristics of the beam structures under excitation of various frequencies with different delamination configurations, such as size, location, and depth. It should also be noted that the proposed modeling method is demonstrated useful to investigate the vibration characteristics of various measurement locations, which is important for the delamination assessment based on the dynamic responses of structures.

2) Secondly, based on the developed analytical model by using the Green's function, the investigation has been done for the effect of various measurement locations on the sensitivity to the particular vibration modes with various delamination configurations. Based on this situation, the methodology based on the modal observability (M_n) and the spatial observability (S_o) is proposed to optimize the structural sensor locations to make the measurement focusing on the vibration modes sensitive to the

delamination, which can improve the delamination assessment. The result demonstrates that the proposed methodology is effective to determine the sensor locations which can provide strong signals with sufficient distributions of the particular vibration modes sensitive to the delamination. So the optimization can improve the delamination assessment effectively based on providing sensitive vibration measurement locations.

3) Thirdly, a methodology based on the phase space topology analysis of the dynamic signals measured from the structures is proposed to assess delamination in composite structures. The phase space topology structures are evaluated by using a method named phase space reconstructed (PSR) method based on the dynamic signals measured by the dynamic sensors. A feature named the change of phase space topology (CPST) is used to describe the effect of delamination on the phase space topology structures. The result demonstrated that the phase space topology structures and CPST are sensitive to delamination. The robustness of the proposed feature to the measured noise has also been tested, which shows that the proposed method and feature have sufficient robustness to the measured noise in applications.

This research also improves the methodology to assess delamination based on the phase space topology analysis by incorporating with the wavelet packet decomposition. The wavelet packet method can decompose a

dynamic signal into several sub-signals in different frequency ranges, which may contain different local information relevant to the delamination. Then the phase space topology structures and the CPSTs of different sub-signals can be evaluated and investigated to analyze the local information. The phase space topology structures of sub-signals decomposed by the wavelet packet method can describe the change of energy distribution of sub-signals in different frequency ranges generated by the delamination. The possibility of the proposed method is demonstrated by the simulation and experiment and the proposed features will be used in the following work;

4) Based on the previous work, a method by using the artificial neural network (ANN) based on the phase space topology analysis to estimate delamination in structures is proposed tested. The ANN can be used to describe the relationship between the delamination and vibration characteristics to estimate the delamination without mechanism analysis for composite structures. The CPSTs of original signals and sub-signals decomposed by the wavelet packet method are used as input factors for the ANN to assess the delamination in composite structures. The accuracy of the ANN for the delamination assessment can be enhanced by training the ANN with more cases. The possibility and the potential are tested in this research. The different performances for various delamination parameters estimate are also analyzed, which shows that the performance for various

delamination parameter assessments is different due to the different effect of delamination on the input factors. Furthermore, the performance of delamination assessment by using the ANN with different input factors is investigated to analyze the effect of input factors on the delamination assessment performance and find the best input factors for ANN in this research. The results show the CPSTs of sub-signals generated by wavelet packet decomposition are the best input factors because this type of feature can provide more information with high sensitivity and good robustness to the measurement noise.

In conclusion, this research will provide a systematic study for the improvement of delamination assessment and development of applicable methods for composite structures based on the dynamic signals by analyzing the phase space topology structures combined with wavelet packet decomposition and ANN. Moreover, the theoretical analysis and optimization for dynamic signal measurement are analyzed to provide explanation and support for the delamination assessment. The potential of the proposed methods for other types of damage in composite structures and other applications are also mentioned in this research.

ACKNOWLEDGEMENT

Firstly, I wish to thank my supervisor, Associate Prof. Dunant Halim. He helped me a lot with my research direction and technical parts. He also showed me how to do a research professional. Only with his help and supervision, I can finish my work and solve the problems in these years. Appreciate his help and support in these years.

I also want to show my appreciation to my other supervisors, Associate Prof. Xiaoling Liu and Prof. Chris Rudd. They gave me a lot of help and support for my research and my life these years. Prof. Xiaoling Liu and Prof. Chris Rudd gave me a lot of support for my experiments. It would be impossible for me to finish this Ph.D. degree without their help.

I also appreciate the composite group lead by Prof. Xiaosu Yi, who provide the software and device for my research. I can get these achievements only supported by the group. Specifically, I wish to acknowledge Prof. Xiaosu Yi, Dr.Rob Pierce, Ning Su, Shuai Cheng, Mingqiang Jiang, Dongyuan Hu, and other members who help me with my research and my life.

I would also like to thank my teammate, Dr. Cong Gao, who help me with my research. With his generous help and accompany, I can finish my work and thesis writing. He is not just a teammate, but also a good friend. It is an honor for me to meet this friend during these years. Best wishes to him and his family.

My thanks also extended to my classmates, Mr. Lizhe He, Miss. Siqi Hao

and Mr. Sicong Yu. They are also my friends who help me with both research and life. They make my work and life wonderful. Best wishes to them.

I also want to thank the University of Nottingham, Ningbo, China (UNNC), and the International Academy for Marine Economy and Technology (IAMET). With their support, I got the opportunities to get knowledge and technologies. Moreover, I also have changes to communicate with scholars. I also need to show my appreciation to and the Faculty of Science and Technology (FoSE), who help me to solve the problems in my research and my life.

Finally, I would thank my other friends on campus and my life. I also appreciate my parents who support me without any requirements. Only with their help and support, I can finish my research. I love them.

Chapter 1 INTRODUCTION

1.1 Background

1.1.1 Delamination in Composite Structure

Composites structures have well-documented advantages such as high modulus, low density, corrosion resistance, and useful energy absorption. They are widely used in aviation and aerospace engineering [1, 2], civil infrastructure [3], biomedical devices [4], and energy conversion devices [5-7]. The mass percentages of polymer composites in the Airbus A-350 XWB and Boeing 787 aircraft are 52% and 50% respectively. Rolls-Royce Group also uses carbon fiber reinforced polymer (CFRP) composite to produce fan blades for its next-generation 'UltraFan' engine [8], reducing mass overall by 700kg. Moreover, composites can be used to create multiple function materials [9] and smart materials [10-13], which are used more and more widely in engineering applications.

For such critical applications, however stringent manufacturing quality control, it should be noted that structural damage is always a statistical possibility in service due to impact events, bird strikes, cyclic loading, and other reasons in applications. Detection and assessment of damage for composite structures are therefore critical to operational safety. The anisotropy and heterogeneity of composite laminates make damage assessment more complex than homogeneous materials [14]. Whilst established non-destructive techniques are available for composites, most of these are difficult or

impossible to apply in-situ. It also should be noted that there is considerable interest therefore in some form of condition monitoring to anticipate in-service failure, which is significant for composite structures application.

There are several types of damages in composite laminate structures [15] amongst which delamination is dominant in applications, such as drilling [16], impact [17], fatigue [18], and some other operations [19, 20]. Delamination will affect the properties and change the dynamic characteristics of structures [21, 22], including reducing natural frequency [23], change mode shape [24, 25], and enhancing deformation [26, 27]. Thus, the identification and assessment of delamination are essential for critical structures.

1.1.2 Analysis of the Dynamic responses of Delamination Structures

Before attempting to screen methods that can detect delamination, it is necessary to understand the effects of delamination on structures theoretically. This research focuses especially on the effect of delamination on the dynamic responses of beam structures and composite laminated panel structures.

Researchers have analyzed the dynamic responses of delaminated beams and investigated the effect of delamination on the beam structures theoretically as mentioned above. There are two general models to simulate the delaminated beam structures, which are called ‘free mode’ model [28] and ‘constrained mode’ model respectively [29]. These two models have been proved analytically and experimentally. The previous results of these two

models indicate that the vibration characteristics will be affected by the delamination, including natural frequency [28-30], mode shapes [31], and dynamic responses [32], which are the result of the changes generated by delamination on the properties of structures, such as stiffness reduction and damping enhancing. Furthermore, other studies used a piecewise-linear spring model to simulate the interaction between surfaces in the delamination region to improve the analysis of delaminated beams [33, 34]. These works indicate that the delamination will generate complex dynamic responses and nonlinear vibration behavior.

Other researchers investigated the delaminated beam numerically. Hasan et al. [35] used contact elements within commercial finite element method (FEM) software ANSYS® to model delaminations and validated the model by compared with analytical models and experiments. Their research indicates that the increasing delamination area reduces the natural frequency and changes the mode shapes of beams due to the stiffness reduction and local deformation of sub-beams. Ju et al. [36] analyzed the dynamic responses of composite beams with delaminations under forced vibration. They used the finite element method (FEM) to conduct modal analysis and investigated the change of response with fixed-free boundary conditions and fixed-fixed boundary conditions respectively. The delamination region was simulated by a node-to-node contact model. The results indicate that the closer the delamination is to the surface of the beam, the more significant the effect on its dynamic responses. It should be noted that both frequency response and impulsive response were affected by delamination, while the effect is different and related to the excitation. Ostachowicz et al. [37] investigated the dynamic

responses of delaminated beams numerically. In their work, the model was simulated based on higher-order shear deformation theory and solved by the finite element method (FEM). They found some additional resonant peaks generated by periodic closing and opening of the delamination region in frequency response function (FRF), which means there are new modes. However, the additional resonant peak would disappear under forced impulse because of the strong intrinsic viscoelastic damping. The transverse displacements were sensitive to both delamination location and length. In a related study, Manoach et al. [38] simulated sub-laminates in contact with each other using elastic foundation elements. The result highlighted additional damping due to interforce and interaction in the delaminated region. Others investigated the response of delaminated beams under moving load [27, 39-41] finding, unsurprisingly, that delamination changes beam deflections due to lower flexural stiffness. However, the analysis of beam structures with delamination still needs to be improved due to the development of complicated models and the theoretical methods.

Similar studies for panel structures have also been reported. Adrian et al. [42] used higher-order theory and a transformation matrix to analyze the dynamic responses of composite plates with delaminations. The natural frequency was reduced as the delamination length increased, which is similar to beam structures. Miroslav et al. [43] analyzed laminated composite plates with embedded delaminations using layerwise plate theory. They investigated the effect of delamination size and position on the dynamic characteristics of the plate with different plate geometry, lamination scheme, and degree of orthotropy. In their conclusion, all these parameters will affect the vibration

characteristics. Moreover, they also find that the delamination generates new modes due to the local deformation of delaminated areas, which are called ‘local mode’ seeded by the inclusion of delaminations. Jinho et al. [44] investigated composite plates with multiple delaminations. They investigated the laminated plate with delamination based on higher-order zigzag theory. The solution was provided by the finite element method (FEM). They indicated that the simulation of delaminated plates by using the FEM still needed to be improved due to the complex interaction between surfaces of the sub-beams in delaminated regions. Susmita et al. [45] investigated the dynamic responses of damped composite laminated plates with embedded delaminations. They developed a finite element model for laminate plates based on the layerwise theory. This model also added springs to prevent interpenetration of surfaces in the delaminated region. Based on the result, they indicate that the delamination also affected the damping of structures due to the interaction of the delamination regions, such as friction between interfaces. These researches illustrate that the effect of delamination on structural dynamic responses is complex and difficult to be analyzed. Therefore, the theoretical analysis and models of plate structure need to be improved. Moreover, the result of the previous work above all can be used as a guideline and explanation for the following parts of this research.

1.1.3 Damage Detection Method for Composite Structures

As introduced above, damage detection based on the structural dynamic responses in laminated composites structures is complicated due to the difficulty and complexity of dynamic responses. Non-destructive evaluation (NDT) and structural health monitoring (SHM) of composite structures have both been developed over many years to improve the accuracy and feasibility of damage detection for composites [46, 47]. The methods can be categorized as follows:

1.1.3.1 Vibration-based Methods

As already established, the damage will change the vibration responses of composite structures and the effect can be used to detect damage. These vibration-based methods used dynamic characteristics to detect damage, include natural frequency, dynamic response characteristics, mode shapes, curvature mode shape, and hybrids thereof [48, 49]. The vibration-based methods can be used for large structures and real-time structural health monitoring (SHM) during the operation. It should also be noted that these methods are easy to use and cost-effective with cheap devices. Therefore, vibration-based methods are used widely in the damage detection of composite structures.

Tate et al. [50] detected delamination in a beam based on natural frequency deviation. They correlated delamination length with natural frequency changes. As elsewhere, they indicate that the natural frequency

decreased with longer delaminations due to the stiffness reduction generated by delamination. Chen et al. [51] confirmed these effects, adding delamination location and depth as variables. Their works indicate that these parameters can be estimated by using natural frequency. Then Zhang et al. [52] used a natural frequency-based method combined with inverse algorithms to estimate the delamination parameters in composites. They used frequency shifts combined with three different algorithms to detect and calculate delamination, including the graphical method, the artificial neural network (ANN) method, and the surrogate-based optimization method. Predictions were validated for a cantilever carbon fiber reinforced beam. In a further study, Zhang et al. [53] also used the natural frequency approach augmented by a new surrogate assisted optimization (SAO) method to improve detection and to estimate based on the change of natural frequency. Validation experiments demonstrated the accuracy of the method. They also used natural frequency as the damage index to detect delamination in curved laminates combined with two inverse algorithms: the artificial neural network (ANN) and the surrogate assisted genetic algorithm (SAGA) [54]. They estimated the parameters of delamination by using these two algorthims based on natural frequency changes. The sensitivity to the damage and the robustness to the noise were also demonstrated in these works for damage detection based on the natural frequency of structures.

Other researchers used mode shapes and curve mode shapes to detect delamination in composite structures. Qiao et al. [55] used PZT (lead–zirconate–titanate) actuator to generate vibrations and measured the curvature mode shape by the scanning laser vibrometer (SLV) and the

polyvinylidene fluoride (PVDF) sensor to detect and locate delamination due to the local deformation and local modes generated by delamination. Cao et al. [56] used a novel multiscale shear-strain gradient analysis for the mode shapes of the plate to detect and locate delaminations. Xu et al. [57] proposed the use of complex-wavelet two-dimensional (2D) curvature mode shapes as the indicator to detect and represent the delamination. They also proposed a new damage indicator for delamination location based on the mode shapes which are sensitive to the delamination and robust to the noise and disturbance [58]. The damage indicator was introduced by a 2D multi-resolution modal Teager-Kaiser energy operator, which is calculated based on the mode shapes. This method is proven by detection delamination in a carbon fiber-reinforced polymer (CFRP) laminates plate. Based on this proposed indicator, the researchers could detect delamination based on mode shapes to enhance the accuracy of damage and reduce sensitivity to noise.

Amongst other studies, researchers developed more dynamic features to detect damage in composite structures. Emil et al. [59] used Poincaré maps of vibration signals to detect damage with temperature variations. In different situations, the shape of Poincaré maps will change due to the amplitude of vibration signals changing. Asif et al. [60] used the deep learning ANN to classify and predict delamination in laminate based on dynamic responses of structures. They measured low-frequency vibration data and used a method named Short Time Fourier Transform (STFT) to process and analyze the response. This method can transform the one-dimension signal into a two-dimensional spectral frame representation, which can be used as the input factor for the deep learning ANN. Then based on these obtained data, they

calculated the damage by a convolutional neural network (CNN). This method showed a classification accuracy of 90.1%. These researches show that more vibration characteristics and methods for dynamic analysis can be used to detect damage in structures. The researches illustrate the potential of vibration-based methods with more new features for delamination detection and assessment.

However, previous researchers mentioned that the sensitivity of vibration-based methods for damage detection to small defects and high noise levels still require improvement as mentioned by several authors [61-64].

1.1.3.2 Guided Wave Methods

Guided wave is another method used widely in structural damage detection [65], including the damage in composite structures [66]. It is widely acknowledged as one of the most encouraging tools for the quantitative identification of damage in composite structures. Guided wave methods for damage detection offer these features [65]: (1) the detection region by using guided wave can be large; (2) the guided wave method can provide information of cross-section of the detection area; (3) the sensitivity and accuracy of the guided wave is good to multiple damages in structures; (4) the lack of devices for guided wave methods to detect damage; (5) the guided wave method is easy to be used with great cost-effectiveness.

To understand the damage detection based on guided wave methods, some researchers analyze the response of guide waves in the composite structures. Siavash et al. [67] detected delamination detection by low frequency guided wave based on the simulation. They proposed a new model

for composite laminate by locally reducing the stiffness to generated the delamination. Then they test the performance of low frequency guided wave for delamination detection. By comparing the result with two existing approaches, the accuracy of the proposed model was verified for guided wave detection. Moreover, they also tried to improve the simulation of damage detection by using guided waves based on the finite element models. They indicate that convergence criteria should be modified and developed to improve the performance of simulation for delamination detection based on the guided wave method for large composite structures, such as wind turbine blades. Luca et al. [68] also proposed a Finite Element (FE) model to simulate the structural health monitoring (SHM) system for real-time damage detection of complex composite structures based on the guided wave method. They compared the result of this model with the experiment to show the accuracy and credibility of this model. Then they used this model to test the feasibility of the guided wave for damage detection and SHM of composite with damage generated by different applications. The simulation and analysis of guided wave to detect and assess damage in composite structures are useful for the application.

Following the simulation about the guided waves, Yelve et al. [69] used Lamb waves to detect delamination in composite laminates, simulated by Teflon film inserts. This work showed the feasibility and credibility of guided waves to detect delamination. It also should be noted that the proposed guided waves were found to be affected by sensor location. Therefore, it is important and significant to choose the location of the sensor to use the guided wave method to detect delamination. While the proposed method based on the

guided wave to detect delamination was demonstrated by both simulation and experiment. In this work, the authors also indicated that the contact between the delamination region is nonlinear, which should be noted and important for delamination detection. This phenomenon was also mentioned in other works. Reza et al. [70] used guided waves to locate delamination in laminate composite beams. They also indicate that the delamination will affect the guided wave and generated nonlinear dynamic responses due to the interaction in the delamination region. This phenomenon should be noted in the following work.

Some researchers tried to improve the detection performance of guide wave methods. Zhao et al. [71] used ultrasonic guided waves to monitor delamination in composite laminates. They prepared a composite double cantilever beam with delamination and used the guided wave signal to detect the delamination combined with three algorithms: Hilbert transform, Fourier transform, and wavelet transform. These three algorithms can be used to analyze and process the guided wave signal to improve the performance of detection with noise. Yu et al. [72] proposed a type of guide wave named ultrasonic feature guided wave to detect damage in quasi-isotropic composite bends. Bo et al. [73] also used a new guided wave named chirp-excited lamb wave to detect delamination in composite structures. This result shows the advantages of these new guided waves and the potential for the development of new methods based on the guided waves.

However, the guided wave method still has limitations for composite structure damage detection. Because of the wave reflection and absorption of interlayers between different materials, the detection region of this method is

limited, and the sensitivity of the guided wave still needs to be improved. Also, the mode of guided waves will have different sensitivity to the damage in composites and the generation of new mode guided waves due to the damage is difficult in practice. Furthermore, multiple damage detection and type recognition remain difficult by using guided wave methods.

1.1.3.3 Ultrasonic Methods

Ultrasound is a well-known approach to detect damage in composites structures and has been in use since the 1940s. Ultrasonic waves are reflected at damage sites, thus the damage can be pinpointed by analyzing changes to the waveform. These methods are active and sensitive to the damage in structures which are effective and can be used for many structures.

Sun et al. [74] used a laser ultrasonic technique to detect delamination in aeronautical composite structures. They used the ultrasonic wave generated by laser technology to scan a carbon fiber reinforced plastic laminate with artificially created delamination. This method can locate delamination in structures with no touching. Duan et al. [75] also used an ultrasonic testing method to detect and analyze the impact damage of carbon fiber reinforced polymer (CFRP) panels. Sedeghi et al. [76] used a double-side ultrasonic assessment to detect and analyze damages of CFRP under the low-velocity impacts. They used double-side Phased-array Ultrasonic Testing to detect damage of CFRP with different energy impacts, which can enhance the sensitivity and reduce the effect of the ultrasonic wave absorption. Their work showed that this arrangement and design for the ultrasonic probe can improve the detection range and accuracy.

Moreover, some researchers want to improve damage detection performance by ultrasonic testing. Teng et al. [77] used recurrence analysis to improve the damage detection for thick multilayer composites by ultrasonic scans. The method enhanced the sensitivity of ultrasonic testing methods and reduced the effect of noise, which improved the identification of blind holes. Hauffe et al. [78] tried to improve the damage detection based on the ultrasonic wave method by using several algorithms, including a pixel count algorithm, a Convex Hull algorithm, a Support Vector Machine algorithm, and a Snake algorithm. The result shows that these algorithms are useful to analyze the ultrasonic signals and improve damage detection by using ultrasonic methods indeed. Short-time Fourier transform analysis was also used to improve damage detection based on ultrasonic scans [79]. A multi-frequency ultrasonic testing method was also adopted to detect delamination to enhance the sensitivity of the ultrasonic method due to the different sensitivity of the different frequency signals to the damage [80]. Some new methods are also developed to improve the performance of ultrasonic testing, such as an ultrasonic phased array method [81] and the time of flight diffraction method [82, 83]. These methods show the ongoing evolution of ultrasonic techniques for damage detection in composites.

However, the limitation of ultrasonic testing methods is obvious. Because the composite structure is made of two or more types of material, the interlayer between different materials will reflect ultrasonic waves which will generate disturbance and noise to affect the damage detection for composite structure [77]. Moreover, the detection region is also limited by the devices and absorption of different materials and interlayers in composite structures

[76]. High-frequency ultrasonic waves are difficult to be used for damage detection in composite structure due to that it is heterogeneous, which is necessary for small size damage [84]. Furthermore, the cost of an ultrasonic method is also one limitation for its application in composite structures [85].

1.1.3.4 Acoustic Emission Methods

Acoustic Emission (AE) is widely used for damage detection and structure monitoring [86-88]. This method is useful and effective for its capability of real-time monitoring over the whole material volume with high sensitivity to damage. It is also easy to be used due to simple devices.

Mailad et al. [89] used the AE method to analyze delamination in composites laminates. Their work shows that AE is a powerful approach in determining the position of the delamination. Lenka et al. [90] analyzed delamination using acoustic emission methods under various environmental conditions. They investigated the delamination growth of composite with different temperatures to test and analyze its properties by AE methods. The result showed the accuracy and ability of AE methods with different temperatures. Anvar et al. [91] used AE to monitor the buckling delamination growth. They used using Gaussian Mixture Model (GMM) to classify the acoustic emission signals to detect damage. The result shows that the AE method is robust to detect damage and classify damage mechanisms.

Other researchers tried to improve the AE method. Yu et al. [92] used acoustic emission to identify the damage in a composite laminate. The Fiber-optic Bragg Grating (FBG) sensors were used to measure acoustic emission signals generated by delamination. This type of sensor is small, and

it can be used in different environments. Kang et al. [93] used AE methods to monitor the delamination failure of composites. In this work, the AE signal was analyzed and decomposed by the empirical mode decomposition to get more information for the delamination. Moreover, the AE methods were also used to recognize the damage mode in composite structures, which is important and special for composite structures, which will generate different types of damage [94, 95].

However, the AE method also has some limitations for damage detection in composites structures. Since it is a passive method, it needs extra load on the composite structure and the procedure cannot be interrupted or reproduced [86]. It also should be noted that the AE methods cannot provide quantitative characterization such as dimensions of damage [84].

1.1.3.5 Other Methods

Because damage will affect the thermal properties of structures. It is possible to detect damage in composite structures by analyzing the changing of thermal behaviors and the thermoelastic response of structures. Ghademazi et al. [96] used step-phase thermography (SPT) to detect delamination in glass-epoxy composites. Shi et al. [97] used laser thermography to detect delamination in carbon fiber reinforced polymer (CFRP) laminate. Such methods detect the damage in structure based on thermal properties which are related to the material and affected by the damage. Ayad et al. [98] also used thermoelastic response mapping to detect delamination in glass fiber reinforced polymer (GFRP). Simulation and experiments have been done to test the possibility of this method. Wang et al. [99] detect delamination based

on the temperature distribution by using differential spread laser infrared thermography (DSLIT).

The electrical properties of composite structures are also likely to be affected by structural damage, which can be used to detect damage. Wandowski et al. [100] used the electromechanical impedance method (EMI) as the damage index to detect delamination in CFRP panels. Ryosuke et al. [101] detect delamination in composite structures based on the change of electric signals changing. They used a method named crack swarm inspection to improve the delamination location and estimate, which is to simulate the damage as a group of cracks. These cracks will affect the electrical properties of structures. They used this method and model to detect the delamination based on the change of voltage. Pegorin et al. [102] used z-pins to detect delamination in composites based on conductance which would be affected by delamination. Han et al. [103] used THz spectroscopy and imaging to detect multi-delamination in glass fiber reinforced polymer (GFRP) composite structure.

These methods mentioned above are possible to detect and diagnose the damage in composite structures. However, it should also note that the device of these methods is expensive and difficult to control. It also should be noted that these methods just can be used to detect damage in special materials and structures, which limits the applications of these methods.

1.2 Introduction of Proposed Methods

This research will investigate the effect of delamination on the dynamic responses of beams by using the Green's function method for the delamination assessment testing and optimization of measurement locations.

This research also aims to enhance the sensitivity and robustness of the vibration-based methods to detect delamination in composite structures by analyzing the phase space topology structures of dynamic responses with wavelet methods and the artificial neural network (ANN). Here is the introduction of the proposed methods:

1.2.1 Green's Function Method

In contrast with previous methods, the Green's function method has a generally reliable performance for forced vibration analysis because it uses relatively simple formulation whilst providing analytical solutions directly without any approximating. This method can be used for dynamic responses analysis of beams under various excitation, including distributed load [104, 105], moving load [106], and concentrated load [107]. M. Abu-Hilal [107] used the Green's function method to solve the forced vibration of beams with various boundary conditions and concentrated harmonic excitation. This work tested the credibility of the proposed method based on the Green's function for the forced vibration analysis of beams. They solved the dynamic responses of

beams with various damping under different excitation. They also compared their result with the previous work using approximate methods and indicated that the Green's function method was more accurate due to no ignoring. Then Kukla et al. [108] used this Green's function method to solve the vibration of loaded stepped beams. They calculated the natural frequencies of stepped beams with various axis loads and showed the accuracy of the Green's function method. They investigated the effect of axis load on the natural frequency of beams. Li et al. [109] investigated how the damping effect on the forced vibration of Timoshenko beams based on the Green's function method. They used the Green's function method to solve the dynamic responses with various boundary conditions and investigated the effect of damping on the dynamic responses. Zhao et al. [110] analyzed the forced vibration of the Euler-Bernoulli beam with crack based on the Green's function and investigated the effect of crack on the dynamic responses. They simulated the crack in the beam as local stffness and divided the beam in different parts. They investigated the effect of crack size on the vibration characteristics and verified the accuracy of the Green's function methods by both FEM and experiments. This work demonstrates the Green's function method is useful for damaged beams. These works illustrate that the Green's function can solve the dynamic responses with simple equations theoretically. Therefore, it is possible to solve the dynamic responses of delaminated beams theoretically.

1.2.2 Phase Space Method for Dynamic responses Analysis and Damage Detection

Phase space methods are used widely in signal analysis in many fields, including dynamic systems, electric systems, thermal systems, and so on. The phase space topology structures can be used to analyze the system, estimate the parameters, and forecast the behavior. Especially, the phase space topology structure is widely used to show the information and motion of unstable and nonlinear dynamic responses of structures. An example of a nonlinear dynamic system named Duffing oscillator is shown as follow:

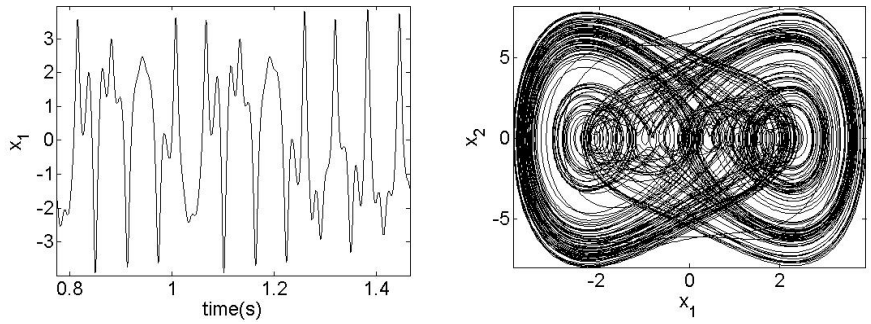

(a) Time domain signal; *(b) Phase space topology structure.*

Figure 1-1 The dynamic responses of the Duffing system [111].

As shown in Figure 1-1, the time domain signal of the Duffing oscillator is difficult to be analyzed, while the phase space topology structure is easy to be investigated to find the mechanism of systems with regular shape. For dynamic responses in applications, it is difficult to be analyzed in the time domain generally, while the phase space topology structures can reveal the mechanism of the dynamic systems, especially the nonlinear target. The similar nonlinear dynamic responses generated by composite structures are also common in applications [112, 113], so these methods based on the phase

space topology analysis are useful for dynamic responses analysis of composite structures. It should also be noted that the phase space topology structures contain all information about dynamic systems, including the change. Therefore, it can be used to detect damage by analyzing the phase space topology structure, which will be affected by structural damages. Previous work has demonstrated that these methods are sensitive to the change of signal and generally resistant to noise. Therefore, researchers analyzed the phase space topology structure of signals to investigate the targets [114].

However, the multiple dimension phase space topology needs at least two types of variates. In engineering applications, it is common to measure one type of variate, which is difficult to construct the phase space topology directly of target systems. For this situation, the Phase Space Reconstructed method was proposed by Takens, to construct the phase space trajectory of dynamic systems based on just one type of dynamic signal [115]. This method can reconstruct the multiple dimension phase space topology structure of dynamic systems with any one type of signal from target structures. Then the dynamic systems with different situations can be analyzed by the phase space method.

1.2.2.1 The Phase Space Topology Structure of Dynamic responses

Following the previous researches, researchers analyzed the phase space topology structures of dynamic responses to detecting damage. Todd et al. [116] used the change of phase space topology structure geometry of vibration

signals to detect and analyze the damage in systems. They built an eight-degree freedom system by springs, mass, and dampers. Then they changed the stiffness of the spring to make the damage. Chaotic excitation was used to drive the system and the phase space topology structure of both input and output was viewed in state space. They used a phase space feature named local attractor variance-ratio to detect damage in systems. The proposed method has high sensitivity and the results revealed the feasibility and good performance of this method. The sensitivity of the proposed method is good. Nichols et al. [117] also used chaotic excitation and phase space features to monitor a cantilever beam. They explored the utility of a phase space feature named attractor-based approaches to improve the performance of damage detection based on vibration signals. These researches show the potential of phase space methods for damage detection.

Nie et al. [118] used the phase space method to detect damage in an arch. They used the phase space reconstructed method to analyze the vibration signal of the arch. A new feature named Change of Phase Space Trajectory (CPST) was used as the index to describe the phase space attractor and analyze the damage in the arch. The sensitivity to the damage and resistance to the noise was investigated and tested by both simulation and experiment. They also used the proposed method and feature to detect and locate damage in concrete [111]. The result shows that the proposed method is more sensitive to damage and resistant to noise compared with previous vibration-based methods. Liu et al. [119] also proposed a new method based on the geometrical variation of phase space transient trajectories to detect the damage. A framework was used as the target to test the method and the proposed

method was test by both simulation and experiment. The improvement generated by the analysis of phase space topology structure is clear for vibration-based methods to detect structural damages.

1.2.2.2 The Phase Space Topology Structures of Nonlinear Signals

Furthermore, some researchers also used the phase space methods to analyze the nonlinear systems for damage detection because of the sensitivity of nonlinear systems to the change of dynamic responses and resistance to noise and disturbance [120]. The nonlinear systems are sensitive to the change of the input signal, while it is complicated to be analyzed. However, the phase space topology structures of the nonlinear dynamic responses are easy to be used to reveal the mechanism of the nonlinear systems. Therefore, it can be used to improve the performance of signal capture, dynamic analysis, and damage detection by investigating the phase space topology structures of nonlinear dynamic systems. Based on these properties, some researchers used nonlinear systems to improve vibration-based damage detection methods by incorporating phase space topology analysis methods. Song et al. [121] used a nonlinear oscillator named Duffing-Holmes oscillator to analyze the acoustic emission signal from cutting processing for tool wear detection. The acoustic signal was captured by the Duffing-Holmes oscillator. Then based on the change of its phase space topology, the information of damage in acoustic signals can be detected and estimated. Andreaus et al. [113] detected damage by analysis of nonlinear characteristics of forced response from beams. They

investigated the nonlinear dynamic responses generated by damage in phase space from the beams under harmonic excitation to identify the damage and estimate the size. Liu et al. [122] used a nonlinear lamb wave method to detect and locate delamination in structure. The nonlinear lamb wave was more sensitive to the damage than the linear type as they mentioned. Then the wave signal was analyzed in phase space by a special feature named Lyapunov exponent which was also used as the damage index. The resistance to noise and sensitivity to the damage was demonstrated by experiments. Zhang et al. [123] used nonlinear oscillators to analyze the guided wave from different structures to capture the change in wave signal and identify the damage in the pipe structure. The change is clearer and easier to be captured by inputting the signal into the nonlinear oscillator and analyzing by the phase space methods. These researches mentioned above all demonstrated the feasibility and advantages of signal analysis based on the phase space method for both linear and nonlinear dynamic systems. The potential of the phase space methods combined with nonlinear systems is also showed by the previous works.

1.2.2.3 The Phase Space Topology Structures for Other Applications

Researchers also analyzed the phase space topology structures of various signals for other applications. Jose et.al. [124] analyzed the phase space topology of the thermal response to estimate the thermoregulatory of Pig. The previous researches also reconstructed the phase space topology of the electric signal for short term load forecasting (STLF) for the electric system, which is

useful and important for efficiency and cost. The STLF is complicated and nonlinear due to a lot of effect factors. However, this problem can be solved by the phase space methods which are useful for nonlinear systems. Similarly, the wind forecasting can also be solved by the phase space topology structures analysis [125, 126]. Some researchers also analyzed the electroencephalogram (EEG) signals to investigate the Brain activities, which are nonlinear [127, 128]. This result can be used for brain-computer interface (BCI) applications. Ryabov et al. [129] also analyzed the phase space topology structure of classical molecular dynamics to investigate the liquid water trajectory. The phase space topology analysis was also used for chemical reaction investigation to reveal their nonlinear response [130]. All these responses are nonlinear and complicated, so it is useful to analyze their phase space topology structures. These applications demonstrate the potential of the phase space topology structures combined with other signals for various systems analysis, which shows the possibility of the phase space topology analysis to investigate the multiple fields signals and functional composite structures.

1.2.3 Other Methods

1.2.3.1 Wavelet Method

The wavelet method is used widely to analyze signals, which is called ‘numerical microscope’ [131]. It can decompose the signal into different levels with different frequency ranges. Based on this property, the signals can be divided into different sub-signals with special frequency ranges, and each of the sub-signals may contain the local information which is weak and

covered in original signals. Then the local information can be got by analyzing the sub-signals in special frequency ranges which will be easier and clearer than original signals in all frequency range. Moreover, the wavelet method also can filter the noise in signals, which has different frequencyies with useful signals. Therefore, this method reduces the cost of signal analysis and enhances the sensitivity to the weak signal and small damage [132].

1) Wavelet Method for Vibration Signal Processing

As shown above, the damage will affect and change the vibration characteristics and dynamic responses of structures. However, the change of vibration responses and characteristics is weak due to the small size and effect of the damage. Therefore, the wavelet method is used to detect damage by decomposing the vibration signals and analyze the sub-signals in different frequency ranges [61]. The result indicates that the wavelet methods are the potential for damages identification of different materials and different damage-structure varieties based on vibration signals and characteristics.

Some researchers used wavelet methods to process the mode shapes to detect damage. Chiariotti et al. [133] used the wavelet method to process the mode shapes to detect damage. The mode shapes are provided by Continuous Scanning Laser Doppler Vibrometer (CSLDV), which is affected by delamination. This method detected and located delamination by using wavelet methods to decompose the mode shapes and find the local deformation generated by delamination. Liu et al. [134] used an empirical wavelet thresholding method to detect faults in the blade bearings based on the vibration signal. The researchers used a wavelet method called empirical

wavelet thresholding to remove the noise and extract weak fault signals for the improvement of damage detection. The diagnostic results show that the proposed method is effective for damage detection of large-scale wind turbine blade bearings. Sha et al. [135] used the wavelet method to analyze the mode shape of laminated composite beams to detect damage. They used the wavelet transform (WT) to analyze mode shapes of the laminated beam to find the local deformation generated by damages. The credibility and accuracy of the proposed method are tested experimentally on cracked laminated composite beams. Jie et al. [136] also used the wavelet method to analyze mode shapes to detect damage in composite laminates with cutouts, which can locate the damage in structures.

Other studies used the wavelet methods to decompose the vibration signals and analyze the energy distribution and spectrum of the sub-signals to detect damage. Y.J et al. [137] used a wavelet packet method to detect delamination in composites plate. They used the energy spectrum of sub-signals generated by wavelet methods as the index to represent the delamination size, which was sensitive to the delamination. The proposed method was demonstrated consistently both in simulation and experiment. Wei et al. [138] also used the wavelet packets method to detect delamination in composite based on the energy spectrum. They analyzed the modal parameters from the samples with different delamination and used the wavelet packet method to decompose the dynamic responses of structures by several levels in different frequency ranges. They also indicated that this method depended on the vibration modes activated in applications. Then Hein et al. [139] used artificial neural networks (ANNs) to improve delamination

detection based on the vibration responses of structures by using wavelet methods. They used ANNs to estimate the damage in structure by using the features generated by wavelet methods from the dynamic responses as input factors. These researchers show the feasibility and advantage of wavelet methods for improvement of the vibration-based damage detection for this research.

2) Wavelet Method for Other Signals Processing

Moreover, the wavelet method is also used to analyze other types of signals for damage detection. Feng et al. [73] used lamb wave and wavelet analysis to detect delamination. In this paper, the lamb waves were input into structures and received by sensors with the information of delamination. Then the information was measured and investigated by wavelet analysis of received lamb waves. Their works tested and shown the feasibility and credibility of the proposed method for different delamination cases. Legendre et al. [140] used the wavelet method to improve the ultrasonic signal to detect damage in composites structures. They used the wavelet method to polish the A-scan signal with disturbance and constructed the C-scan based on the new A-scan signal processed by wavelet methods.

Elena et al. [141] also used the wavelet method to reduce the disturbance and improve the ultrasonic signal and detect damage in complex titanium/carbon fiber composite joints which was complicated to analyze. Other researchers also used the wavelet method to reduce the noise for ultrasonic detection improvement, because the noise frequency is generally different from signals frequency [142-144]. The wavelet method is also used

to improve the digital image correlation (DIC) technique to improve the damage detection performance by reducing the noise [145]. These researchers proved the potential of the wavelet method in different types of signal processing and damage detection improvement based on these signals for further research.

1.2.3.2 Artificial Neural Network

Artificial Neural Networks (ANNs) are designed following the idea of the function and mechanism of biological neurons in the human brain. By learning from a set of given data, ANNs can predict and classify the unknown data without theoretical analysis. Therefore, the ANNs are useful to investigate complicated systems and complex relationships, which are difficult to be analyzed and revealed. The ANNs can be used for data analysis [146], dynamic responses analysis [147], and damage detection [148]. An ANN is composed of three parts, including the input layer, the hidden layer, and the output layer. Figure 1-2 shows a typical structure of the ANNs:

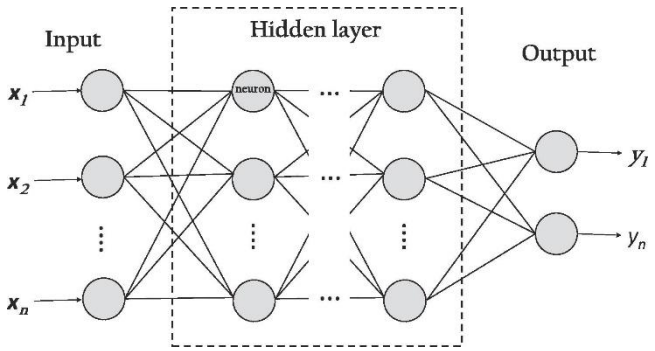

Figure 1-2 The structure of Neural Network [148].

The ANN is used widely in image recognition, signal classification, and

model establishing. It can be used for both linear and nonlinear systems. Therefore, it is a good choice for damage assessment and classification. Many researchers used these methods and demonstrated their feasibility for damage detection.

1) ANN for Damage Detection and Estimate based on Vibration Signals

Researchers used vibration signals and characteristics as the input factors for damage detection based on the ANN because of the advantages of vibration signals to the damage, such as sensitivity and resistance to the disturbance. Chakraborty et al. [149] presented a method based on the ANNs. The proposed method used ANN to predict and detect delamination in laminated by learning the natural frequencies as indicative parameters. A fiber-reinforced plastic composite laminate was used as the target to test this method in simulation. The result showed that the ANNs can identify the damage and estimate its parameters, such as size, shape, and location. Khan et al. [60] also used a deep learning neural network to analyze the structural vibration responses to detect delamination based on vibration characteristics processed by using the Short-Time Fourier Transform (STFT) method as mentioned above.

Yam et al. [62] combined wavelet transform and neural network to analyze the vibration of composites structures to identify the damage. They used wavelet transform to improve the estimate of the ANN by processing vibration characteristics as input factors. Chathyrdara et al. [150] used vibration characteristics, including natural frequency and mode shapes, as

input factors to detect damage based on an ANN named autoencoder neural networks. After trained by a lot of data, the relationship between vibration characteristics and structural damage was learned by the ANN. Then the ANN can identify and estimate damage based on the vibration characteristics. Khairul et al. [151] used a non-probabilistic artificial neural network to detect damage based on vibration signals. This method was used for a steel frame and it identified the damage in the structures. Osama et al. [64] proposed a method based on one-dimensional convolutional neural networks with vibration signals to detect delamination in structures. Tan et al. [152] used modal strain energy as input factors for ANN to detect damage in a steel beam. This proposed method was tested by simulation and experiments. Gu et al. [153] used natural frequency and temperature as input factors to improve damage detection under varying temperatures by using ANN at the same time. This proposed method eliminated the temperature effects on the damage detection by using ANN. The research used a steel grid structure as the sample to indicate the advantage and credibility of ANN to estimate the damage with various temperature conditions. Chen et al. [154] combined impact-synchronous modal analysis (ISMA) and ANN to improve the damage detection in a rectangular Perspex plate. The ISMA de-noising method can reduce noise to improve the frequency response function and vibration characteristics calculation, which was used as input factors for ANN to classify the damage states with high accuracy usefully. In their research, the accuracy of some cases can be even 100%. These researches demonstrated the possibility and advantages for damage detection based on neural network by using vibration signal as input factors. It is potential to detect delamination by

the ANN method combined with vibration signal and other methods, which will be used in this research.

2) ANN for Damage Detection and Estimate based on Other Signals

ANN also can identify the damage by classifying other types of signal data from targets. Any signal related to the damage can be used as input factors for ANNs. Yao et al. [155] used a convolutional neural network to detect and recognize the corrosion damage in hull structures. They used ANN to recognize corrosion damage based on the corrosion images as input data. The proposed method was proved by detecting the corrosion in the structures, which illustrated the potential of ANN for damage detection by classifying the images. Davide et al. [156] used ANNs to analyze the acoustic emission (AE) signal to detect damage and predict its evolution. The results showed that the ANN could correctly classify the specimens with different situations based on the AE signals. Piotr et al. [157] used ANN to process lamb waves signal to detect damage in aluminum and composite element. In this work, the Auto-associative Neural Network was used to classify the lamb wave signals to detect the damage in the structure.

Seo et al. [158] used electrical resistance as the input factor for ANN to detect damage in carbon fiber reinforced polymer (CFRP) laminates. The experiment demonstrated the credibility and accuracy of the artificial neural network for damage detection. Mario et al. [159] used Electromechanical Impedance (EMI) as the input signal to detect damage based on ANN. They analyzed two types of ANN, simplified fuzzy ARTMAP Network (SFAN) and

Probabilistic neural network (PNN), for damage detection. Their research showed that these two ANNs can detect damage by EMI. While the performance of SFAN was better than PNN. Kim et al. [160] used a magnetic flux leakage (MFL) method to detect damage in wire-rope by combining with ANN.

Furthermore, with parameters of structures, the ANN can also predict the response and damage in different applications. Eileen et al. [161] used ANN to predict fatigue damage generated by vortex-induced vibration (VIV) as input factors. Six main parameters were used as input factors: riser outer diameter, wall thickness, top tension, water depth, surface, and bottom current velocity. By being trained with a lot of data, this research estimated the damage by using the ANN. Karnik et al. [162] used ANNs to analyze the delamination in carbon fiber reinforced plastics (CFRP) generated by high-speed drilling. They used ANNs to analyze and predict the delamination based on drilling process parameters as input factors. The parameters include the spindle speed, feed rate, and point angle of drilling. A multilayer feed-forward ANN architecture was employed for this purpose and these parameters from a lot of cases were used to train ANNs. This method was tested by experiments and the result demonstrated the advantage of employing higher speed in controlling the delamination during drilling. Zhang et al. [163] used a parameter called the equivalent stress intensity factor as the input factor to train a radial basis function (RBF)-ANN to evaluate the fatigue crack in aluminum alloy specimens. These researches demonstrated the feasibility and advantages of the ANN for damage detection and prediction with various types of input factors, which can be used for further research.

1.3 Research Gaps

Based on the literature review above, it can be observed there are still several challenges for delamination analysis and assessment for the composite structures that need to be addressed as follows:

(a) Because the delamination is a type of local damage, which will reduce the local stiffness and change the local deformation of structures [22, 36, 39], the effect of delamination on the different parts of structures is various. It is necessary to investigate how delamination affects the vibration characteristics of composite structures. However, for the analysis of the effect generated by the delamination on the structures, some previous work just investigated the effect of delamination on the global vibration characteristics of structures, such as natural frequency and mode shape [22, 164, 165], which are the global properties of structures. The other researchers analyzed the dynamic responses of delaminated structures, but they used numerical methods [36] and approximate methods [27, 39], which have cited limitations to reveal the localized effect of delamination to the structures. Currently, there is limited work to develop analytical models to investigate the change of vibration characteristics of the structures with different delamination configurations under excitation of various frequencies, which need to be analyzed;

(b) Due to the local effect of the delamination, the vibration characteristics of different parts of the structures have various changing trends with various delamination configurations, which make the sensitivity of the different parts of structures being various. Therefore, it is necessary to optimize the measurement locations to find the best measurement locations that allow the dynamic signals from these locations to be sensitive to the different delamination parameters. However, most of the previous work focused on the optimization of measurement for intact beams. Limited work investigated the optimization of sensor location for delaminated beams with considering the effect of delamination on the structures, which need to be developed;

(c) The effect of damage on the dynamic responses of composite structures is more complicated than the effect of homogeneous structures due to more components and materials with different properties. It also should be noted that there are more types of damage in composite structures, which is different from homogeneous structures. Therefore, the sensitivity of previous damage detection methods is not enough for delamination in the composite structures [14, 47]. The effect generated by delamination may be covered and affected by the interaction between different components in composite structures and other types of damage since the delamination is a type of local damage, which will just make weak changes in the global properties of structure when the delamination size is small. However, the previous work using the

global dynamic features to assess the delamination cannot identify the delamination with small size due to the effect is not sufficient to affect the global features, such as natural frequency and mode shapes [48]. While most work investigates the effect of damage on the global features, which can provide limited sensitivity to the delamination in the composite structures. Previous work also indicates that different situations may make the same features used as damage index due to the same effect on the same properties, such as natural frequency [48]. So it will make errors to assess damage based on these features and methods because it is impossible to recognize different situations by the same features. Therefore, it is necessary to improve the vibration-based methods and develop new features with higher sensitivity and better accuracy to the delamination in the composite structures;

(d) Moreover, the damage detection methods for composite structures need to be resistant to measured noise in applications that cannot be avoided, which will affect the accuracy of delamination assessment. The noise may cover useful signals about damage and change the features which are used to identify and assess the damage. Therefore, noise can generate significant influences on delamination detection and assessment for composite structures. It is necessary to develop new methods and new features resistant to noise to reduce the effect of disturbance on the performance of delamination assessment.

1.4 Aim and Objective

Aim 1: Develop a new method based on the Green's function to analyze the delaminated beams structures and investigate the effect of delamination on the dynamic responses of different parts in the beams

For this purpose, there are several objectives:

1) Propose new analytical modeling methods based on the Green's function with the ability to investigate the free vibration and forced vibration of the beams with different delamination configuration;
2) Investigate the effect of delamination on the vibration characteristics and the dynamic responses of different parts in beams to reveal the relationship between the delamination and the vibration characteristics of various measurement locations in beams;
3) Develop an optimization methodology for the measurement locations of the beams by considering the effect of delamination to improve the delamination assessment;

Aim 2: Develop a new applicable method based on the phase space topology structures incorporating with wavelet packet decomposition and ANN to assess delamination in composite structures;

To achieve this aim, several objectives need to be done:

1) Analyze the phase space topology structures of dynamic responses from composite structures with various delamination to test the sensitivity and the robustness of the proposed vibration-based methods by using the phase space topology structures and provide

useful features as damage index;

2) Analyze the phase space topology structures of sub-signals generated by the wavelet packet method from the dynamic responses of composite structures to test the possibility of the proposed methods based on the phase space topology analysis and provide more useful features with different local information about delamination in composite structures to improve the accuracy of delamination assessment based on vibration signals;

3) Use the artificial neural network (ANN) to estimate the delamination parameters in structures by using proposed damage indexes as input factors to test the possibility of the methods based on the ANN for delamination assessment and investigated the effect of different input factors on the performance of delamination assessment to find the best input factors in this research;

1.5 Research Novelty and Significance

The main contributions of this research are:

1. Developing an analytical model based on the Green's function can investigate the effect of delamination on the vibration characteristics of the structures. This research will analyze the dynamic responses of delaminated beams and investigate the effect of delamination on the dynamic responses under concentrated harmonic excitation by using the analytical model based on Green's function methods. In applications,

forced vibration is common and it is useful for damage detection due to the effect generated by damage. However, most previous work only evaluates the global vibration characteristics, such as natural frequency and mode shapes. Other research provides approximate analytical solutions and numerical solutions of the dynamic responses of delaminated beams [40, 166, 167]. Compared with previous work, the Green's function method can solve the dynamic responses of delaminated beams under harmonic excitation theoretically without any approximating. The result shows that the dynamic responses are affected by the delamination and related to the locations of antinodes and nodes of mode shapes.

2. The investigation of the measurement location optimization for the vibration signal from beams with various delamination can improve the delamination assessment based on the vibration characteristics. The optimization of vibration measurement focused on the intact structure and ignored the effect of damage. This research will optimize the measurement locations by considering the delamination parameters. The possibility of the proposed method will be tested and demonstrated for delaminated beams. The result shows that the optimization of measurement locations is affected by different delamination parameters. The optimization can enhance the sensitivity and robustness of the vibration-based methods for delamination detection and assessment by providing optimal measurement location which can measure strong signals with a high distribution of vibration modes sensitive to the delamination;

3. The development of new methodologies based on the phase space topology analysis improves the delamination assessment based on the dynamic responses, this research will also investigate the effect of delamination on the phase space topology structures of dynamic responses. As mentioned above, the phase space topology analysis can show the information of dynamic systems, including the change generated by damage. It contains useful information about structures, including the damage. The phase space topology structures are sensitive to the change in the signals and robust to the noise due to the phase space topology structures related to both frequency and amplitude of dynamic signals. Based on these properties, the sensitivity and robustness to the measured noise can be improved by analyzing the phase space topology structures of dynamic responses and using the features of phase space as the damage index. This research will provide potential methods to improve the delamination assessment based on the dynamic responses with high sensitivity and good robustness.

4. Moreover, the development of the new methodology based on the phase space topology analysis combined with wavelet packet decomposition can improve the accuracy of delamination assessment. As shown in previous work, the wavelet methods can decompose the vibration signals into several sub-signals with different frequency ranges, which will contain the different local information of structures and damages. By analyzing the phase space topology structures and calculating the features of sub-signals, it can provide more information and details of the delamination in the composite structures, which may be weak and covered in the original

signals. This proposed method can provide a series of features that can show the effect of delamination on the energy distribution in the sub-signals in different frequency ranges. This will improve the accuracy of the delamination assessment based on the vibration signals effectively by avoiding the mistakes generated by the methods based on only one feature.

5. Finally, the development of a new applicable method using artificial neural networks (ANNs) can assess delamination based on the proposed features for various composite structures. As mentioned above, the artificial neural network can analyze the relationship and classify the result without theory and mechanism. It can establish nonlinear mathematic modeling between input and output to reveal the relationship between input factors and targets. Therefore, it is useful to assess damage in composite structures which are difficult to be analyzed as mentioned above due to the complexity. Furthermore, the performance of the ANN to assess delamination by using different input factors is different due to different sensitivity, robustness, and accuracy. The effect of three different types of input factors will be investigated and compared to find the best input factors, including the two proposed features in this research.

1.6 The Structure of Thesis

The structure of the thesis is as follows:

1) **Chapter 1** reviews previous work relating to the analysis of delaminated structures and delamination assessment. This chapter also

reviews the application and advantages of the researches about the Green's function methods, the phase space topology analysis, the wavelet method, and the artificial neural network (ANN), all of which are incorporated in subsequent work;

2) **Chapter 2** proposes the analysis model based on the Green's function and shows the analytical result of the delaminated beams for free vibration and forced vibration;

3) **Chapter 3** optimizes the location for dynamic signal measurement locations and shows the benefit of the optimization for vibration signals measurement;

4) **Chapter 4** then analyze the effect generated by various delamination on the phase space topology of dynamic responses and the CPST. The sensitivity and robustness to the noise of the proposed methods and feature are demonstrated and tested;

5) **Chapter 5** seeks to refine the delamination detection and assessment based on the phase space topology of vibration signals by incorporating the wavelet packet decomposition method to enhance the accuracy of delamination assessment following the result in Chapter 4. The sensitivity and robustness of the proposed method based on the phase space topology analysis combined with wavelet packet decomposition will be tested as well as the feasibility;

6) **Chapter 6** uses an artificial neural network (ANN) to estimate and locate the delamination in structures by using the proposed index mentioned in previous chapters to test the possibility of the ANN to estimate the delamination parameters. Moreover, the estimated result based on ANN results with three types of input factors will be compared to investigate the effect of input factors on the performance of ANN;

7) **Chapter 7** sets out the conclusions from this research. The conclusions are summarized in this chapter, the potential and the direction for the future work of the proposed methods are also indicated;

Chapter 2 A THEORETICAL MODEL OF DELAMINATED BEAM STRUCTURES BASED ON THE GREEN'S FUNCTION METHOD

This chapter will investigate the effect of delamination on a homogeneous beam under forced excitation. For delamination assessment based on structural vibration, it is necessary to investigate the effects of delamination on structural dynamic responses. Some researchers have analyzed the delaminated structure and investigated the effect of delamination on the dynamic responses of structures as described in Chapter 1. However, it also indicates that most analysis for delaminated beams is calculating the vibration characteristics, such as natural frequency and mode shapes. The other analysis for dynamic responses under excitation is using approximate approaches and numerical methods, which can not provide accurate results. Therefore, this chapter will improve the previous work and investigate how the delamination affects the dynamic responses of beams by using the Green's function method. The Green's function method can develop analytical models to solve the dynamic responses of beams under harmonic excitation compared with previous work. Based on the theoretical analysis of the dynamic responses for delaminated beams, the result can provide the mechanism and

explanation for delamination assessment in the following chapters.

2.1 Analysis of Delaminated Beams

2.1.1 Model of Delaminated Beams

In this section, the modeling of a delaminated beam and the procedure of solution for forced vibration responses based on the Green's function method is proposed. As mentioned in [22], both the free mode model and the constrained mode model can be used to predict the dynamic responses for delaminated beams. Some researchers indicate that the constrained mode model is closer to the experiment [31], while others also show the splits between the sub-beams in the delamination region consistent with the free mode model by the experiment [30]. Researchers indicate that the change of the vibration characteristics generated by delamination calculated based on the constrained mode model is generated by the stiffness reduction, while the free mode model's effect is the result of stiffness reduction and different thickness of sub-beams in delaminated beams [22]. Therefore, both these two models need to be considered to simulate the beams with various delamination. The following part will analyze the result based on the two models both.

A beam model with single delamination is shown in Figure 2-1. As noted in the figure, there is delamination over the width of the beam and it divides the beam into four sub-beam parts. Here, sub-beam 1 and sub-beam 4 are the left and right intact parts, while sub-beam 2 and sub-beam 3 are the respective

upper part and lower part of the delaminated region.

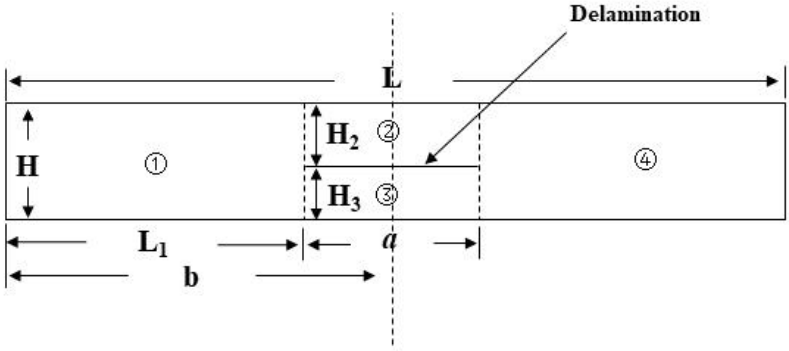

Figure 2-1 The model of a beam with delamination.

2.1.1.1 The Free Mode Model

The 'free mode' of a delaminated beam indicates that the delamination region parts (sub-beam 2 and sub-beam 3 in Figure 2-1) are free and the deformation of them is different [28]. For this particular model, the beam is divided into 4 sub-beams and the governing equations of each sub-beam can be described using the classical Euler-Bernoulli beam theory as:

$$EI_i \frac{\partial^4 u_i}{\partial x^4} + c\frac{\partial u_i}{\partial t} + \rho A_i \frac{\partial^2 u_i}{\partial t^2} = F_i(x,t), (i = 1,2,3,4) \quad (2\text{-}1)$$

where EI_i is the bending stiffness of the ith sub-beam, ρ is mass density, and A_i is the cross-sectional area of the i-th sub-beam and c is the attenuation coefficient related to the damping of the materials. Consider $F_i(x,t)$ as a harmonic excitation force applied to the beam in the following form:

$$F_i(x,t) = F_i(x)e^{i\omega t}, \quad (2\text{-}2)$$

where the ω is drive frequency. The solution of equation (2-1) can then be represented as:

$$u_i(x,t) = u_i(x)e^{i\omega t}. \tag{2-3}$$

Substituting equation (2-2) and (2-3) into equation (2-1), the following formulation can be obtained:

$$\frac{\partial^4 u_i}{\partial x^4} - k_i^4 u_i = f_i(x),\ (i = 1,2,3,4) \tag{2-4}$$

where $k_i^4 = \frac{\omega^2 \rho A_i - ic\omega}{EI_i}$ and $f_i(x) = \frac{F_i(x)}{EI_i}$ for the i-th sub-beam.

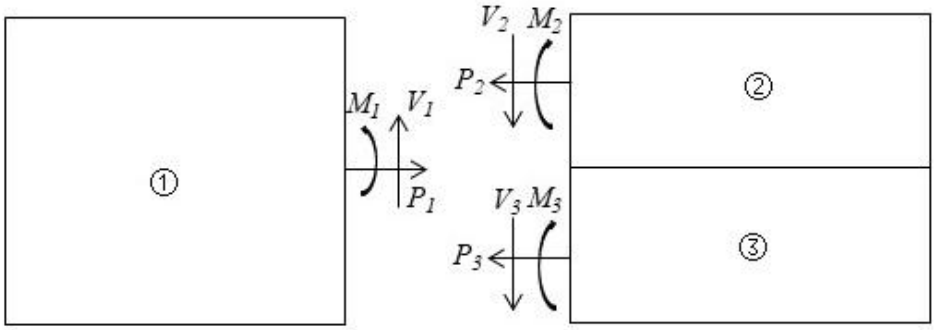

Figure 2-2 The continuity of shear force and bending moment at $x = L_1$.

The continuity conditions of sub-beams 1-3 at $x = L_1$ can be described in Figure 2-2. For satisfying the continuity conditions, the sub-beams 1-3 must be the same deflection and slope, which can be described as:

$$u_1 = u_2, \tag{2-5a}$$

$$u_1^{'} = u_2^{'}. \tag{2-5b}$$

$$u_1 = u_3, \tag{2-6a}$$

$$u_1^{'} = u_3^{'}. \tag{2-6b}$$

The continuity for shear force and bending moment at $x = L_1$ as shown in Figure 2-2 can be described as:

$$V_1 = V_2 + V_3, \tag{2-7}$$

$$M_1 = M_2 + M_3 + P_2(\frac{H_2}{2}) + P_3(H_2 + \frac{H_3}{2}), \quad (2\text{-}8)$$

where

$$V_i = -EI_i u_i''', \quad (2\text{-}9)$$

$$M_i = -EI_i u_i''. \quad (2\text{-}10)$$

Here, the parameter P_i describes the axial force which is generated by the compatibility for the stretching/shortening of the delaminated layers and it can be solved by the equation as follows [28, 164]:

$$\frac{P_3 a}{E_3 A_3} - \frac{P_2 a}{E_2 A_2} = (u_1'(L_1) - u_4'(L_2))\frac{H_2+H_3}{2}, \quad (2\text{-}11)$$

$$P_1 = P_2 + P_3 = 0. \quad (2\text{-}12)$$

Then equations (2-7) and (2-8) can be expressed as

$$EI_1 u_1''' = EI_2 u_2''' + EI_3 u_3''', \quad (2\text{-}13)$$

$$EI_1 u_1''(L_1) + \frac{(H_2+H_3)^2 E_2 A_2 E_3 A_3}{4a(E_2 A_2 + E_3 A_3)} \times (u_1'(L_1) - u_4'(L_2)) = EI_2 u_2''(L_1) + EI_3 u_3''(L_1). \quad (2\text{-}14)$$

At location $x = L_2$ ($L_2 = L_1 + a$, which is the point between sub-beam 2/3 and sub-beam 4), similar continuity conditions of sub-beams 2-4 can be used:

$$u_4 = u_2, \quad (2\text{-}15a)$$

$$u_4' = u_2'. \quad (2\text{-}15b)$$

$$u_4 = u_3, \quad (2\text{-}16a)$$

$$u_4' = u_3'. \quad (2\text{-}16b)$$

$$EI_4 u_4''' = EI_2 u_2''' + EI_3 u_3'''. \quad (2\text{-}17)$$

$$EI_4 u_4''(L_1) + \frac{(H_2+H_3)^2 E_2 A_2 E_3 A_3}{4a(E_2 A_2 + E_3 A_3)} \times (u_1'(L_1) - u_4'(L_2)) = EI_2 u_2''(L_1) + EI_3 u_3''(L_1). \quad (2\text{-}18)$$

Considering the beam's boundary conditions are set as clamped-clamped, the following formulation is used:

$$u_1(0) = 0, \quad (2\text{-}19a)$$

$$u_1'(0) = 0. \quad (2\text{-}19b)$$

$$u_4(L) = 0, \quad (2\text{-}20a)$$

$$u_4'(L) = 0. \quad (2\text{-}20b)$$

Therefore, there are 16 equations from (2-5), (2-6), (2-13), (2-14), (2-15)-(2-20), that used to develop the 'free mode' model.

2.1.1.2 The Constrained Mode Model

For the constrained mode model of the beam structure, the delamination is considered to be 'closed', so the displacements of sub-beam 2 and sub-beam 3 are constrained to one another and they must be the same, where $k_2^4 = k_3^4 = (\omega^2\rho(A_2+A_3) - ic\omega)/(EI_2+EI_3)$ for sub-beams 2 and 3 in equation (2-4) [29]. Therefore, equation (2-4) can be formulated as:

$$\frac{\partial^4 u_i}{\partial x^4} - k_i^4 u_i = f_i(x), (i = 1,2,4) \quad (2\text{-}21)$$

The continuity conditions for deflection and slope at $x = L_1$ are described by

$$u_1 = u_2, \quad (2\text{-}22a)$$

$$u_1' = u_2'. \quad (2\text{-}22b)$$

The continuity conditions for shear and bending moment, considering the axial force at $x = L_1$, are [164]:

$$EI_1 u_1'''(L_1) = (EI_2 + EI_3) u_2'''(L_1). \quad (2\text{-}23)$$

$$EI_1 u_1''(L_1) + \frac{(H_2+H_3)^2 E_2A_2E_3A_3}{4a(E_2A_2+E_3A_3)} \times (u_1'(L_1) - u_4'(L_2)) = (EI_2 + EI_3) u_2''(L_1). \quad (2\text{-}24)$$

At $x = L_2$, the same continuity conditions are given as:

$$u_4 = u_2, \quad (2\text{-}25a)$$

$$u_4' = u_2'. \quad (2\text{-}25b)$$

$$EI_4 u_4'''(L_2) = (EI_2 + EI_3) u_2'''(L_2). \quad (2\text{-}26)$$

$$EI_4 u_4^{''}(L_2) + \frac{(H_2+H_3)^2 E_2 A_2 E_3 A_3}{4a(E_2A_2+E_3A_3)} \times (u_1^{'}(L_1) - u_4^{'}(L_2)) = (EI_2 + EI_3) u_2^{''}(L_2). \quad (2\text{-}27)$$

The clamped-clamped boundary conditions are described by:

$$u_1(0) = 0, \quad (2\text{-}28a)$$

$$u_1^{'}(0) = 0. \quad (2\text{-}28b)$$

$$u_4(L) = 0, \quad (2\text{-}29a)$$

$$u_4^{'}(L) = 0. \quad (2\text{-}29b)$$

Therefore, there are 12 equations from equations (2-22) to (2-29) associate with the 'constrained mode' model.

2.1.2 The Green's Function

The Green's function of the four sub-beams could be determined by these equations as follow, which is come from the method proposed as [107]:

$$\frac{\partial^4 G_i(x,\xi)}{\partial x^4} - k_i^4 G_i(x,\xi) = \frac{\delta(x-\xi)}{EI_i}, \quad (2\text{-}30)$$

where $G_i(x,\xi)$ describes the Green's function of each sub-beam due to a concentrated load at an arbitrary position located at ξ. In equation (2-30), the Dirac function has the following property:

$$\int_0^L F_i(\xi)\, \delta(x-\xi) d\xi = F_i(x). \quad (2\text{-}31)$$

Based on this property and equation (2-31), the solution of equation (2-4) can be solved using the solution of equation (2-30):

$$\int_0^L F_i(\xi)\, G_i(x,\xi) d\xi = u_i(x), \quad (2\text{-}32)$$

while the equation (2-30) could be solved by using the Laplace transform method:

$$\widehat{G}_i(s,\xi) = \frac{1}{(s^4-k_i^4)} \left[\frac{e^{-s\xi}}{EI_i} + s^3 G_i(0) + s^2 G_i^{'}(0) + s G_i^{''}(0) + G_i^{'''}(0)\right], (i = 1,2,3,4.) \quad (2\text{-}33)$$

The expression for the Green's function is obtained from the inverse Laplace transform:

$$G_i(x,\xi) = \frac{\varphi_{4i}(x-\xi)H(x-\xi)}{EI_i k_i^3} + G_i(0)\varphi_{1i}(x) + \frac{G_i^{'}(0)}{k_i}\varphi_{2i}(x) + \frac{G_i^{''}(0)}{k_i^2}\varphi_{3i}(x) + \frac{G_i^{'''}(0)}{k_i^3}\varphi_{4i}(x), \quad (2\text{-}34)$$

where $H(.)$ represents the Heaviside function and

$$\varphi_{1i}(x) = \frac{1}{2}(\cosh(k_i x) + \cos(k_i x)), \quad (2\text{-}35a)$$

$$\varphi_{2i}(x) = \frac{1}{2}(\sinh(k_i x) + \sin(k_i x)), \quad (2\text{-}35b)$$

$$\varphi_{3i}(x) = \frac{1}{2}(\cosh(k_i x) - \cos(k_i x)), \quad (2\text{-}35c)$$

$$\varphi_{4i}(x) = \frac{1}{2}(\sinh(k_i x) - \sin(k_i x)), \quad (2\text{-}35d)$$

with the above functions having the following relationships:

$$\varphi_{1i}^{'} = k_i\varphi_{4i}, \varphi_{1i}^{''} = k_i^2\varphi_{3i}, \varphi_{1i}^{'''} = k_i^3\varphi_{2i}, \quad (2\text{-}36a)$$

$$\varphi_{2i}^{'} = k_i\varphi_{1i}, \varphi_{2i}^{''} = k_i^2\varphi_{4i}, \varphi_{2i}^{'''} = k_i^3\varphi_{3i}, \quad (2\text{-}36b)$$

$$\varphi_{3i}^{'} = k_i\varphi_{2i}, \varphi_{3i}^{''} = k_i^2\varphi_{1i}, \varphi_{3i}^{'''} = k_i^3\varphi_{4i}, \quad (2\text{-}36c)$$

$$\varphi_{4i}^{'} = k_i\varphi_{3i}, \varphi_{4i}^{''} = k_i^2\varphi_{2i}, \varphi_{4i}^{'''} = k_i^3\varphi_{1i}, \quad (2\text{-}36d)$$

Substituting equations (2-35) and (2-36) into equations (2-5)-(2-6), (2-13)-(2-14), (2-15)-(2-20) and (2-22)-(2-29), the following equation in a matrix form can be obtained:

$$T(\omega)X = S. \quad (2\text{-}37)$$

where the $T(\omega)$ is a 16×16 matrix for the 'free mode' or 12×12 for the 'constrained mode' which is dependent on the drive frequency ω as shown in the Appendix. Here, X is an unknown 16×1 vector for the 'free mode' or 12×1 for the 'constrained mode' as shown in the respective equations (2-38a) and (2-38b), which need to be solved to describe the beam deformation. S is

a 16×1 vector for the 'free mode' or 12×1 for the 'constrained mode' that is dependent on ξ as shown in the Appendix.

$$X = \left[G_1(0) \quad G_1^{'}(0) \quad G_1^{''}(0) \quad G_1^{'''}(0) \quad G_2(0) \quad G_2^{'}(0) \quad G_2^{''}(0) \quad G_2^{'''}(0) \right.$$
$$\left. G_3(0) \quad G_3^{'}(0) \quad G_3^{''}(0) \quad G_3^{'''}(0) \quad G_4(0) \quad G_4^{'}(0) \quad G_4^{''}(0) \quad G_4^{'''}(0)\right], \text{(2-38a)}$$

$$X = \left[G_1(0) \quad G_1^{'}(0) \quad G_1^{''}(0) \quad G_1^{'''}(0) \quad G_2(0) \quad G_2^{'}(0) \right.$$
$$\left. G_2^{''}(0) \quad G_2^{'''}(0)) \quad G_4(0) \quad G_4^{'}(0) \quad G_4^{''}(0) \quad G_4^{'''}(0)\right], \qquad \text{(2-38b)}$$

2.2 Free Vibration Responses of a Delaminated Beam

This section will calculate the vibration characteristics of the beams with various delamination by using the Green's function to test the accuracy and feasibility of this proposed method for vibration analysis. In this work, a rectangular delaminated beam structure is used for a case study, with clamped-clamped boundary conditions. The delamination is set over the width of the beam. For the general analysis, the natural frequency is normalized by using $\omega = \sqrt{(\rho A/EI)L^4}\omega_0$ as mentioned in a previous reference [28]. For the free vibration case, equation (2-37) is simplified as there is no driving force applied to the beam:

$$T(\omega)X = 0. \qquad \text{(2-39)}$$

The formulation in equation (2-34) can thus be simplified as:

$$G_i(x,\xi) = G_i(0)\varphi_{1i}(x) + \frac{G_i^{'}(0)}{k_i}\varphi_{2i}(x) + \frac{G_i^{''}(0)}{k_i^2}\varphi_{3i}(x) + \frac{G_i^{'''}(0)}{k_i^3}\varphi_{4i}(x). \qquad \text{(2-40)}$$

Based on the non-trivial solution of X, the matrix T must satisfy the

following equation:

$$\det(T(\omega)) = 0. \tag{2-41}$$

Then the natural frequency could be obtained as well as mode shape by equations (2-39) to (2-40). To verify the model, comparisons have been made with previous analytical results calculated by classical beam theory [164] and numerical results solved by finite element methods (FEM) [168] based on the free mode model and the constrained mode model for homogeneous beams with delamination. Table 2-1 shows the natural frequency ω with different normalized delamination size replaced as a/L. The normalized depth was set as $H_2 = H/2$ and the axial location of delamination was at *L1=(L-a)/2* (i.e. $b = L/2$), which means the delamination is in the middle span of the beam. The result is shown in Tables 2-1 to 2-3.

Table 2-1 The 1st mode natural frequency ω (rad/s) for different delamination sizes

a/L	**Analytical** [164]	**FEM** [168]	**Free mode**	**Constrained mode**
0	22.37	22.36	22.37	22.37
0.1	22.37	22.36	22.37	22.37
0.2	22.36	22.35	22.35	22.35
0.3	22.24	22.23	22.24	22.24
0.4	21.83	21.82	21.83	21.83
0.5	20.89	20.88	20.89	20.89

Table 2-2 The 2nd mode natural frequency ω (rad/s) for different delamination sizes

a/L	**Analytical** [164]	**FEM** [168]	**Free mode**	**Constrained mode**
0	61.67	61.61	61.67	61.67
0.1	60.81	60.74	60.81	60.81
0.2	56.00	55.95	56.00	56.00
0.3	49.00	48.97	49.00	49.00
0.4	43.89	43.86	43.89	43.89
0.5	41.52	41.50	41.52	41.52

Table 2-3 The 3rd mode natural frequency ω (rad/s) for different delamination sizes

a/L	**Analytical** [164]	**FEM** [168]	**Free mode**	**Constrained mode**
0	120.90	120.68	120.90	120.90
0.1	120.83	120.62	120.83	120.83
0.2	118.87	118.69	118.87	118.87
0.3	109.16	109.03	109.16	109.16
0.4	93.59	93.51	93.59	93.59
0.5	82.29	82.23	82.30	82.30

Based on Tables 2-1 to 2-3, the natural frequency of the proposed method is almost the same as the analytical model in reference [164], which demonstrates the proposed model and solution based on the Green's function method credible. There is some difference between the proposed method and the FEM result which is because of the limitation of numerical analysis. These

data also show that the natural frequency is reduced when the beam has delamination. The reduction value will increase with the delamination size being larger due to the stiffness reduction generated by delamination. While it should be noted that when the delamination size is 0.5L, the drop of the fundamental natural frequency is the smallest about 1.49 rad/s, while the change values of the second and third modes are 20.15 rad/s and 38.60 rad/s respectively, which is as the result of different sensitivity to the delamination of vibration modes. It also can be observed that the result indicates that when the delamination in the mid-plane of beams (i.e., $H_2 = H/2$), the natural frequencies of 'free mode' and 'constrained mode' are the same because the thickness and displacement of sub-beams are the same as mentioned in the previous work [22, 29].

The natural frequency of beams with different delamination depth is shown in Table 2-4 with delamination location at $L_1 = (L - a)/2$.

Table 2-4 The 1st mode natural frequency ω (rad/s) of different delamination depth

a/L	H_2=0.25H			H_2=0.5H		
	Reference [28]	**Free mode**	**Constrained mode**	**Reference** [28]	**Free mode**	**Constrained mode**
0	22.39	22.37	22.37	22.39	22.37	22.37
0.1	22.37	22.37	22.37	22.37	22.37	22.37
0.2	22.35	22.35	22.37	22.35	22.35	22.35
0.3	22.16	22.16	22.32	22.24	22.24	22.24
0.4	21.37	21.38	22.14	21.83	21.83	21.83
0.5	18.80	18.80	21.71	20.88	20.89	20.89

Table 2-4 indicates that when the delamination is not in the mid-plane of the beam, the result of the two models has a clear difference. The reason for this phenomenon is that the displacement of the sub-beams with different thicknesses in the free mode model is different due to there is no contact between them. It should be also noted that when the delamination size is smaller than 0.2L, the difference between the two models is not clear because of the small size delamination affecting little. Moreover, the changing trend of the two models is different. For example, the result of the free mode model increase from 18.80 rad/s to 20.88 rad/s with the delamination depth from 0.25L to 0.5L, when the delamination size is 0.5L, while the result from the constrained mode model is decreasing from 21.71 rad/s to 20.88 rad/s. A similar phenomenon was mentioned in previous work [29], which indicates that this is generated by the local deformation of sub-beams and new modes in the free mode model. In this table, the result of the free mode model is closer to the reference result because the reference is also calculating the delaminated beam by using the free mode model. Then when the delamination depth is $H_2 = 0.5H$, which means the delamination is in the mid-plane of the beam, the result of the two models is the same as the previous result solved based on the free mode model due to the same thickness and displacement of the sub-beams as mentioned in previous researches [28, 164, 169]. It should also be noted that with the same delamination size, the natural frequency has almost no change generated by various delamination depths, which means the

effect of delamination depth is smaller than the delamination size due to the stiffness change generated by various delamination depths is smaller.

The effect on the natural frequencies of delamination locations with various sizes was also analyzed. The natural frequencies of the first modes with various normalized delamination center locations b/L (i.e. $b = L_1 + a/2$) was shown in Figure 2-3:

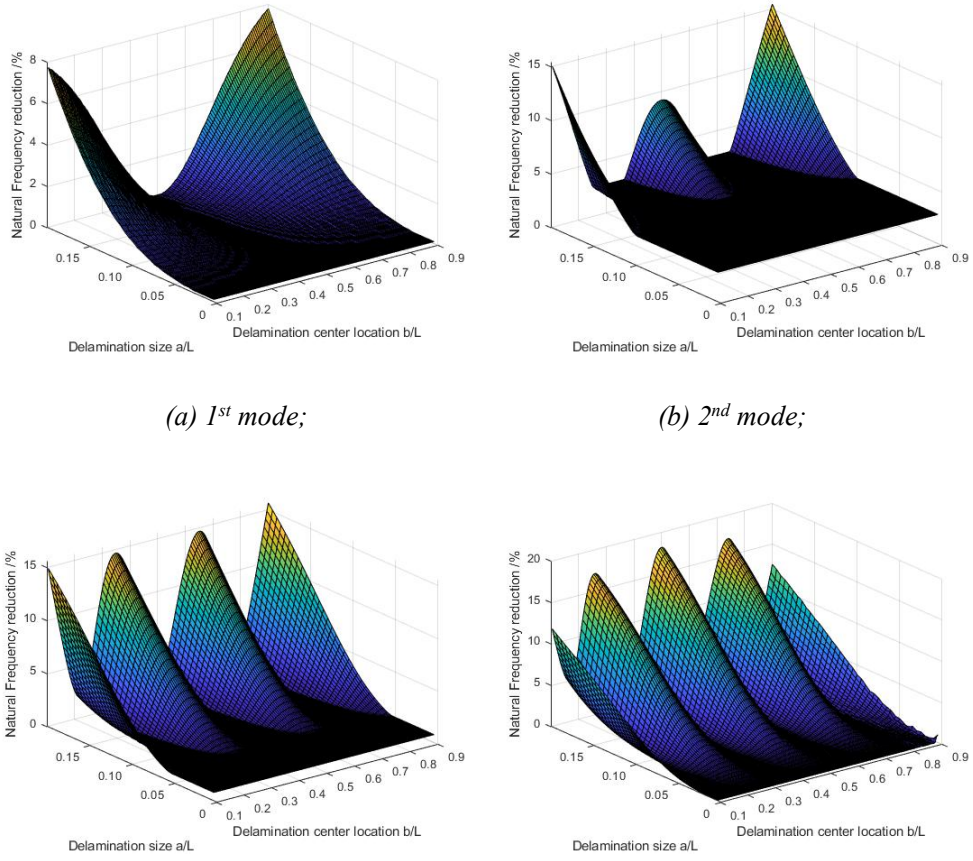

(a) 1st mode; *(b) 2nd mode;*

(c) 3rd mode; *(d) 4th mode;*

Figure 2-3 The reduction of natural frequency generated by delamination location and size from the constrained mode model.

Based on Figure 2-3, it can be seen that both delamination location and size will affect the natural frequency when the delamination depth is both fixed.

However, when the delamination size is small, the change is not clear with delamination at various locations, which means the effect of delamination size is larger than the delamination locations. This is because the reduction is generated by the local stiffness decreasing in the delamination region. Small delamination size generated a small reduction of stiffness, which makes less effect on the natural frequency. It also should be noted that when the delamination center is located at the nodes of mode shape, the reduction of natural frequencies will be the largest. As observed in [31], this phenomenon generates two peaks in the 1st mode, three peaks in the 2nd mode, four peaks in the 3rd mode, and 5 peaks in the 4th mode in the natural frequency reduction due to the number of nodes in each vibration mode, including the fixed boundaries of the beam which can be thought as nodes of modes. As shown in Figure 2-3, the change of the natural frequency for the higher mode is larger than the lower mode with the same delamination size. For example, the natural frequency of the 4th mode will decrease by about 20% with delamination size being 0.5L, while the 1st mode's natural frequency will only decrease by about 8%. The reason for this result is because of the different sensitivity to the delamination size of various modes to the delamination size.

Furthermore, the mode shapes of the beam with different delamination were also investigated. The mode shape of beams with various delamination sizes calculated based on the free mode model is shown in Figure 2-4:

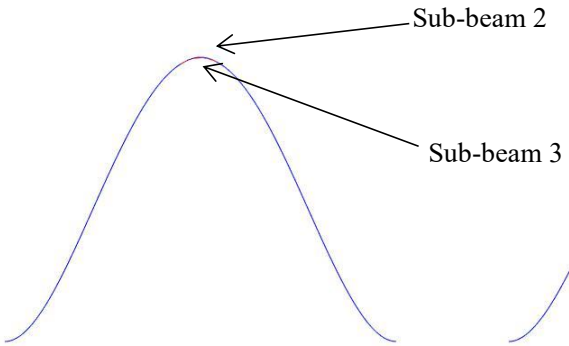

(a) $a = 0.1L$*;*

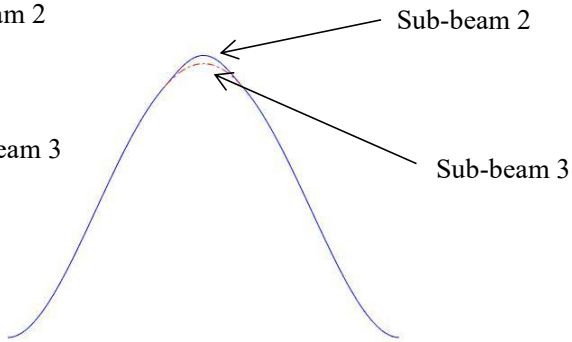

(b) $a = 0.2L$*;*

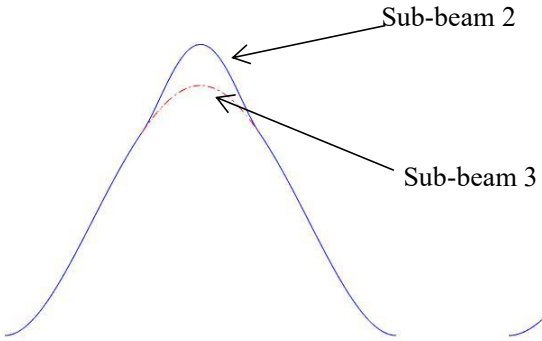

(c) $a = 0.3L$*;*

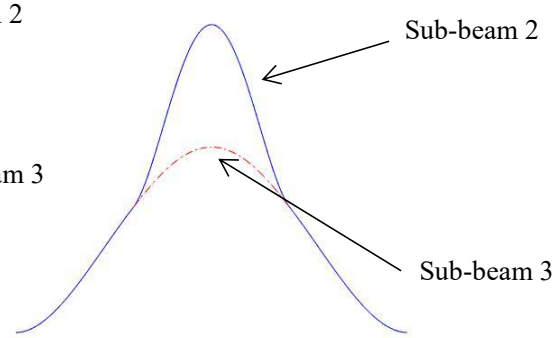

(d) $a = 0.4L$*;*

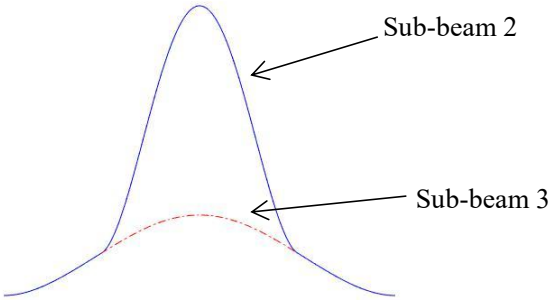

(e) $a = 0.5L$*;*

Figure 2-4 The mode shape of the delaminated beam with different length based on the free mode model ($H_2/H = 0.25,\ L_1 + a/2 = 0.5L$).

Figure 2-4 shows that the distance of sub-beam 2 and sub-beam 3 will increase as the delamination size being larger because the delamination region

becomes larger, which makes the difference of the deformation of the sub-beams larger. The split is generated by the different deformation of the sub-beams. When the length of delamination is smaller than $0.1L$, sub-beam 2 and sub-beam 3 are almost unseparated as shown in Figure 2-4(a) due to the small delamination size. It also should be noted that sub-beam 2 has larger deformation due to its thickness and bending stiffness EI are smaller as shown in Figure 2-4 (b-d).

The mode shape of beams with various delamination depths calculated based on the free mode model is shown in Figure 2-5：

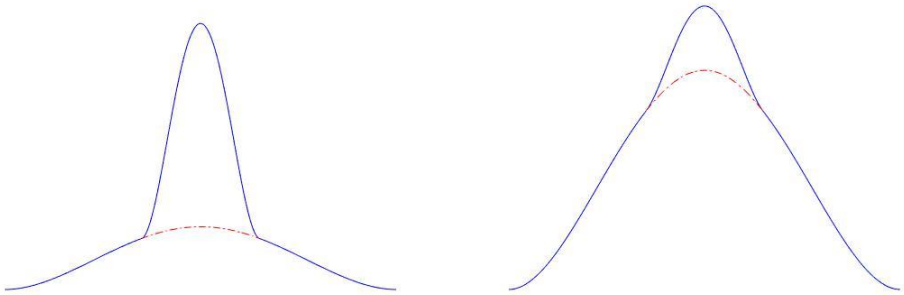

(a) $H_2 = 0.1H$*;* *(b)* $H_2 = 0.2H$*;*

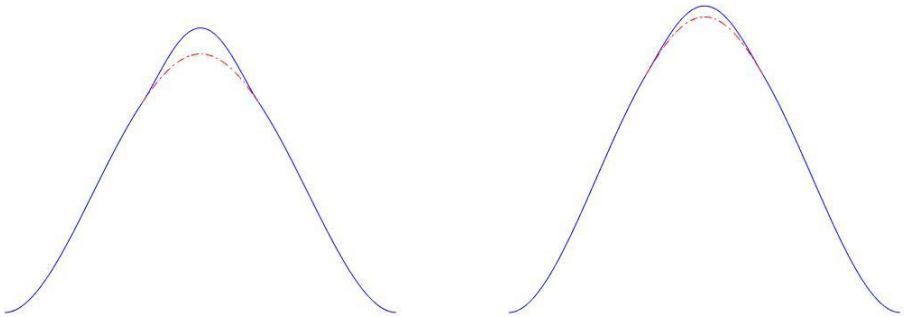

(c) $H_2 = 0.3H$*;* *(d)* $H_2 = 0.4H$*;*

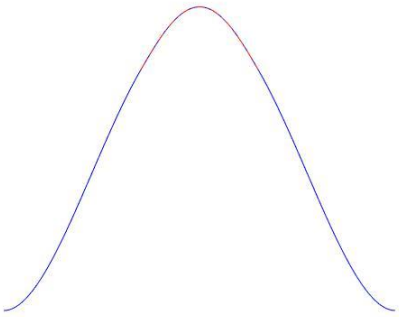

(e) $H_2 = 0.5H$*;*

Figure 2-5 The mode shape of the delaminated beam with different depth based on the free mode ($a/L = 0.3,\ L_1 + a/2 = 0.5L$).

Figure 2-5 shows the 1st mode shape of the free mode beam model with different delamination depth. The distance between sub-beam 2 and sub-beam

3 will decrease as the depth of delamination increases due to the thickness of sub-beam 2 being closer to sub-beam 3, which makes the bending stiffness of these two sub-beams being closer. When the delamination is in the middle of the beam ($H_2 = H_3 = 0.5H$), the distance between sub-beam 2 and sub-beam 3 disappears. For the mode shapes, a similar result can be found in previous researches [164, 170].

The consistency of the natural frequency and mode shapes calculated by using the Green's function with the previous work [164, 170] as shown above demonstrates the feasibility and the accuracy of the proposed method in this chapter.

2.3 Forced Vibration Analysis of a Delaminated Beam

The previous section demonstrated the feasibility and accuracy of the proposed modeling method for free vibration analysis and vibration characteristics calculation for a homogeneous beam with various delamination through comparison with previous work. However, these previous methods were focused on free vibration analysis instead of on a more general forced vibration of beam structures with delamination. Therefore, this work will extend the development of the model to allow for analyzing the vibration responses of the delaminated beam under concentrated harmonic excitation based on the Green's function. The model of delaminated under concentrated

harmonic excitation is shown in Figure 2.6:

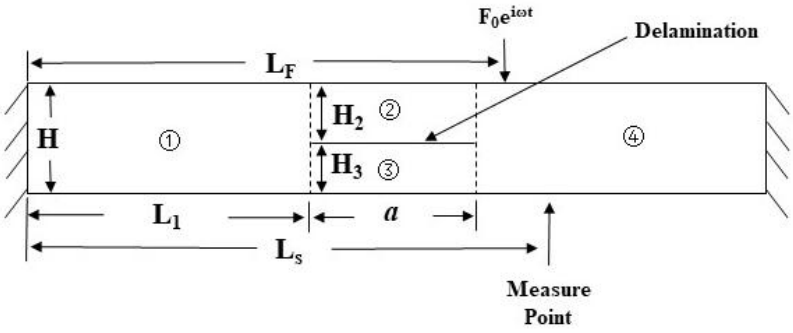

Figure 2-6 The model of a delaminated beam with excitation.

A concentrated harmonic excitation with drive frequency $\omega = \omega_F$ is applied at the axial location $L = L_F$ of the beam. For the forced vibration solution, equation (2-37) needs to be solved. Equation (2-37) can be described in the following formulation:

$$X = T^{-1}(\omega_F)S(\xi). \tag{2-42}$$

where $T^{-1}(\omega_F)$ represents the inverse matrix of $T(\omega_F)$ which is just related to the drive frequency $\omega = \omega_F$. By solving vector X and utilizing equation (2-34), the Green's function for the delaminated beam under the applied excitation can be obtained. In this work, the excitation is in the form of a concentrated harmonic force at location L_F as shown in Figure 2-6:

$$F(x) = F_0\delta(x - L_F). \tag{2-43}$$

Therefore, the solution can be solved from equation (2-32) as follow:

$$\int_0^L F_0\delta(\xi - L_F)\, G(x,\xi)d\xi = F_0G(x, L_F), \tag{2-44}$$

where $G(x, L_F)$ as a function of ω_f, is described by equations (2-34). The solution of equation (2-1) is noted as:

$$u(x,t) = F_0G(x, L_F)e^{i\omega t}. \tag{2-45}$$

Based on equation (2-44), the vibration responses of the beam with delamination under harmonic excitation can be analyzed. For general analysis, the result was shown as a non-dimensional value as calculated by $\overline{u}(x,t) = u(x,t)/(F_0 L^3/EI)$, where F_0 refer to the magnitude of excitation.

The excitation was set at the axial location $L_F = 0.80L$ to avoid the delamination region. The boundary conditions were clamped-clamped. The result was normalized for general analysis. It also was compared with a finite element model of a delaminated beam developed by ABAQUS software, which is a finite element analysis software that is used widely in delaminated structure simulation [171-174]. In this work, the beam was modeled by using 8-node elements C3D8R following the previous work. The number of elements is related to the delamination size because the delamination region needs smaller size elements compared with the intact part of the beam. For the undamaged case, 10,000 elements were used to develop the model of the beam structures.

2.3.1 Dimensionless Beam Displacement under Various Excitation Frequencies

The deformation of delamination beams under concentrated harmonic excitation with various frequencies is calculated based on the proposed method to show the effect of delamination on the structural dynamic responses. This section also investigated the effect of damping on the dynamic responses.

The damping ratio is defined as [107]:

$$\zeta = c/(2\rho A\omega_1), \tag{2-46}$$

while the ω_1 is the fundamental natural frequency of the delaminated beams. The dimensionless displacement of delaminated beams with different damping ratio is shown in Figure 2-7:

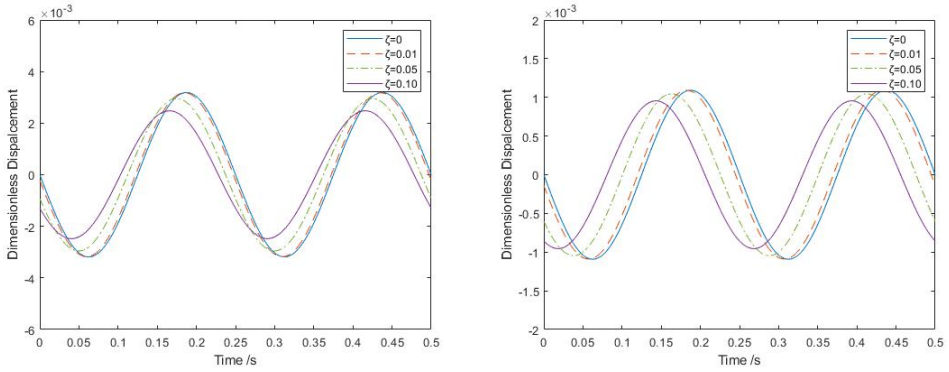

(a) L_s=0.20L; *(b) L_s=0.85L;*

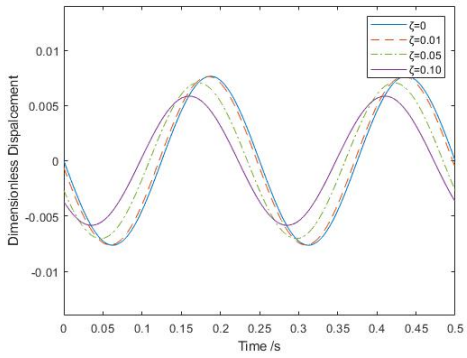

(c) L_s=0.5L;

Figure 2-7 The dimensionless displacement under 4Hz excitation with different damping ratios for the beam with delamination (delamination parameters: $H_2 = 0.5H$, $a = 0.1L$, $b = 0.5L$) from the constrained mode model.

It can be observed that the increasing damping reduces the structural deformation as the damping ratio is increased. For the damping ratio $\zeta = 0.01, 0.05, 0.1$ the structural displacement at axial location L_s=0.2L is reduced

to 99.7%, 92.8%, and 77.8%, respectively, as shown in Figure 2-7(a). In another aspect, it also can be seen that the damping will also modify the phase of dynamic responses. The deflection of the delaminated beams with various damping ratio under various excitation frequencies is shown in Figure 2-8:

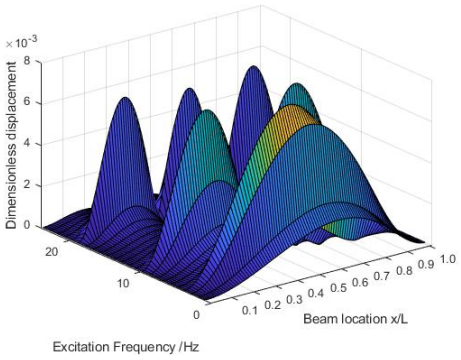

(a) 3 dimension view;

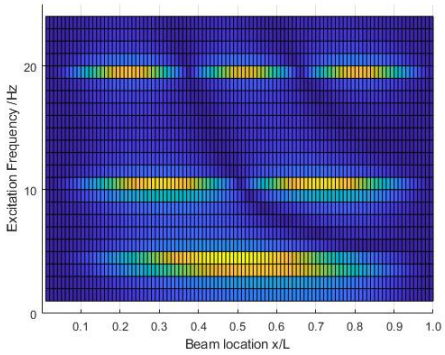

(b) 2 dimension view;

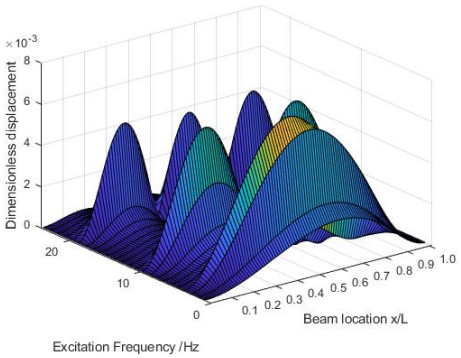

(c) 3 dimension view;

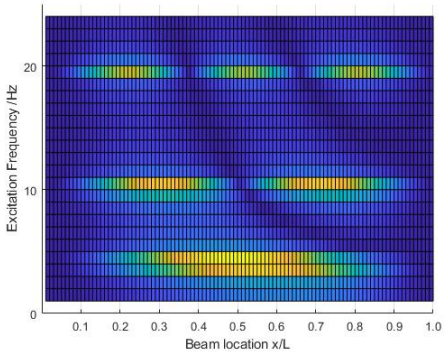

(d) 2 dimension view;

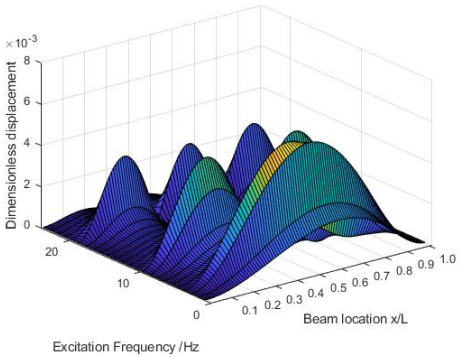

(e) 3 dimension view;

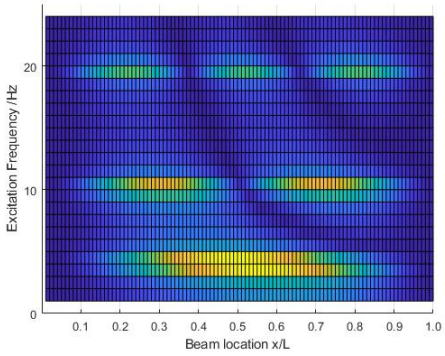

(f) 2 dimension view;

Figure 2-8 The deformation of delaminated beams under various excitation frequency of the constrained mode model with damping ratio $\zeta = 0.01$ *(a-b),* $\zeta = 0.05$ *(c-d),* $\zeta = 0.1$ *(e-f) (delamination parameters:* $H_2 = 0.5H,\ a = 0.1L,\ b = 0.5L$*)*

Figure 2-8 indicates that the deformation will be reduced with the damping

increasing due to vibration energy dissipation increased. In the other aspect, the natural frequency of each mode has no clear change due to the damping ratio is small as shown in Figures 2-8 (c), (e), and (f).

Under different excitation frequencies, the structural deflections of the delaminated beam at various axial locations are shown in Figure 2-9:

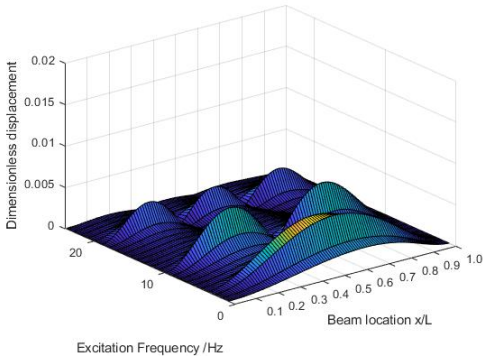

(a) 3 dimension view;

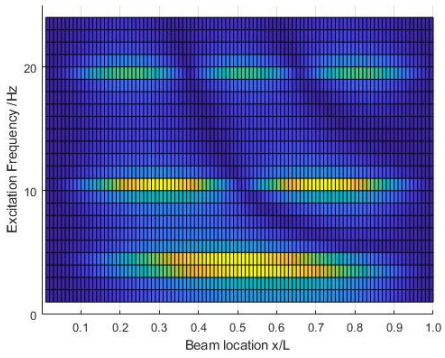

(b) 2 dimension view;

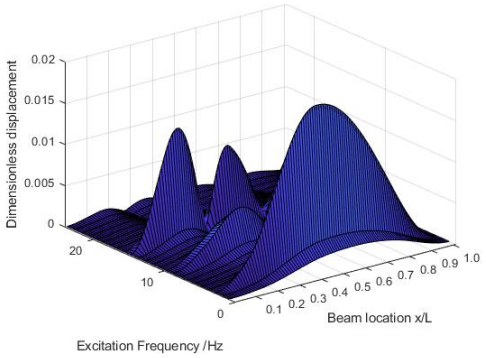

(c) 3 dimension view;

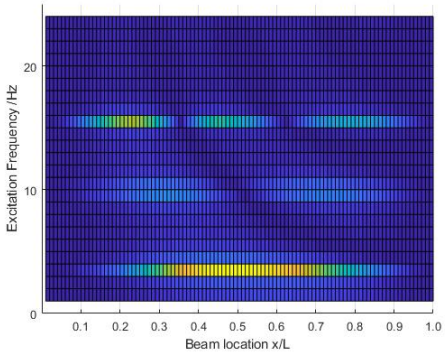

(d) 2 dimension view;

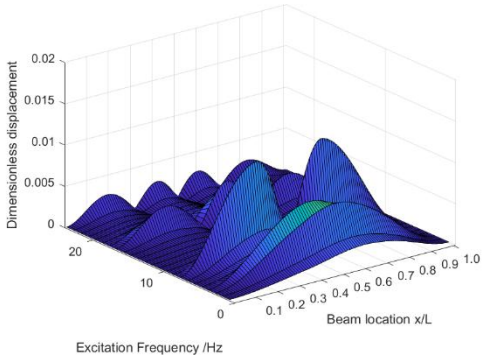

(e) 3 dimension view;

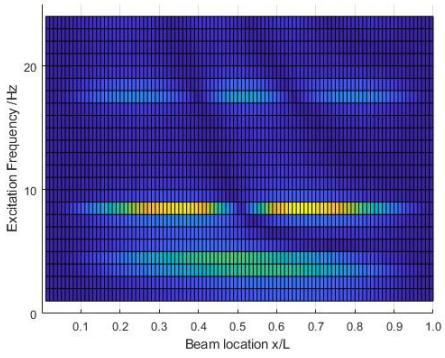

(f) 2 dimension view;

Figure 2-9 The deformation of two beams under various excitation frequency of the constrained mode model with delamination at different locations: 1) Undamaged beam (a-b); 2) $H_2 = 0.5H,\ a = 0.3L,\ L_1 = 0.15L$ (c-d); 3) $H_2 = 0.5H,\ a = 0.3L,\ L_1 = 0.35L$ (e-f).

Figure 2-9 shows that the natural frequencies of delaminated beams at various locations are different from those mentioned in Section 2.2. Specifically, Figure 2-9 shows that the mode shapes are affected by the delamination location differently. The reason is the same as the cases for different delamination sizes due to the variation of structural deformation at the corresponding antinodes and nodes of each mode shape as well as due to the local stiffness reduction generated by delamination. as shown in Figure 2-9 (c), the two peaks of the 3rd mode shapes in the left side are larger when the delamination was located at 0.15L since the delamination region from 0.15L to 0.45L covers the part between the antinodes of the two peaks in the left side, which are located at 0.22L and 0.45L. Also, as the delamination is located between 0.35L and 0.65L, the 2nd mode shape became larger due to the boundary of delamination close to the antinodes of the 2nd mode (0.36L to 0.66L). This phenomenon may be caused by the change of the axial load changing. Previous work mentioned that the delamination will give rise to additional axial loads in sub-beams as shown in Figure 2-2 due to the different bending stiffness and thickness of sub-beams generated by delamination [29] as shown in Figure 2-10:

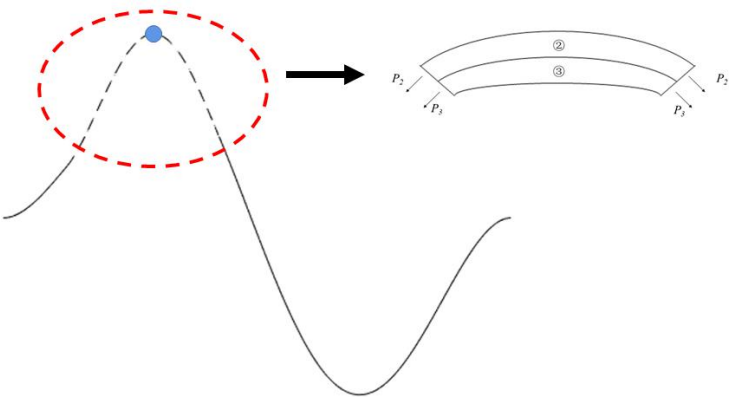

(a) The delamination center at the antinodes.

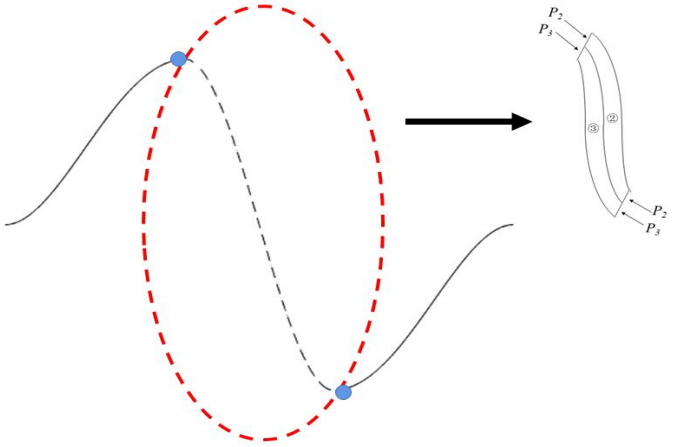

(b) The delamination between antinodes.

Figure 2-10 The axial load of sub-beams in the delaminated region based on the constrained mode model.

In Figure 2-10, the weak black line is the delaminated region, which contains sub-beams 2 and 3. The blue point is the location of antinodes. Based on Figure 2-10, it can be seen when the delamination is between the antinodes, the sub-beams in the delaminated region are under a compressive axial load due to the mode shapes [175], which will enhance the deformation of sub-beams as mentioned in previous work [176]. Therefore, the mode shape will be larger when the delamination is located in the parts between antinodes.

In addition, for a fixed delamination size, the location of delamination

also affects the locations of antinodes and nodes in each mode. In the first sample, the antinode of the first mode was located at 0.49L with the delamination center located at 0.3L as shown in Figures 2-9 (c-d). In the second sample, however, the location of the antinode has changed to 0.56L as the delamination center moved to 0.5L as shown in Figures 2-9(e-f). The possible reason for these findings may be due to the local stiffness reduction generated in different delamination regions.

The deflection of beams with different delamination sizes under various excitation frequencies is shown in Figure 2-11:

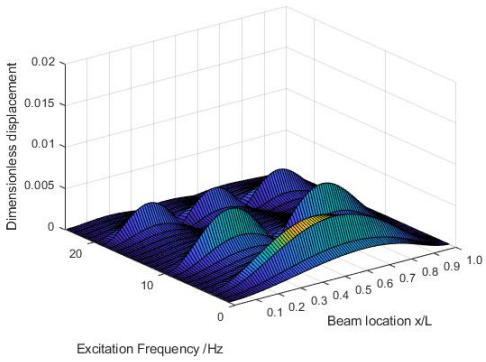

(a) 3 dimension view;

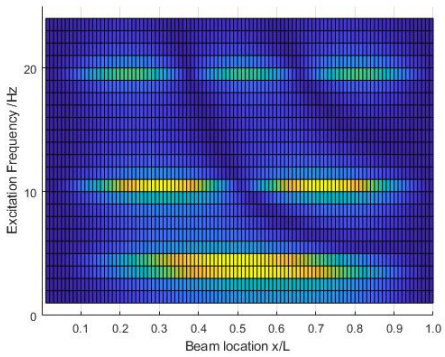

(b) 2 dimension view;

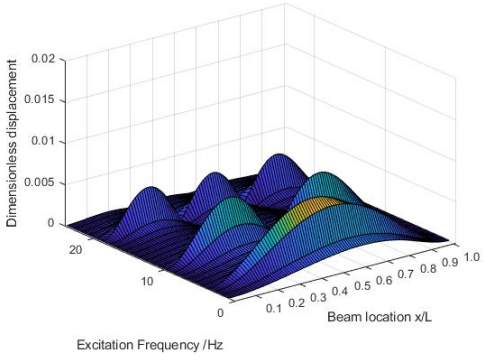

(c) 3 dimension view;

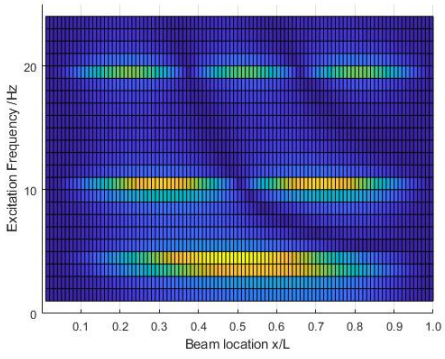

(d) 2 dimension view;

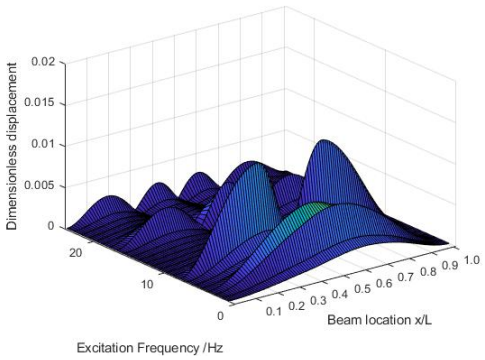

(e) 3 dimension view;

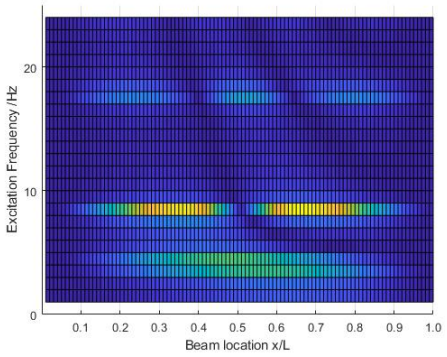

(f) 2 dimension view;

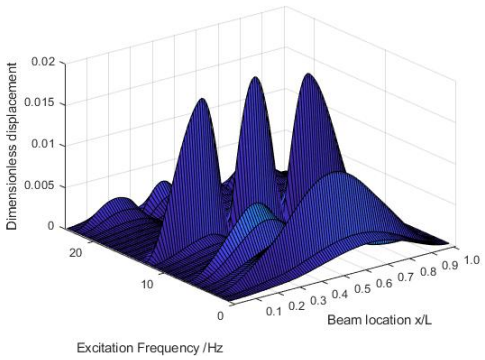

(g) 3 dimension view;

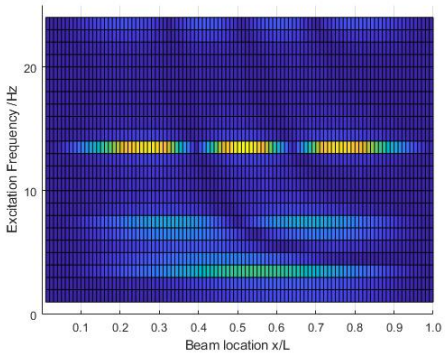

(h) 2 dimension view;

Figure 2-11 The deformation of beams under various excitation frequency of the constrained mode model with different delamination sizes a: 1) undamaged (a-b); 2) $H_2 = 0.5H,\ a = 0.1L,\ b = 0.5L$ *(c-d); 3)* $H_2 = 0.5H,\ a = 0.3L,\ b = 0.5L$ *(e-f); 4)* $H_2 = 0.5H,\ a = 0.5L,\ b = 0.5L$ *(g-h).*

As shown in Figures 2-11 (b), (d), (f), and (h), the natural frequency is reduced delamination size due to the reduced local stiffness part being larger. The frequency reduction of the 2nd and 3rd vibration modes is more obvious because they are more sensitive to the delamination size than the 1st mode as mentioned above.

Moreover, it should be noted that the mode shapes will be different due to the local stiffness reduction in the delaminated region. For example, when the delamination size is 0.3L, (i.e. the delamination from 0.35L to 0.65L,

which is located between the antinodes of the 2nd mode shape at 0.36L and 0.66L), the amplitude of the beam deformation associated with the 2nd mode is larger than other modes, while the amplitude will reduce when the delamination size becomes 0.5L because the delamination is located between the nodes of the beam deformation associated with the 2nd, which will make the axial loads as tension load to constrain the deformation of sub-beams in the delaminated region. Therefore, the beam deformation associated with the 2nd mode shape is smaller as shown in Figures 2-11(c) and 2-11(g). A similar phenomenon also appears at the 3rd mode when the delamination size is 0.5L from 0.25L to 0.75L, which has a large amplitude due to the part between the antinodes of a large beam deformation associated with the 3rd mode from 0.27L and 0.76L. These findings agreed with the previous analysis of beams with various delamination sizes, which is due to a large magnitude of axial load generated by the delamination being large when the delamination is located between the antinodes.

It also can be obtained that the locations of antinodes and nodes are also affected by the delamination size. In the first sample, the delamination size is 0.1L, and the antinodes of the 2nd mode are at 0.30L and 0.71L, respectively as shown in Figures 2-11 (c) and (d). The antinodes then changed to 0.36L and 0.65L when the delamination size is changed to 0.3L in the second sample as shown in Figures 2-11(e) and (f). This is caused by the local stiffness reduction with different size regions.

The deformation of beams with delamination at different depths under various excitation frequencies is shown in Figure 2-12:

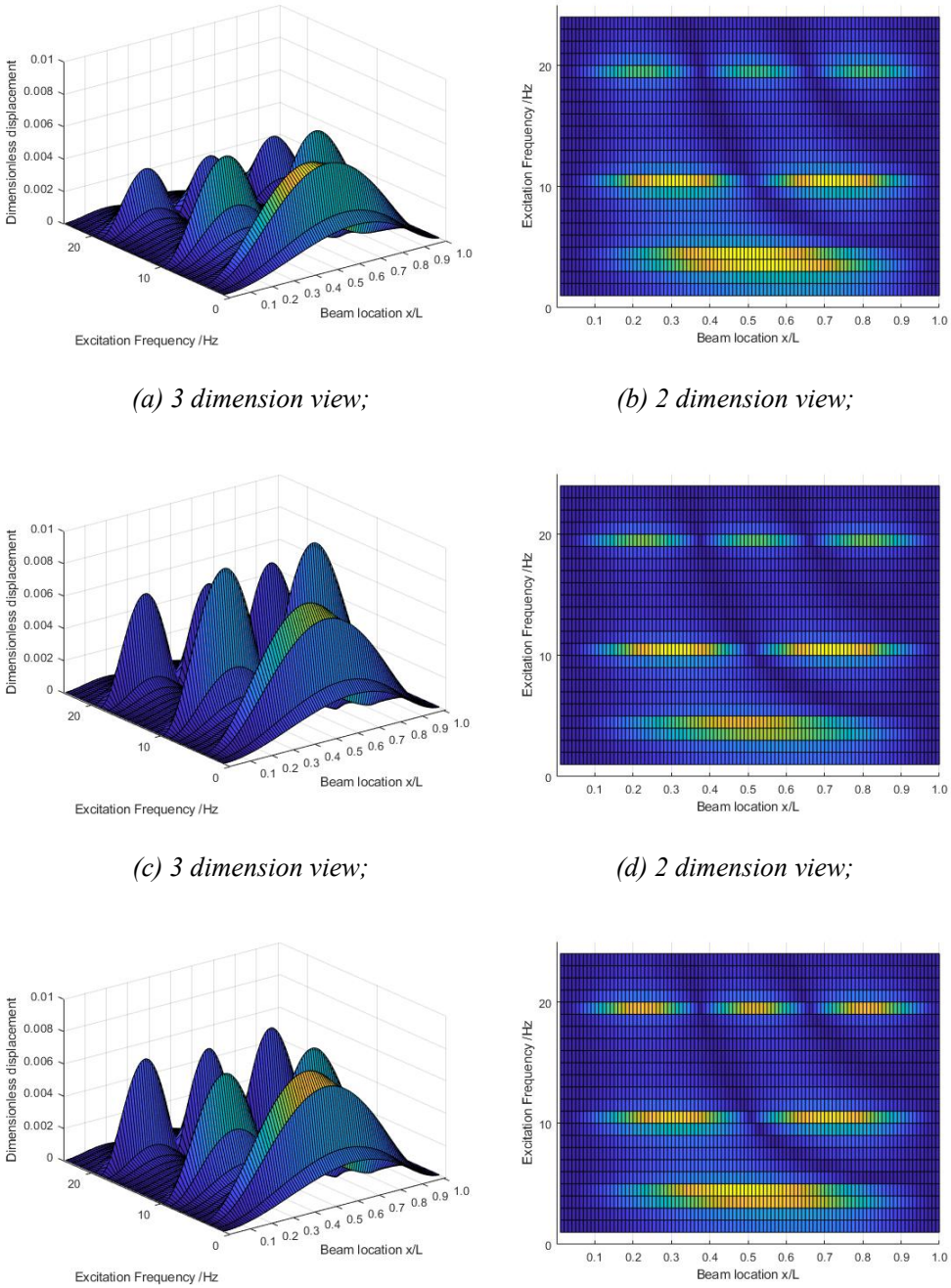

(a) 3 dimension view; *(b) 2 dimension view;*

(c) 3 dimension view; *(d) 2 dimension view;*

(e) 3 dimension view; *(f) 2 dimension view;*

Figure 2-12 The deformation of two delaminated beams under various excitation frequency of the constrained mode model: 1) undamaged (a-b); 2) $H_2 = 0.25H,\ a = 0.1L,\ b = 0.5L$ *(c-d); 3)* $H_2 = 0.5H,\ a = 0.1L,\ b = 0.5L$ *(e-f).*

Figure 2-12 indicates that the delamination depth affects the amplitude of

dynamic responses under harmonic excitation, although the change in amplitude is relatively small due to the less effect of delamination depth on the dynamic responses. It should be noted that the amplitudes are reduced with the delamination depth increasing, which is because the bending stiffness is increasing due to the thickness of sub-beams increasing. Moreover, the amplitude of the 2nd mode shape will be changed clear due to the effect of the fixed delamination size and location for this sample affect much on the 2nd mode shape as mentioned above due to the delamination located between the antinodes of the 2nd mode shape in this cases as mentioned above, which are moved from 0.35L to 0.65L and 0.36L to 0.66L, respectively. Therefore, when the depth of delamination changes, the effect will be larger on this mode shape than on others.

It should also be noted that the delamination depth affects the locations of antinodes and nodes of mode shapes. In Figure 2-12 (c), the antinodes of the 2nd mode are 0.36L and 0.65L with delamination depth being 0.25H, while the antinodes are changed to 0.32L and 0.68L in Figure 2-12 (e) with the same delamination size and location. The reason for this phenomenon is due to the different effects of delamination with different depths. As mentioned in previous work, the effect of delamination is significant when the delamination is close to the surface. Therefore, the mode shape will be affected much, including the locations of antinodes and nodes.

Moreover, this research also compares the result of the two models. For

the calculation of deflection based on the free mode model, the deformation of the delamination region is defined as to show the effect of delamination :

$$u(x) = (u_2(x) + u_3(x))/2, \tag{2-47}$$

where the $u_2(x)$ and $u_3(x)$ are the deflection of sub-beam 2 and sub-beam 3 respectively. As mentioned before [22], the difference between the free mode model and the constrained mode model only appears when the delamination is not at the mid-plane. Therefore, the following work focuses on the cases with delamination depth being $H_2 = 0.25H$. The result is shown as follows:

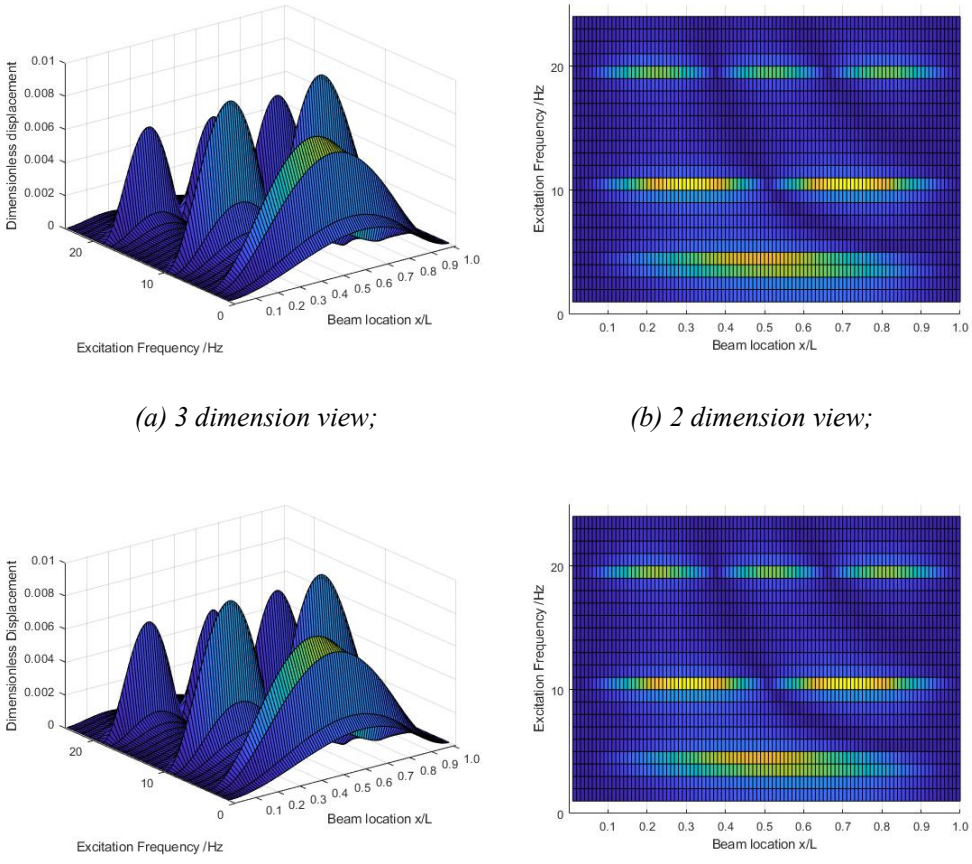

(a) 3 dimension view; *(b) 2 dimension view;*

(c) 3 dimension view; *(d) 2 dimension view;*

Figure 2-13 The deformation of delaminated beams under various excitation frequency of sample ($H_2 = 0.25H,\ a = 0.1L,\ b = 0.5L$) from the constrained mode model (a-b) and the free mode model (c-d).

Based on Figure 2-13, it can be seen that the difference between the free mode model and the constrained mode model is small under harmonic excitation in this case. The difference between the two models is related to delamination and excitation, which will be shown in the following work.

The results in Figures 2-7 to 2-13 demonstrate that the deformation and deflection of beams are affected by the delamination parameters and the excitation frequency. Therefore, the following work focuses on the effect of various delamination and excitation frequencies on the dynamic responses of different measurement locations.

2.3.2 Vibration Responses of Different Points with 1Hz Excitation

Following the previous work, this section investigates the dynamic responses of delaminated beams under the concentrated harmonic excitation with the drive frequency set as $f = 1Hz$ (i.e. $\omega_{\mathrm{F}} = 2\pi\, rad/s$). The vibration responses of different points with various distance L_s from the left end of the beam as shown in Figure 2-14 was measured. The displacement of four points with axial position L_s of the beam was measured as shown in Figure 2-14:

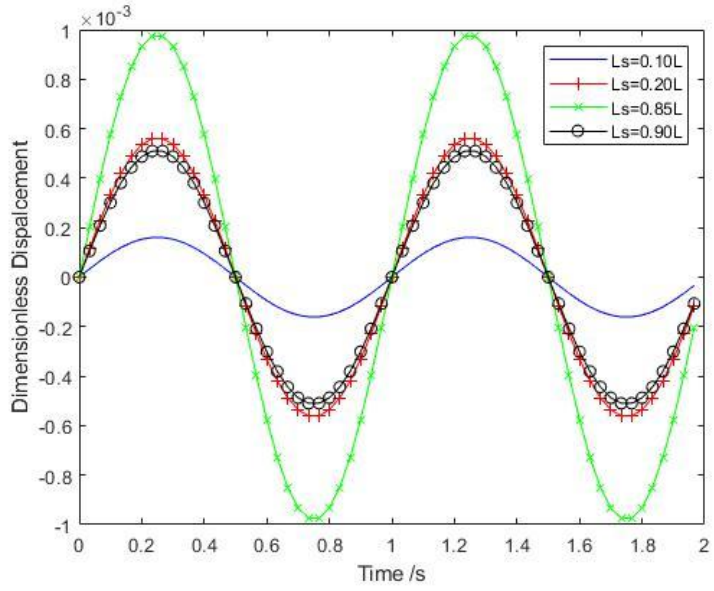

(a)

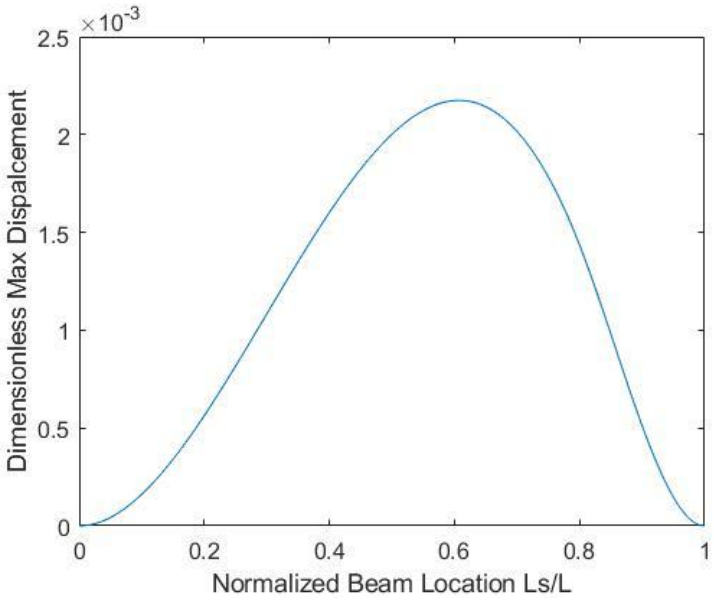

(b)

Figure 2-14 The vibration responses of different points: (a) vibration responses of four axial positions L_s of the beam ($L_s = 0.10L$, $L_s = 0.20L$, $L_s = 0.85L$, $L_s = 0.90L$); (b) the relationship between max displacement and measure points location.

Based on Figure 2-14(a), the different locations of the beam will have different vibration responses. Figure 2-14(b) shows that the largest

displacement was close to the location when L_s is about $0.6L$. This is because the excitation is on the point near the right side of the beam and the drive frequency is close to the natural frequency of 1st mode. Considering the delamination effect on the measurement of vibration responses, the point $L_s = 0.20L$ and $L_s = 0.85L$ were chosen from sub-beam 1 and sub-beam 4 respectively, as measured point to avoid the delamination region (from $0.25L$ to $0.75L$) and drive excitation which was on the point $L_F = 0.80L$.

2.3.2.1 Different Delamination Sizes

The vibration responses of the beam with different delamination sizes a were investigated under concentrated harmonic excitation. The max displacement with different delamination size of the beam was calculated as shown in Figure 2-15, which should appear at a quarter of the period (i.e. t=0.25s) when the depth was set as $H_2 = 0.5H$ and the location of delamination is in the middle of spanwise of the beam (i.e., $L_1 = (L - a)/2$)

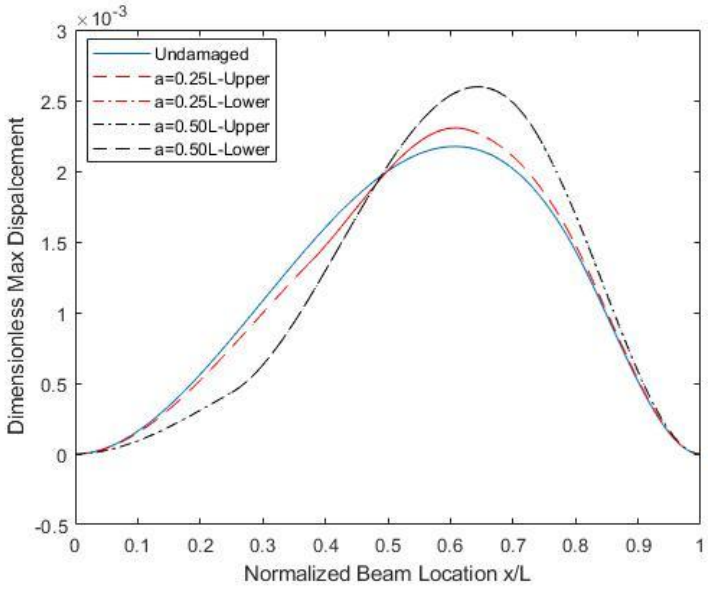

(a) Free Mode Model.

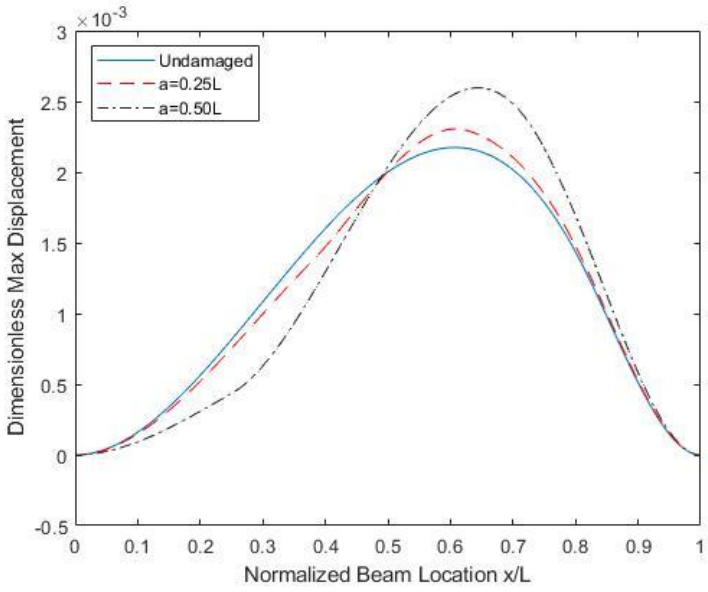

(b) Constrained Mode Model.

Figure 2-15 The Max Displacement of different locations in the beam.

Figure 2-15 shows that the deformation and change of the dynamic responses calculated by the free mode model are the same as the constrained mode model where the sub-beams in the delamination region are not split because the thickness of the sub-beams is the same as well as the displacement as

mentioned in previous work [22]. These two models both indicate that the deformation of the beam will be changed by various delamination sizes, which makes different parts of the beam having different changing trends due to the delamination size changing. The displacement of part from 0 to about 0.5L will decrease, while the rest part of the beam (form 0.5L to L) will increase. Moreover, the largest displacement location is changing, which is being closer to 0.7L, with the delamination size increasing. It should also be noted that the value of the max displacement increases with delamination size increasing due to the reduction of stiffness. Figure 2-16 show the deformed shapes of the delaminated beam with 0.25L delamination in mid-plane at different values of time:

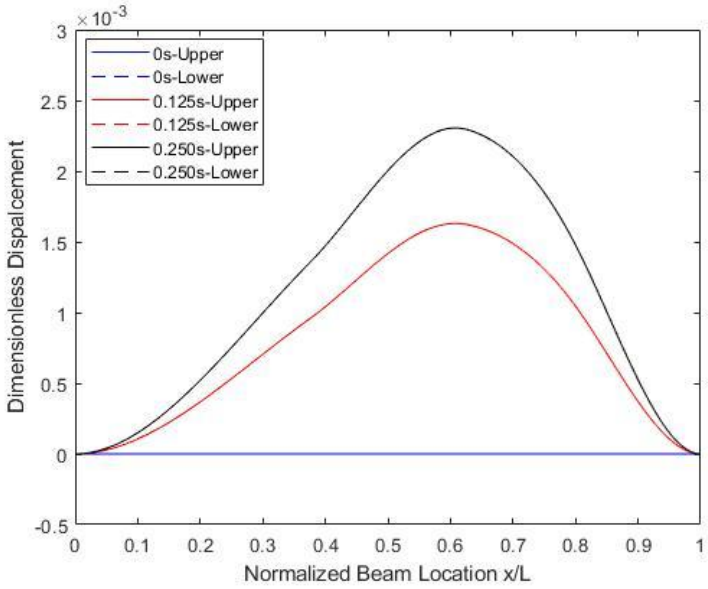

(a) Free mode model.

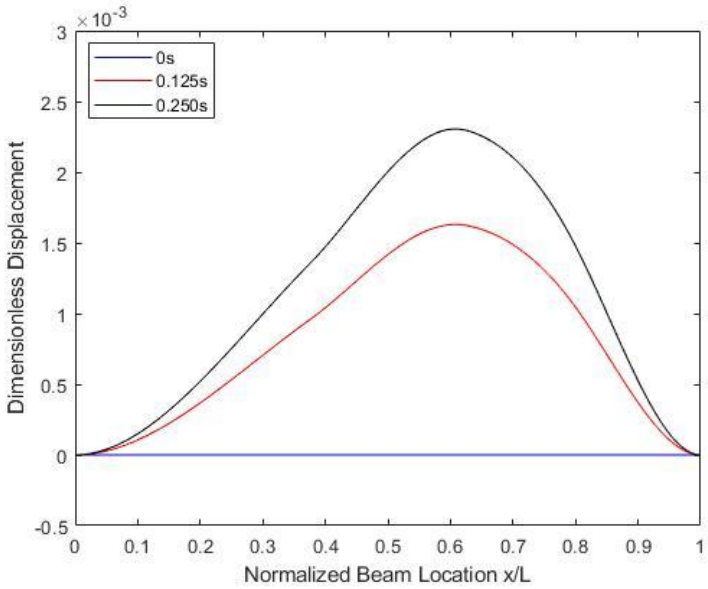

(b) Constrained mode model.

Figure 2-16 The shape of the beam with 0.25L delamination at different values of time.

The following figures show the deformed shapes of the delaminated beam with 0.5L delamination in mid-plane at different values of time:

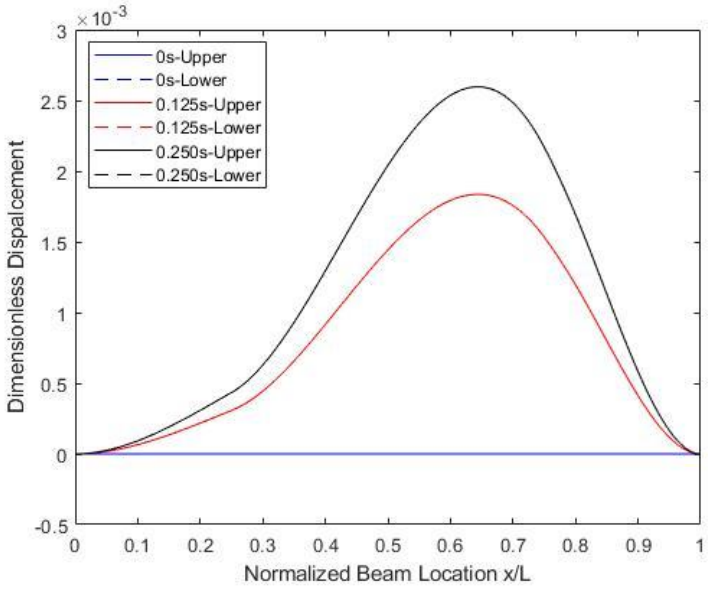

(a) Free mode model.

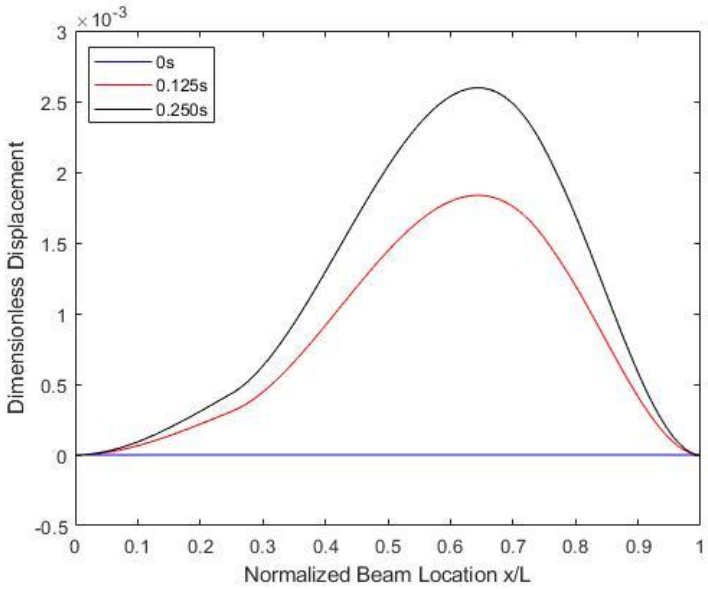

(b) Constrained mode model.

Figure 2-17 The shape of the beam with 0.5L delamination at different values of time.

Based on Figures 2-16 and 2-17, the result illustrates that the dynamic responses of the delaminated beam from the two models are the same with different delamination sizes when the delamination is in the mid-plane of the beam. There is no split between the sub-beams of the free mode model at

different times due to the displacement of the sub-beams being the same. The max displacement from different locations is shown as follows:

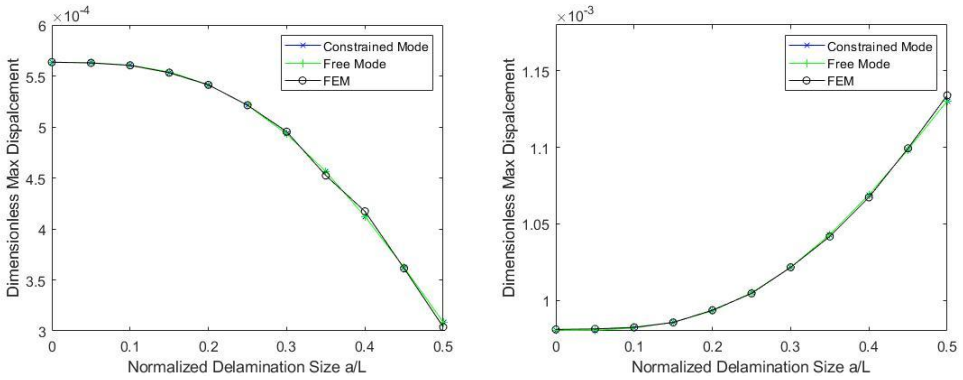

(a) $L_s = 0.20L$; *(b)* $L_s = 0.85L$;

Figure 2-18 The relationship between delamination size and max displacement.

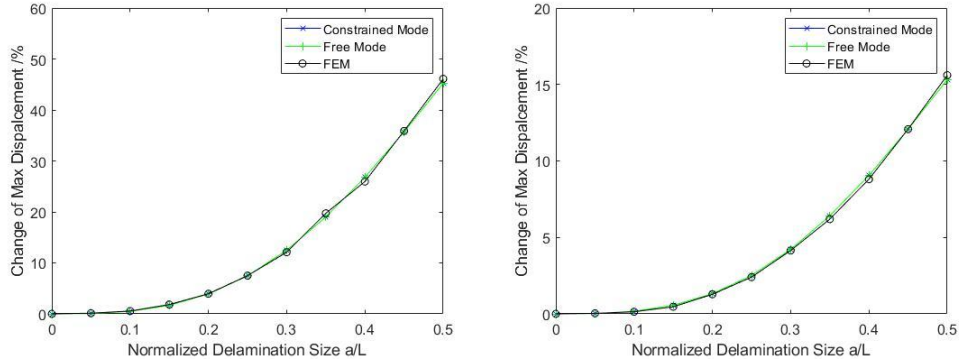

(a) $L_s = 0.20L$; *(b)* $L_s = 0.85L$;

Figure 2-19 The change ratio of max displacement with different delamination size.

Based on Figure 2-18, The result of free mode is the same as the constrained mode model when the delamination is in the mid-plane of the beam with low-frequency concentrated excitation.

Moreover, with delamination size increasing, the displacement of L_s=0.85L is increasing, while the displacement of L_s=0.20L decreasing due to the delamination change the deformation under the same excitation as shown

in Figure 2-15. While the max displacement value of L_s=0.85L is larger than L_s=0.20L because of the deformation changing as shown in Figure 2-18. However, the change ratio of point L_s=0.20L is larger, which is almost 45% with 0.5L delamination size, than L_s=0.85L with just about 15% as shown in Figure 2-19, which means the point L_s=0.20L is more sensitive to the delamination size with 1Hz excitation. The FEM result is also close to the analytical result based on the two models which show that the proposed method result is credible.

2.3.2.2 Different Delamination Depths

The vibration responses of the beam with different delamination depths were also investigated. The max displacement with different delamination depths of the beam was calculated as shown in Figure 2-20. The size was set as $a = 0.3L$:

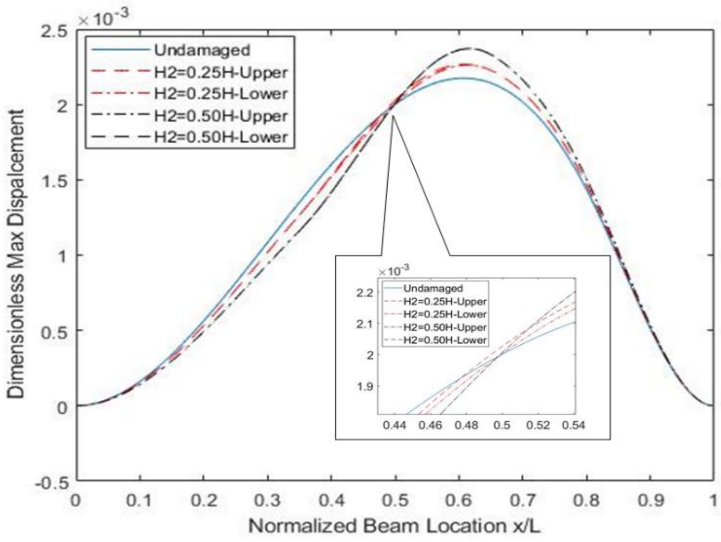

(a) Free Mode Model;

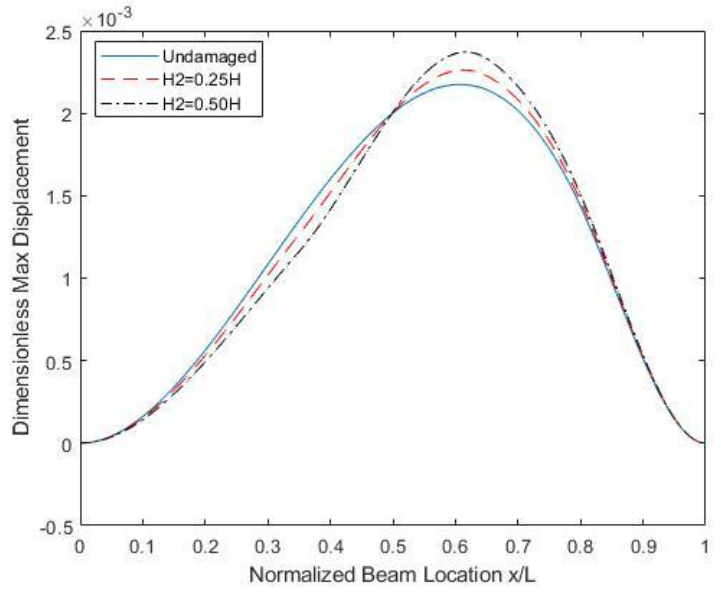

(b) Constrained Mode Model;

Figure 2-20 The Max Displacement of different locations in the beam.

Figure 2-20(a) illustrates that sub-beams of the delamination region have split when the delamination is not in mid-plane based on the free mode model, such as the delamination depth being 0.25H. The reason for this phenomenon is that the thickness of the sub-beams is different and there is no contact between

the sub-beams. The distance between the sub-beams calculated by the free mode model will be larger when the delamination is closer to the surface as mentioned in the previous work [22] due to the larger difference of the sub-beams thickness and displacement. However, the distance between the sub-beams is very small as shown in Figure 2-20(a) because of the small size of delamination. When the delamination is at the mid-plane of the beam, the split disappears because the thickness and displacement of the sub-beams are the same. Moreover, the two models both indicate that different parts of the beam will have different change trends and the largest displacement location is changing, which is because of the deformation change generated by the various delamination depth. The displacement of part from 0 to about 0.5L will decrease, while the rest part of the beam (form 0.5L to L) will increase. While the max displacement location is being closer to 0.65L. It also should be noted that the deformation of the delaminated beam is being larger with the delamination being closer to the mid-plane, which means the deeper delamination affects dynamic responses more. The deformed shape of the delaminated beam with 0.25H delamination depth at different moments is shown in the following figures:

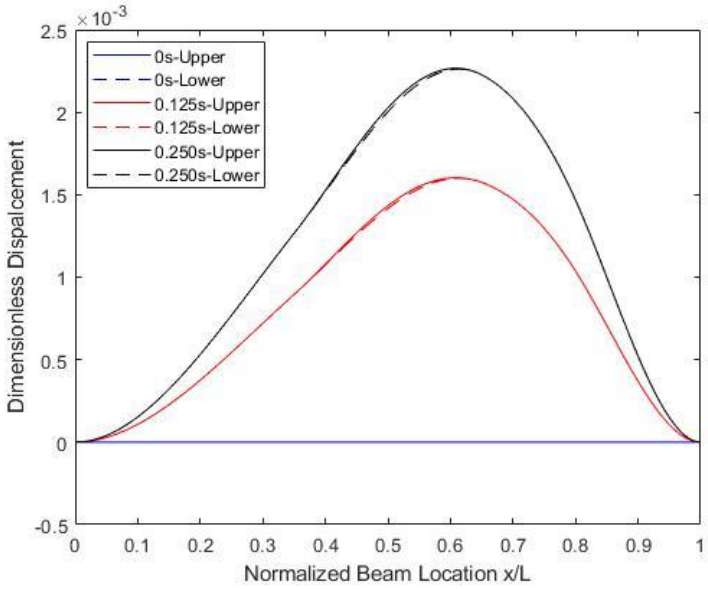

(a) Free mode model;

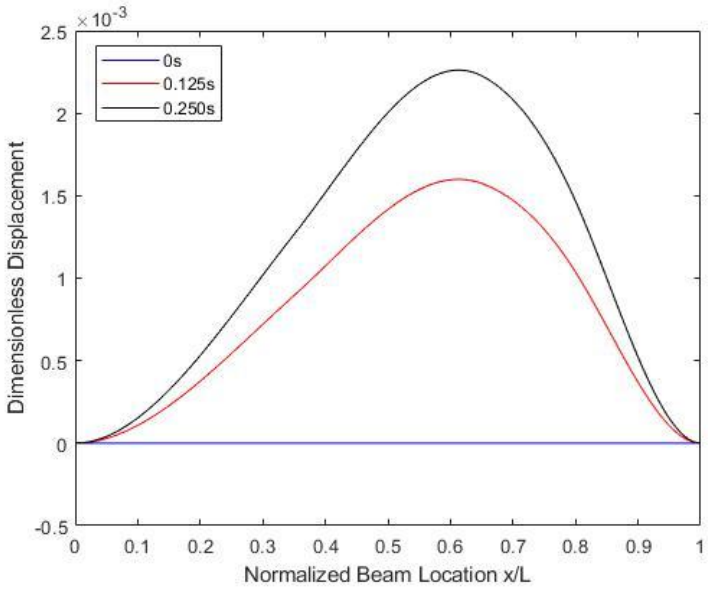

(b) Constrained mode model;

Figure 2-21 The shape of the beam with $0.25H$ *delamination at different values of time.*

The following figures show the deformed shapes of the delaminated beam with 0.5H delamination depth at different values of time:

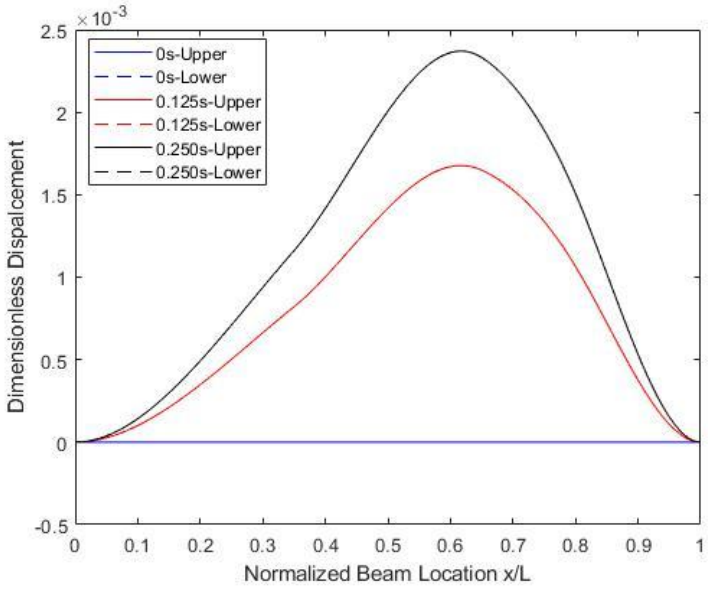

(a) Free mode model;

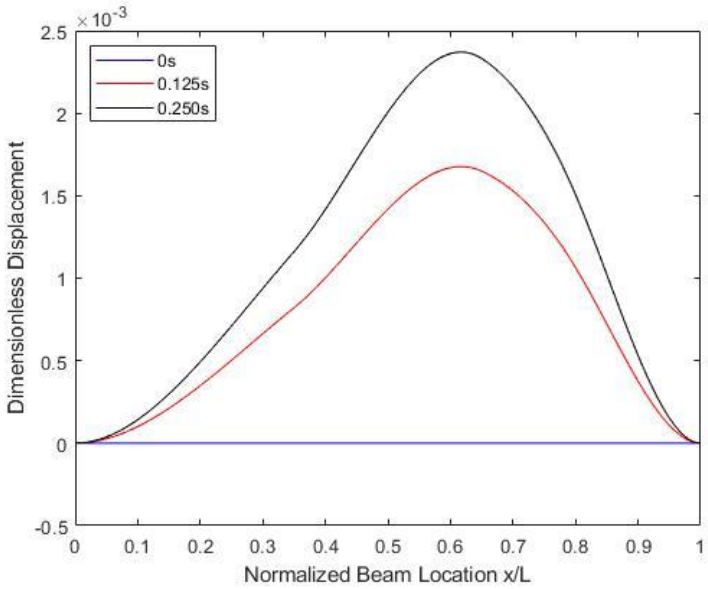

(b) Constrained model;

Figure 2-22 The shape of the beam with $0.5H$ *delamination at different values of time.*

The result in Figure 2-21 indicates that the deformation of the delaminated beam from the free mode model is different from the constrained mode model at different values of time when the delamination is not in the mid-plane. However, the difference is small as well as the split between sub-beams in the

free mode model. It also should be noted that the split between sub-beams is different at different values of the time due to the deformation of the beam being different at various times. Moreover, based on Figure 2-22, the difference between the two models disappears when the delamination is in the mid-plane of the beam. The max displacement from different locations is shown as follows:

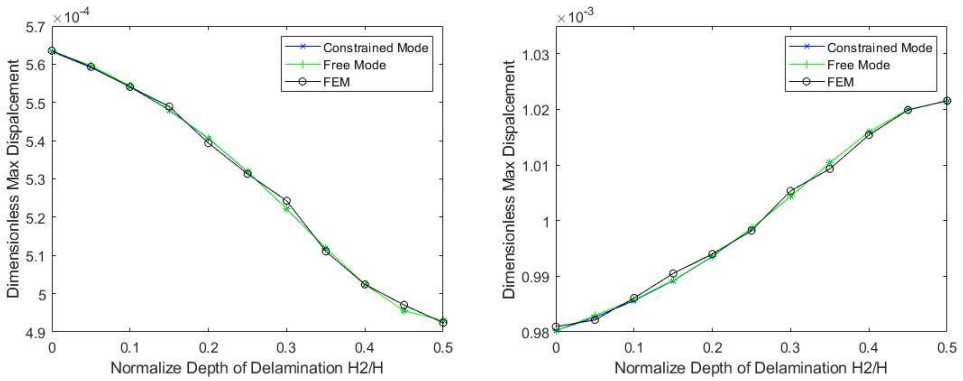

(a) $L_s = 0.20L$; *(b)* $L_s = 0.85L$;

Figure 2-23 The vibration responses of delamination in different depths.

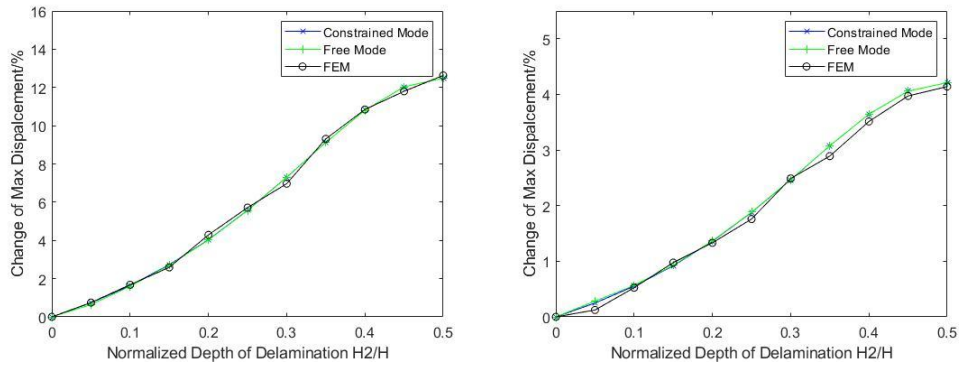

(a) $L_s = 0.20L$; *(b)* $L_s = 0.85L$;

Figure 2-24 The change ratio of max displacement with different delamination depths.

Figure 2-23 indicates that the difference between the two models is small for forced vibration with 1Hz concentrated excitation for delamination depth

changing due to the small difference between these two models as shown in Figure 2-21 generated by small delamination size.

Furthermore, with delamination depth increasing, the displacement of L_s=0.85L is increasing, while the displacement of L_s=0.20L is decreasing. This result is shown in Figure 2-20. It also can be obtained that the displacement of L_s=0.85L is larger than L_s=0.20L as shown in Figures 2-23 and 2-24, while the change ratio of point L_s=0.20L is about 12.5% with 0.5H delamination depth, which is larger than L_s=0.85L with about 4%, which means the point L_s=0.20L is more sensitive to the delamination depth as shown in Figure 2-24. The result has been demonstrated by FEM as shown in Figures 2-23 and 2-24. Figures 2-19 and 2-24 indicate that the effect of delamination size is larger than the delamination depth both in the proposed two points, which means the delamination size affects the dynamic responses of beams under 1Hz excitation more.

2.3.3 Vibration Responses of Different Points with 5Hz Excitation

Then another example with the drive frequency set as $f = 5Hz$ (i.e. $\omega_F = 10\pi\, rad/s$). The vibration responses of different points were measured and analyzed.

2.3.3.1 Different Delamination Sizes

The vibration responses of the beam with different delamination sizes

were investigated. The beam shape with different delamination size at 0.05s (i.e. a quarter of period) of the beam was calculated as shown in Figure 2-25 when the depth was set as $H_2 = 0.5H$ and location was $L_1 = (L - a)/2$:

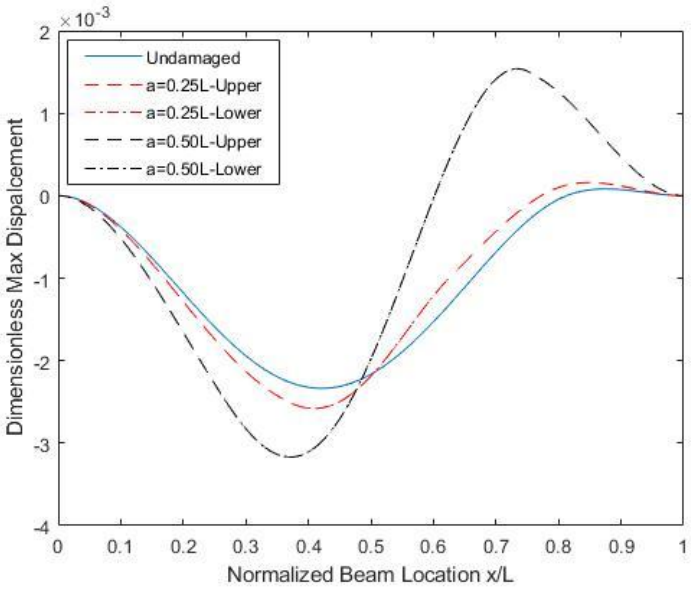

(a) Free Mode Model.

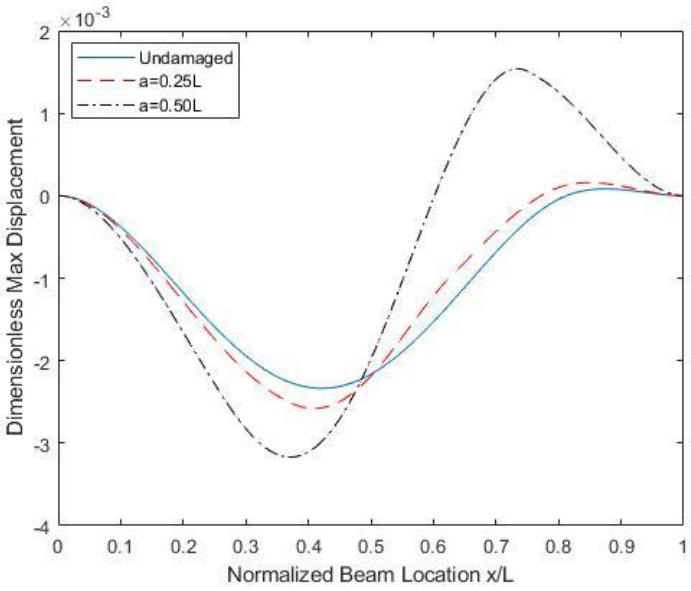

(b) Constrained Mode Model.

Figure 2-25 The Max Displacement of different locations in the beam.

Based on Figure 2-25, the result shows that the free mode model result is the

same as the constrained mode model where the sub-beams in the delamination region are not split when the delamination is in the mid-plane because the displacement of the sub-beams is the same. Moreover, the beam shape is closer to the second mode shape with the delamination size increasing, due to the drive frequency is being closer to the 2^{nd} mode natural frequency. It should be also noted that the deformation of the beam increase with the delamination size increasing as the result of the stiffness reduction generated by delamination. The deformation of the beam at different values of time is shown in Figures 2-26 to 2-27:

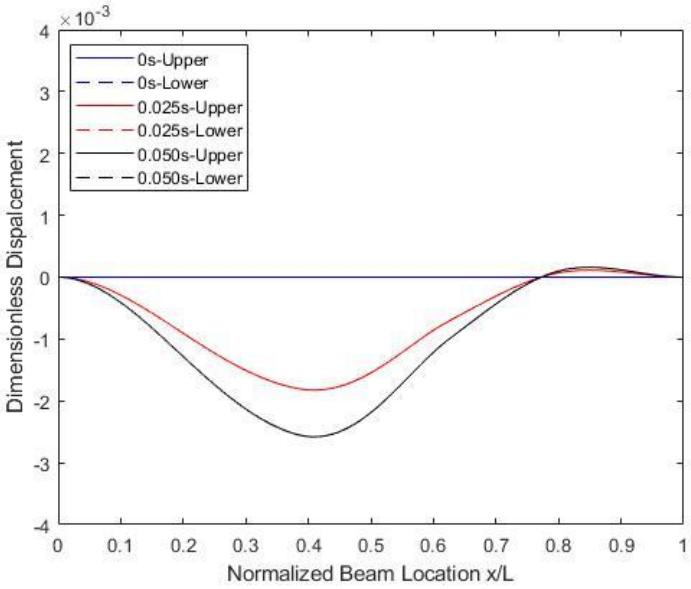

(a) Free mode model.

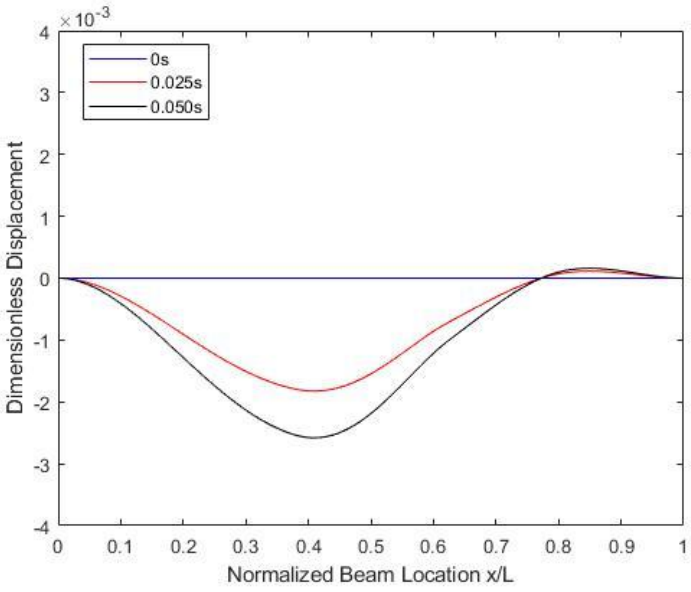

(b) Constrained mode model.

Figure 2-26 The shape of the beam with $0.25L$ *delamination at different values of time.*

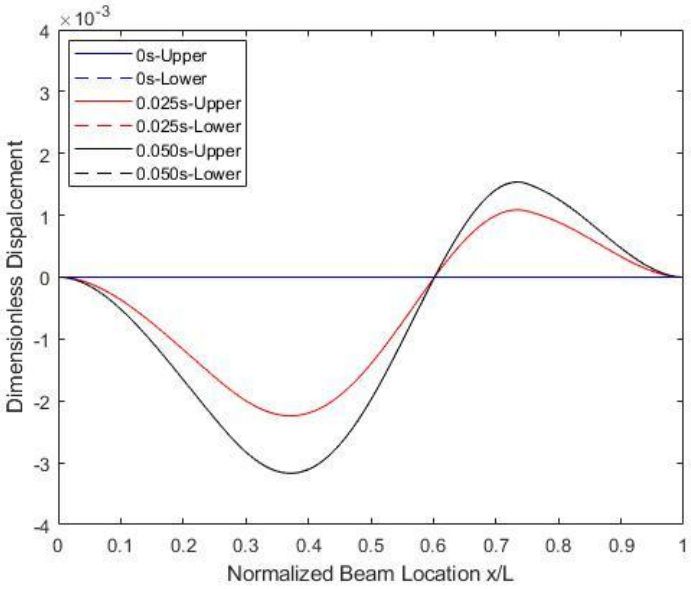

(a) Free mode model.

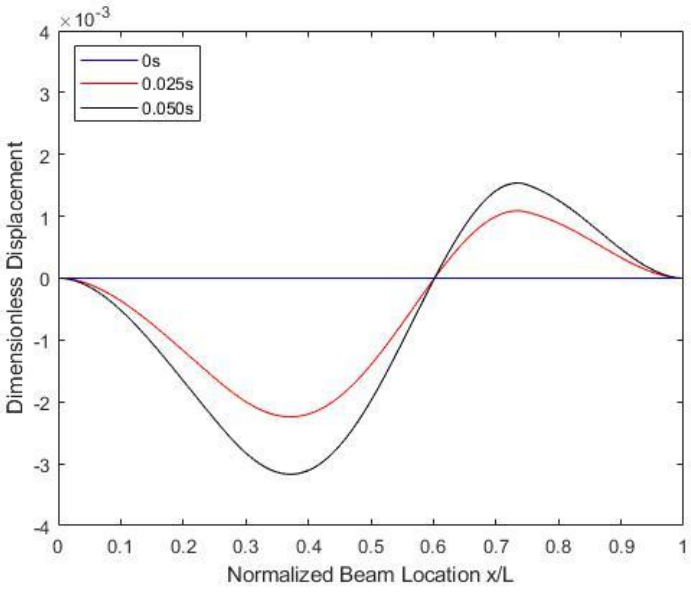

(b) Constrained mode model.

Figure 2-27 The shape of the beam with $0.5L$ *delamination at different values of time.*

Based on Figure 2-26 and Figure 2-27, the result shows that the deformation of the beam from the two models is the same at different values of time when the delamination is in the mid-plane of the beam. There is no split between sub-beams of the free mode model at all times due to the same thickness and

the same displacement of the sub-beams. The max displacement from different locations is shown respectively in Figures 2-28 to 2-29:

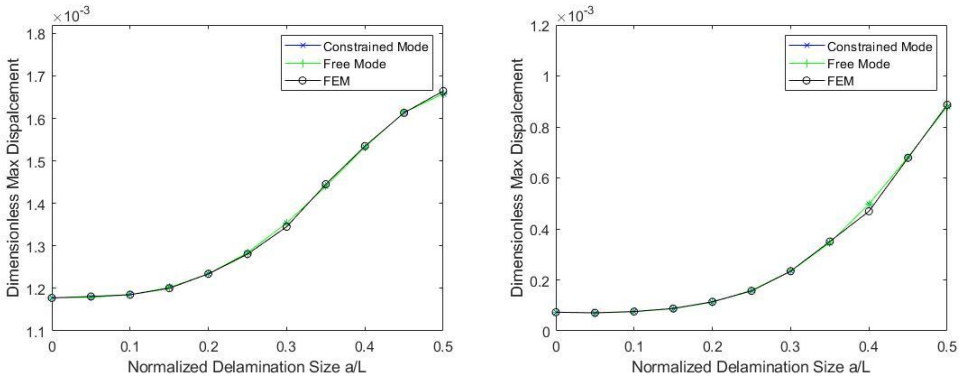

(a) $L_s = 0.20L$*;* *(b)* $L_s = 0.85L$*;*

Figure 2-28 The relationship between delamination size and max displacement.

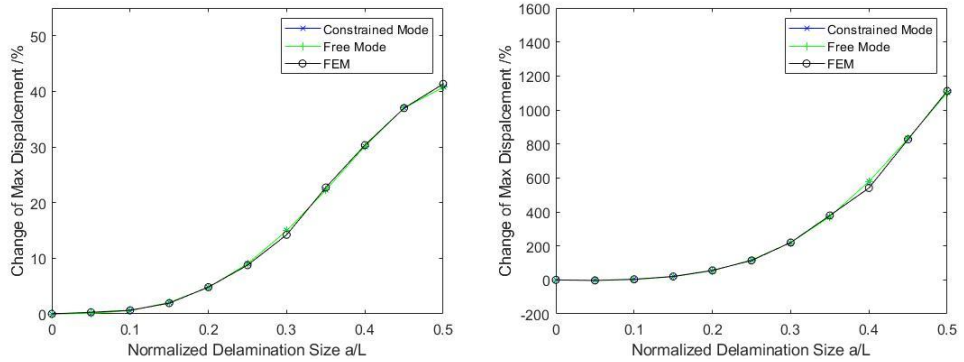

(a) $L_s = 0.20L$*;* *(b)* $L_s = 0.85L$*;*

Figure 2-29 The change ratio of max displacement with different delamination sizes.

Based on Figure 2-28, The result of free mode is the same as constrained mode when the delamination is in the mid-plane of the beam with low-frequency concentrated excitation.

Moreover, with delamination size increasing, the max displacement of $L_s = 0.20L$ and $L_s = 0.85L$ are both increasing because of the deformation changing as shown in Figure 2-25. While the displacement of $L_s = 0.20L$ is

larger than $L_s = 0.85L$. However, the change ratio of point $L_s = 0.85L$ is about 1100%, much larger than $L_s = 0.20L$ with 40% by Figure 2-29, which means the point $L_s = 0.85L$ is more sensitive to the delamination size when the drive frequency is 5Hz. The result generated by the various delamination sizes has been demonstrated by the FEM method.

The result of excitation with 5Hz is different from 1Hz comparing Figures 2-20 to 2-22 and Figures 2-28 to 2-29 for different delamination sizes. The max displacement of both two measure points are increasing with delamination size increasing with 5Hz excitation as shown in Figure 2-28, while the max displacement of the point $L_s = 0.20L$ is decreasing when the delamination size is increasing with 1Hz excitation. Moreover, the sensitivity of these two points is different from the delamination size. The sensitivity of the point $L_s = 0.20L$ is higher with 1Hz excitation, while the dynamic responses of point $L_s = 0.85L$ is more sensitive to the delamination size with 5Hz excitation. While the sensitivity of the two points under 5Hz excitation is larger than 1Hz excitation due to the dynamic responses generated by higher frequency excitation are more sensitive to the delamination size changing.

2.3.3.2 Different Delamination Depths

The vibration responses of the beam with delamination in different depths were also investigated. The beam shape with different delamination depth was calculated as shown in Figure 2-30 at t=0.05s where the size was

set as $a = 0.3L$ and the location was $L_1 = (L - a)/2$:

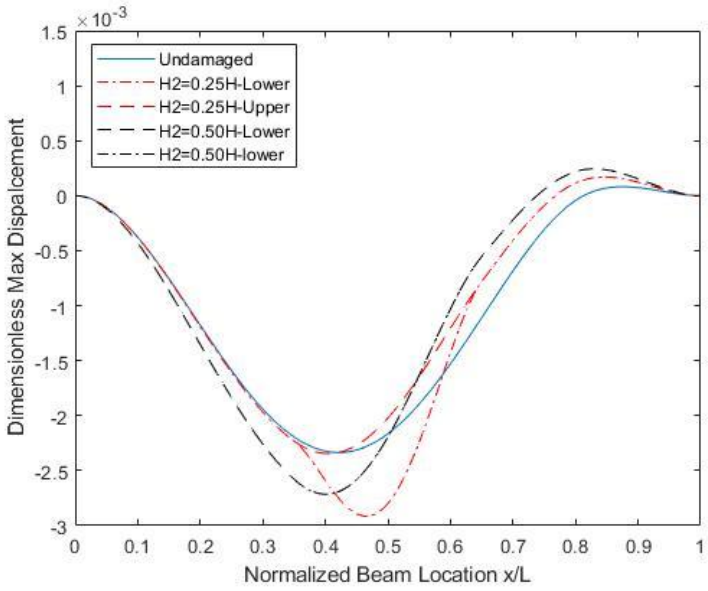

(a) Free Mode Model.

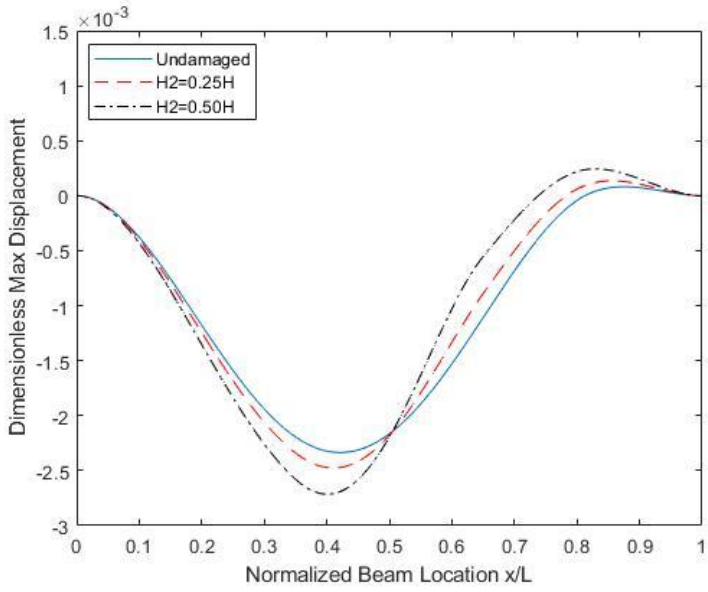

(b) Constrained Mode Model.

Figure 2-30 The Max Displacement of different locations in the beam.

Based on Figure 2-30, it is obvious that sub-beams of the delamination region have a clear split when the delamination is not in mid-plane as delamination depth is 0.25H because the deformation of the sub-beams is different and there

is no contact between them. When the delamination is at the mid-plane, the split disappears due to the same deformation [22]. Compared with Figure 2-18(a), Figure 2-30(a) also shows that the split is larger with drive frequency increasing from the free mode model, which means the difference between the free mode model and the constrained mode model is related to the drive frequency. While it also should be noted that the deformation changes much when the delamination depth is 0.25, which means the effect of delamination depth is not monotonic based on the free mode model due to the local deformation. The deformation of the beam at different moments is shown as follows:

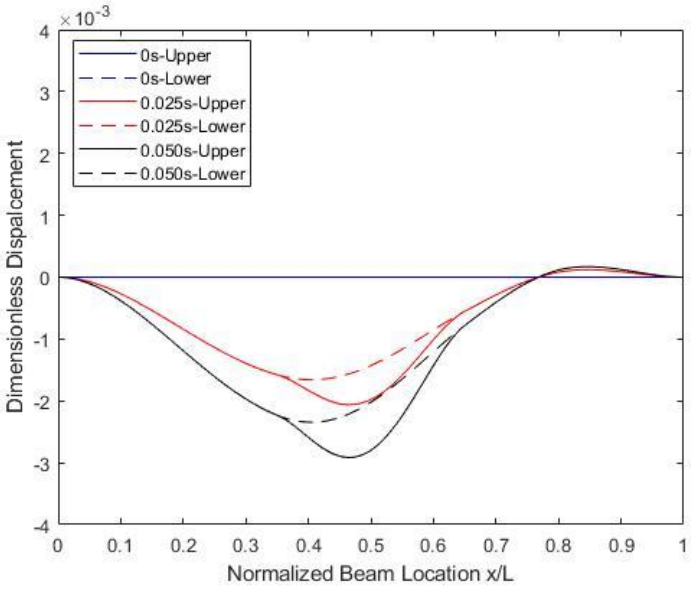

(a) Free mode model.

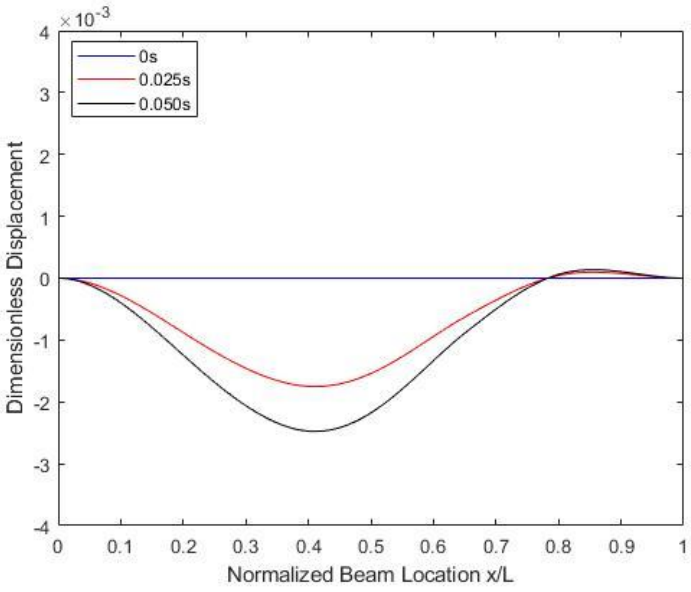

(b) Constrained mode model.

Figure 2-31 The shape of the beam with $0.25H$ *delamination at different values of time.*

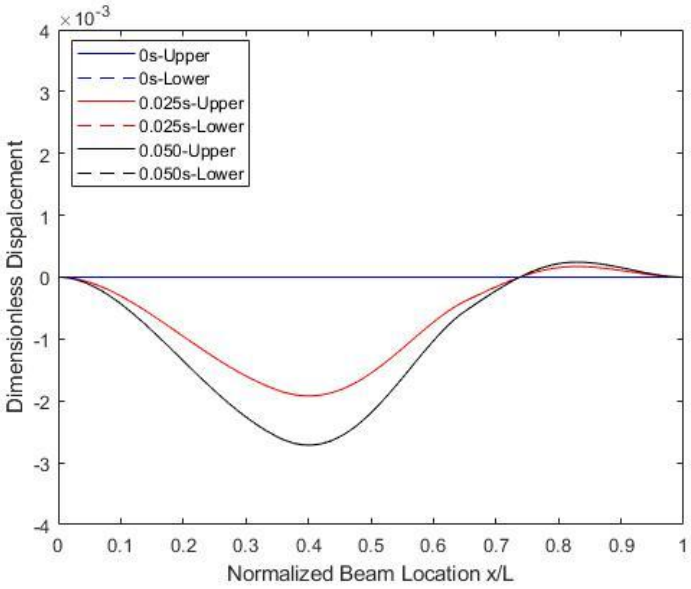

(a) Free mode model.

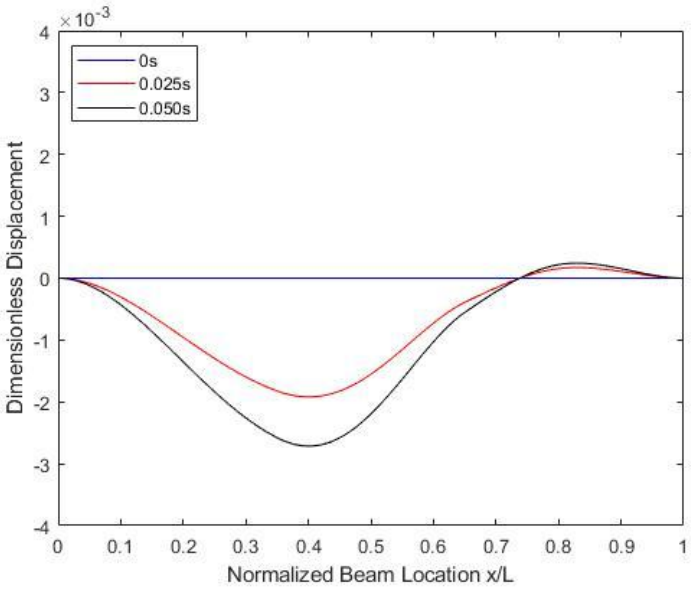

(b) Constrained model.

Figure 2-32 The shape of the beam with $0.5H$ *delamination at different values of time.*

Based on Figure 2-31, the result indicates that the deformation of the delaminated beam from the free mode model is different from the constrained mode model when the delamination is not in mid-plane. Figure 2-32(a) shows that the distance between the sub-beams in the delaminated region is different

at different values of time in the free mode model due to the deformation of the beam at different moments. While the split of sub-beams from the free mode model disappears when the delamination in the mid-plane is shown in Figure 2-32(a). The result from different delamination depth is shown in Figures 2-33 to 2-34:

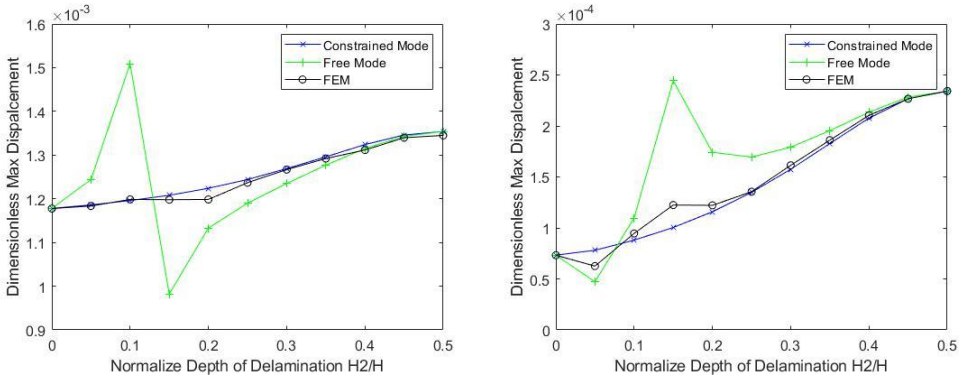

(a) $L_s = 0.20L$; *(b)* $L_s = 0.85L$;

Figure 2-33 The vibration responses of delamination in different depths

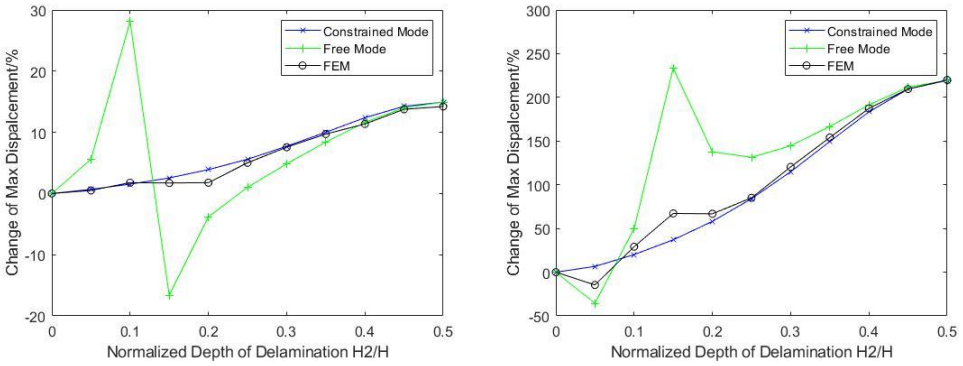

(a) $L_s = 0.20L$; *(b)* $L_s = 0.85L$;

Figure 2-34 The change ratio of max displacement with different delamination depths.

Figure 2-33 indicates that the difference between the two models is clear for forced vibration when the depth of delamination is small which means the delamination is far from mid-plane with the drive frequency being 5Hz. This

is the result of the local deformation of sub-beams in the delamination region as shown in Figure 2-31(a) for the free mode model. With the depth increasing and delamination closer to mid-plane, the difference is becoming smaller because of the smaller difference between the sub-beams. Moreover, the changing trend of displacement from the free mode model fluctuates drastically when the depth of delamination is smaller than 0.25H generated of the local deformation of sub-beam 2 due to the small thickness. The value of the FEM method is closer to the 'constrained mode' model but it has a similar fluctuated trend with the free mode at measured point L_s=0.85L as shown in Figures 2-33(b) and 2-34(b).

It should be noted that the displacement of the point $L_s = 0.20L$ is larger than $L_s = 0.85L$ because of the deformation changing as shown in Figure 2-24. However, the change ratio of L_s=0.85L is much larger than $L_s = 0.20L$ which means the point $L_s = 0.85L$ is more sensitive to the delamination depth with excitation frequency being 5Hz as shown in Figure 2-34.

Based on Figure 2-23 and Figure 2-26, it indicates that the effect of delamination size is larger than the delamination depth, which means the effect of the delamination size is larger than the delamination depth under 5Hz excitation as same as 1Hz excitation mentioned in Section 2.3.1.

Moreover, it also should be noted that the result under 5Hz excitation is different from 1Hz comparing Figures 2-20 to 2-24 with Figures 2-30 to 2-34.

The change range of dynamic responses and deformation under 5Hz excitation is larger than 1Hz excitation because the dynamic responses generated by higher drive frequency excitation is more sensitive to delamination.

2.4 Conclusions

This chapter proposed a method based on the Green's function to analyze the dynamic responses of beams with various delamination. Both the free mode model and constrained mode model of delaminated beams with clamped-clamped boundary conditions were analyzed by this method. There is some conclusion as follows:

1. The proposed method based on the Green's function can be used for vibration analysis of structures with delamination. The result demonstrates that this method is credible and accurate for the vibration analysis of beams with various single delamination due to its analytical methods without any approximating. The natural frequencies and mode shapes calculated by this method based on both the free mode model and the constrained mode model are the same as previous work as well as the effect of delamination on these vibration characteristics, which demonstrates the credibility of the proposed methods. The result indicates that all the parameters of delamination will affect the vibration characteristics, including reducing the natural frequency, changing the mode shape and the locations of nodes and antinodes, and generating new local modes and local deformation of the beams.

2. The result also indicates that the delamination will generate additional axial load in the continue point between intact sub-beams and sub-beams at the delaminated boundaries, which will affect the deformation of mode shapes and locations of antinodes and nodes. When the delaminated part is between the antinodes, the axial load will be compressive loads, which will enhance the deformation of sub-beams and the mode shapes.
3. For the forced vibration under concentrated harmonic excitation, the difference between these two models is related to the excitation frequency and the delamination depth. When the delamination is in the mid-plane of the beam, the result of the two models is the same due to the same thickness of sub-beams in the delaminated region. Otherwise, the difference between the two models is clear due to the different thicknesses and local deformation of sub-beams, which have different displacements in the free mode model. It should be also noted that the difference is related to the excitation frequency because the local deformation is different with various excitation frequencies.
4. All delamination parameters will affect the dynamic responses of the beams under concentrated harmonic excitation. The change trends and effects in the same location in the beam with various delamination depths and sizes are different due to the difference of deformation generated by the delamination with various sizes and depths. Furthermore, delamination size will influence forced vibration responses more than delamination depth under harmonic concentrated load in the same part of beams. The

relationship between delamination depth and max displacement fluctuates when the delamination is close to the surface based on the free mode model due to the local deformation of the sub-beams in delaminated regions. The FEM result is closer to the constrained mode result but it has similar fluctuation with the free mode model when the delamination is close to the surface. It should also be noted that the effect of delamination is related to the excitation frequency due to that the deformation is different under various excitation frequencies.

5. The delamination will change the vibration responses and displacement of beams under harmonic concentrated excitation. However, the different parts will have different change trends and change ratios with various delamination parameters under harmonic concentrated excitation with various frequencies, which means the different parts have different sensitivities to the delamination sizes and depths with various excitation, including the drive frequency. Therefore, it is important and necessary to optimize the signal measurement locations for the improvement of delamination detection and assessment based on vibration characteristics and dynamic responses.

This chapter analyzed the dynamic responses of the delaminated beam based on the Green's function method. The result can be used for the optimization of vibration signal measurement location and delamination assessment based on the dynamic responses in the following chapters.

Chapter 3 THE OPTIMIZATION FOR DYNAMIC RESPONSES MEASUREMENT FOR DELAMINATED BEAMS

This chapter developed the optimization methods for the signals measurement locations for the delamination assessment in a homogeneous beam based on the previous methods and result in Chapter 2.

As mentioned in Chapter 2, the delamination will affect the vibration responses of structures, while the effect on different locations is various and related to the delamination parameters. As a result, it will influence the performance of delamination detection based on the dynamic signal from different locations because of the different sensitivities and changes from various measurement locations [22]. Moreover, previous researchers also mentioned that the accuracy can be improved by selecting vibration characteristics of particular modes that are more sensitive to the damage and robust to the noise [177]. The significance and advantage of sensor location optimization for structure monitoring have been demonstrated by researches for detection, control, and smart structure design, which can measure the vibration of particular modes with high distribution effectively [178, 179]. Therefore, it is necessary to optimize the signal measurement locations for the delamination assessment in composite structures.

For vibration monitoring and controlling, previous researchers used

modal observability and spatial observability to optimize the sensor locations. Halim et al. [180] used the spatial observability measure to investigate the effect of sensor location in observing certain vibration modes. It is found that an optimized sensor location over the target structure can effectively enhance the sensing performance by selecting particular modes. Then some researchers optimized the sensor locations for signal measurement by using observability and controllability for detection and control [181-183]. Daraji et al. [184] used spatial observability and controllability to find the optimal locations for sensor/actuator (s/a) pairs for the active vibration control in a cantilever plate. They indicate that the optimization can enhance the effectiveness of the s/a pairs for active vibration control by focusing on modes with a high distribution. The optimization based on observability is also useful for the vibration active control of composite structures [178]. Zoric et al. [185] used a self-tuning fuzzy logic controller to control the vibration of composite plates by analyzing the mode shape and controllability. They tried several samples with different structures and all the cases demonstrated the effectiveness of the actuator optimization for vibration control. Some researchers also mentioned that the optimization based on observability for vibration signals is potential for complex structures with special geometry and real-life structural monitoring [179, 186, 187]. These researchers illustrate that the vibration signal measurement from the optimal location can enhance the ratio of particular modes and reduce the disturbance generated by other modes. The

optimization for measurement locations based on modal observability and spatial observability has been demonstrated by previous researches.

However, the methods based on spatial observability and modal observability were used for undamaged structures. The dynamic responses of intact structures will not change. While for the delaminated beams, the modal observability and spatial observability will be affected by the delamination, which will change the observability of fixed locations. It is important for delamination assessment based on the dynamic responses of beams. Therefore, this chapter tries to find the optimal vibration signal measurement locations for assessing delamination in beam structures by considering the effect of various delamination parameters. The modal observability (M_n) and the spatial observability (S_o) of beams with various delamination were calculated based on the Green's function method as shown in Chapter 2 to show the effect of delamination on the deformation and displacement of the beam. The optimization of the vibration signal measurement locations for the various delamination in homogenous beams was done, which can provide support for the following parts of this research.

3.1 The Effect of Delamination on the Dynamic responses of Different Location

As mentioned in Chapter 2, the effect of delamination on the dynamic responses of different axial locations is affected variously by the delamination

parameters and excitation frequency. The dynamic responses and the changing trend of different axial locations are affected by the excitation frequency. The max displacement of different axial points L_s under various concentrated harmonic excitations calculated by the Green's function method is shown as:

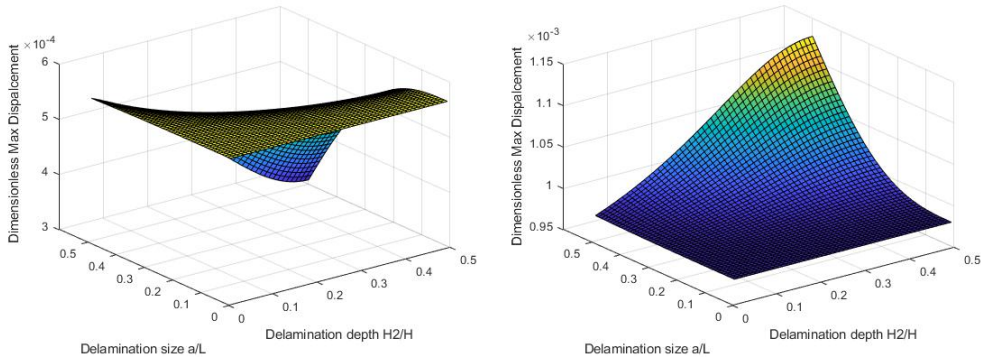

(a) L_s=0.20L; *(b) L_s=0.85L;*

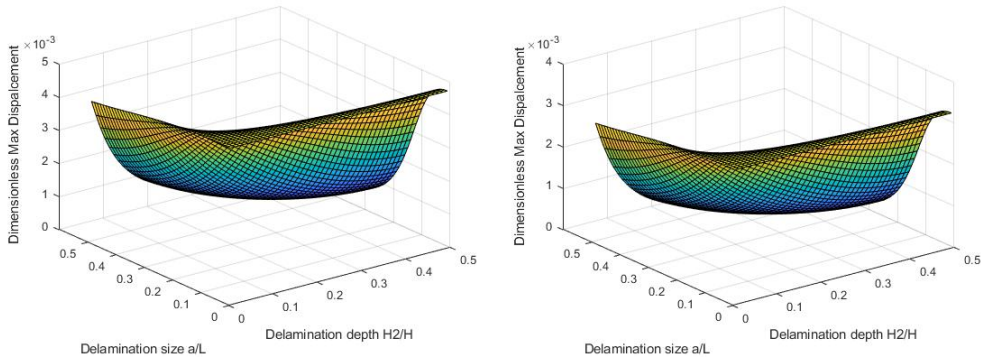

(c) Ls=0.20L; *(d) Ls=0.85L;*

Figure 3-1 The max displacement of different axial points based on the constrained mode model with 1Hz excitation (a-b) and 10Hz excitation (c-d)

Figure 3-1 shows the displacement of two different axial locations under two different excitations with various delamination sizes and depths. The result indicates that the changing trend of these two points is different. When the excitation frequency is 1Hz, the displacement of $L_s = 0.2L$ is decreasing as

shown in Figure 3-1(a), while the $L_s = 0.85L$ increases with size and depth is larger as shown in Figure 3-1(b), due to the local stiffness reduction and deformation changing of the beam as mentioned in Chapter 2. However, when the excitation frequency is 10Hz, the changing trend of these two points is similar to decrease, which is because the excitation frequency is close to the natural frequency of the 2nd mode, so the deformation of the beam is close to the 2nd mode shape, while these two axial points are almost symmetric by the middle spanwise of the beam. Therefore, there will be similar changing trends of these two points. But it also should be noted that the value of displacement is different, while the change value of $L_s = 0.2L$ is larger than $L_s = 0.85L$ as shown in Figure 3-1(c) and Figure 3-1(d). These results show that the dynamic responses of beams are different under various excitation frequencies. In another aspect, the delamination parameters will also affect the dynamic responses and changing trends of different axial locations. The max displacement of two axial locations is calculated as shown in Figure 3-2:

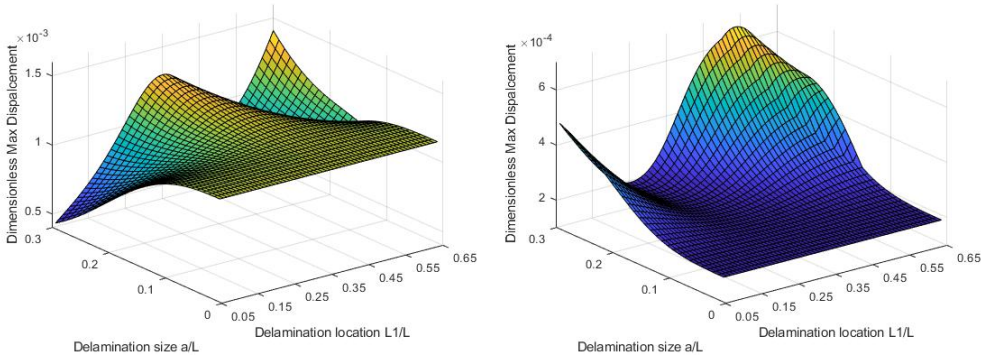

(a) L_s=0.20L; *(b) L_s=0.85L;*

Figure 3-2 The max displacement of different axial points with 5Hz excitation based on the constrained mode model

Figure 3-2 shows the displacement of two axial points with different delamination sizes at various axial locations. It can be seen that when the delamination size is smaller than 0.1L, the change of displacement from these two points are not clear with delamination at various locations due to the small delamination has less effect on the dynamic responses of beams. With the delamination being larger, the change becomes larger due to more reduction of stiffness. It should also be noted that when the delamination size is larger than 0.2L, the change of displacement with various delamination locations fluctuates. The reason for this phenomenon is that the excitation frequency is being closer to the 2^{nd} mode natural frequency, which decreases due to the stiffness reduction generated by the delamination. Therefore, the deformation of the delaminated beams will have two antinodes, while the deformation change will be larger when the delamination boundaries close to the antinodes due to the additional axial load generated by delamination. So there will be two peaks in the changing trend. A similar phenomenon can be found in the displacement changing with various delamination depth at different locations below:

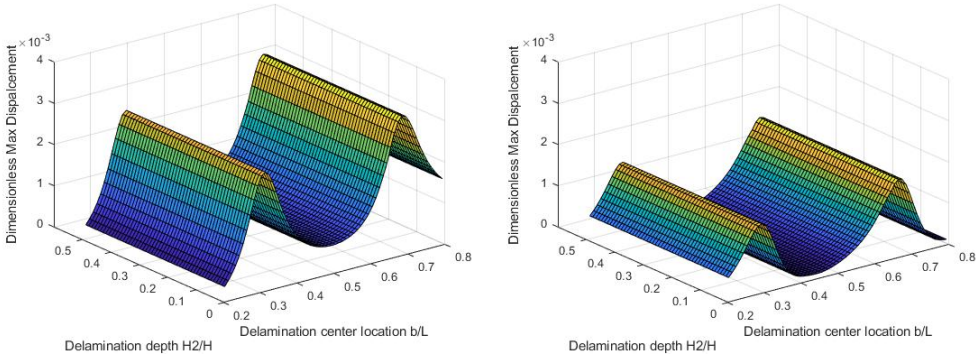

(a) L_s=0.20L; *(b) L_s=0.85L;*

Figure 3-3 The max displacement of different axial points with 10Hz excitation based on the constrained mode model.

Figure 3-3 illustrates that when the delamination is located at 0.35L and 0.75L, the change of displacement is the largest due to the delamination boundaries close to the antinodes of the 2nd mode. However, with various delamination depths, the change of displacement is small as the result of the small effect generated by various delamination depths on the dynamic responses.

As mentioned in Chapter 2, the delamination between the antinodes will affect the deformation of beams. The max displacement of location L_s=0.2L with delamination at different locations is shown below:

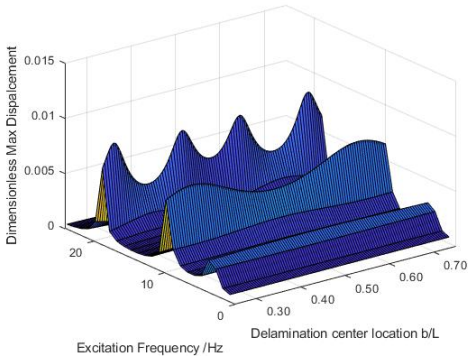

(a) 3 dimension view;

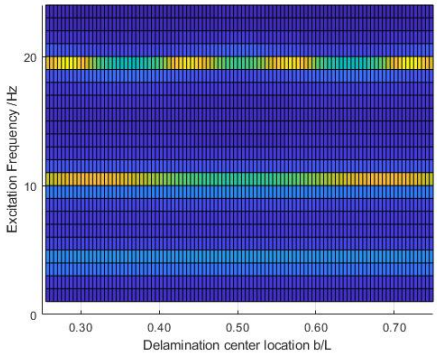

(b) 2 dimension view;

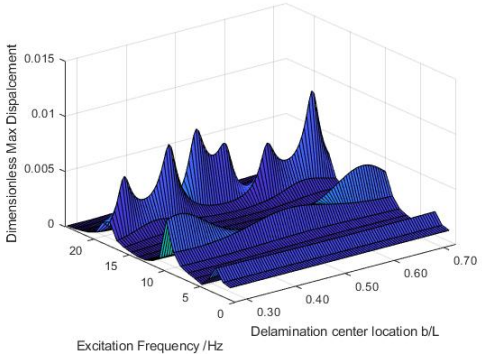

(c) 3 dimension view;

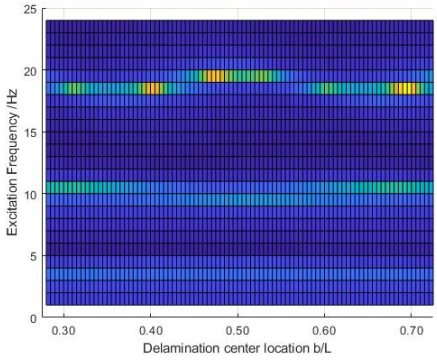

(d) 2 dimension view;

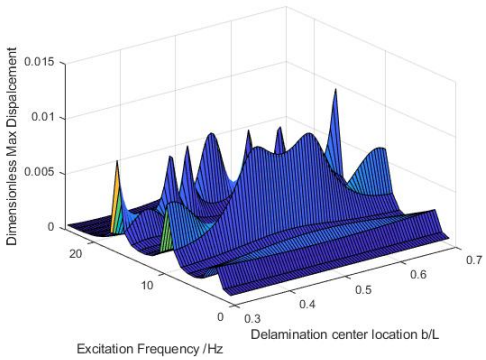

(e) 3 dimension view;

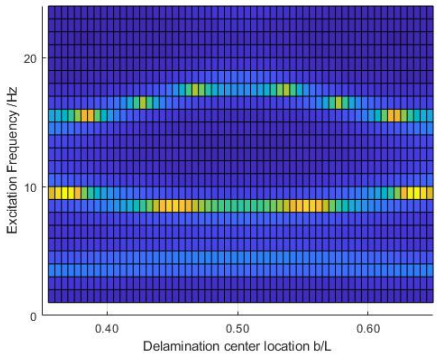

(f) 2 dimension view;

Figure 3-4 The displacement of measurement locations based on the constrained mode model with delamination at different locations: 1) $H_2 = 0.5H, a = 0.1L$ *(a-b); 2)* $H_2 = 0.5H, a = 0.15L$ *(c-d); 3)* $H_2 = 0.5H, a = 0.2L$ *(e-f).*

The result in Figure 3-4 shows that the displacement of measurement location is various with delamination location changing. As mentioned in Chapter 2,

the displacement will be large when the delamination boundaries are close to the antinodes due to the additional axial loads generated by the delamination. Therefore, it can be seen there are two peaks of the displacement for the 2nd mode due to there are two antinodes in the part from 0.30L to 0.70L. The displacement is large when the delamination size is 0.1L and the center of delamination is located at 0.30L because the delamination region is from 0.25L to 0.35L, which is close to the antinode located at 0.36L as shown in Figure 3-4(a). It should be noted that the 3rd mode will have four peaks in the region from 0.3L to 0.7L when the delamination size is 0.1L as shown in Figure 3-4(a). However, as shown in Figures 3-4 (c) and (e), there are more peaks in the same region, which is because the location of antinodes will also be affected with delamination location changing.

These results indicate that the effect of various delamination parameters and the different excitation on the dynamic responses of various locations is different. This is because the delamination will change the mode shapes, including the locations of antinodes and nodes, the amplitude. Therefore, the dynamic responses from beams with various delamination will be complicated. For delamination assessment and detection based on the dynamic responses, it is necessary to optimize the measurement locations by considering the effect of delamination on beam structures.

3.2 Optimization for Signal Measurement

As mentioned in the previous section, the dynamic responses and changing trends of different axial locations are various, which is related to the excitation frequency and delamination parameters. Therefore, it is necessary to optimize the measurement locations by considering the effect of delamination parameters. This section will try to investigate the optimization of the measurement locations for the delaminated beams by considering the effect of delamination based on the modal observability and spatial observability.

Based on reference [188], the modal observability and spatial observability can be calculated and analyzed based on the mode shape $u_n(x)$ solved by the Green's function in Chapter 2 for a delaminated beam. First, for a beam structure, the dynamic equation under excitation can be described as:

$$EI\frac{\partial^4 u}{\partial x^4} + c\frac{\partial u}{\partial t} + \rho A\frac{\partial^2 u}{\partial t^2} = F(x,t). \tag{3-1}$$

While the solution of equation (3-1) can be represented by the generalized coordinate $q_n(t)$ and the eigenfunctions $u_n(x)$ as:

$$u(x,t) = \sum_{n=1}^{\infty} q_n(t)u_n(x). \tag{3-2}$$

For the eigenfunctions $u_n(x)$, there are the orthogonality properties as follows:

$$\int_0^L u_n(x)u_p(x) = \delta_{np}, \tag{3-3a}$$

$$\int_0^L \frac{\partial^2}{\partial x^2}(u_n(x)u_p(x)) = \omega_n^2\delta_{np}, \tag{3-3b}$$

$$\int_0^L \frac{\partial}{\partial x}(u_n(x)u_p(x)) = \omega_n\delta_{np}, \tag{3-3c}$$

where the δ_{np} is the Dirac function, which has properties as $\delta_{np} = 1, (n = p)$ and $\delta_{np} = 0, (n \neq p)$. The ω_n is the natural frequency of the n-th mode. For the excitation $F(x,t)$ at location x_0, it can be described as $F(x,t) = \delta(x - x_0)f(t)$. Then equation (3-1) can be solved by using the Laplace transform method and orthogonality properties of eigenfunctions $u_n(x)$ shown in equation (3-4) as:

$$\frac{\widetilde{q_n}(s)}{\tilde{f}(s)} = \int_0^L u_n(x)\delta(x-x_0)dx \Big/ \bar{a}s^2+2\bar{c}\omega_n s+\omega_n^2. \quad (3\text{-}4)$$

Set $T(s,x_s) = \sum_{n=1}^{\infty} \frac{\widetilde{q_n}(s)}{\tilde{f}(s)} u_n(x_s)$, which is defined as the output of the sensor at location x_s generated by the excitation force at the point x_0. $\tilde{f}(s)$ is the Laplace transform of excitation time factor $f(t)$. The coefficients $\bar{a} = \frac{\rho A}{EI}$ and $\bar{c} = \frac{c}{EI}$, which are related to the material properties set as in Section 2, including the bending stiffness EI, mass density ρ, cross-sectional area A, and attenuation coefficient c. The L is the length of the beam. It should be noted that $\int_0^L u_n(x)\delta(x - x_0)dx = u_n(x_0)$ due to the property of the Dirac function. Therefore, the output of the measurement location x_s can be described as:

$$T(s,x_s) = \sum_{n=1}^{\infty} \frac{u_n(x_0)}{\bar{a}s^2+2\bar{c}\omega_n s+\omega_n^2} u_n(x_s). \quad (3\text{-}5)$$

For equation (3-1), it should be noted that this equation is for the undamaged beam as a sample. For delaminated beam, the eigenfunction $u_n(x)$ is calculated based on the $u_{nm}(x), (m = 1,2,4)$ by equations (2-34) to (2-38). Then the spatial norm $\ll T(s,x) \gg_2^2$ of the transform function $T(s,x)$ can be calculated by:

$$\ll T(s,x_s) \gg_2^2 = \frac{1}{2\pi}\int_{-\infty}^{\infty}\int_0^L trace\{T(j\omega,x) * T(j\omega,x)\}dx_0 d\omega = \sum_{n=1}^{\infty} \left\|\widetilde{T}_n(s)\right\|_2^2, \quad (3\text{-}6)$$

The equation (3-6) also uses the orthogonality of the eigenfunctions $u_n(x_0)$ as shown in equation (3-3). Therefore, based on equation (3-6), the $\widetilde{T}_n(s)$ can be solved as:

$$\widetilde{T}_n(s) = u_n(x_s)/(\bar{a}s^2+2\bar{c}\omega_n s+\omega_n^2). \quad (3\text{-}7)$$

Based on equation (34), a new function is defined as [27]:

$$f_n(x_s) = \left\|\widetilde{T}_n\right\|_2. \quad (3\text{-}8)$$

Then the modal observability M_n of each mode is defined as [27]:

$$M_n(x_s) = \frac{f_n(x_s)}{max_{x_s\in(0,L)}(f_n(x_s))} \times 100\%. \quad (3\text{-}9)$$

The L means the total length of the beams. The spatial observability S_o is defined as [27]:

$$S_o(x_s) = \frac{\sqrt{\sum_{n=1}^{N} f_n(x_s)^2}}{max_{x\in(0,L)}(\sqrt{\sum_{n=1}^{N} f_n(x_s)^2})} \times 100\%, \quad (3\text{-}10)$$

where the N is the highest frequency mode number. Based on equation (3-8) to (3-10), it can be seen that the higher mode will have less contribution in the observabilities due to the larger natural frequency ω_n of the higher mode. Moreover, for free vibration, the distribution of low-frequency modes is higher than the high-frequency modes. Furthermore, the effect of the high modes is small and weak in the delamination assessment based on the dynamic responses. So the research will focus on the first four modes. The optimization will try to find the location with high distribution from the first three modes and less effect of the 4th mode due to the first three modes will be distributed the most energy of the vibration.

It should be noted that this section will consider the cases with various delamination. Therefore, the average of the spatial observability and modal observability is used as the target for the optimization, which is different from the previous work for undamaged structures. Based on this definition, the measurement location optimization problem can be defined as:

$$\begin{aligned} & max_{x_s \in (0,L)} \qquad \bar{S}_o(x_s) = \frac{1}{J}\sum_{j=1}^{J} S_{oj}, \\ \text{Subject to} \quad & \bar{M}_n(x_s) = \frac{1}{J}\sum_{j=1}^{J} M_{nj}(x_s) \geq 50\%, n = 1,2,3, \\ & \bar{M}_n(x_s) = \frac{1}{J}\sum_{j=1}^{J} M_{nj}(x_s) \leq 50\%, n = 4 \end{aligned} \tag{3-11}$$

where the $S_{oi}(x)$ and $M_{ni}(x)$ means the spatial observability and modal observability of the *i*th case with fixed delamination, while the $\bar{S}_o(x)$ and $\bar{M}_n(x)$ represent the average of the spatial observability and modal observability for *m* cases. The largest average spatial observability S_o can provide strong vibration signals. Moreover, limiting the distribution of the 4th mode under 50% can reduce the disturbance generated by this mode effectively, which is small than the distributions of the first three modes, but it will affect the vibration signal analysis. To verify the method for measurement optimization, a rectangular delaminated beam was used for testing with fixed-fixed boundary conditions as the same sample in Chapter 2 as shown in Figure 2-1. The delamination is through the width of the beam. This section is divided into two parts for the constrained mode model and the free mode model, respectively. All the parameters are noted in that figure. The following sections are divided into two parts for optimization based on two models, with

various delamination size a, delamination depth H_2 and the location b of the delamination center, respectively.

3.3 Result of the Constrained Mode Model

The optimization based on the constrained mode model was investigated based on the modal observability (M_n) and the spatial observability (S_o). It should be noted that there is no split between the sub-beams in the delamination region. Therefore, it just needs to show the mode shape of one sub-beam in the delamination region. In this section, the mode shape of sub-beam 2 in Figure 2-1 was used.

3.3.1 Different Delamination Sizes

The natural frequency of different delamination size was calculated by equation (2-41) for different delamination, while the normalized depth was set as $H_2 = H/2$. The normalized size was replaced as a/L. The location of delamination was set as $L_1 = (L - a)/2$ (i.e $b = L/2$), which means that the delamination was in the mid-span of the beam. The natural frequency of beam with different delamination size is shown as follows:

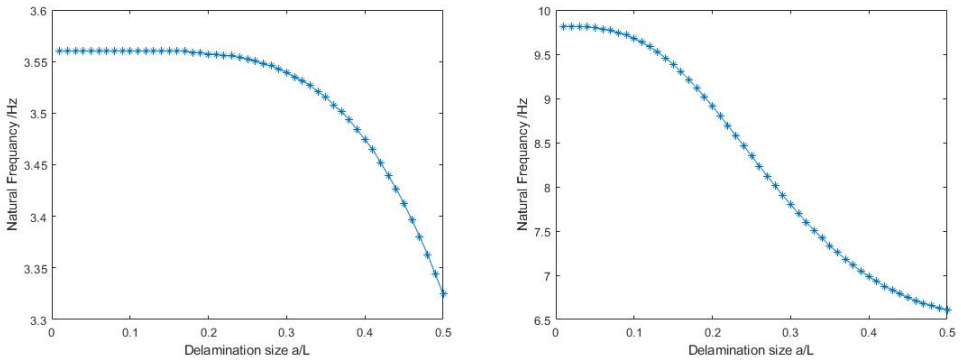

(a) 1st mode;

(b) 2nd mode;

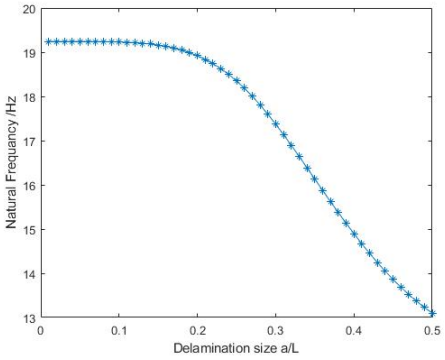

(c) 3rd mode;

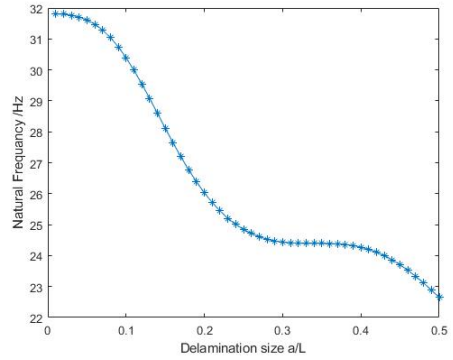

(d) 4th mode;

Figure 3-5 The Natural Frequency of the beam with different delamination sizes.

As shown in Figure 3-5, the natural frequency will decrease with the size of delamination increasing as the same as the calculated result in Chapter 2 and previous work due to the reduction of stiffness being larger [28]. The changing trend of vibration modes is different, while the effect of delamination size on the higher modes is larger than the lower modes. The 4th mode's reduction is about 10Hz, while the change of the 1st mode is just about 0.25Hz. This is related to the effect of delamination on the mode shapes. It should be also noted that the change of the 4th mode natural frequency fluctuates while delamination size is increasing. The modal observability of *n*th mode (M_n) is

shown as:

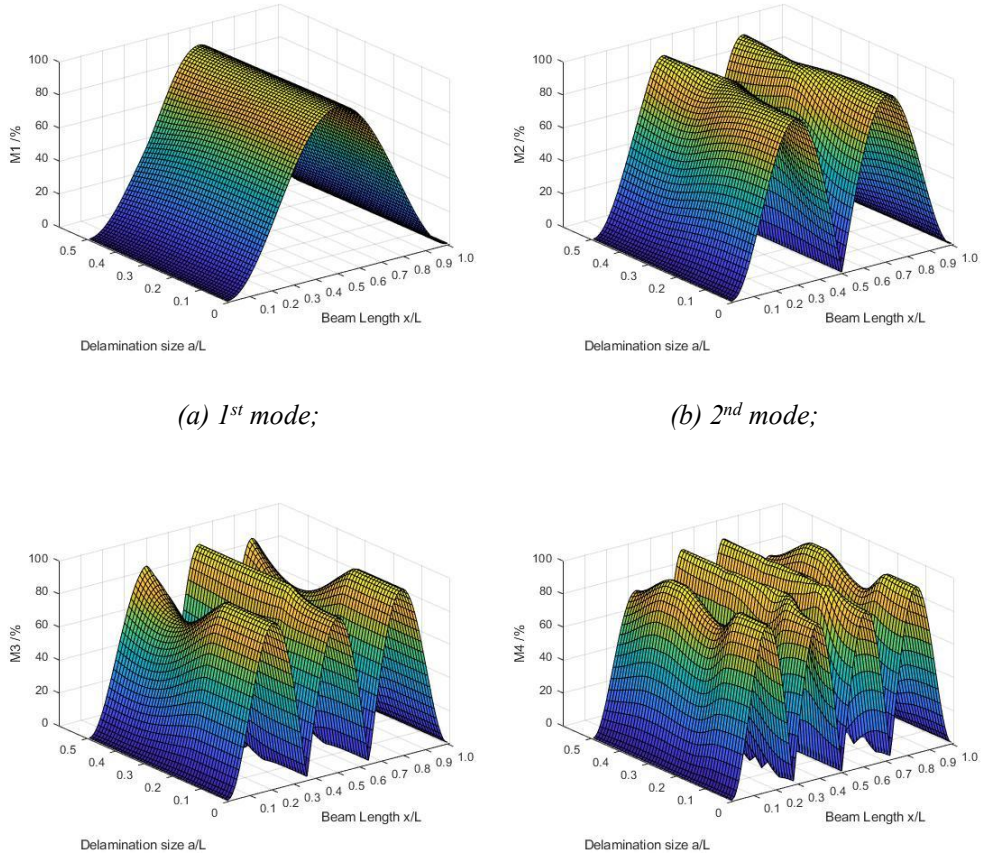

(a) 1st mode; *(b) 2nd mode;*

(c) 3rd mode; *(d) 4th mode;*

Figure 3-6 The modal observability (M_n) of the beam with different delamination sizes.

Based on Figure 3-6, the mode shapes of beams with different delamination sizes are different due to that delamination just reduce local stiffness. It should be noted that in Figure 3-6 (b)-(d), there are clear changes of observabilities when the delamination region boundaries are close to the antinodes of the mode shape because the delamination just reduces local stiffness and the deflection of antinodes is the largest as well as the change. For example, the M_3 has a significant change when the delamination size is about 0.33L and its ends are close to the antinodes of the 3rd mode shape, which are 0.33L and

0.66L, respectively. The change in the 1st mode shapes is small with various delamination sizes because there is just one antinode. This phenomenon indicates that the change of the dynamic responses of beams with various delamination sizes may be complicated and not monotonic due to various antinodes in different modes. Therefore, the optimization for sensor location is necessary to get good dynamic signals. It also should be noted that the antinodes are changed with various delamination sizes, such as when the delamination size is 0.01L, the antinodes of the 3rd mode are 0.22L, 0.51L, and 0.80L, while then the antinodes are changed to 0.27L, 0.51L, and 0.75L when the delamination size is 0.5L. This phenomenon is the result of the local stiffness of different regions. The spatial observability (S_o) for the first three modes is shown as follow:

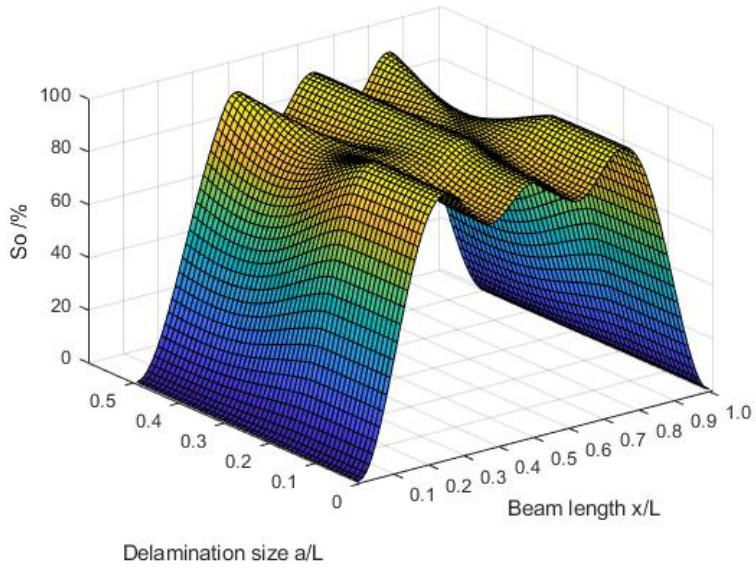

Figure 3-7 The spatial observability (S_o) of the first three modes.

Based on Figure 3-7, it should be noted that the points with high spatial observability are almost between 0.2L to 0.8L. The points with 100% S_o are

different when the delamination size is changing, which means the point will have different spatial observability and dynamic responses with various delamination sizes. Therefore, it is necessary to find a location with a good response with various delamination sizes. The optimization problem for the beams with different delamination sizes can be solved by equation (3-11). The optimum solution is obtained at $x_0=0.73L$ and $x_0=0.27L$ due to the symmetric boundary conditions. The response of the optimal location is as shown:

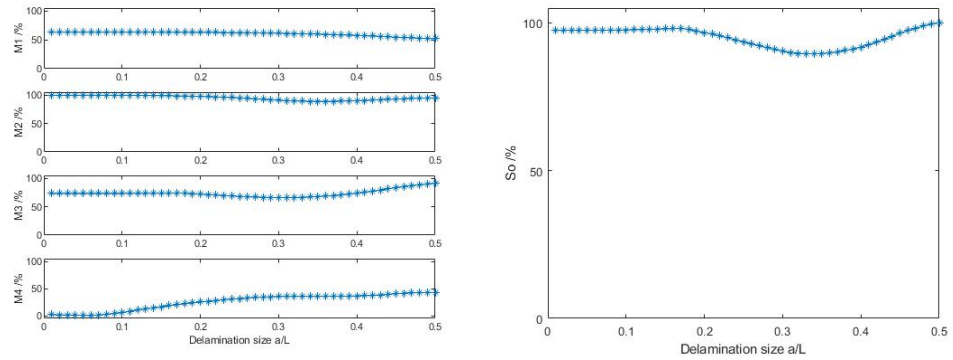

(a) Modal observability (M_n); *(b)Spatial observability (S_o);*

Figure 3-8 The response of optimal location $x_0=0.73L$.

Based on Figure 3-8(a), the result shows the M_4 from all cases is below 50%, while the M_1 to M_3 are more than 50%. The average values of M_n are 60.49%, 95.01%, 90.67% for M_1 to M_3, respectively, which the average value of M_4 is 25.40%. These illustrate that the optimal location fills the constraints. Figure 3-8(b) shows that the S_o is close to 100% for all cases which means the signal amplitude is still strong enough for measurement with less effect of the 4th mode, while the average value of S_o is 95.05%. It also needs to be noted the

M_4 being larger with delamination size, which is because the nodes of the 4th mode are changed and the optimal locations become farther from the nodes of the 4th mode. The Frequency Response Function (FRF) of the point at $x_0 = 0.73L$ (optimal location) and two other points are shown as follows:

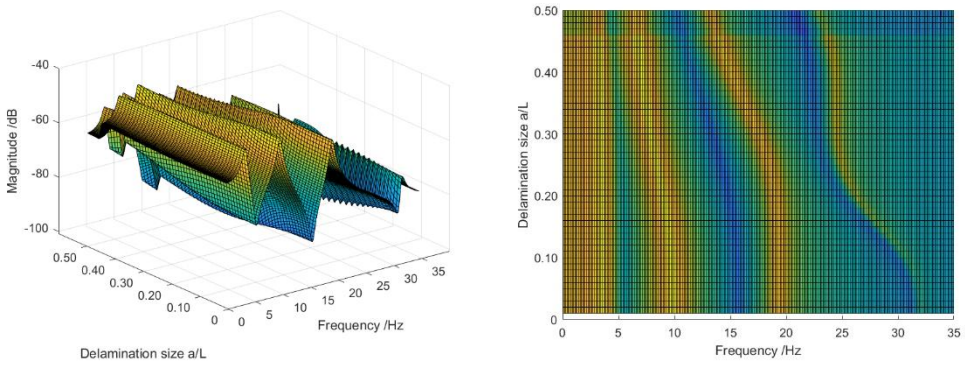

(a) 3-dimensional view; *(b) 2-dimensional view;*

Figure 3-9 The Frequency Response Function (FRF) of optimal location x_0=0.73L.

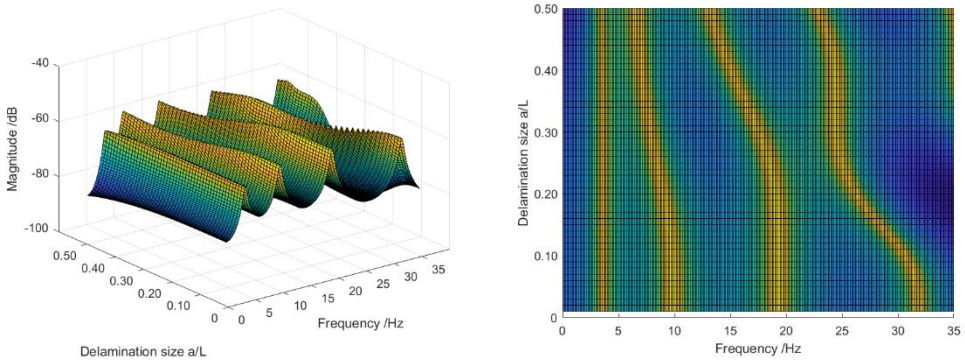

(a) 3-dimensional view; *(b) 2-dimensional view;*

Figure 3-10 The Frequency Response Function (FRF) of location x_0=0.10L.

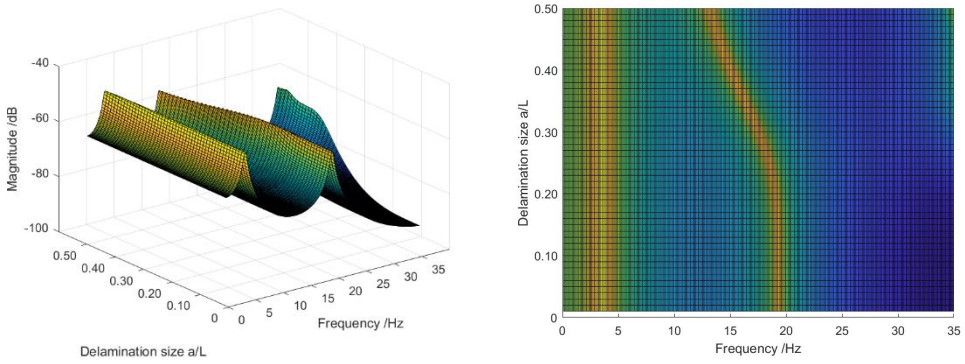

(a) 3-dimensional view; *(b) 2-dimensional view;*

Figure 3-11 The Frequency Response Function (FRF) of location x_0=0.50L.

It should be noted that the FRF shows the first three peaks clearly, which is the first three modes' frequency as well as their change with various delamination sizes. The shift of the third natural frequency is larger than the first two modes as shown in Figure 3-9(b), which is mentioned above. It should be noted that the amplitude of the 4th mode shape is small compared with the FRF of point $x_0=0.10L$ in Figure 3-10, due to the optimal location close to the node of the 4th mode, which is from 0.74L to 0.70L with various delamination sizes. It should be also noted that the FRF of location $x_0=0.50L$ just has two peaks and loses the second mode compared with the FRF of optimal location due to this point located at the node of the 2nd mode, which is the target of the optimization. Therefore, the signals from this optimal point can provide good resolution about the first three modes with less disturbance generated by higher modes.

3.3.2 Different Delamination Depths

Then the natural frequency of different depth was calculated while the normalized size was set as $a = 0.1L$ and the depth was normalized as H_2/H. The location of delamination was set as $L_1 = (L - a)/2$ (i.e $b = L/2$), in the middle of the beam. The natural frequency of different delamination depth is shown as follows:

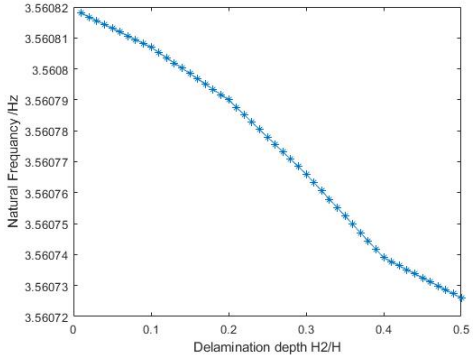

(a) 1st mode;

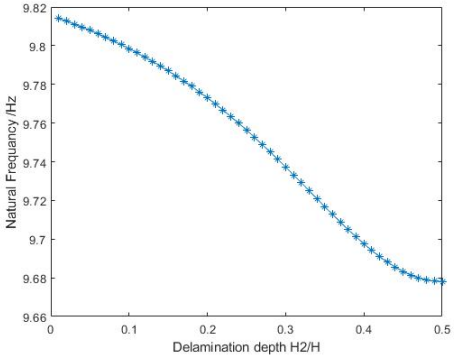

(b) 2nd mode;

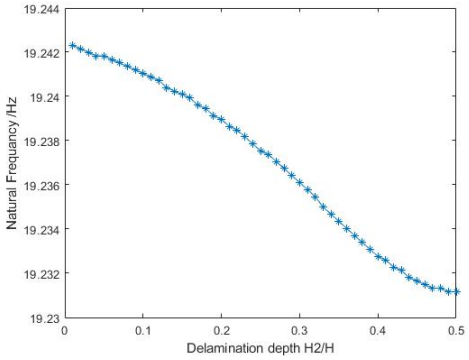

(c) 3rd mode;

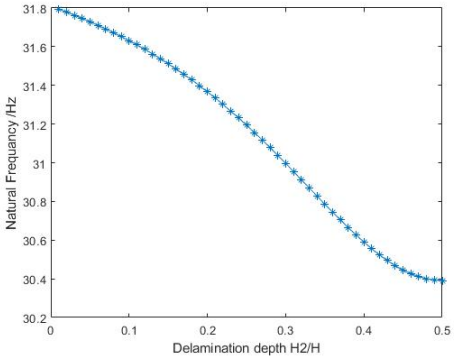

(d) 4th mode;

Figure 3-12 The Natural Frequency of the beam with different delamination depths.

Figure 3-12 illustrates that the natural frequency of the beam will decrease with the depth of delamination increasing due to the stiffness reduced more. However, the change in all modes is small compared with the various delamination sizes. It means the effect of delamination depth is smaller with fixed size and location of delamination. The largest change in the 4th mode for various delamination depths is just about 1.4Hz. The modal observability of *n*th mode (M_n) is shown as follows:

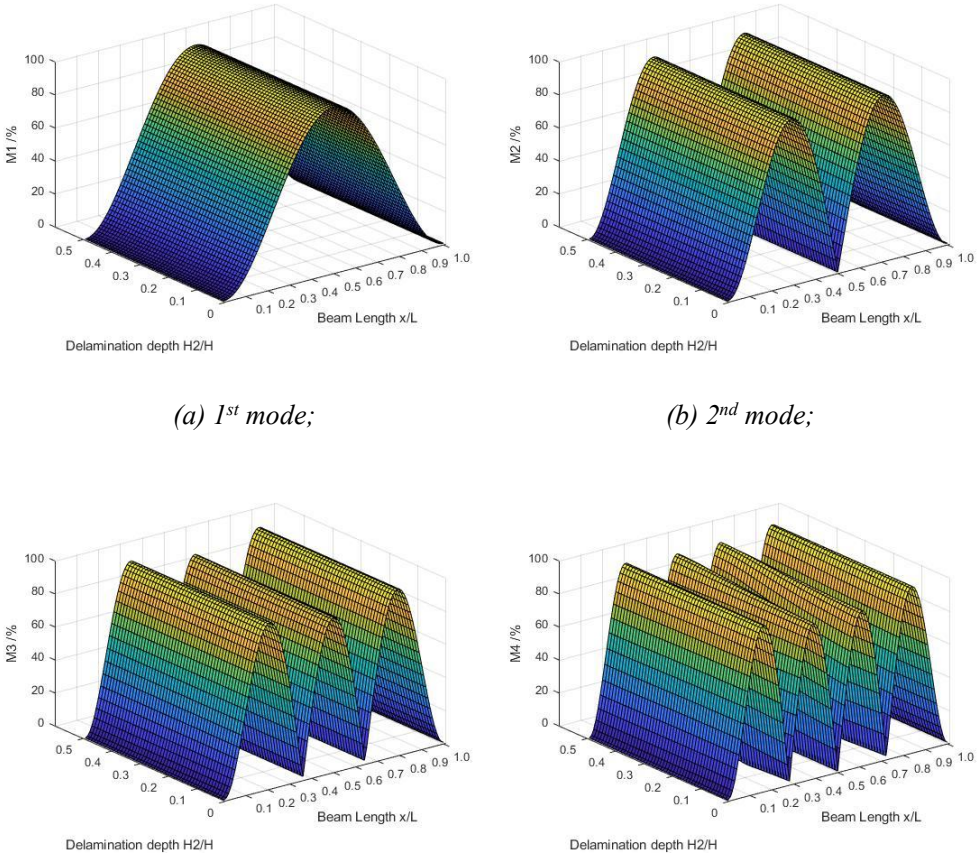

(a) 1st mode; *(b) 2nd mode;*

(c) 3rd mode; *(d) 4th mode;*

Figure 3-13 The modal observability (Mn) of the beam with different delamination depths.

Figure 3-13 shows that the mode shapes don't have clear change with different delamination depths because the effect of delamination depth is small and the delaminated region has no change. The spatial observability (S_o) of the first three modes is shown as follow:

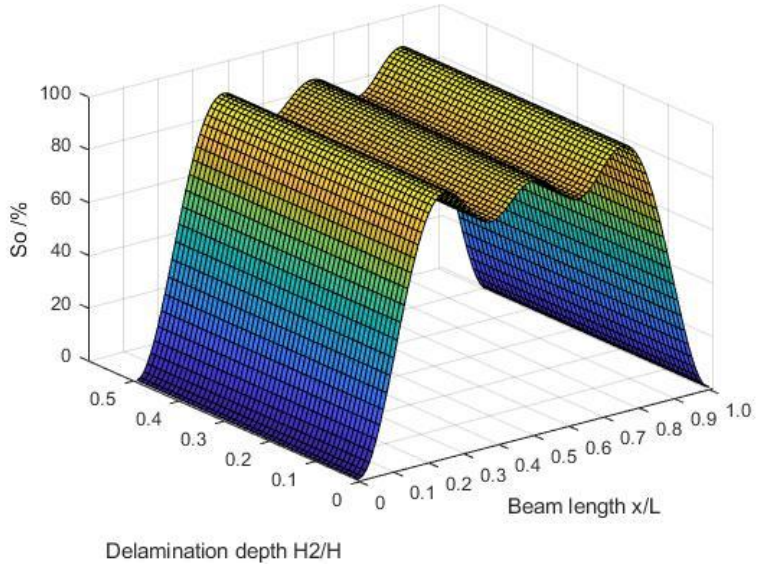

Figure 3-14 The spatial observability (S_o) of the first three modes.

According to Figure 3-14, the points with high spatial observability are concentrated in the part from 0.2L to 0.8L. However, the spatial observability of all the parts of the beam has small changes with various delamination depths. Based on equation (3-11), there are two optimal locations, which are $x_0=0.76L$ and $x_0=0.24L$ due to the symmetric boundary conditions. The response of the optimal location is as shown in Figure 3-15:

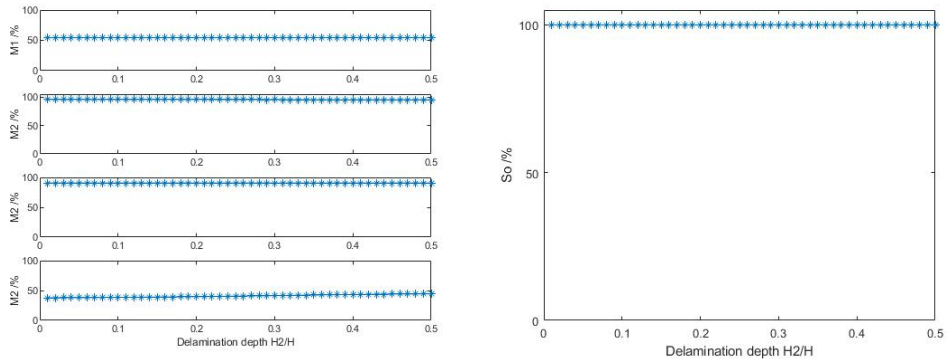

(a) Modal observability (M_n); *(b)Spatial observability (S_o);*

Figure 3-15 The response of optimal location.

Based on Figure 3-15(a), although there is not clear change with various

delamination depths, the M_1 to M_3 of optimal location are more than 50%, while M_4 is less than 50% for all cases. The average values from M_1 to M_4 are 54.36%, 95.49%, 90.67%, and 40.90%, respectively, which are filled with the constraints in equation (3-11). Therefore, the optimal locations can provide signals with high distributions of the first modes and less effect of the 4th mode. The spatial observability is almost 100% in the optimal location for all cases with different delamination depths to keep the measurement signal strong enough. There is no clear change due to the effect of delamination depth on the mode shape is small with fixed size and location. The Frequency Response Function (FRF) is shown as:

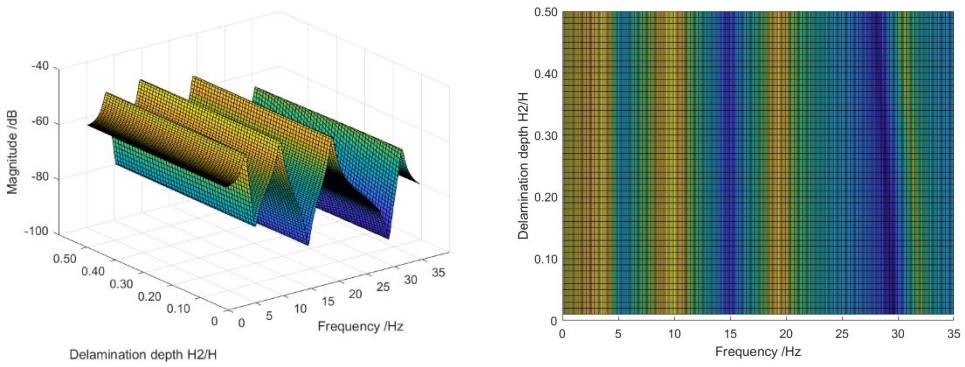

(a) 3-dimensional view; *(b) 2-dimensional view;*

Figure 3-16 The Frequency Response Function (FRF) of optimal location x_0=0.76L.

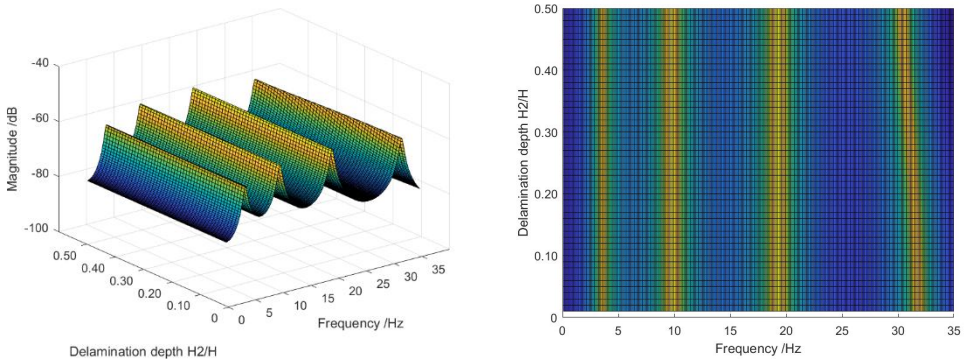

(a) 3-dimensional view; *(b) 2-dimensional view;*

Figure 3-17 The Frequency Response Function (FRF) of location x_0=0.10L.

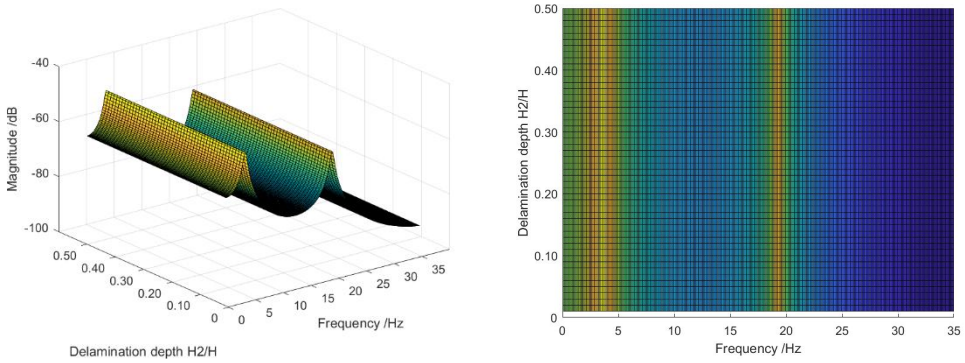

(a) 3-dimensional view; *(b) 2-dimensional view;*

Figure 3-18 The Frequency Response Function (FRF) of location x_0=0.50L.

As shown in Figure 3-16, the FRF result from the optimal location shows clear about the first three peaks, while the other peaks are small compared with the result of point x_0=0.10L in Figure 3-17 due to the optimal location close to the node of the 4th mode, which is about 0.73L. It should also be noted that the FRF of the point x_0=0.50L just has two peaks, which lose the second mode as shown in Figure 3-18 due to this point located at the node of the 2nd mode. Therefore, the measurement from the optimal location can provide the signal with less effect of the disturbance generated by other modes.

However, it should be noted that there is no clear shift of the natural frequency in Figure 3-16 to Figure 3-18 which means the change of the natural frequency is not clear.

3.3.3 Different Delamination Locations

Then the optimization for beams with delamination at various locations is investigated in this section. The natural frequency of different location replaced by normalized various as b/L was calculated while the normalized size was set as $a = 0.1L$. The depth of delamination was set as $H_2 = H/2$ which means that the delamination was in the mid-plane of the beam. The natural frequency of different delamination size is shown as:

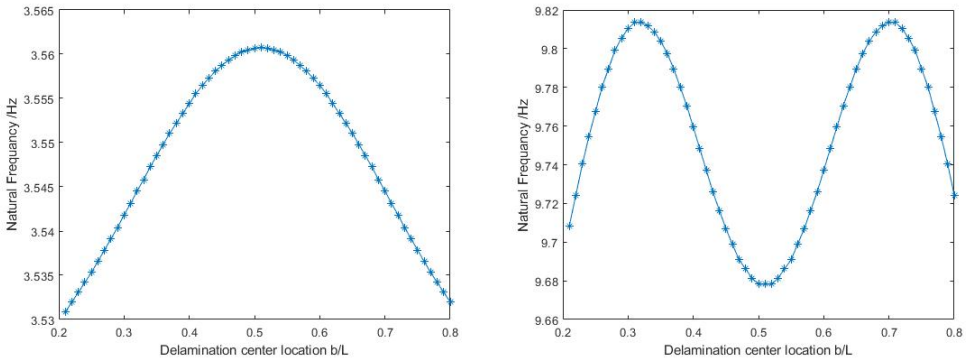

(a) 1st mode;

(b) 2nd mode;

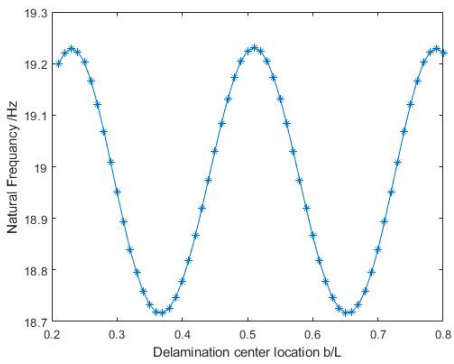

(c) 3rd mode;

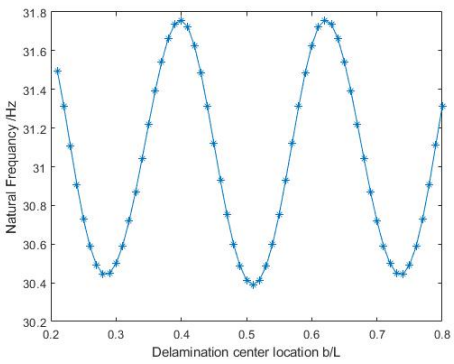

(d) 4th mode;

Figure 3-19 The Natural Frequency of the beam with delamination at various locations.

Figure 3-19 shows that the natural frequency will have different changing trends for different modes due to the location of delamination. It should be noted that the natural frequency fluctuates with delamination at various locations because the delamination just can reduce the local stiffness. Moreover, the changing trend of the natural frequency with delamination at various axial positions of the beam is symmetric since the boundary conditions are the same in right and left end as mentioned in previous work [31]. It also shows that the effect of delamination on the natural frequency is significant when the delamination center is located at the node of mode shapes as mentioned in previous reference [31]. Compared with the result in Section 3.3.1 and Section 3.3.2, the effect of delamination location is a little larger than the depth but much smaller than the size with the largest change being 1.4Hz in the 4^{th} mode, which is because the delamination just reduces local stiffness in the delamination region, while the delamination size has no change in this section. The modal observability of *n*th mode (M_n) is shown as follows:

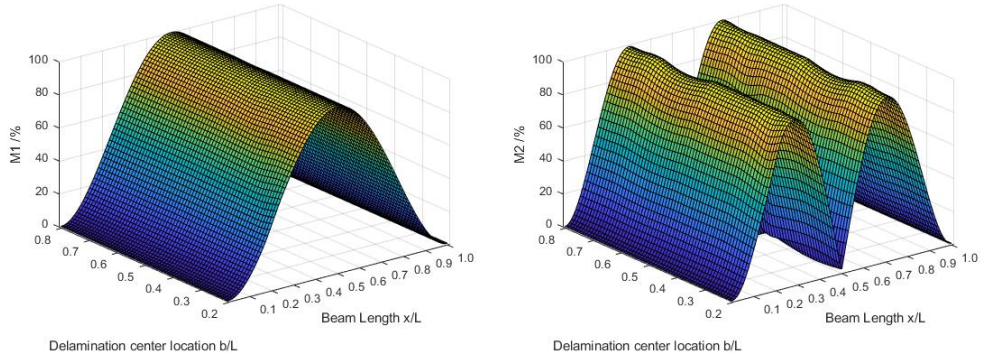

(a) 1st mode; *(b) 2nd mode;*

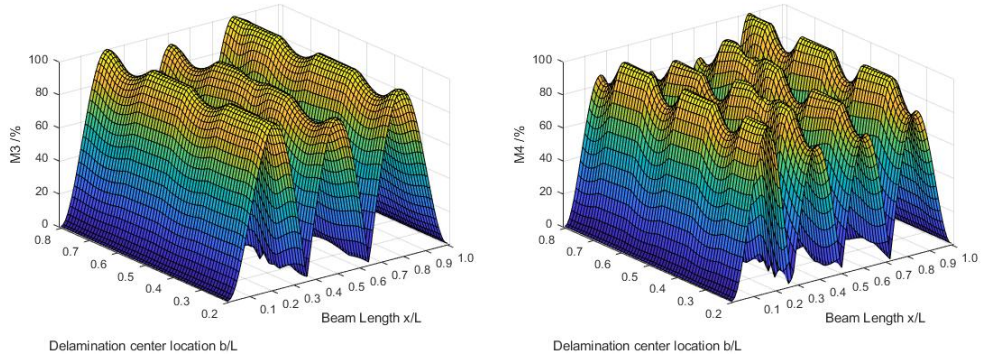

(c) 3rd mode; *(d) 4th mode;*

Figure 3-20 The modal observability (M_n) of the beam with delamination at various locations.

As shown in Figure 3-20, the M_n has clear change with different delamination locations in the 2nd, 3rd, and 4th modes. It should be noted the 2nd, 3rd, and 4th mode shapes have clear change with various delamination locations, while the change generated by the delamination location is more complicated than the delamination size and depth due to the local stiffness reduction. This is because that the delamination just reduces the local stiffness in the region where it is located. Moreover, it should be noted the change generated by delamination is larger when the delamination boundaries are close to the

antinodes of mode shapes. Therefore, it can be seen that the change generated by various delamination locations fluctuates related to the number and locations of antinodes in each mode. As result, the change of displacement from different locations will be complicated and nonlinear. It should be also noted that delamination location affects the nodes and antinodes of each mode, but the change is not clear. For example, when the location L_1 is 0.15L, the antinodes of the 2nd mode are 0.29L and 0.71L, while they are changed to 0.30L and 0.72L with the delamination located at 0.45L, which is due to the small fixed delamination size. The spatial observability (S_o) of the first three modes is shown as follow:

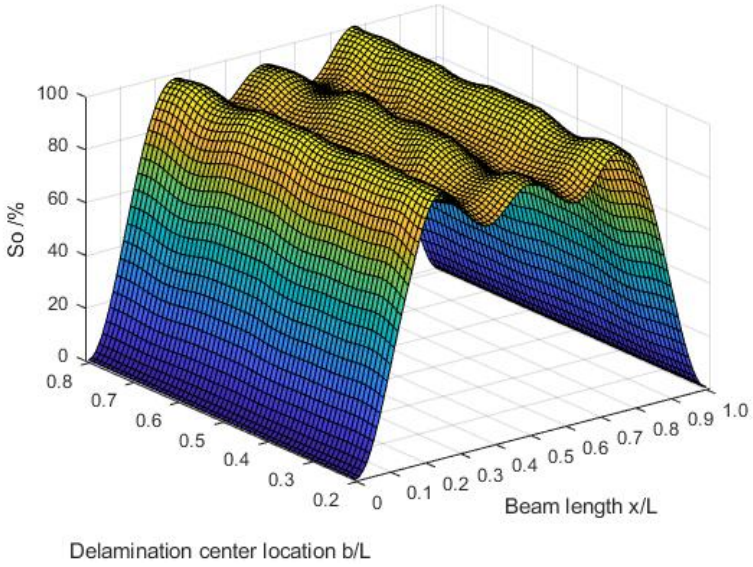

Figure 3-21 The spatial observability (S_o) of the first three modes.

The result in Figure 3-21 illustrates that the points with high spatial observability are concentrated in the middle part from 0.2L to 0.8L due to the boundary conditions. While the points with 100% spatial observability are various from cases with delamination at different locations. The S_o and M_n of

each measurement point will have a fluctuated change trend with delamination at various axial positions of the beam. Based on equation (3-11), the optimal locations are $x_0=0.76L$ and $x_0=0.24L$ due to the same boundary conditions on the two sides. It can be seen that this result is the same as Section 3.3.2. The reason may be because the depth affects the observabilities less, while the change of beams with delamination at different locations is symmetric change with various delamination locations due to the same boundary conditions on the two sides. Therefore, their result is close to the intact beams. Therefore, the optimization for measurement points needs to be improved to find the location for more than one parameter of delamination changing at the same time. The response of the optimal location $0.76L$ is shown in Figure 3-22:

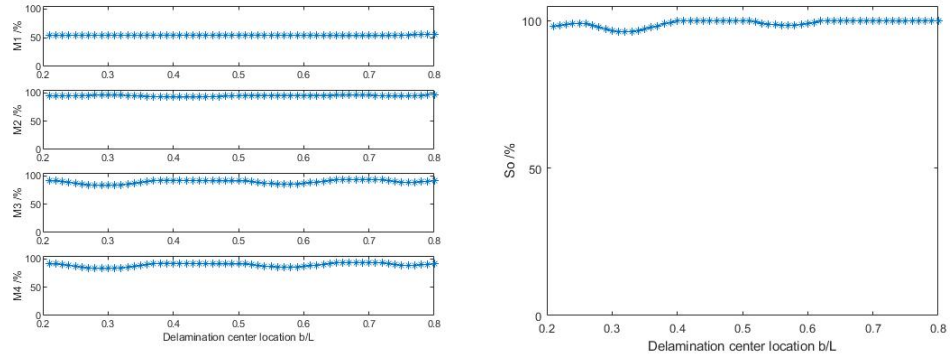

(a) Modal observability (M_n); *(b)Spatial observability (S_o);*

Figure 3-22 The response of optimal location.

Based on Figure 3-22, it shows that although there is fluctuation with delamination location changing, the M_1 to M_3 are more than 50% in optimal location while M_4 is less than 50% for all cases with different delamination location. While the average values from M_1 to M_4 are 54.14%, 94.66%,

89.22%, and 38.11%. The S_o is close to 100% from all cases, which the average value is 99.14%. These illustrate that the signals from the optimal locations are filled with the constraints in equation (3-11). It should be noted that the modal observabilities and spatial observability of the optimal location fluctuate with various delamination locations, which is related to the delamination locations. The Frequency Response Function (FRF) of the optimal location is shown as:

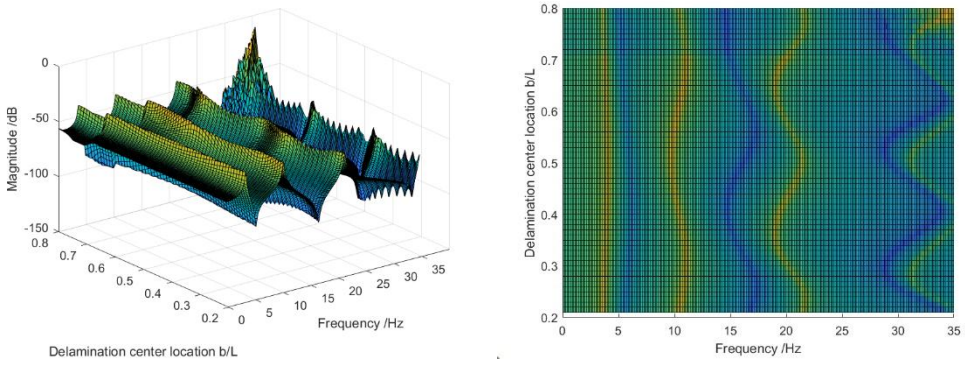

(a) 3-dimensional view; *(b) 2-dimensional view;*

Figure 3-23 The Frequency Response Function (FRF) of optimal location x_0=0.76L

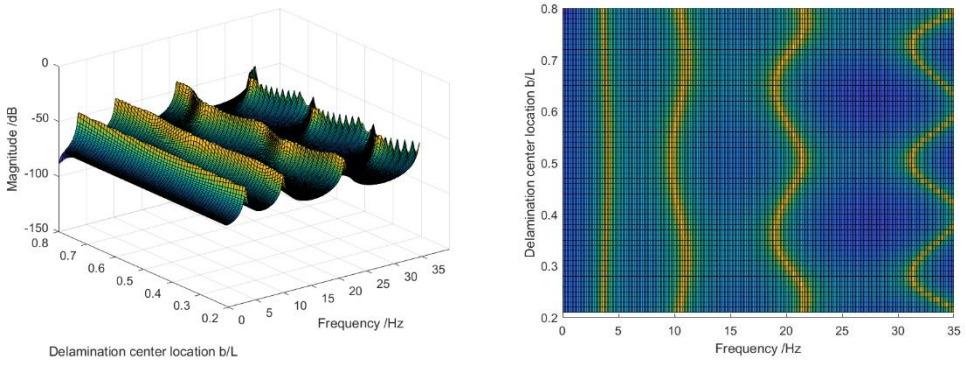

(a) 3-dimensional view; *(b) 2-dimensional view;*

Figure 3-24 The Frequency Response Function (FRF) of location x_0=0.10L.

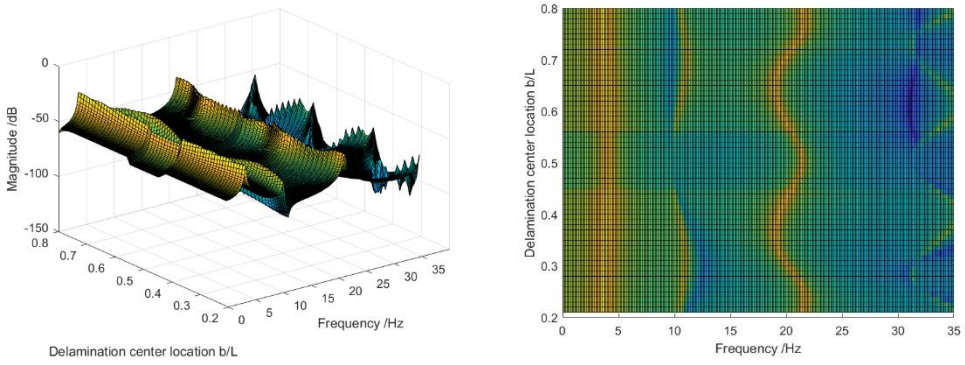

(a) 3-dimensional view; *(b) 2-dimensional view;*

Figure 3-25 The Frequency Response Function (FRF) of location x_0=0.50L.

As shown in Figure 3-23, the FRF of optimal location can provide the first three peaks at the frequency domain clearly, while other peaks are small compared with the FRF of point $x_0 = 0.10L$ as shown in Figure 3-24, due to the optimal locations close to the nodes of the 4th mode. It can be also observed that the FRF of point $x_0 = 0.50L$ only has two clear peaks, which loses the distribution of the second mode as shown in Figure 3-25, because this point is located at the node of the 2nd mode. Therefore, the optimization of the chapter is useful, which can find the optimal point to provide signals with delamination at different locations and the energy is most for the first three modes.

3.3.4 Different Delamination Locations and Sizes

The previous work indicates that the optimal measurement points for various locations and depths of delamination are the same, which both are x_0=0.76L and x_0=0.24L. However, the optimal results of various delamination

sizes are different from this result, which are x_0=*0.73L* and x_0=*0.27L*. Therefore, this section investigates the optimization of beams with various delamination sizes at different locations and find the optimal measurement location for the two parameters changing simultaneously. The delamination depth is set as $H_2 = 0.5H$. The natural frequency of delaminated beams with various location and size is calculated as shown in Figure 3-26:

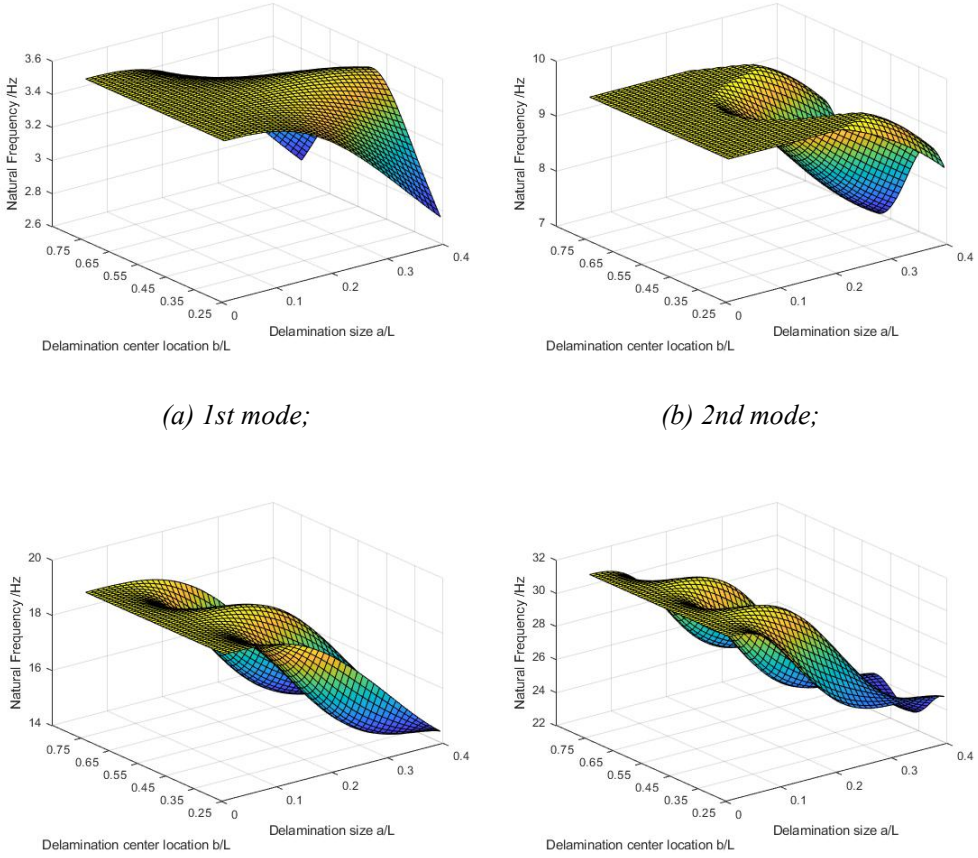

(a) 1st mode; *(b) 2nd mode;*

(c) 3rd mode; *(d) 4th mode;*

Figure 3-26 The Natural Frequency of beams with different delamination.

Figure 3-26 shows that both locations and sizes of delamination will affect the natural frequency, so there is fluctuation in the changing trend due to the different effects of delamination size and location. It should be noted that the

natural frequency will decrease with delamination size increasing, while the change of the natural frequency with delamination at different locations will fluctuate and the largest change will happen when the delamination center (i.e. b=L1+a/2) is close to the nodes of mode shapes as mentioned in Section 3.3.3 and previous work [31]. The change of natural frequency is symmetric due to the same boundary conditions at the two sides of the beam. Then the average observability of the nth mode (M_{na}) for various delamination sizes at a fixed location was defined to find the optimal measurement locations as the following formulation:

$$M_{na}(x) = \frac{f_{na}(x)}{max(f_{na}(x))} \times 100\%, \tag{3-12}$$

where $f_{na}(x)$ means the sum of $f_n(x)$ (i.e. $f_{na}(x) = \sum f_n(x)$) calculated in equation (3-4) with various delamination size when the delamination location is fixed. The average modal observability of nth mode (M_{na}) calculated by equation (3-8) is shown in Figure 3-27:

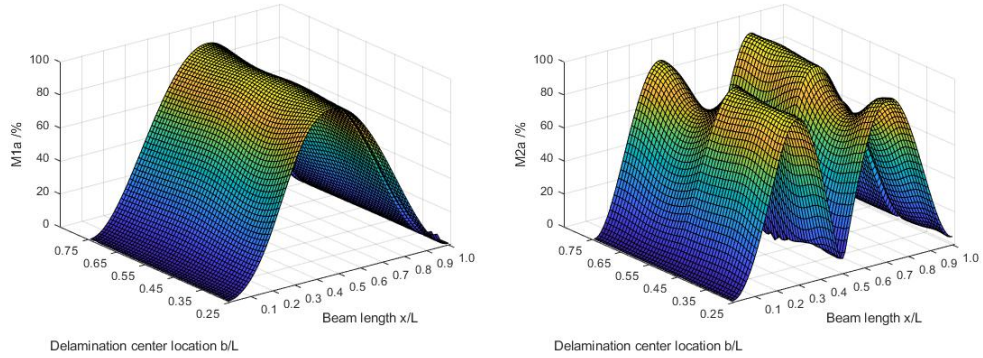

(a) 1st mode; *(b) 2nd mode;*

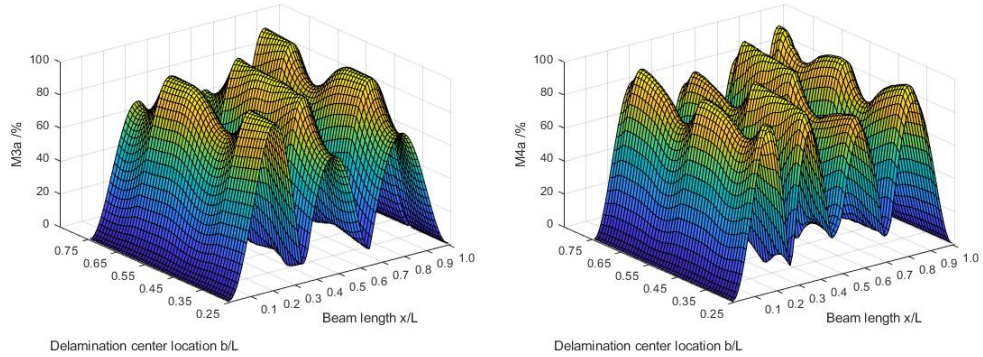

(c) 3rd mode; *(d) 4th mode;*

Figure 3-27 The average modal observability (M_{na}) of beams with different delamination.

Figure 3-27 shows the delamination location will affect the mode shape. Moreover, by comparing it with Figure 3-16, the result in Figure 3-27 indicates that the delamination size also affects the mode shape with delamination at various locations. Therefore, the result is different from the result in Section 3.3.3. For this section, the average spatial observability is defined as:

$$S_{oa}(x) = \frac{\sqrt{\sum_{n=1}^{N} f_{na}(x)^2}}{max(\sqrt{\sum_{n=1}^{N} f_{na}(x)^2})} \times 100\%. \quad (3\text{-}13)$$

The average spatial observability (S_{oa}) is shown as follows:

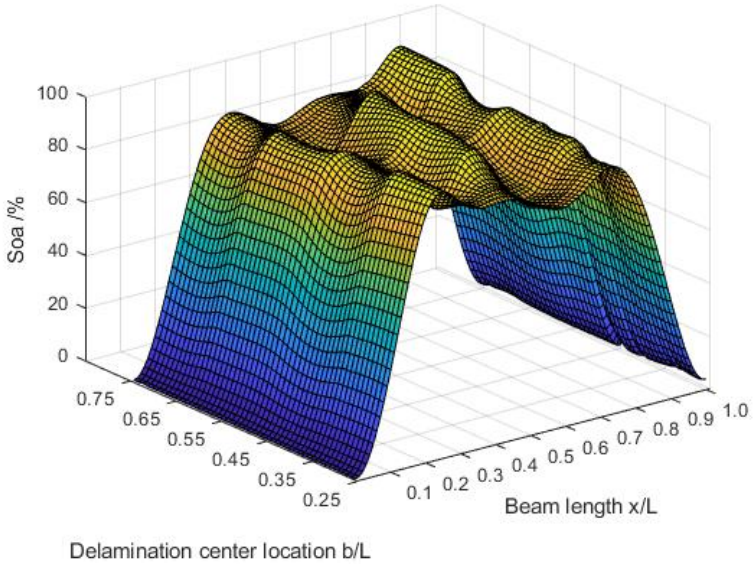

Figure 3-28 The spatial observability (S_{oa}) of the first three modes.

Figure 3-28 illustrates that the locations with high spatial observability are still concentrated in the part from 0.2L to 0.8L due to the beam ends are clamped. Based on equation (3-11), the optimization location is $x_0=0.24L$ and $x_0=0.76L$ due to the same boundary conditions on the two sides. This result is the same as the result for various delamination locations due to the effect generated by the various delamination location on the observabilities is larger than the various delamination size. The response of the optimal location 0.76L is shown in Figure 3-29:

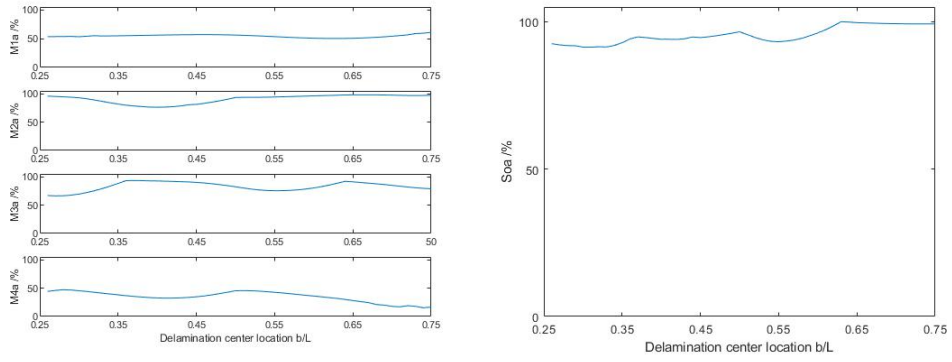

(a) M_{na}; *(b) S_{oa};*

Figure 3-29 The response of optimal location.

Figure 3-29 illustrates that the dynamic responses measured at the optimal locations can provide strong signals with more than 50% distribution of the first three modes and the distribution of the 4th mode is less than 50% with different delamination sizes at various locations for all cases. The average values of M_{1a} to M_{4a} are 54.48%, 90.67%, 82.80%, and 34.92%, which are filled with the constraints in equation (3-11). This means the measurement at these two points can provide signals focus on the first three modes with less disturbance generated by the 4th mode. While the S_{oa} is close to 100% for all cases, which average value is 95.48%. This means the signals from optimal locations can provide strong signals. Therefore, for the delamination at various locations with different sizes, the effect of the size is larger than the locations, which should be considered in the following chapters.

3.3.5 Different Delamination Depths and Sizes

Furthermore, the optimization for beams with various delamination sizes and depths are investigated in this section to find the optimal measurement locations for these two parameters of delamination. The delamination location is set as $L_1 = (L - a)/2$ (i.e $b = L/2$), which means the delamination center is located in the middle of beams. The natural frequency affected by delamination size and depth changing at the same time is shown below:

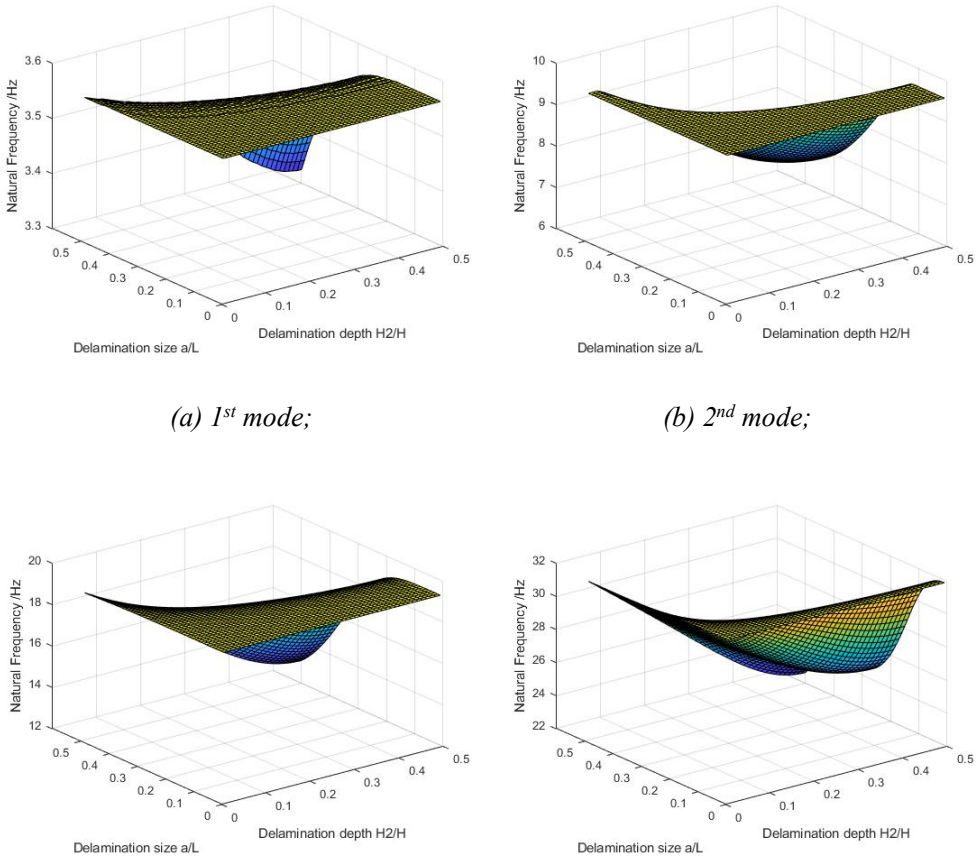

(a) 1st mode; *(b) 2nd mode;*

(c) 3rd mode; *(d) 4th mode;*

Figure 3-30 The natural frequency of beams with various delamination sizes and depths.

Based on Figure 3-30, it can be seen that when the delamination size is smaller than 0.1L, the effect of delamination depth is not clear due to the

effect of delamination depth is smaller with a small delamination size. Moreover, when the delamination depth is small and the delamination is close to the surface, the change generated by various delamination sizes on the natural frequency is small as mentioned by previous work [29]. To investigate the optimization for delamination size and depth, average modal observability of the *n*th mode for various delamination depths is defined by:

$$M_{nh}(x) = \frac{f_{nh}(x)}{max(f_{nh}(x))} \times 100\%, \tag{3-14}$$

where the $f_{nh}(x)$ is the sum of $f_n(x)$ calculated by equation (3-4) for different delamination depths with a fixed delamination size. The average modal observabilities are calculated by equation (3-11) and shown in Figure 3-31:

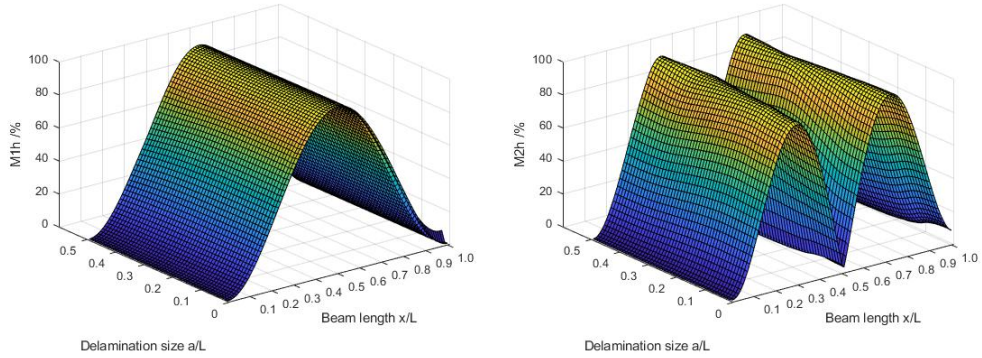

(a) 1st mode; *(b) 2nd mode;*

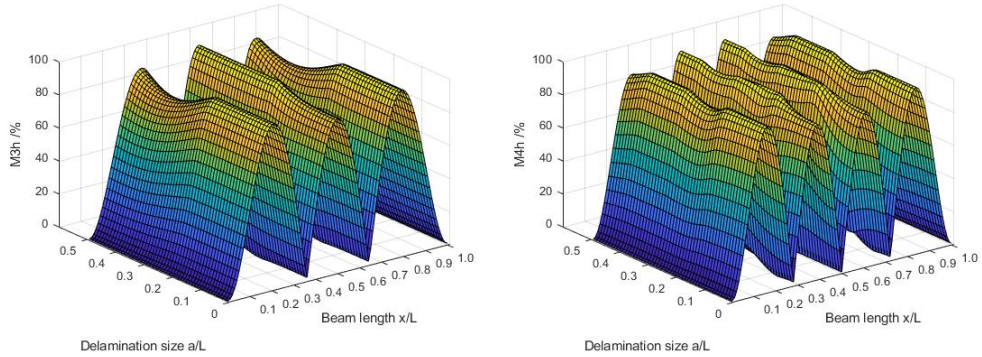

(c) 3rd mode; *(d) 4th mode;*

Figure 3-31 The average modal observability (M_{nh}) of beams with different delamination sizes and depths.

By compared with Figure 3-6, Figure 3-31 shows a similar result for various delamination sizes. This is because the effect of delamination depth is small on the mode shape as shown in section 3.3.1. However, there is still a difference between Figure 3-31(c-d) and Figure 3-6(c-d). The average modal observability has a smaller fluctuation than the modal observability with various delamination sizes in these figures, which is because the average modal observability can eliminate some effect generated by the delamination depth, while the effect on the vibration characteristics is the most significant

when the delamination depth is 0.5H as set in Section 3.3.1 as mentioned in previous work [29]. The average spatial observability is defined by the following equation:

$$S_{oh}(x) = \frac{\sqrt{\sum_{n=1}^{N} f_{nh}(x)^2}}{max(\sqrt{\sum_{n=1}^{N} f_{nh}(x)^2})} \times 100\%. \quad (3\text{-}15)$$

Following equation (3-11), the average of spatial observability is shown as:

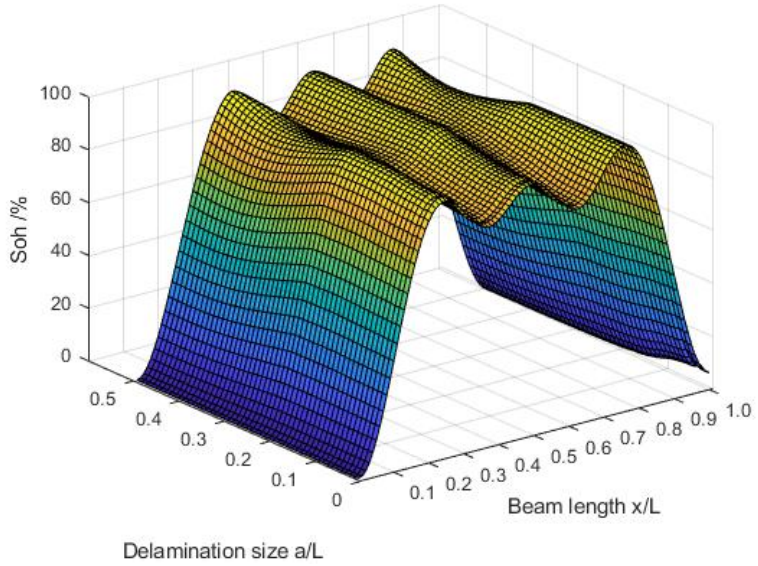

Figure 3-32 The spatial observability (S_{oh}) of the first three modes.

The average spatial observability shown in Figure 3-32 with various delamination sizes is also similar to the result in Figure 3-6 due to the small effect of delamination depths, while the locations with high spatial observability are concentrated in the part from the 0.2L to 0.8L, which is the result of the clamped-clamped boundary conditions. Then the optimal locations calculated by equation (3-11) are $x_0=0.27L$ and $x_0=0.73L$ due to the same boundary conditions on the two sides, which is the same as the result in section 3.3.1 with delamination size-changing due to the larger effect of

delamination size on the mode observabilities and spatial observability. The average modal observability and average spatial observability of the optimal location 0.73L are shown as follows:

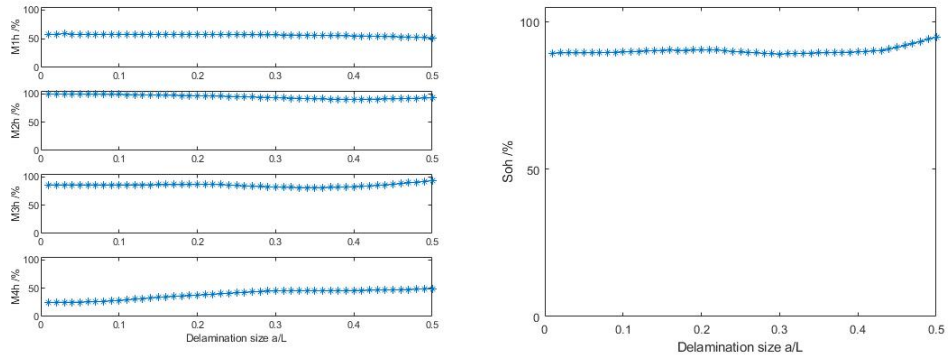

(a) M_{nh}; *(b) S_{oh};*

Figure 3-33 The response of optimal location.

Compared with the result in Figure 3-8 and Figure 3-15, the response shown in Figure 3-33 is a little different from just considering one parameter of delamination. However, the M_{1h} to M_{3h} from the optimal location are more than 50% with various delamination sizes, while the distribution of the 4th mode is less than 50%. The average values from M_{1h} to M_{4h} are 56.13%, 94.71%, 85.03%, and 38.96%, while the M_{4h} is the smallest, which means the measurement in the optimal locations can reduce the disturbance generated by the 4th mode effectively by measuring in the optimal locations. Moreover, the average spatial observability of the optimal locations is 90.15% with various delamination sizes, which means the measurement can provide strong signals at the optimal locations.

3.4 Result of the Free Mode Model

With the same procedure, then the optimization of the measurement location based on the free mode model by using the modal observability (M_n) and spatial observability (S_o) was investigated. For the optimization based on the free mode model, it should be noted that the spatial observability (S_o) and modal observability (M_n) need to be improved for the calculation because of the split in the delamination region. Therefore, the average eigenfunction of sub-beam 2 and sub-beam 3 was used and defined as:

$$u_n(x) = (u_{n2}(x) + u_{n3}(x))/2, x \in (L_1, L_2), \quad (3\text{-}16)$$

where the $u_{n2}(x)$ and $u_{n3}(x)$ are the eigenfunction of sub-beam 2 and sub-beam 3 calculated by equation (2-39) to (2-40) in Chapter 2. The L_1 and L_2 are the axial boundaries of the delaminated region in the beams. The following analysis and calculation will use equation (3-15) to compute and find the optimal points.

Moreover, as mentioned in Chapter 2 and previous work [22, 29], when the depth of delamination is at the mid-plane of the beam, the dynamic responses, and the vibration behavior is the same based on the constrained mode model and the free mode model. Therefore, the following sections will focus on the cases when the delamination is not at the mid-plane of the beams.

3.4.1 Different Delamination Depths

First, this section will investigate the optimization of the beams with various delamination depths based on the free mode model. The normalized size was set as $a = 0.1L$ and the depth was normalized and represented as H_2/H. The location of delamination was set as $L_1 = (L - a)/2$ (i.e $b = L/2$), which means that it was in the middle spanwise of the beam. The natural frequency of different delamination depth is shown as follows:

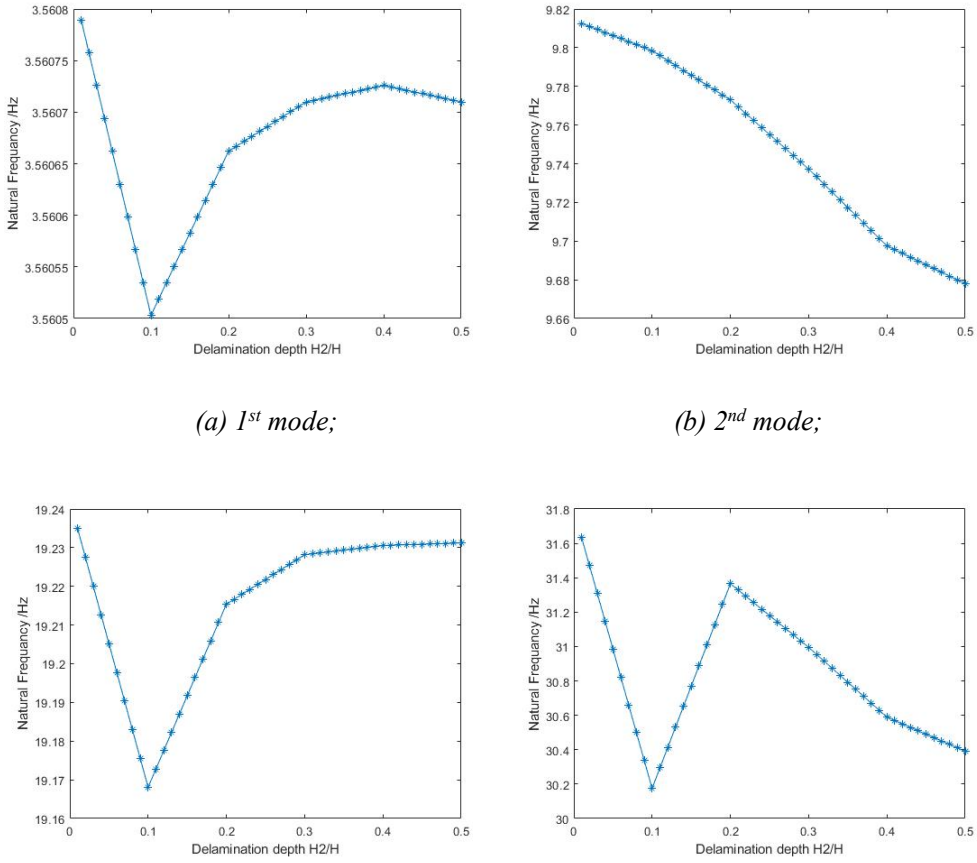

(a) 1st mode; *(b) 2nd mode;*

(c) 3rd mode; *(d) 4th mode;*

Figure 3-34 The Natural Frequency of the beam with different delamination depths.

Figure 3-34 shows that the natural frequency of the beam will decrease with the depth of delamination increasing due to the stiffness reduction. However,

the natural frequency will have drastic fluctuation when the depth of delamination is from 0 to 0.25H in the 1st, 3rd, and 4th modes. This is because the sub-beams will have different dynamic responses, which will generate local deformation and local modes due to the difference between their thickness generated by the delamination which is not at the mid-plane as mentioned in previous work [30]. In these modes, the natural frequencies are not just affected by the stiffness reduction, but also affected by the thickness of sub-beams. Therefore, there is a large change in the natural frequency changing trend due to more factors affecting it.

It also should be noted that the change in natural frequencies from different modes is different, which is because the effect of the delamination depth on different mode shapes is not the same due to the different sensitivity of each mode to delamination. Moreover, the change of natural frequency generated by delamination depth is smaller than delamination size, which means delamination depth affects natural frequency less than delamination size with the largest change being about 1.4Hz in the 4th mode as shown in Figure 3-34(d). The modal observability of *n*th mode (M_n) is shown in Figure 3-35:

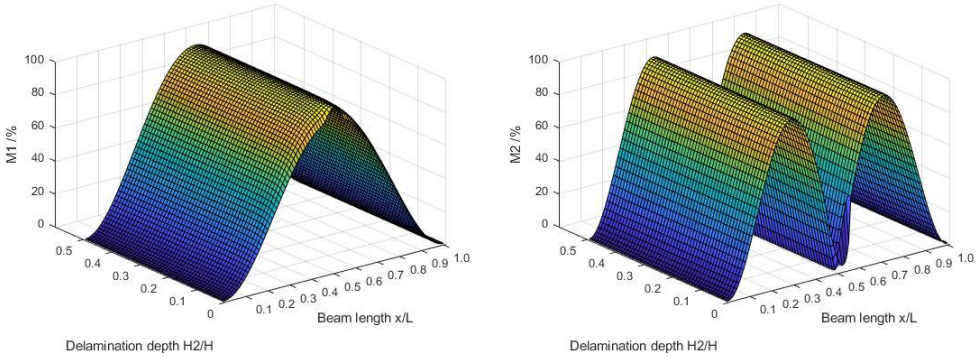

(a) 1st mode; *(b) 2nd mode;*

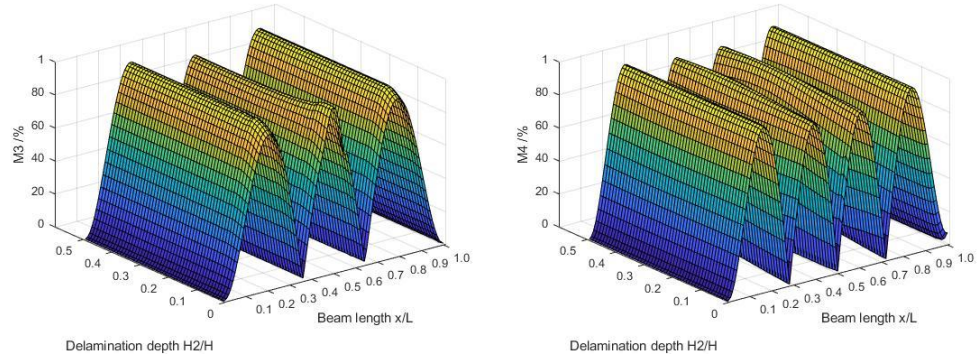

(c) 3rd mode; *(d) 4th mode;*

Figure 3-35 The modal observability (M_n) of the beam with different delamination depths.

Figure 3-35 shows that the mode shapes will have local deformation when the depth of delamination is small due to the different responses of the sub-beams with different thicknesses. With the delamination depth increasing, the local deformation disappears because of the thickness and deformation of sub-beams being closer. So the effect of delamination depth on the mode shape is being close to the constrained mode model. The phenomenon in the mode shapes changing can be related to the fluctuations in the natural frequencies changing trend, which is the result of the stiffness reduction and thickness change of sub-beams. Based on these situations, the spatial

observability (S_o) is calculated and shown as follow:

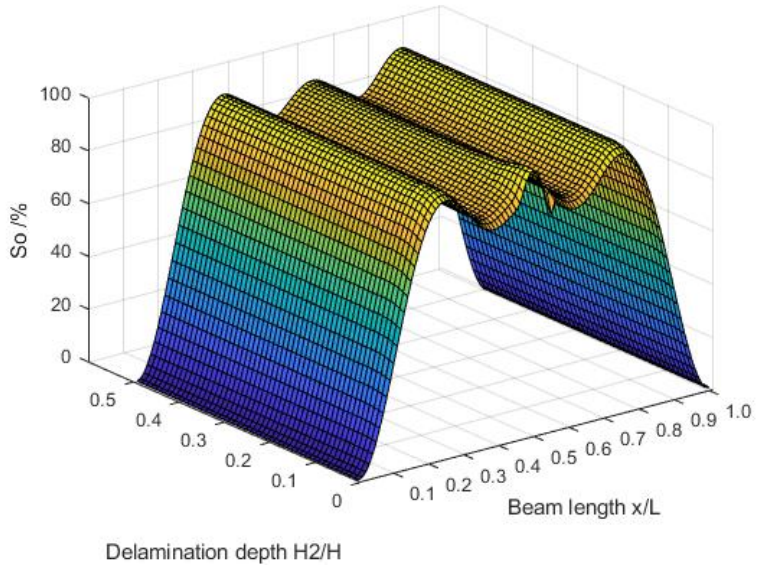

Figure 3-36 The spatial observability (S_o) of the first three modes.

Figure 3-36 indicates that the points with high spatial observability are concentrated between 0.2L to 0.8L. Moreover, it should be noted that there is local deformation in the part between 0.45L to 0.55L, when the dimensional depth of delamination is smaller than 0.1H due to the local deformation of sub-beams in the delamination region. However, this local deformation is small, and this part is still with high spatial observability so that it will not affect the optimal location much. The result should be close to the constrained mode model. Based on equation (3-11), the optimal locations are $x_0=0.76L$ and $x_0=0.24L$, which are the same as the result based on the constrained mode model. This is because the local deformation only happens with small delamination depths, which can be generated split in the delamination region. So the difference between the free mode model and the constrained mode model is clear when the delamination is very close to the surface. However,

the effect of delamination on the dynamic responses is small when the delamination is close to the surface as mentioned before [29]. Moreover, it should be noted that the effect of delamination depth is small with fixed size and location. Therefore, the optimization based on the free mode model is close to the constrained mode model. So, this optimal location can be used for all cases with various delamination depths in the following sections and chapters. The response of the optimal location is as shown:

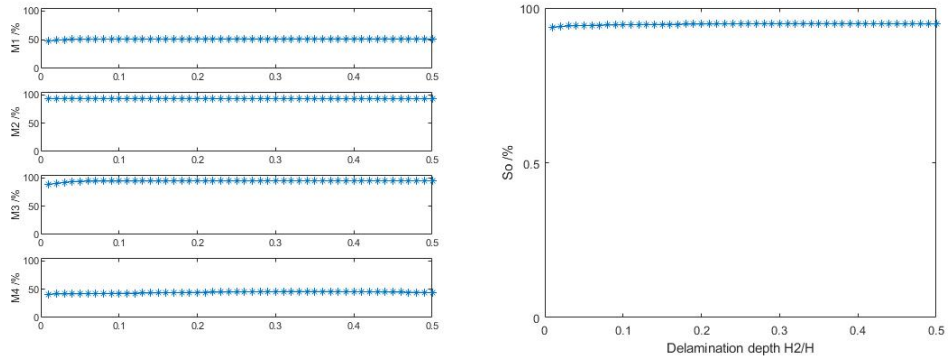

(a) Modal observability (M_n); *(b)Spatial observability (S_o);*

Figure 3-37 The response of optimal location.

Based on Figure 3-37(a), there is a little fluctuation in both modal observability and spatial observability when the delamination depth is close to 0 (i.e. the delamination is close to the top surface) due to local deformation of sub-beams. Then there is no clear change from all cases. While the M_1-M_3 of optimal location is more than 50% and M_4 is less than 50% for all cases. The averages values of M_1 to M_4 are 50.14%, 93.10%, 94.15%, and 44.15%. This means the signals from the optimal locations focus on the first three mode distribution with less effect of the 4th mode. While the S_o is almost 100% in

the optimal location for all cases with different delamination depths to keep the measurement signal strong enough as shown in Figure 3-37(b), which average value is 94.74%. The Frequency Response Function (FRF) is shown as follows:

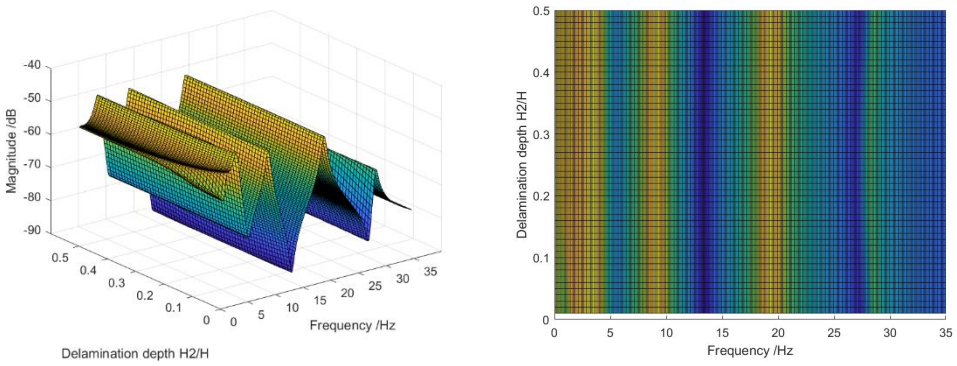

(a) 3-dimensional view; *(b) 2-dimensional view;*

Figure 3-38 The Frequency Response Function (FRF) of optimal location.

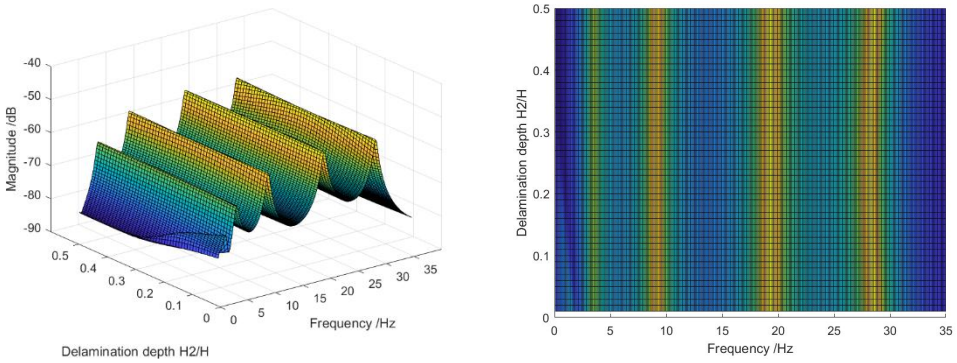

(a) 3-dimensional view; *(b) 2-dimensional view;*

Figure 3-39 The Frequency Response Function (FRF) of location x_0=0.10L.

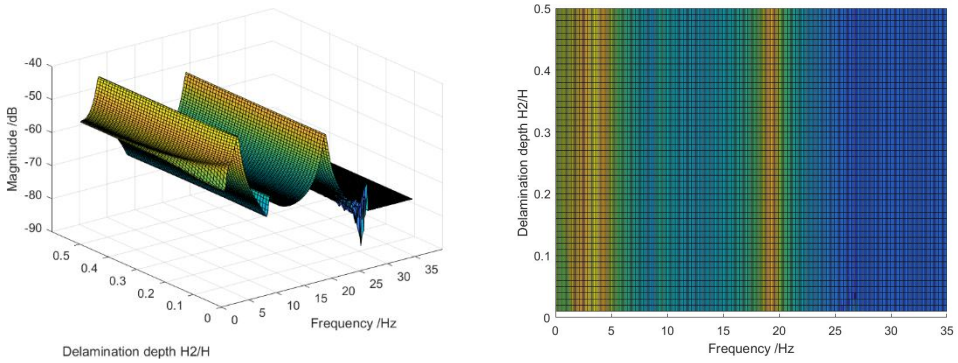

(a) 3-dimensional view; *(b) 2-dimensional view;*

Figure 3-40 The Frequency Response Function (FRF) of location x_0=0.50L.

The response uses the average of sub-beams in the delaminated region when the measurement points are in the delamination region. As shown in Figure 3-38, It needs to be noted that there is fluctuation when the depth is small in all points, which is generated by the local deformation of sub-beams. This is a little different from the result of the constrained mode model as shown in Figures 3-16 to 3-18. However, the fluctuation disappears with delamination depth increasing due to the thickness of sub-beams being closer. It also can be found that the first three peaks in the FRF of the optimal location are clear so that the optimal point can provide clear information of the first three modes with less effect of the 4th mode. While the FRF of point x_0=0.10L will be affected by the 4th modes more compared with the FRF of optimal location as shown in Figure 3-39, and the FRF of point x_0=0.50L lose the 2nd mode in Figure 3-40 due to it located at the node of mode shape, which is the target for measurement. This result illustrates that the optimization can find the optimal location with a high distribution of particular modes and less of other modes.

The result also indicates that the result of the free mode model is close to the constrained mode model. Therefore, the optimization and delamination detection based on vibration signals can ignore the model type for simulation.

3.4.2 Different Delamination Sizes

To investigate the optimization of measurement locations based on the free mode model, this section will analyze the optimization for beams with various delamination sizes, which are not at the mid-plane of the beams. The normalized depth was set as $H_2 = H/4$. The normalized size was replaced as a/L. The location of delamination was set as $L_1 = (L - a)/2$ (i.e $b = L/2$), which means that the delamination was in the mid-span of the beam. The natural frequency of beam with different delamination size is shown as follows:

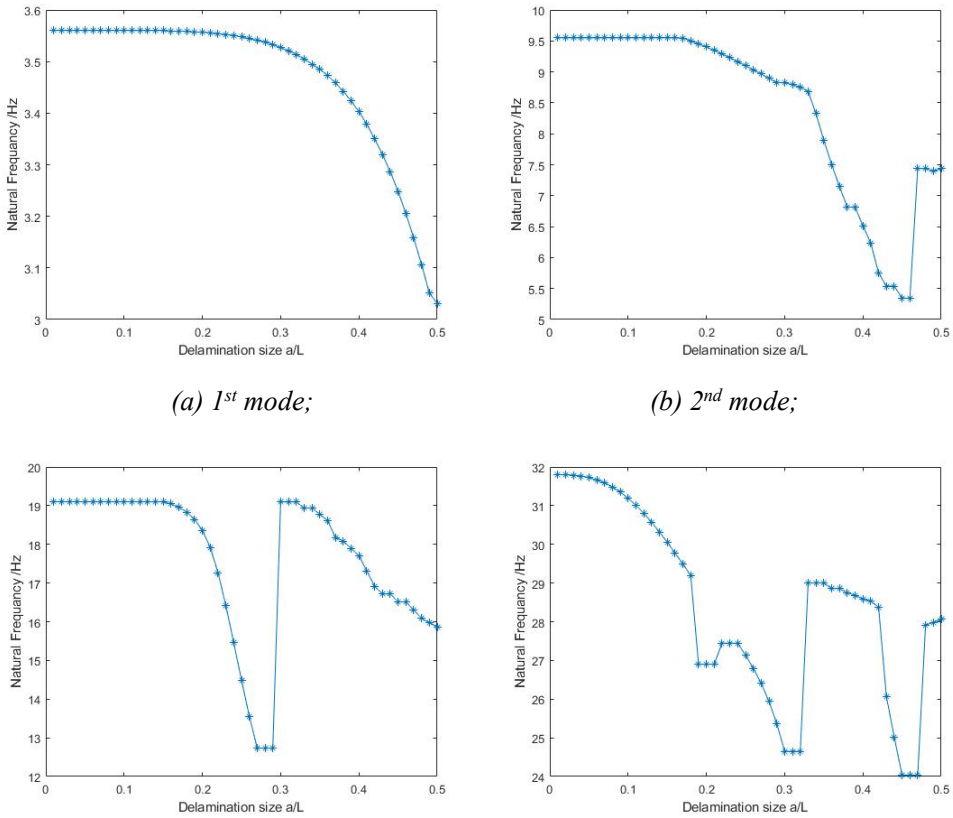

(a) 1st mode; *(b) 2nd mode;*

(c) 3rd mode; *(d) 4th mode;*

Figure 3-41 The Natural Frequency of the beam with different delamination sizes.

As shown in Figure 3-41, the natural frequency will decrease with delamination size increasing. However, it should be noted that the change is small when the delamination size is less than 0.1L, due to the less local stiffness generated by the delamination. The change in different modes is various due to the different sensitivity of modes. The largest change of the 4th mode is about 8Hz when the delamination size is about 0.45L as shown in Figure 3-41(d), while the largest change of the 1st mode is about 0.5Hz with the delamination size being 0.5L as shown in Figure 3-41(a).

Moreover, it can be observed that the changing trend of natural frequencies will fluctuate in the 2nd, 3rd, and 4th modes. This is generated by the local deformation and local modes calculated based on the free mode

model due to different deformation and displacement of sub-beams in delaminated regions [22]. These modes will generate new natural frequencies which have a significant difference from the other global modes due to the vibration characteristics of local modes not just related to the local stiffness reduction but also affected by the thickness and length of sub-beams in delaminated beams as mentioned in previous work. Therefore, the changing trend is not monotonic due to more factors influencing it. The modal observability of *n*th mode (M_n) is shown as:

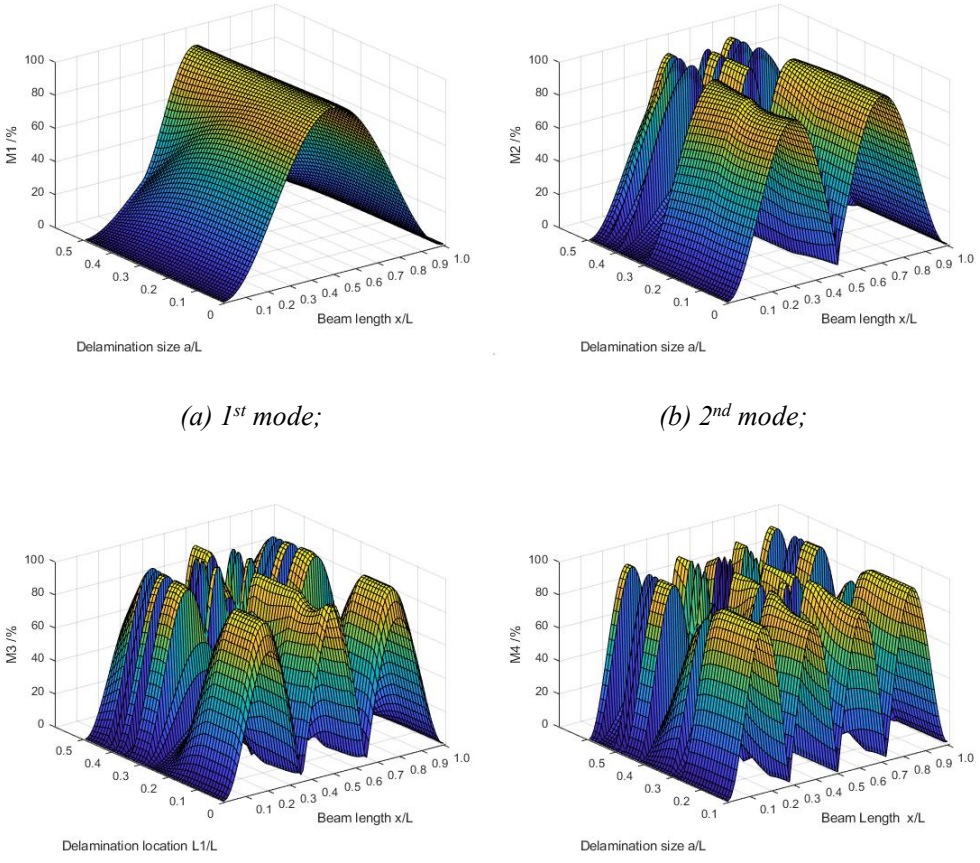

(a) 1st mode; *(b) 2nd mode;*

(c) 3rd mode; *(d) 4th mode;*

Figure 3-42 The modal observability (M_n) of the beam with different delamination sizes.

Based on Figure 3-42, it can be seen there is no clear local deformation in the

1st mode (M_1) with various delamination sizes due to the delamination at the middle span of beams and the sub-beams has close and similar deformation. But it should also be noted that the M_1 is being concentrated to the middle part of beams due to the top thinner sub-beam will have larger deformation with delamination size increasing as shown in Figure 3-42(a). While the other three modes have clear local deformation with particular delamination sizes generated by the different deformation of sub-beams in the local modes. The local deformation is because when the delaminated beam is in the local mode, the amplitudes of sub-beams are different and there is a clear split between the sub-beams, the average of the sub-beams with these modes will be different from the global modes. It can be observed that local modes will have the same delamination size when the natural frequencies of these modes have a clear drop, such as the 2nd mode happened with delamination size being about 0.3L as shown in Figure 3-41(b), while there is a local mode shape with the same delamination size in Figure 3-42(b). It also should be noted that the local modes just happens with particular delamination sizes since they are generated by the additional axial load due to the delamination and thickness of sub-beams in the delaminated regions as mentioned in previous work [22, 189]. Therefore, the modal observabilities are not continuous in the last three modes. The spatial observability (S_o) for the first three modes is shown as follow:

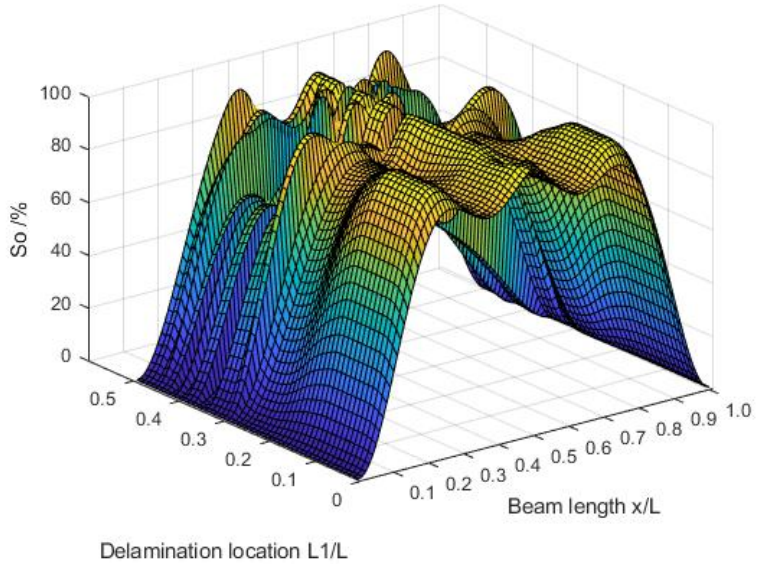

Figure 3-43 The spatial observability (S_o) of the first three modes.

Based on Figure 3-43, it should be noted that although the spatial observability of different locations fluctuates, the points with high spatial observability are still almost between 0.2L to 0.8L due to the fixed-fixed boundary conditions. It is also the result of local deformation of the top thinner sub-beam in the middle part of beams, which has large observability. The points will have different spatial observability and dynamic responses with various delamination sizes. The optimization problem for the beams with different delamination sizes can be solved by equation (3-11) based on the modal observabilities and spatial observability. The optimum solution is obtained at $x_0=0.73L$ and $x_0=0.27L$ due to the symmetric boundary conditions. The result is the same as Section 3.3.1 due to the effect generated by the depth is small and the location of delamination is the same. The other reason for the same result also may be that the difference between the free mode model and the constrained mode model is generated by the local modes and split between

sub-beams in the delaminated region, which happened less than the global modes only with particular delamination sizes as shown in Figure 3-42. Moreover, the points with high observability are still concentrated in the middle parts of the beams. Therefore, the optimization based on the free mode model will be close to the constrained mode model. The response of the optimal location is as shown:

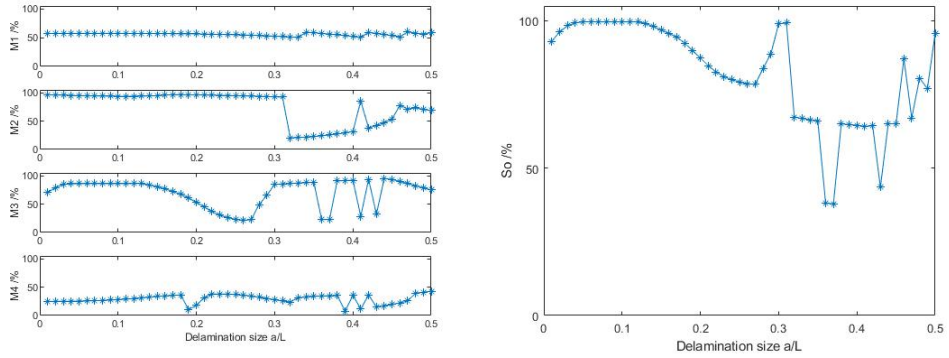

(a) Modal observability (M_n); *(b)Spatial observability (S_o);*

Figure 3-44 The response of optimal location x_0=0.73L.

Based on Figure 3-44(a), the result shows the M_1 to M_3 have high distributions to the signal from the optimal locations when the delamination size is smaller than 0.2L. Although there is fluctuation generated by the local modes in the modal observability of the 2nd mode and the 3rd mode with delamination size larger than 0.2L, the average value of the first three modes for all cases are more than 50%, which are 55.9%, 75.81%, and 70.11%, respectively. A similar phenomenon is in spatial observability changing trend with various delamination sizes as shown in Figure 3-44(b). It can be seen that there are some cases with spatial observability of about 50%, but the average

value of observability is 82.37% for cases with various delamination sizes. While it should be noted that the M_4 is still smaller than 50% for all cases, whose average value is 29.01%. Therefore, the optimal locations fill the constrain and requirements set in equation (3-11). The Frequency Response Function (FRF) of the point at $x_0=0.73L$ (optimal location) and two other points is shown in Figures 3-45 to 3-47:

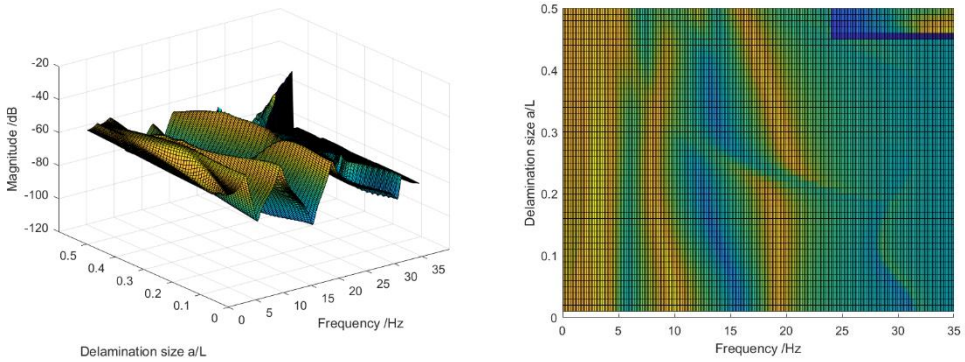

(a) 3-dimensional view; *(b) 2-dimensional view;*

Figure 3-45 The Frequency Response Function (FRF) of optimal location $x_0=0.73L$.

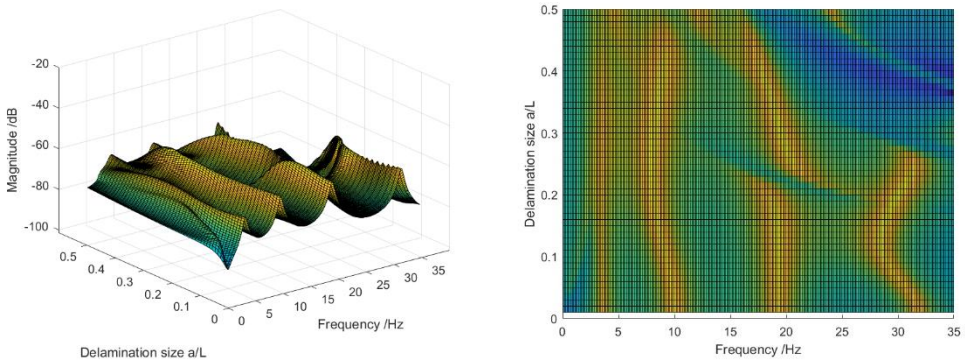

(a) 3-dimensional view; *(b) 2-dimensional view;*

Figure 3-46 The Frequency Response Function (FRF) of location $x_0=0.10L$.

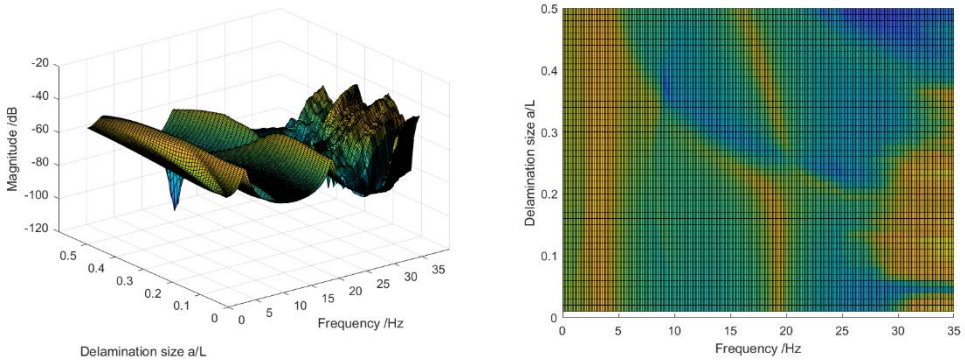

(a) 3-dimensional view; *(b) 2-dimensional view;*

Figure 3-47 The Frequency Response Function (FRF) of location x_0=0.50L.

It should be noted that the FRF of the optimal location shows the first three peaks clearly, which is the first three modes' frequency as well as their change with various delamination sizes as shown in Figure 3-45. The response uses the average of sub-beams when the delamination region covers the measurement points. It should be noted that the amplitude of the 4th mode shape is small compared with the FRF of point x_0=0.10L in Figure 3-46, due to the optimal location close to the node of the 4th mode. While the FRF of location x_0=0.50L almost loses the second mode compared with the FRF of optimal location due to this point located at the node of the 2nd mode, which is the target of the optimization as shown in Figure 3-47. Therefore, the signals from this optimal point can provide good resolution about the first three modes with less disturbance generated by higher modes.

From Figure 3-45(b) to Figure 3-47(b), there is a clear cutoff in the 3rd mode with the delamination size being about 0.25L, which is generated by the local modes. It can be also observed that the natural frequency of the 4th mode

fluctuates as well as the amplitude due to more local modes appearing.

3.4.3 Different Delamination Locations

Then the optimization for beams with delamination at various locations is investigated based on the free mode model in this section when the delamination is not at the mid-plane of beams. The natural frequency of different location replaced by normalized various as b/L was calculated while the normalized size was set as $a = 0.1L$. The depth of delamination was set as $H_2 = H/4$. The natural frequency of different delamination size is shown in Figure 3-48:

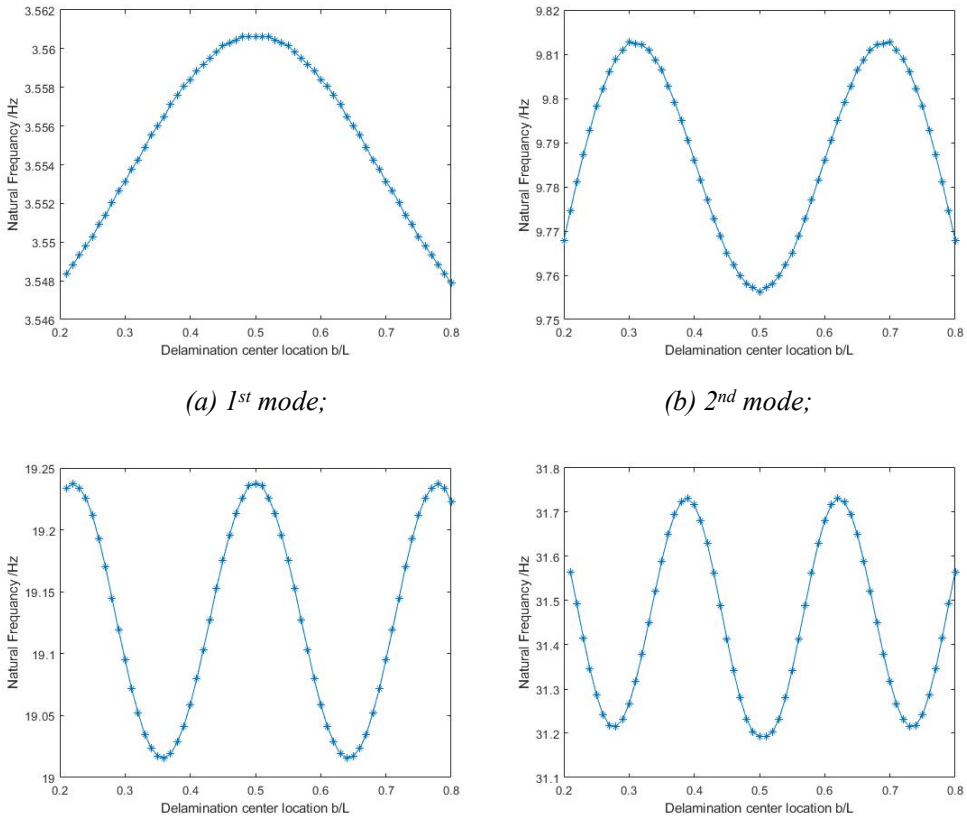

(a) 1st mode; *(b) 2nd mode;*

(c) 3rd mode; *(d) 4th mode;*

Figure 3-48 The Natural Frequency of the beam with delamination at various locations.

Figure 3-48 shows that the natural frequency will fluctuate with delamination

at various locations. This result is similar to the constrained mode model with the delamination depth being 0.5H as shown in Figure 3-19. As mentioned in previous work [31], the natural frequency reduction will be significant when the center of delamination is located at the node of modes. Therefore, when the location L_1 is about 0.45L (i.e. the location of delamination center $b = L_1 + a/2 = 0.5L$), the change of natural frequency in the second mode is the largest since there is a node in the 2nd mode close to the delamination center. While the largest change of the 3rd mode will happen when the location L_1 is 0.30L (i.e. $b = 0.35L$) and 0.60L (i.e. $b = 0.65L$) which means the locations of the delamination center are the nodes of the 3rd mode. Three locations will have the largest reduction of natural frequency in the 4th, which are 0.25L (i.e. $b = 0.30L$), 0.45L (i.e. $b = 0.50L$), and 0.70L (i.e. $b = 0.75L$), as the same with nodes of the 4th mode. It should be also noted that compared with the result in Figure 3-19, the change of natural frequency is smaller with delamination depth being 0.25H, which is because the effect of delamination depth is small with small delamination size as mentioned in previous work [29]. The modal observability of *n*th mode (M_n) is shown as follows:

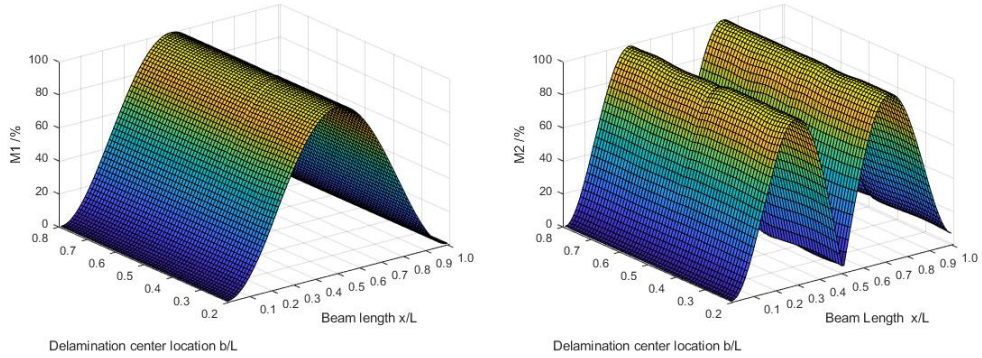

(a) 1st mode; *(b) 2nd mode;*

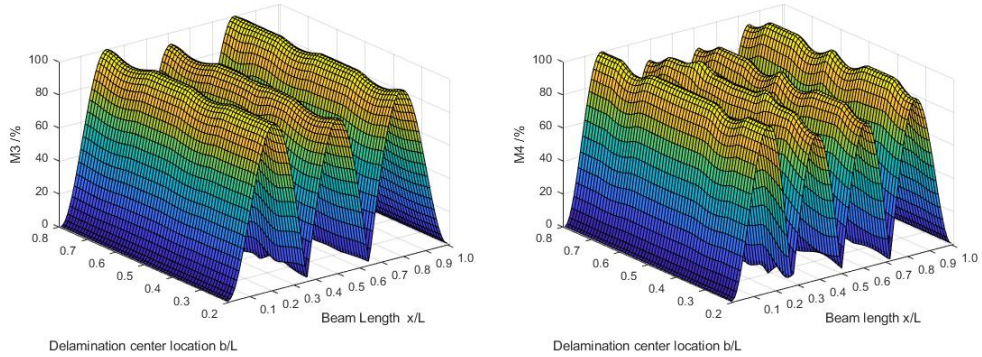

(c) 3rd mode; *(d) 4th mode;*

Figure 3-49 The modal observability (M_n) with delamination at various locations.

As shown in Figure 3-49, it can be seen that there is no clear local mode in the first four modes due to the small delamination size. Moreover, it should be noted that the change of mode shapes with delamination depth being 0.25H, is smaller than the result in Figure 3-20 with delamination depth being 0.5H, due to the reason mentioned in previous work, which indicates that the effect will be smaller with delamination being closer to the top surface [29]. It also should be noted that the change of deformation will be significant when the delamination is between antinodes due to that the compressive axial load generated by the delamination when the delamination between antinodes. The

spatial observability (S_o) of the first three modes is shown as follow:

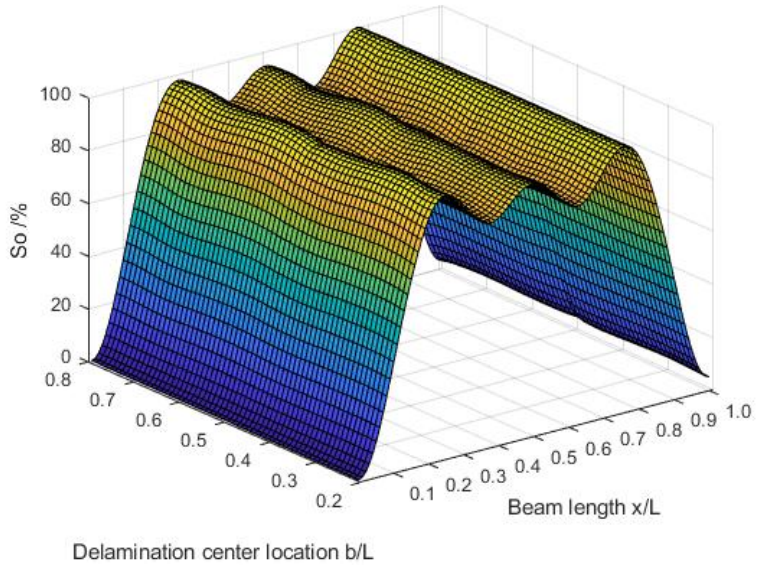

Figure 3-50 The spatial observability (S_o) of the first three modes.

The result in Figure 3-50 illustrates that the locations with the high spatial observability are concentrated in the middle part, from 0.2L to 0.8L, which is similar to the result in Figure 3-21 based on the constrained mode model. The reason is that the difference between the free mode model and the constrained mode model is small when the delamination size is small. Moreover, the effect of depth on the natural frequency and mode shapes is small as mentioned in Chapter 2. Therefore, the spatial observability is close to the result based on the constrained mode model with delamination depth being 0.5H. Based on equation (3-11), the optimal locations are $x_0=0.76L$ and $x_0=0.24L$ due to the same boundary conditions on the two sides. The result is the same as Section 3.4.1. The reason may be because the depth affects the observabilities less, while the change of beams with delamination at different locations is symmetric change with various delamination locations due to the same

boundary conditions on the two sides. Therefore, their result is close to the intact beams. The optimal result is also the same as the result in Section 3.3.3 due to the small effect of delamination depth. The observabilities of the optimal location *0.76L* are shown in Figure 3-51:

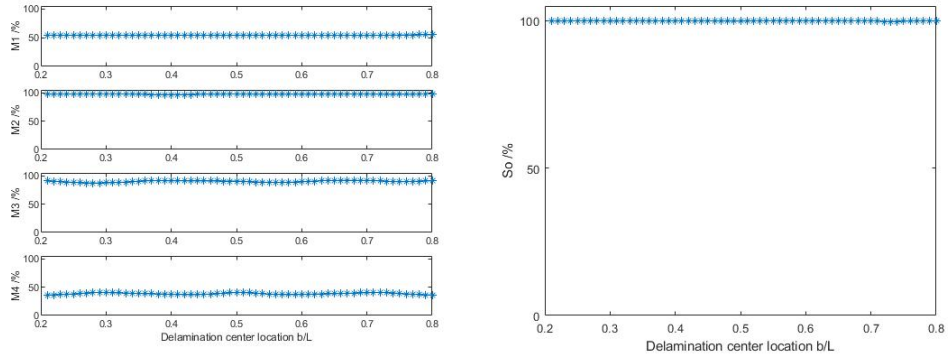

(a) Modal observability (M_n); *(b)Spatial observability (S_o);*

Figure 3-51 The response of optimal location.

Based on Figure 3-51 (a), it can be seen that with various delamination locations, the M_1 to M_3 is more than 50%. The M_2 is the highest due to the optimal location is close to the antinode of this mode, which is about 0.30L and 0.73L. The average values of M_1 to M_4 are 54.26%, 97.47%, 90.02%, and 38.45%, which are filled with the constraints in equation (3-11). The spatial observability from the optimal location is almost about 100% with various locations as shown in Figure 3-51 (b), while the average value is 99.92%, which means this optimal location can provide strong signals. While the M_4 is less than 50% for all cases and the average value is the smallest in the four modes, which means the signals from the optimal locations has less distribution of the 4^{th} mode due to the optimal locations are close to the nodes

of this mode at about 0.28L and 0.73L. Therefore, the measurement of vibration signals at the optimal locations can reduce the disturbance of the 4th mode. The Frequency Response Function (FRF) of the optimal location is shown as:

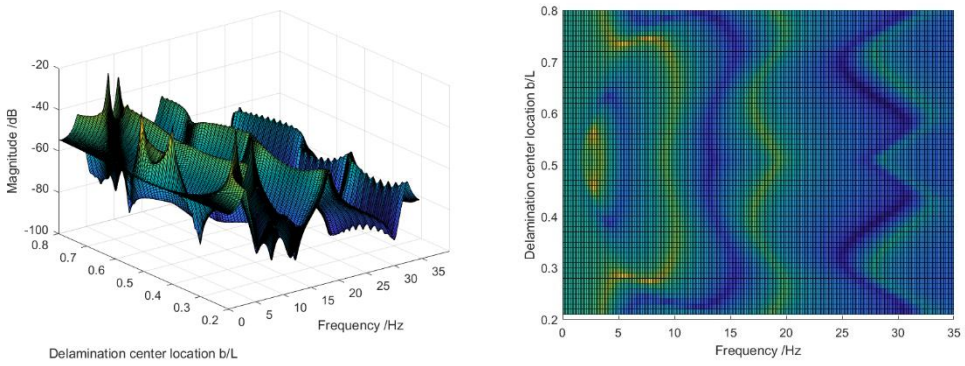

(a) 3-dimensional view; *(b) 2-dimensional view;*

Figure 3-52 The Frequency Response Function (FRF) of optimal location x_0=0.76L.

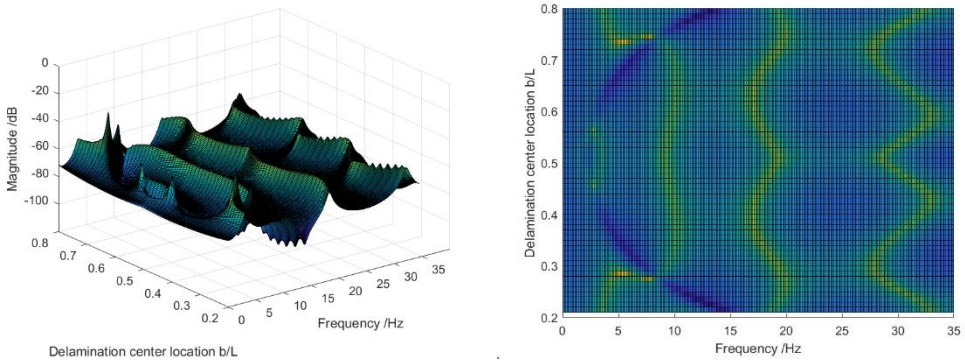

(a) 3-dimensional view; *(b) 2-dimensional view;*

Figure 3-53 The Frequency Response Function (FRF) of location x_0=0.10L

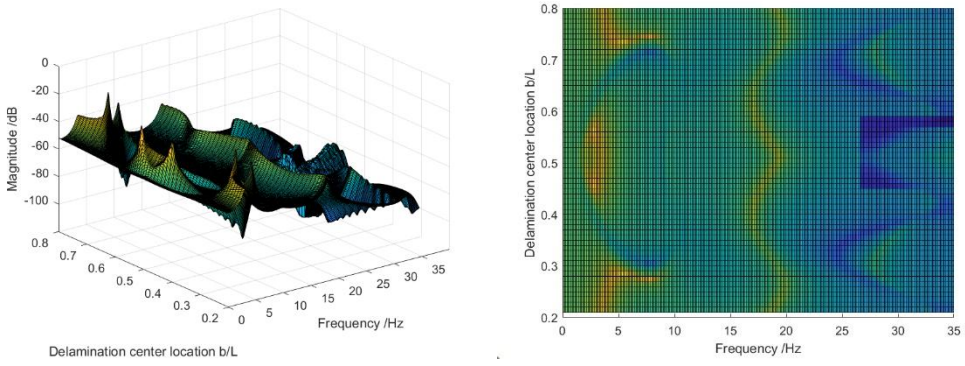

(a) 3-dimensional view; *(b) 2-dimensional view;*

Figure 3-54 The Frequency Response Function (FRF) of location x_0=0.50L.

The response uses the average of sub-beams in the delaminated region when the measurement points are in the delamination region. As shown in Figure 3-52, the FRF of optimal location can provide the first three peaks at the frequency domain clearly, while the 4th peak is small compared with the FRF of point $x_0 = 0.10L$ as shown in Figure 3-53, due to the optimal locations close to the nodes of the 4th mode. Moreover, the FRF of point $x_0 = 0.50L$ loses the distribution of the second mode as shown in Figure 3-54 because this point is located at the node of the 2nd mode. Therefore, the optimization of the chapter is useful, which can find the optimal point to provide signals with delamination at different locations and the energy is most for the first three modes. It also should be noted that there still some local deformation when the location of delamination is close to the middle span and sides of beams, due to the local modes and split of the sub-beams in the delaminated region.

3.4.4 Different Delamination Locations and Sizes

Furthermore, the optimization for various delamination sizes and locations simultaneously is investigated when the delamination is not at the mid-plane of the beams. The delamination depth is set as $H_2 = 0.25H$. The natural frequency of delaminated beams with various location and size is calculated as shown in Figure 3-55:

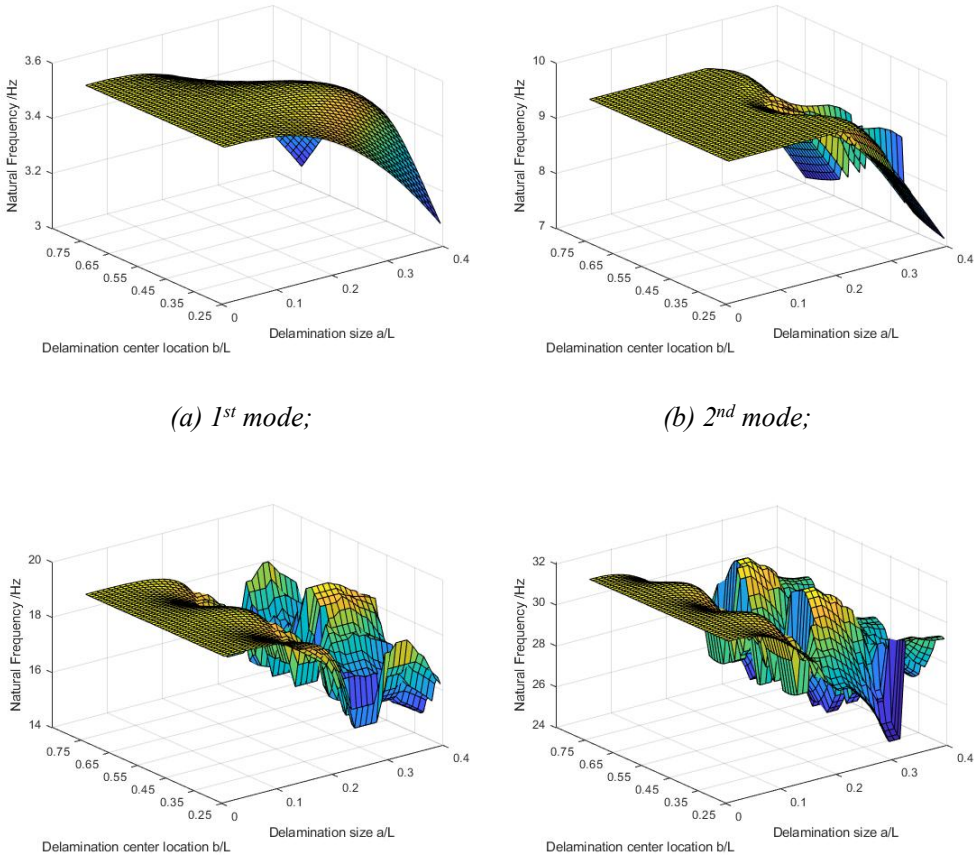

(a) 1st mode; *(b) 2nd mode;*

(c) 3rd mode; *(d) 4th mode;*

Figure 3-55 The Natural Frequency of beams with different delamination sizes at various locations.

Figure 3-55 shows that both locations and sizes of delamination will affect the natural frequency, so there is fluctuation in the changing trend due to the different effects of delamination size and location. It should be noted that the natural frequencies will fluctuate when the delamination size is larger than $a = 0.1L$ due to the local modes as mentioned in Section 3.4.2. Moreover, the fluctuation of the natural frequencies with various delamination locations is related to the delamination center and nodes of mode shapes as mentioned in Section 3.4.3. Then the average observability of the nth mode (M_{na}) was

defined to find the optimal measurement locations as the following formulation:

$$M_{na}(x) = \frac{f_{na}(x)}{max(f_{na}(x))} \times 100\% \quad (3\text{-}17)$$

where $f_{na}(x)$ means the average of $f_n(x)$ calculated in equation (3-4) with various delamination size when the delamination location is fixed. The modal observability of nth mode (M_{na}) is shown as follows:

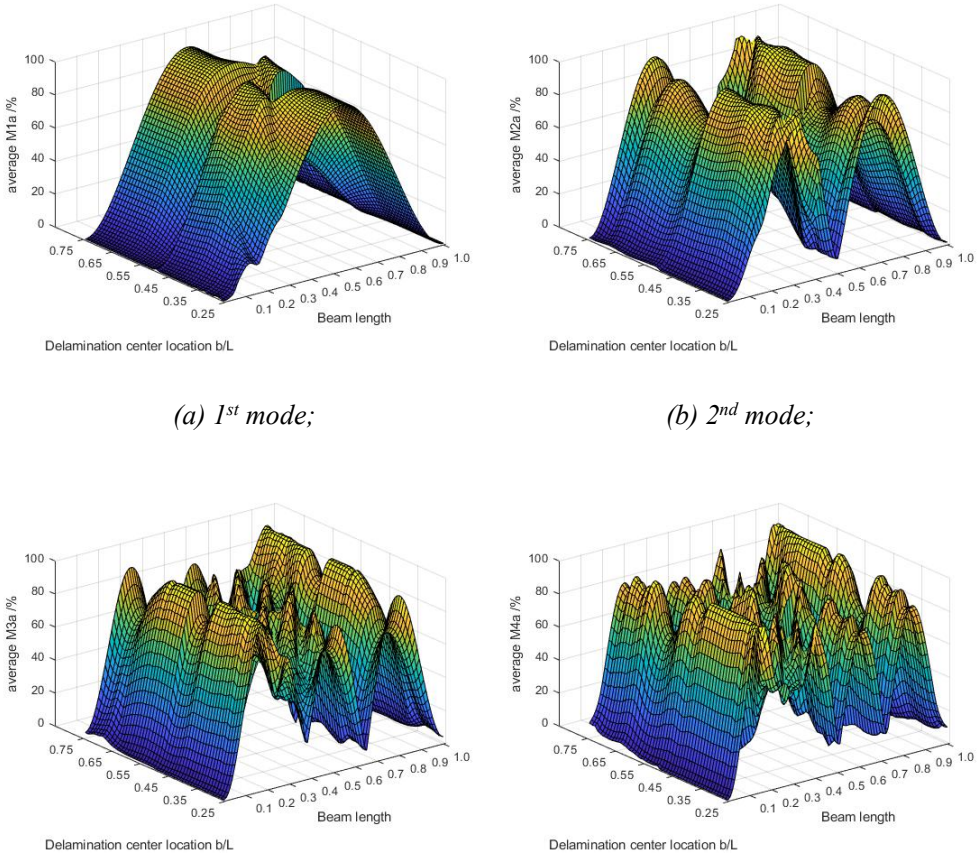

(a) 1st mode; *(b) 2nd mode;*

(c) 3rd mode; *(d) 4th mode;*

Figure 3-56 The average modal observability (M_{na}) of beams with different delamination sizes at various locations.

Figure 3-56 shows the average modal observability is complicated due to the local modes of the free mode model with delamination size increasing.

Therefore, the result is different from the result in Section 3.3.3. For this section, the average spatial observability is defined as:

$$S_{oa}(x) = \frac{\sqrt{\sum_{n=1}^{N} f_{na}(x)^2}}{max(\sqrt{\sum_{n=1}^{N} f_{na}(x)^2})} \times 100\%. \quad (3\text{-}18)$$

The average spatial observability (S_{oa}) is shown as follows:

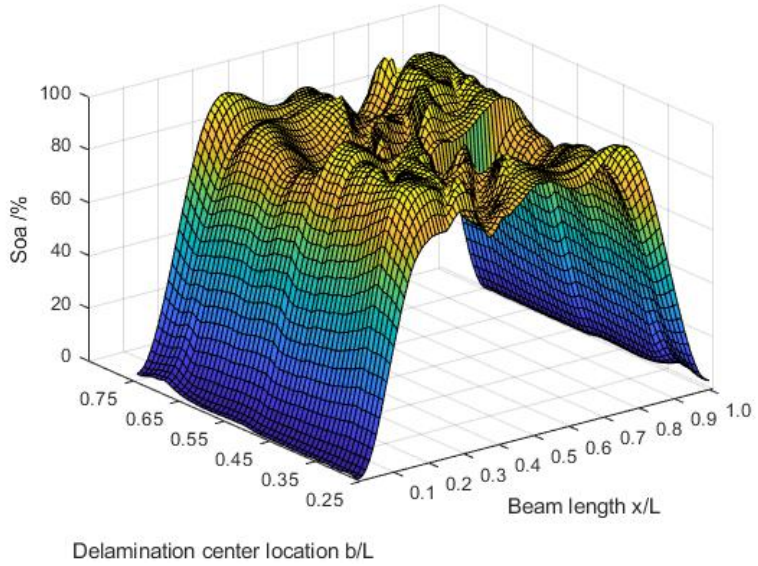

Figure 3-57 The spatial observability (S_{oa}) of the first three modes.

Figure 3-57 illustrates that although the spatial observability is different from the result in Figure 3-28, the locations with high spatial observability are still concentrated in the part between 0.2L to 0.8L as the result of the fixed-fixed boundary conditions. Based on equation (3-11), the optimal locations are x_0=0.27L and x_0=0.73L, which is the same as the result in Section 3.4.2. The result is due to the effect of delamination size is larger than the delamination locations based on the free mode model due to the local deformation of the sub-beams in the delaminated region. The response of the optimal location x_0=0.27L is shown as follows:

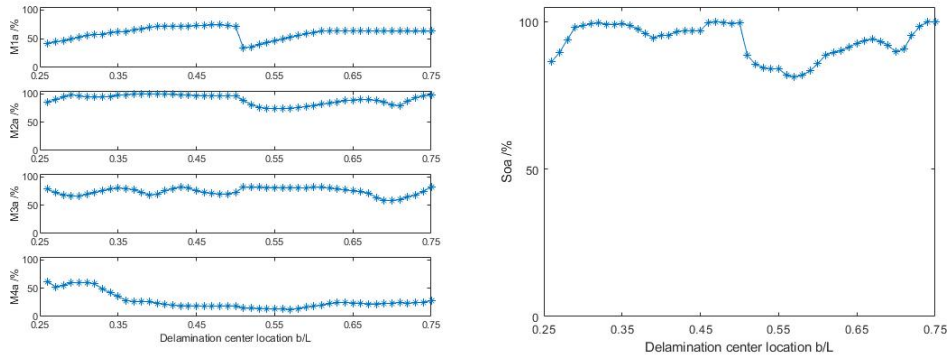

(a) M_{na}; *(b) S_{oa};*

Figure 3-58 The response of optimal location.

The response uses the average of sub-beams when the delamination region covers the measurement points. Figure 3-58(a) illustrates that the M_{1a} to M_{3a} are more than 50% for all cases. Furthermore, the fluctuation is smaller than the result in Figure 3-44 due to this is the average of cases for beams with various delamination sizes, which can eliminate the local deformation. The average values of the first three modes are 60.21%, 89.88%, and 74.23%, which are filled with constraints in equation (3-11). Moreover, the M_{4a} is smaller than 50% for all cases with the average value being 27.03%, so the vibration signals measurement at the optimal locations can reduce the disturbance generated by the 4^{th} mode. The average spatial observability showed in Figure 3-58(b) is more than 75% with the average value being 93.34%, which means the signal from the optimal locations is strong, which can improve the delamination detection based on the dynamic responses. It should be noted the spatial observability will decrease when the delamination

size is larger than 0.25L due to the local modes, which will change the energy distribution of the vibration for the beams.

3.5 Conclusions

This chapter illustrates the effect of optimization for dynamic signal measurement. It is necessary and important for the delamination assessment based on the structural vibration characteristics and response. According to the above discussion, the following conclusion can be drawn:

1. The result shows that the proposed method based on modal observability and spatial observability can optimize the measured locations for large spatial observability values with a high distribution of the particular modes and less effect of the other modes. The possibility and significance of the optimization based on the proposed method for delaminated beam structures were demonstrated in this chapter. The result indicates that different locations have various sensitivity to the delamination, which is also affected by the delamination. Therefore, the optimization of the measurement locations for damage detection needs to consider the effect of various damage parameters.
2. The result of the free mode model and the constrained mode model is the same for the homogeneous beams with one type of delamination parameters changing. The optimal locations for different sizes, depths, and locations are the same from these two models, so the following

chapter can use these optimal points without considering the types of models.

3. The result illustrates that the optimal locations for various delamination locations and depths are the same, while the optimal location for various delamination sizes is another point. Overall, the result also indicates that the effect of delamination depth is smaller than the size and location. The delamination size affects the natural frequency much, while the delamination location changes the mode shape more based on the constrained mode model. It also should be noted that the effect of delamination on the natural frequency will be significant when the center of delamination is located at the nodes of mode shapes. While the effect of delamination on the mode shape is significant when the delamination is between the antinodes of mode shapes as mentioned in Chapter 2.
4. It also should be noted that the optimal locations for delamination location and size changing at the same time are the same as the result of various delamination locations due to the larger effect of delamination location on the observability based on the constrained mode model. However, when the size and depth of delamination change at the same time, the result is the same as the delamination size-changing due to the larger effect of delamination size. Moreover, it can be found for size and location changing at the same time based on the free mode model, which is because the effect of delamination size on the observabilities based on

the free mode model is larger due to the local modes and split between sub-beams in the delaminated region. Therefore, the optimization for two damage parameters changing will be close to the result of the parameter which has a larger effect on the observabilities.

Based on these results, delamination detection can be guided and improved by the proposed method to find the optimal sensor location. The optimization of sensor placement can enhance the performance of delamination detection by measuring the signals from special modes and reducing the other signals for different delamination conditions. This chapter tested the proposed method based on the observabilities for delaminated beams, which is potential for structures with other types of damage.

Chapter 4 THE DELAMINATION DETECTION AND ASSESSMENT USING A VIBRATION-BASED PHASE SPACE RECONSTRUCTED METHOD

The work in this chapter is focused on the effect of delamination on the phase space topology structures of dynamic responses measured from the composite structures. As mentioned in Chapter 1, the phase space topology structures contain useful information about the structure, including the damage in structures. It can be used to describe both linear and nonlinear characteristics of structures with various situations, which is useful to investigate the delamination in composite structures with complexity due to the different properties of materials. Moreover, the phase space topology structures are related to the frequency and amplitude in the time domain of dynamic signals measured in specific locations, so it is more sensitive to the change of dynamic responses generated by the local damage in the structures compared with the global features, such as natural frequency, which can be used to improve the delamination assessment based on the dynamic responses of structures. However, the effect of delamination in composite structures on the phase space topology structures is more complicated compared with the homogeneous structures, which needs to be investigated, because the delamination is not just reducing the stiffness and enhance the deformation,

but also changing the deformation and energy distribution of structures. Therefore, this chapter will analyze the phase space topology structures of the dynamic responses for composite structures with various delaminations to test the possibility of the phase space topology to improve the delamination based on the dynamic responses.

4.1 The Phase Space Topology Analysis of Structural Dynamic responses

In this section, the phase space topology structure construction method named the phase space reconstruction [115] will be introduced as well as the calculation method of the feature named the change of phase space topology (CPST) [118].

4.1.1 The Phase Space Topology Analysis using Phase Space Reconstructed (PSR) Method

In this section, a method named Phase Space Reconstructed (PSR) is introduced. In phase space, all possible states of a dynamic system are represented, and each possible state of the system is associated with one unique point in the phase space topology structures. For dynamic systems, the phase space usually consists of all possible values of position (displacement) and momentum (velocity) variables. For a dynamic system, the response time series is the comprehensive reflection of many physical factors' interaction

which can be shown in phase space both for linear and nonlinear systems. It contains useful information on variables in the dynamic system which will vary when one of the factors changes. Therefore, the phase space could be used as a good candidate for structural damage identification [115, 118].

However, in practical applications, the motion of a dynamic system is often unknown. Moreover, measuring more than two types of dynamic signals simultaneously, such as displacement and velocity, maybe also difficult to achieve at the same time. Normally in applications, only one type of signal can be measured, and it even may not be displacement or velocity because of the available type of sensors. In this chapter, the dynamic parameter measured was displacement for the beam target and acceleration for the composite laminate panel target. Therefore, it is necessary to find a method to reconstruct the phase space of the system by these two dynamic signals.

The Phase Space Reconstruction (PSR) method proposed by Taken is employed here to construct the phase space topology of the linear and nonlinear dynamic responses by one type of signal [115]. This method has been used to construct the phase space topology structure based on one type of dynamic signal by previous work for vibration signal analysis and damage detection [111, 118]. By this method, the phase space topology can be reconstructed structures by any type of signal from dynamic systems. This time, the acceleration signal was measured to construct the phase space topology structure of the targets. It should be noted that the acceleration signal

has the same phase as the displacement signal. Therefore, the optimization in Chapter 3 can still be used for the following parts.

First, a vibration signal in the time domain is measured from the target structure shown as $x(n)$, where $n = 1,2,\cdots,N$, N is the total number of measured data points. With the commonly used delay coordinate approach, the time domain signal $x(n)$ can be used to construct a matrix to show the phase space topology [115]:

$$\mathbf{X}(m) = [x(n), x(n+\tau), \cdots, x(n+(m-1)\tau)] \tag{4-1}$$

where m is the embedding dimension of the phase space $\mathbf{X}(m)$ and τ is the time delay. Based on the equation (4-1), the phase space of the time series can be reconstructed as follows:

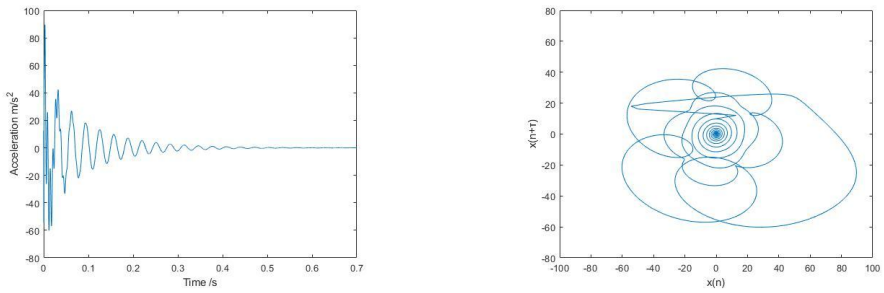

(a) Time series of a signal; *(b) Phase space;*

Figure 4-1 The Phase Space Reconstruction of time series.

In this procedure, the embedding dimension m and the time delay τ are important to keep the properties of time series in phase space and related to the dynamic properties of the structure. Only when the time-delayed τ is large enough so that the phase space structure from the dynamic responses can be unfolded well. For the calculation of time delay τ, there is a method named

normalized autocorrelation function that can be used [115]. The formulation is as:

$$C_{xx}(\tau) = \frac{\sum_{n=0}^{N-1}[x(n)-\bar{x}][x(n+\tau)-\bar{x}]}{\sum_{n=0}^{N-1}[x(n)-\bar{x}]^2}. \quad (4\text{-}2)$$

In equation (4-2), the $\bar{x}$ is the average of the time domain data x. The smallest τ with the $C_{xx}(\tau)$ being close to zero is the best time delay. Then it can be obtained that the $\tau = 13$ for the beam in Section 4.2 and $\tau = 97$ for the plate in Section 4.3 are the best choices respectively. Figure 4-2 shows the phase space of different time delay value:

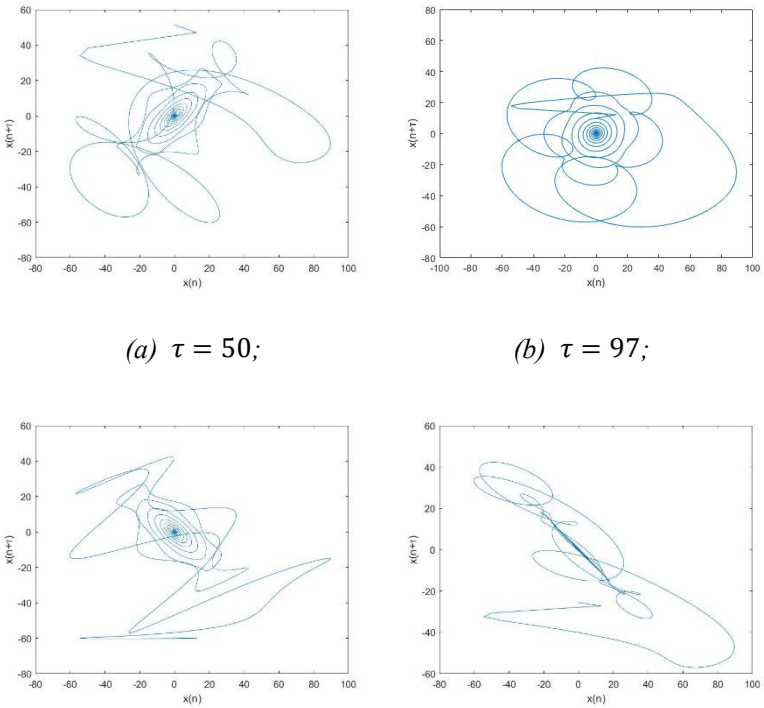

(a) $\tau = 50$*;* *(b)* $\tau = 97$*;*

(c) $\tau = 150$*;* *(d)* $\tau = 200$*;*

Figure 4-2 The Phase Space reconstructed with different time delay τ.

Figure 4-2 indicates that the time delay will affect the phase space reconstruction performance and shape of the phase space topology structures. If the selected time delay is not good, the phase space topology structures

cannot unfold very well for analysis, as emphasized in [115].

Regarding embedding dimension m, it is critical to choose a suitable value to ensure the attractor unfolds well to reveal the dynamic properties of the structure. However, for the damage detection, the low dimension is enough to show the change of phase space structures in different situations effectively. In the previous work [118], which used this method to detect and assess structural damage, the embedded dimension value $m = 2$ is chosen to reconstruct the phase space structures of structure with various damages, which shows enough sensitivity to the damage. Based on the previous work, this research also used $m = 2$ as the embedded dimension.

4.1.2 The Change of Phase Space Topology (CPST)

For the damage detection purpose, it is important to find a suitable feature of phase space to describe the properties of the phase space topology. The Change of Phase Space Topology (CPST) is chosen to show the dynamic properties of phase space topology for different cases [111, 118, 190]. In this section, the CPST is introduced. First, based on the equation (4-1), the phase space topology of vibration signal from the structure can be described after phase space reconstructed as:

$$\begin{cases} \mathbf{X_0}(1) = [x_0(1), x_0(2), \cdots, x_0(N-(m-1)\tau)] \\ \mathbf{X_0}(2) = [x_0(1+\tau), x_0(2+\tau), \cdots, x_0(N-(m-2)\tau)] \\ \vdots \\ \mathbf{X_0}(m) = [x_0(1+(m-1)\tau), x_0(2+(m-1)\tau), \cdots, x_0(N)] \end{cases}, \quad (4\text{-}3)$$

$$\begin{cases} \mathbf{X_D}(1) = [x_{\mathrm{D}}(1), x_{\mathrm{D}}(2), \cdots, x_{\mathrm{D}}(N-(m-1)\tau)] \\ \mathbf{X_D}(2) = [x_{\mathrm{D}}(1+\tau), x_{\mathrm{D}}(2+\tau), \cdots, x_{\mathrm{D}}(N-(m-2)\tau)] \\ \vdots \\ \mathbf{X_D}(m) = [x_{\mathrm{D}}(1+(m-1)\tau), x_{\mathrm{D}}(2+(m-1)\tau), \cdots, x_{\mathrm{D}}(N)] \end{cases}, \quad (4\text{-}4)$$

where the $\mathbf{X_0}(m)$ is the phase space topology of the undamaged structure generated by the time signal $x_0(n)$ and $\mathbf{X_D}(m)$ is the phase space structure of damaged structure generated by the time signal $x_D(n)$. Here, N is the total number of the time signal. A fiducial point on the topology corresponding to the damaged structure is selected with an arbitrary time index s as $\mathbf{X_D}(s)$ as shown in Figure 4-3:

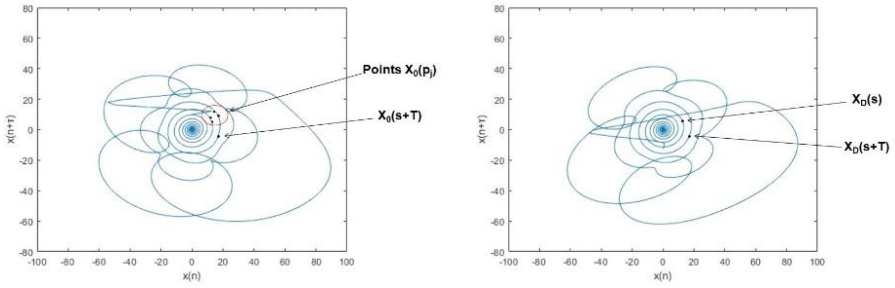

(a) undamaged; *(b) damaged;*

Figure 4-3 The phase space topology structures of points.

The nearest p neighbors of this point are then selected on the base topology (undamaged phase space) as:

$$\mathbf{X_0}(p_j): min\left\|\mathbf{X_0}(p_j) - \mathbf{X_D}(s)\right\|, j = 1,2,\cdots,p \quad (4\text{-}5)$$

where p denotes the nearest neighbors to the fiducial point and the $\|\cdot\|$ operator means the Euclidean norm as shown in Figure 4-3(a). It should be noted that the time indices of the neighbors do not need to have any relation in time to the fiducial point as the search is made based on the Euclidean norm

only. Then the future value of $\mathbf{X_D}(s)$ in damaged phase space was used to compute the damage index, which is shown as $\mathbf{X_D}(s+T_d)$ at a number of time steps T_d followed the topology from point $\mathbf{X_D}(s)$ in damaged phase space. While the future value showed as $\mathbf{X_0}(s+T_d)$ at a number of time steps T_d in undamaged phase space can be calculated as:

$$\mathbf{X_0}(s+T_d)=\frac{1}{p}\sum_{j=1}^{p}\mathbf{X_0}(p_j+T_d)\,,j=1,\cdots,p \tag{4-6}$$

Then the damage index named Changes of Phase Space Topology (CPST) is defined as [118]:

$$\mathrm{CPST}=\frac{1}{p}\|\mathbf{X_0}(s+T_d)-\mathbf{X_D}(s+T_d)\|, \tag{4-7}$$

where $\mathbf{X_D}(s+T_d)$ is the values with T_d time steps of the fiducial point in damaged phase space. In this chapter, $p=10$ and $T_d=20$ is chosen.

4.2 Delamination Assessment for Beam Sample

To analyze the effect of delamination on the phase space topology structures, a homogeneous beam with various delamination was used as samples in this section. The model of the beam was established by ABAQUS as Shown in Figure 4-4:

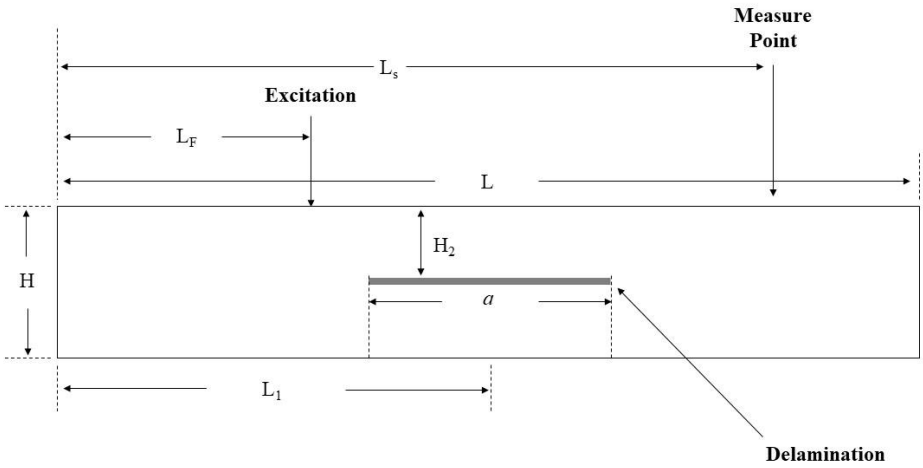

Figure 4-4 The model of the delaminated beam.

As noted in Figure 4-4, the delamination size and depth are represented by a and H_2. The properties of the samples are shown in Table 4-1

Table 4-1 The properties of beam samples.

Modulus /GPa	**Density /kg/m^3**	**Length (L) /m**	**Width (b) /m**	**Thickness (H) /m**
30	1000	1	0.1	0.01

The excitation is located at $L_F = 0.2L$ and the measured point is located at $L_s = 0.73L$ for different delamination sizes and $L_s = 0.76L$ for different delamination depths based on the result in Chapter 3. This chapter used a rectangular pulse load to generate vibration as:

$$F(t) = \begin{cases} q_0, 0 \le t \le t_1 \\ 0, t_1 \le t \end{cases}. \tag{4-8}$$

The duration of the pulse t_1 is considered as 0.001s and the amplitude of the pulse q_0 is 1N. The displacement was measured in the sensor location L_s. This method was tested by the simulation made by ABAQUS. The beam was modeled by using 8-node elements C3D8R. while the number of elements is related to the delamination size which needs to use smaller size elements

compared with the intact part. For the undamaged case, there were 10,000 elements in the model by the size of elements is $0.1 \times 0.1 \times 0.001mm$. In this simulation, the sampling frequency is $f = 1000Hz$. The total time is T=2s which means there is 2000 data for each case. The natural frequencies of the first two modes were also calculated as comparing.

4.2.1 Delamination Size Assessment

First, the effect of the delamination size was investigated. The delamination was set in the mid-plane of the beam ($H_2 = 0.5H$) and in the mid-span ($L_1 = L/2$). The result is shown in Table 4-2:

Table 4-2 Natural frequency of the first two modes and CPST for different delamination sizes.

Normalized Delamination size a/L	**1st mode /Hz**	**2nd mode /Hz**	**CPST**
0	56.21	154.88	5.8940×10^{-8}
0.05	56.02	154.07	5.9684×10^{-8}
0.10	56.00	151.94	6.3680×10^{-8}
0.15	56.00	147.09	1.0625×10^{-7}
0.20	55.95	139.29	1.9792×10^{-7}
0.25	55.86	130.23	3.4927×10^{-7}
0.30	55.64	121.44	5.4142×10^{-7}
0.35	55.25	114.19	8.1625×10^{-7}
0.40	54.56	108.73	1.1598×10^{-6}
0.45	53.54	105.12	1.5582×10^{-6}
0.50	52.08	102.99	1.8570×10^{-6}

As shown in Table 4-2, the natural frequency will decrease when the delamination size increase from 56.21Hz to 52.08Hz, and 154.88Hz to 102.99Hz respectively, while the CPST is being larger, from 5.8940×10^{-8} to 1.8570×10^{-6}. This is since the delamination will reduce the stiffness of beams which will reduce the natural frequency and change the deformation of the beam. While both natural frequency and deformation of the beam will affect the phase space topology structure, so the CPST will increase which means that the change of the phase space topology structures becomes larger. Figures 4-5 to 4-9 show the result of samples with various delamination sizes:

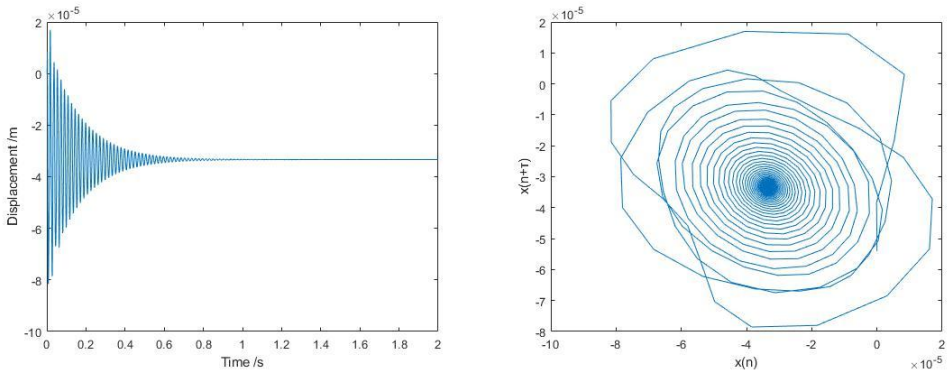

(a) Time Domain; *(b) Phase Space topology;*

Figure 4-5 Undamaged beam.

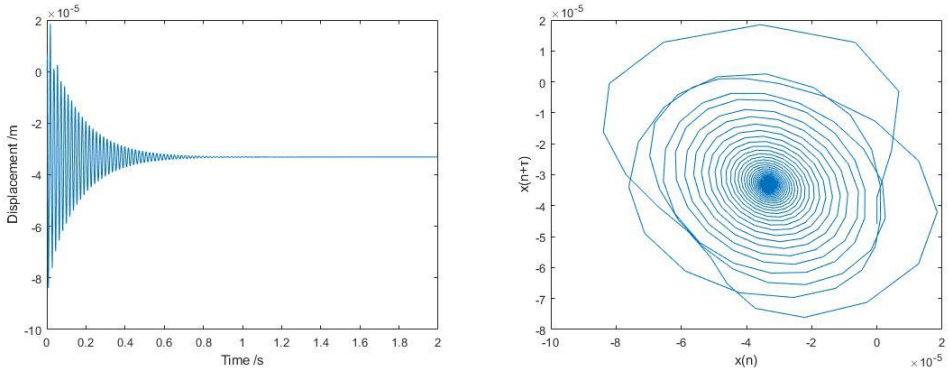

(a) Time Domain; *(b) Phase Space topology;*

Figure 4-6 Beam with delamination size $a/L = 0.1$.

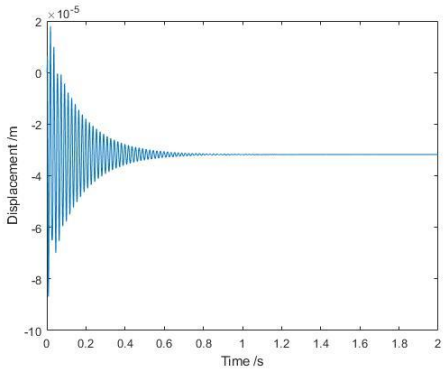

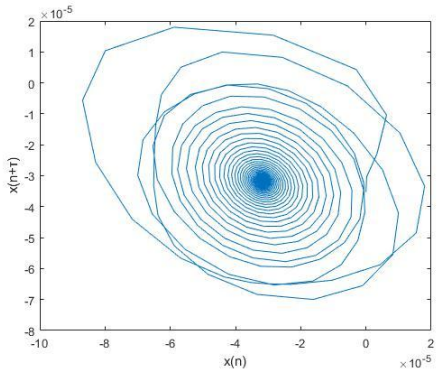

(a) Time Domain; *(b) Phase Space topology;*

Figure 4-7 Beam with delamination size $a/L = 0.2$.

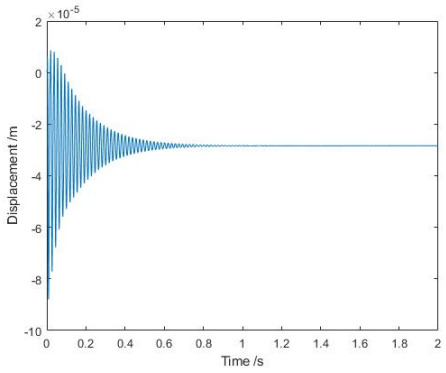

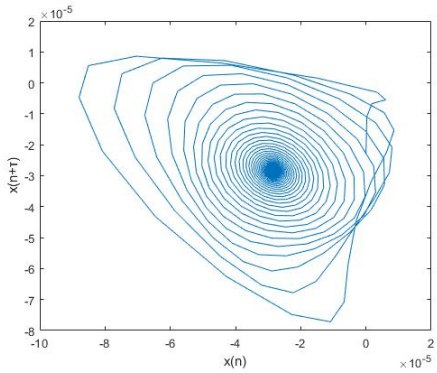

(a) Time Domain; *(b) Phase Space topology;*

Figure 4-8 Beam with delamination size $a/L = 0.3$.

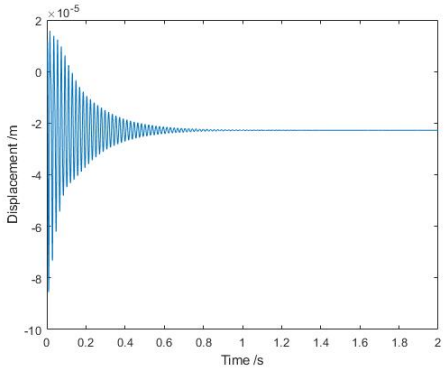

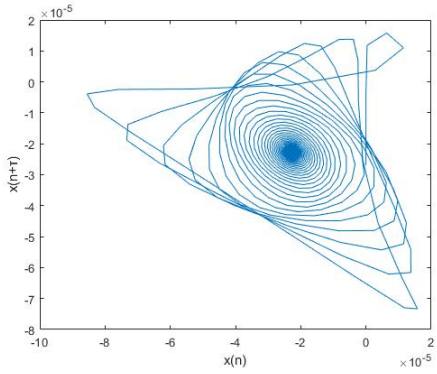

(a) Time Domain; *(b) Phase Space topology;*

Figure 4-9 Beam with delamination size $a/L = 0.4$.

The displacement signal of delaminated beams was measured. Based on Figures 4-5 to 4-9, the phase space topology has a difference with delamination length changing both in shape and size, while it is difficult to find the difference between different signals in the time domain. The phase

space topology will be smaller with delamination size increasing due to the amplitude of signals decrease in the measured point $L_s = 0.73$ as the result of optimization in Chapter 3. It also should be noted that the shape of the beam with different delamination is different. This is because the delamination will affect the natural frequency of structure which is related to the time delay τ and shape of phase space topology as shown in Table 4-2. The CPST was calculated by equation (4-7). The natural frequencies of the first two modes were calculated by ABAQUS for comparison. The changing trend is shown in Figure 4-10:

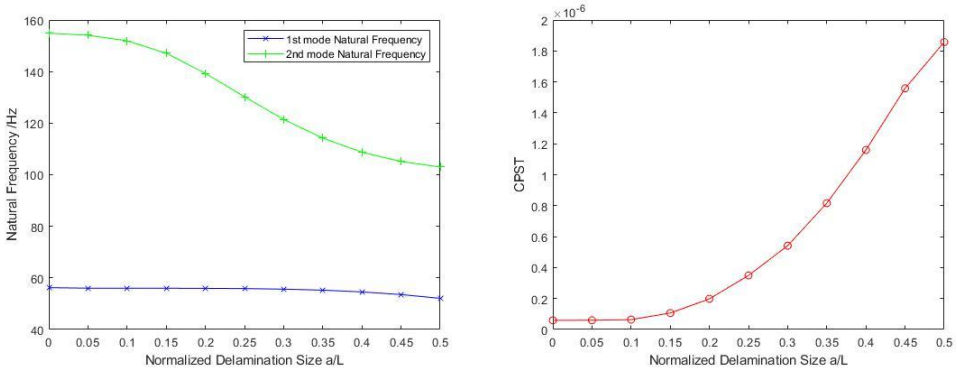

(a) Natural Frequency; *(b) CPST;*

Figure 4-10 The result of delamination with different sizes.

Based on the result in Figure 4-10, the natural frequency will decrease with delamination size increasing due to the stiffness reduction, while the CPST is becoming larger as the result of the change from deformation and natural frequency generated by the delamination. The change of the 2nd mode natural frequency is larger than the 1st mode natural frequency as observed in Chapter 3 because of the various sensitivity of different mode's natural frequencies.

Then the change ratio of these features for cases with various delamination size is calculated:

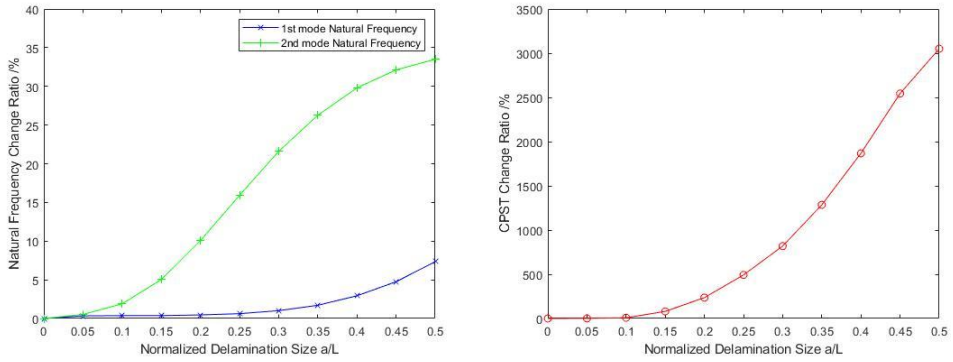

(a) Natural Frequency; *(b) CPST;*

Figure 4-11 The change ratio of Natural Frequency and CPST.

Based on Figure 4-11, the change of the 2nd mode natural frequency is larger than the 1st mode natural frequency, which is from 0 to about 34% and 0 to about 8%, respectively. This means that the 2nd mode natural frequency is more sensitive to the delamination size changing. However, although the value of the CPST in Table 4-2 is small, the change ratio of CPST is much larger than the natural frequency of the first two modes, which is from 0 to about 3000%. Because the CPST is related to both natural frequency and amplitude of measurement signals, which makes the CSPT more sensitive. Therefore, the CPST is more sensitive to the delamination size-changing than the natural frequency of the first two modes.

4.2.2 Delamination Depth Assessment

Second, the effect of delamination depth to the top surface of the samples

was investigated. The delamination size was set as $a = 0.1L$ and it was located at the mid-span (i.e. $L_1 = L/2$) of the beam. The result is shown in Table 4-3:

Table 4-3 Natural frequency of 1st and 2nd modes and CPST with different delamination depths.

Normalized Delamination depth H_2/H	**1st mode /Hz**	**2nd mode /Hz**	**CPST**
0	56.21	154.88	5.1370×10^{-8}
0.05	56.59	154.78	5.5053×10^{-8}
0.10	56.21	154.59	5.8975×10^{-8}
0.15	56.04	153.93	6.4319×10^{-8}
0.20	56.00	153.56	6.8412×10^{-8}
0.25	56.00	153.39	6.8629×10^{-8}
0.30	56.00	152.92	7.1648×10^{-8}
0.35	56.00	152.71	7.2786×10^{-8}
0.40	56.00	152.26	7.5535×10^{-8}
0.45	56.00	152.17	7.6528×10^{-8}
0.50	56.00	151.94	7.7601×10^{-8}

As shown in Table 4-3, the CPST will increase with delamination becoming deeper, which is from 5.1370×10^{-8} to 7.7601×10^{-8}, while the natural frequency will decrease from 56.21Hz to 56.00Hz and 154.88Hz to 151.94Hz respectively. The reason for this phenomenon is the reduction generated by the various delamination depth on the local stiffness of beams. It should be noted

that the effect of delamination depth on the natural frequency and CPST is smaller than the effect of delamination size by comparing Table 4-3 and Table 4-2, especially the drop value of the natural frequencies of the first two modes are just 0.21Hz and 2.94Hz for delamination depth being 0.5H, while the reduction is about 4.13Hz and 51.89Hz, respectively. The reason is that the effect of delamination depth on the dynamic responses is small as mentioned in Chapter 3. The phase space topology is shown in Figures 4-12 to 4-16:

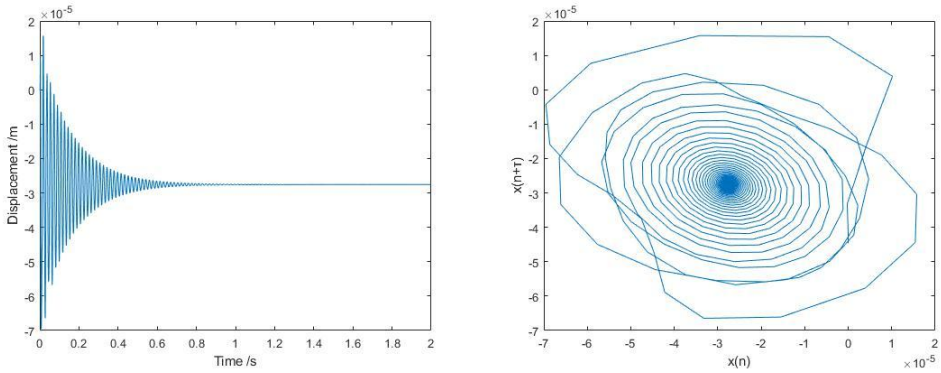

(a) Time Domain; *(b) Phase Space topology;*

Figure 4-12 Undamaged beam.

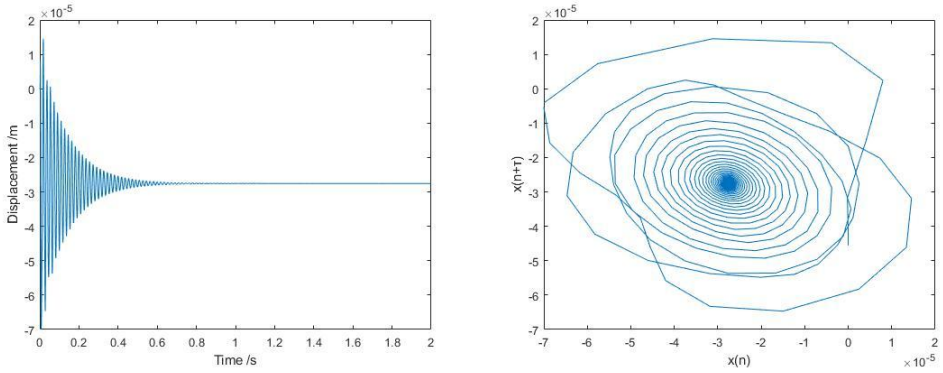

(a) Time Domain; *(b) Phase Space topology;*

Figure 4-13 Beam with delamination depth $H_2 = 0.1H$.

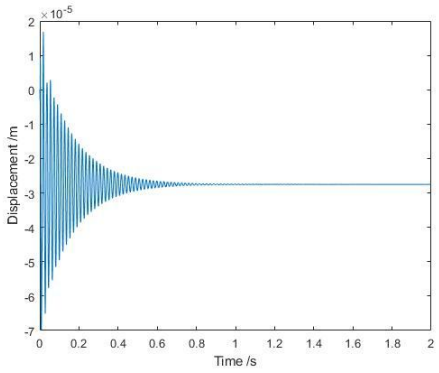

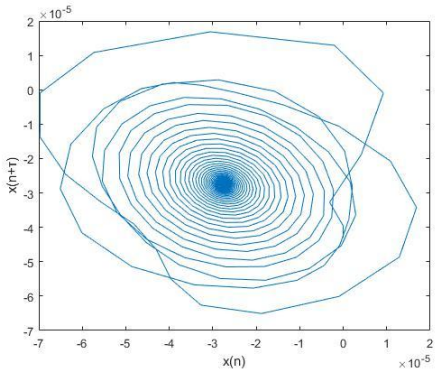

(a) Time Domain; *(b) Phase Space topology;*

Figure 4-14 Beam with delamination depth $H_2 = 0.2H$.

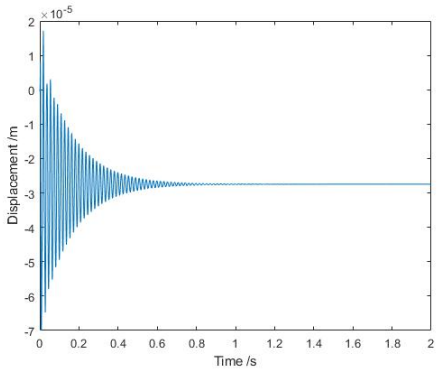

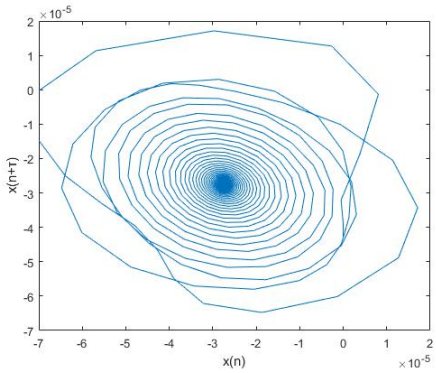

(a) Time Domain; *(b) Phase Space topology;*

Figure 4-15 Beam with delamination depth $H_2 = 0.3H$.

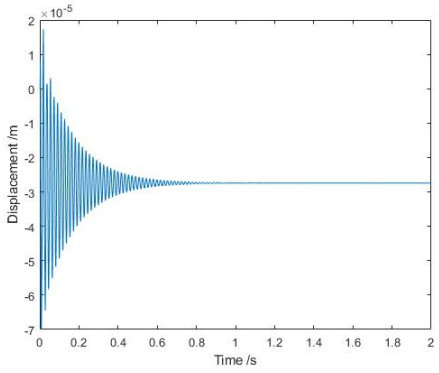

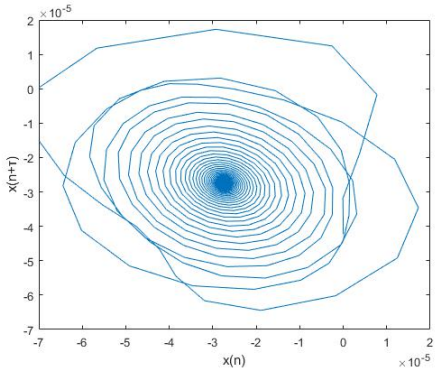

(a) Time Domain; *(b) Phase Space topology;*

Figure 4-16 Beam with delamination depth $H_2 = 0.4H$.

Figures 4-12 to 4-16 show that the phase space topology has a small change

since the effect of the delamination depth is small as mentioned in Chapters 2 and 3. The changing trend and changing ratio of the damage index is shown in Figures 4-17 and 4-18:

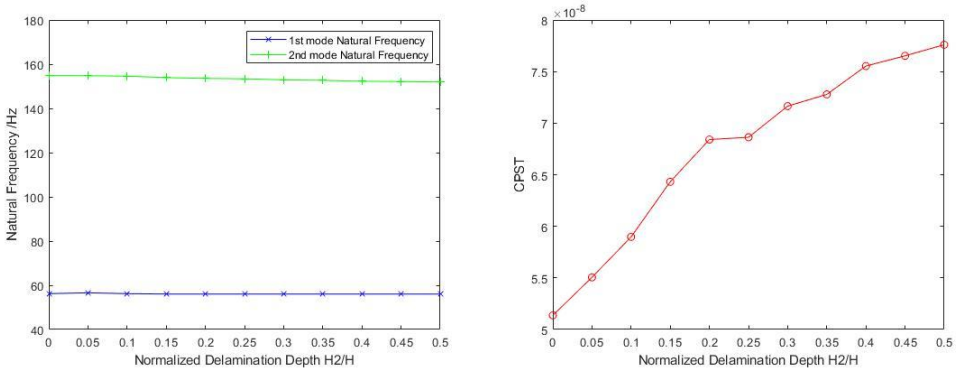

(a) Natural Frequency; *(b) CPST;*

Figure 4-17 The result of delamination with different depths.

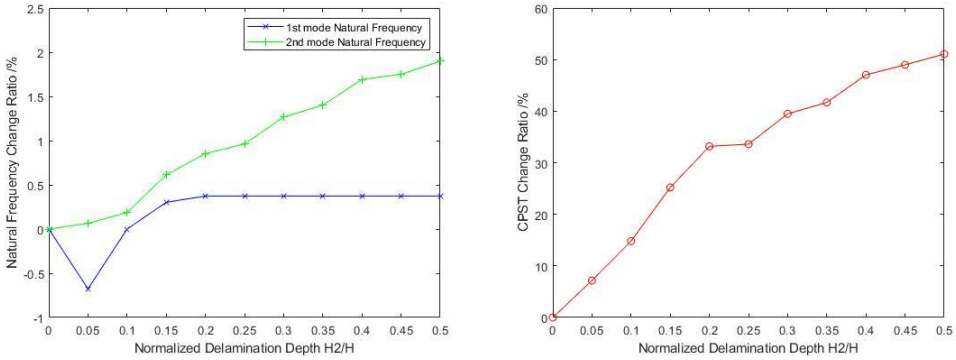

(a) Natural Frequency; *(b) CPST;*

Figure 4-18 The change ratio of Natural Frequency and CPST.

Figures 4-17 and 4-18 show that the changing of CPST for different cases with different depths is clearer than the first two natural frequencies. The result in Figure 4-18 shows that the changing ratio of CPST is from 0 to 50%, which is much larger than the changing ratio of natural frequencies, whose largest change is from 0 to 1.8% from the second mode. This result illustrates

that the proposed method based PSR with CPST is more sensitive to the depth of delamination than the natural frequency of the first two modes due to that it is related to both natural frequency and amplitude of measured signals in the time domain, which can improve the delamination detection and assessment effectively. Moreover, it needs to be noted that the change of first mode natural frequency has a fluctuation when the depth of delamination is smaller than 0.1H, which indicates that the effect of delamination depth on the dynamic responses of the beam is not monotonic due to that the natural frequency is from the local mode generated by delamination when it is close to the surface as indicated in Chapters 2 and 3. However, the CPST has no similar phenomenon because the natural frequency is a global feature, while the CPST is just a feature to describe the change of the phase space structures and it's not the feature of structures that will not be affected by delamination. This may make the delamination depth assessment easier based on analyzing the phase space topology structures and CPST. But it also should be noted that there is a fluctuation when the delamination depth is about 0.25H, which should be investigated and analyzed more in the following chapters.

4.3 Delamination Assessment for Laminated Panel

Then the phase space topology structures of the dynamic responses from the composite laminated panel with various delaminations were analyzed both

by simulation and experiments in the following sections:

4.3.1 Simulation

In this section, a model of a carbon fiber reinforce polymer (CFRP) composite laminate panel with delamination damage was constructed by commercial finite element software ABAQUS. The detailed configuration of the composite laminate is shown in Figure 4-19. The rectangular laminate panel was clamped at one side creating a cantilever panel configuration and the panel was modeled using 8-node elements C3D8R. The dimensions of the panel were chosen randomly $320mm \times 300mm \times 3.96mm$ with a total of 12 layers in the laminate for general testing. The size of the element resolution in the x-y section was 8mm, while for the damaged part, to improve the accuracy of simulation, the resolution was 1mm. The size of the element resolution in the x-z section was 0.33mm.

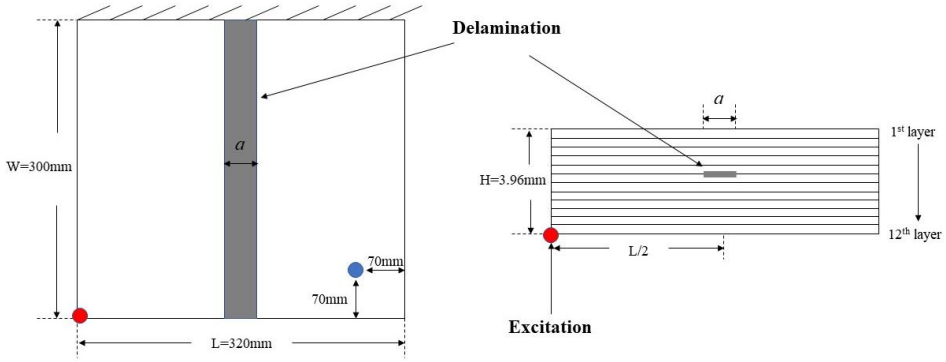

(a) Top View; *(b) Side View;*

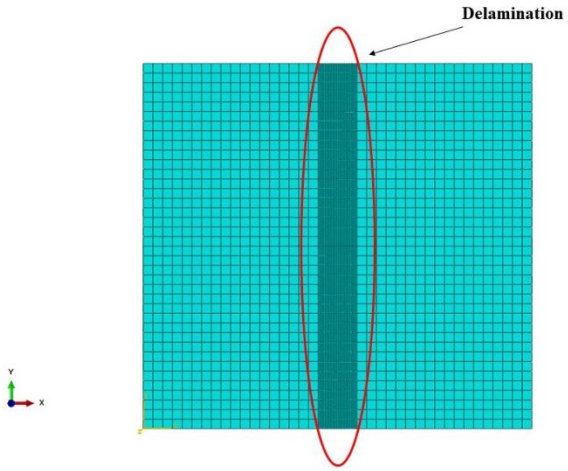

(c) Top view of ABAUQS model;

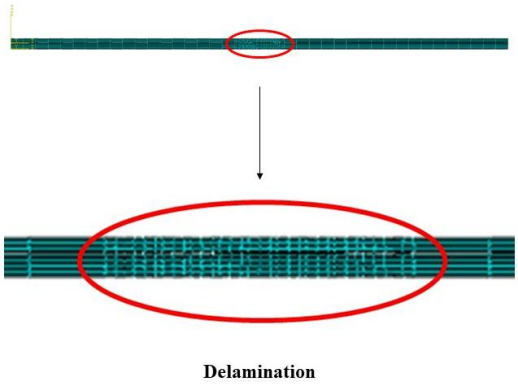

(d) Side view of the ABAQUS model;

Figure 4-19 The model of a composite laminate with delamination.

The values for the elastic modulus (E_{ij}), shear modulus (G_{ij}), and Poisson ratio (v_{ij}) used in the simulation of a composite laminate are described in Table 4-4.

Table 4-4 The properties of the composite laminate.

E_{11}(GPa)	E_{22}(GPa)	E_{33}(GPa)	G_{12}(GPa)	G_{13}(GPa)	G_{23}(GPa)	ν_{12}	ν_{13}	ν_{23}
27	27	4.7	4.7	4.7	4.7	0.28	0.1	0.1

In this model, the delamination is created by the cohesive interaction. As shown in Figure 4-19(c), the delamination was set across the width of the panel and it was located in the middle of the length. The acceleration was measured at the location indicated by the blue point in the intact part to avoid the effect on delamination, which is 70mm to the right boundary and bottom boundary. A rectangular pulse load with the amplitude being $q_0 = 10N$ and duration $t_1 = 0.00106s$ as shown in equation (4-8) was used as input excitation to generate the vibration responses in laminate at the location indicated by the redpoint in the left corner. The vibration signal is generated by impulse excitation which is common in engineering applications [118]. The length of the delamination a showed in Figure 4-19 was changed to different values in the simulation. The sampling frequency was $f = 12794$ Hz.

4.3.1.1 Delamination Size Assessment

The samples with different delamination sizes a were investigated. In the model, the delamination is defined to locate between the 5th and 6th layer. For each specific delamination size, the corresponding natural frequency of the first two modes and the CPST value were calculated. Their sensitivity to the size of delamination is thus obtained and compared with each other. The results are presented in Table 4-5:

Table 4-5 Natural frequency of 1st and 2nd modes and CPST with different delamination sizes.

Delamination size *a*/mm	**1st mode (Hz)**	**2nd mode (Hz)**	**CPST**
0	31.819	168.17	0.0759
16	31.801	161.67	0.1424
32	31.795	154.23	0.1601
48	31.733	145.40	0.1632
64	31.626	135.59	0.1749
80	31.468	125.46	0.1962
96	31.257	115.69	0.1943
112	30.991	106.71	0.1974
128	30.669	98.717	0.2261
144	30.292	91.749	0.2380
160	29.863	85.731	0.2354

Table 4-5 shows that with delamination size increasing, the natural frequencies of the first two modes are reduced, while the CPST is increasing. The reason for this phenomenon is due to the stiffness reduction and deformation changing generated by the delamination as mentioned in previous work [25, 43, 45]. The dynamic signals from different cases and the phase space topology structures are shown as:

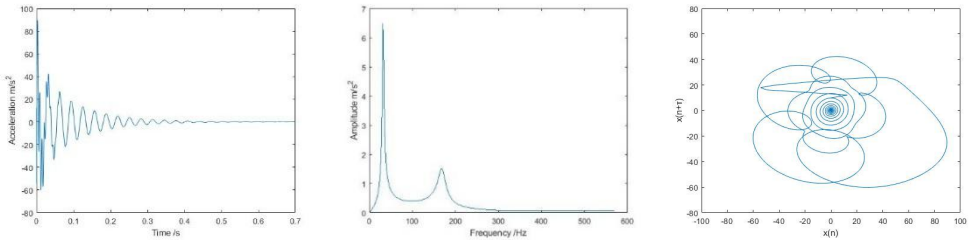

(a) Time domain; *(b) Frequency domain;* *(c) Phase Space topology;*

Figure 4-20 The undamaged result.

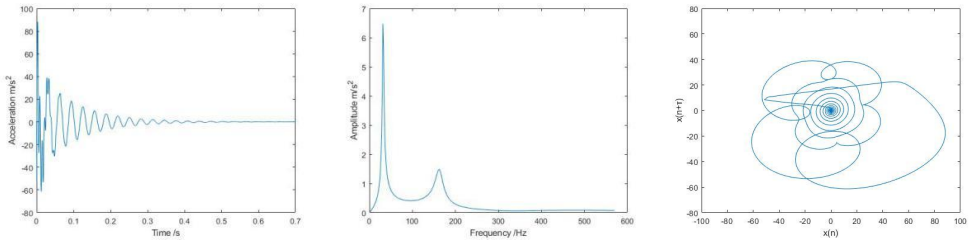

(a) Time domain; *(b) Frequency domain;* *(c) Phase Space topology;*

Figure 4-21 The result of laminate with delamination size a=16mm.

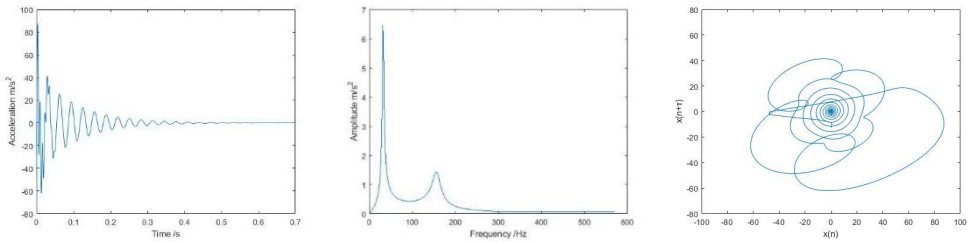

(a) Time domain; *(b) Frequency domain;* *(c) Phase Space topology;*

Figure 4-22 The result of laminate with delamination size a=32mm.

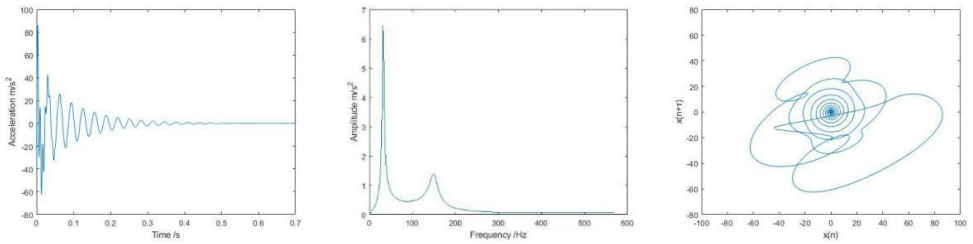

(a) Time domain; *(b) Frequency domain;* *(c) Phase Space topology;*

Figure 4-23 The result of laminate with delamination size a=48mm.

Figures 4-20 to 4-23 show the phase space topology of samples with different delamination sizes. The frequency-domain signals are generated by

using the Fourier Transform method from the time domain signals, while the phase space topology structures are constructed by the phase space reconstructed method. The result in the frequency domain shows that only 1st mode and 2nd mode are clear enough to be captured in the frequency domain due to the impulse excitation being easy to active low-frequency modes. Therefore, the following discussion will use the first two modes as compared to the proposed method.

Comparing to the phase topology shape when no delamination is introduced, there is a clear change in the topology shapes when there is delamination. The shape of phase space topology is related to the frequency and amplitude of signals. With the increasing of delamination size, the change of topology shape is clearer as shown in Figures 4-20 to 4-23 as the result of natural frequency changing and deformation changing due to the delamination. However, there is no clear change of the time domain signal and the 1st natural frequency in Figures 4-20 to 4-23 when the delamination size is small as shown in Table 4-5, while the change of the 1st mode is just about 1.9560Hz with delamination size being 160mm. Although the change of the 2nd mode natural frequency is larger, the amplitude of this mode is very small as shown in Figure 4-20 to Figure 4-23, which will be affected and covered by the measured noise in practical applications. Therefore, compared with the method using time and frequency domain signals for analysis, the phase space topology shapes are more sensitive to the delamination size with more

obvious changes. This result illustrates the potential for the improvement to assess and detect the delamination based on the vibration responses of composite laminate plates by analyzing the phase space topology structures due to the clearer changes generated by delamination in the phase space.

It also should be noted that the size of phase space topology from different cases decreases with the size of delamination increasing. The reason for this phenomenon is the change of deformation generated by the delamination in structure. The size of the phase space topology structure is related to the amplitude of the signal and vibration energy of the measured point in the intact part of delaminated samples, while these two factors are determined by the deformation of structure vibration. There is some local deformation in the delaminated part which will change the energy distribution as observed in the previous work [43]. Therefore, the energy of the intact parts of the panel will become smaller, which makes the phase space topology structure size smaller.

To further reveal the sensitivity of phase space topology, the changing trend of natural frequencies of the first two modes and CPST values are shown in Figure 4-24 with various delamination sizes.

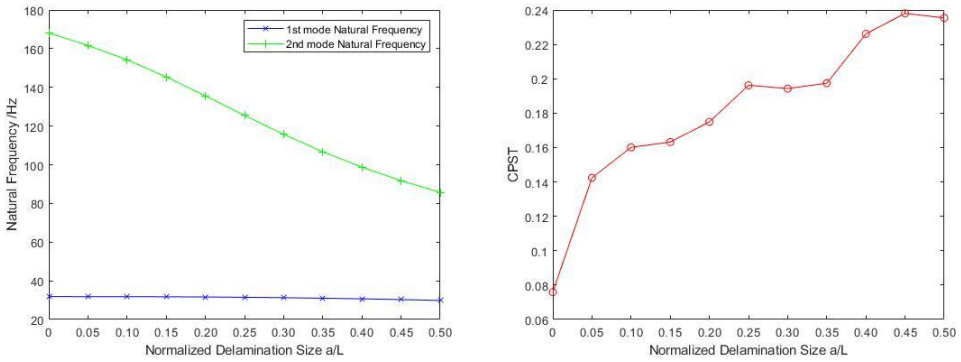

(a) Natural Frequency; *(b) CPST;*

Figure 4-24 The result of delamination with different sizes.

According to Figure 4-24(a), the natural frequencies decreased when the length of delamination increases, but the changing of 1st mode natural frequency is too small to be recognized due to the small sensitivity of the 1st mode natural frequency to the delamination, which is a global feature as previous work mentioned for homogenous structure damage detection [22, 191-193]. On the other hand, the CPST increases when the delamination size increases as shown in Figure 4-24(b). Since the CPST is related to the frequency and amplitude of signals. Moreover, the change of CPST has some fluctuation due to that it is related to both the natural frequency and amplitude of the signals in the time domain, which have different changing trends with various delamination sizes.

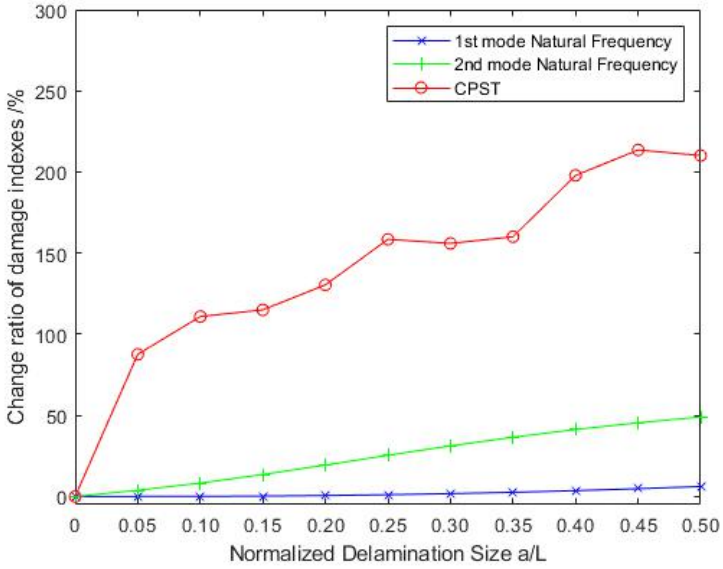

Figure 4-25 The change ratio of two features of delamination with various sizes.

Figure 4-25 compared the change ratio of Nature Frequency and CPST. The change ratio of 1st mode natural frequency is only about 0%-6%. The 2nd natural frequency will drop by about 50% even if the delamination size is 160mm (as half of the laminate width) but its energy is lower than the 1st mode natural frequency as shown in Figures 4-20 to 4-23.

Although the value of CPST is small, its change is clearer than the first two mode's natural frequencies due to it related to both frequency and energy. Compared with the method that uses the natural frequency, the CPST ratio value will experience a larger change along with the adjustment of delamination size, from 0% to more than 200%. The different sensitivity of the natural frequencies and CPST is because the natural frequencies are global features related to the boundary conditions and other global parameters of the whole structure. However, the delamination was local damage and its effect on the whole structure is weak when the size of delamination is small.

Therefore, the existence of delamination may not change the structure properties effectively. On the other hand, the CPST is related to both the frequency and the energy of the signal measured at one point, which is a local feature. Therefore, the proposed method and new feature as the index could provide a clearer indication of the size-changing of delamination in a composite laminates panel compared with the natural frequency. Based on this result, it demonstrated that the CPST of the Phase space topology structures is more sensitive to the size of delamination than the first two orders of natural frequencies and it has better feasibility for application.

4.3.1.2 The Analysis of the Robustness to the Noise

In applications, noise and disturbance cannot be avoided in dynamic signal measurement. The noise will cover useful signals and affect the accuracy and credibility of damage indexes. Therefore, this section will test the robustness of phase space topology structures and CPST, which will be used as the index for delamination detection. The Phase Space topology of the undamaged case with different Signal-to-Noise Ratio (SNR) is shown in Figure 4-26.

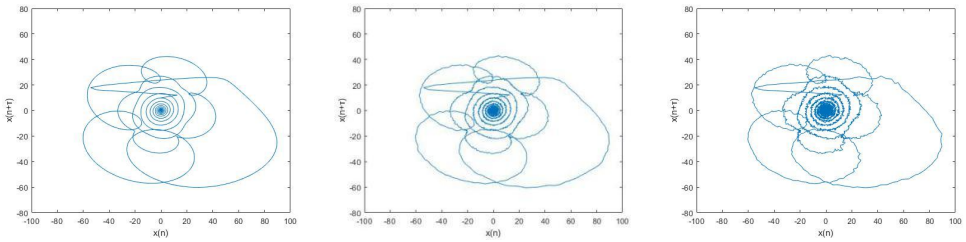

(a) No noise; *(b) SNR=10dB;* *(c) SNR=5dB;*

Figure 4-26 The phase topology of the undamaged sample with different noise levels.

In Figure 4-26, although the trajectories of those with noise become rough compared with no noise, the shape of the topology does not change much so its shape can still be recognized. This is because the noise energy is small and its frequency is different from the signals, which is easy to be recognized in phase space. Therefore, the effect of noise on the phase space topology analysis is small. Figure 4-27 shows the changing trend of CPST under different noise level:

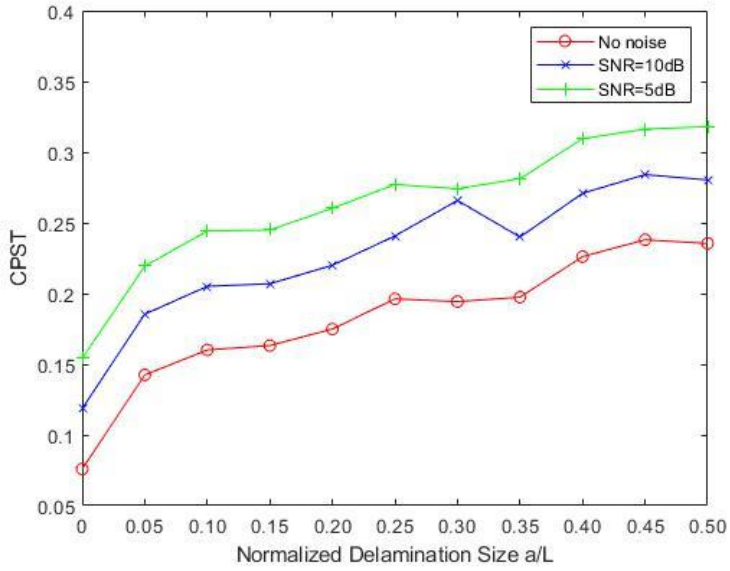

Figure 4-27 The changing trend of CPST with different noise levels.

Based on the results in Figure 4-27, it is found that the introduced noise increased the value of CPST, but the changing trend and relationship between CPST and delamination size are barely influenced. This is because the CPST was averaged for measured data, the error from each data point is eliminated and keep the regularity. Therefore, the CPST has the capability of noise-proof and is reliable to be used as an index for delamination detection.

4.3.2 Experiment

This section will investigate the phase space topology structures of dynamic responses from the delaminated composite laminate plates to verify the credibility of the finite element models and validate the feasibility of proposed methods based on the phase space topology structures. The experimental equipment and setting are shown in Figure 4-28.

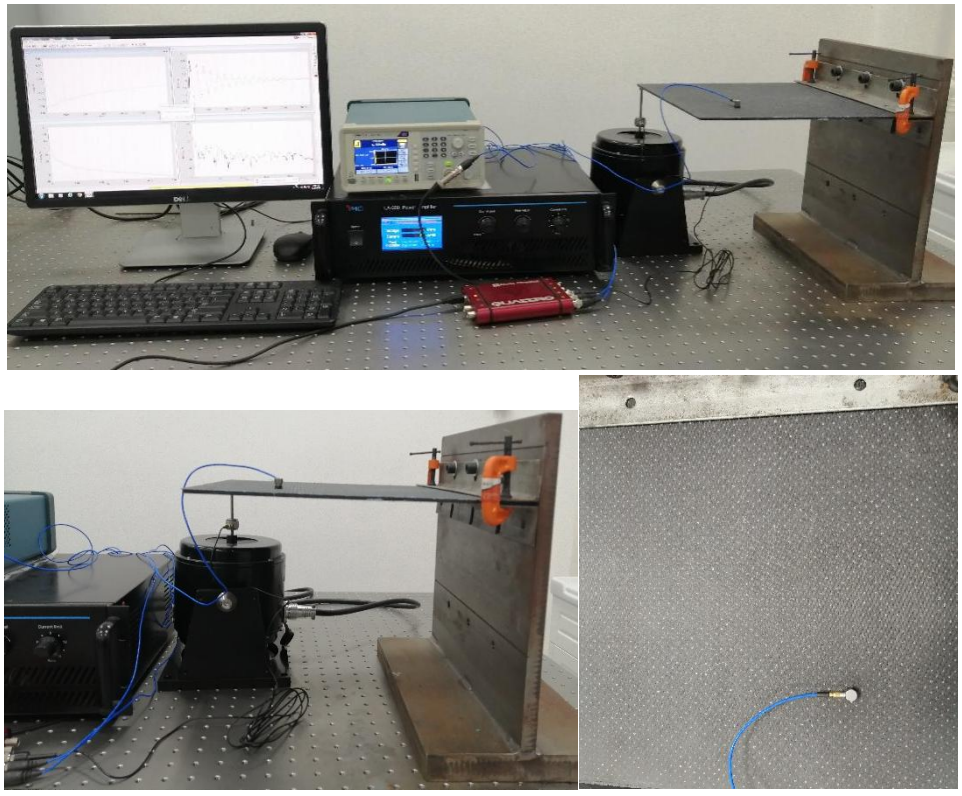

Figure 4-28 The arrangement of the experiment.

The equipment was put on the optical isolation platform to avoid environmental disturbance. The carbon fiber-reinforced polymer (CFRP) plates were manufactured based on the woven prepreg by the hot press method with various delamination. In the testing, the sample is one side clamped, and an accelerometer (PCB 352C65) is attached to the plate to measure the vibration responses on the location shown in Figure 4-19(a) by

the blue point. Data is collected and initially analyzed by SignalCalc Ace from Data Physics. An MS-200 shaker and LA-200 Power Amplifier with AFG1022 Arbitrary Function Generator were used to generate impulse excitation. A stinger is used to connect the shaker with the plate for excitation signal input on the location shown in Figure 4-19(a) by the redpoint. Polytetrafluoroethylene (PTFE) film was embedded in the laminate panel to make delamination. The material properties and dimensions are the same with simulation as shown in Table 4-4. The samples are shown in Figure 4-29:

(a) Sample No.1; *(b) Sample No.2;* *(d) Sample No.3;*

Figure 4-29 The samples for experiments.

Three samples were made for the experiment as shown in Figure 4-29: 1) The panel with no damage; 2) The size of delamination is 32×300mm; 3) The delamination size is 64×300mm. Table 4-6 shows the features of the samples' experiment and simulation results.

Table 4-6 Natural frequency of 1st mode and CPST for cases with different delamination.

Sample No.	Delamination size	Natural Frequency /Hz			CPST		
		Simulation	Experiment	Error /%	Simulation	Experiment	Error /%
1	Undamaged	31.819	31.812	0.02	0.0759	0.0568	33.6
2	32×300 mm	31.795	31.375	1.3	0.1601	0.1752	8.6
3	64×300 mm	31.626	30.687	3.1	0.1749	0.1871	6.5

Based on Table 4-6, the experiment result is close to the simulation results. It should be also noted that the value of CPST from different cases is different. Therefore, the feasibility of the proposed method to detect delamination is tested in these experiments. The errors may be caused by the difference between experiment and simulation settings, such as the boundary conditions and driving force. Furthermore, based on the result of Section 4.2, the value of CPST will be affected by noise and disturbance. Therefore, the difference between experiment and simulation is acceptable. Figures 4-30 to 4-32 show the phase space topology of each sample compared with the simulation. The changing trend of phase space topology is the same both in simulation and experiment, which will be smaller with the size of delamination increasing, due to the amplitude reduction of the dynamic responses and the natural frequency shift.

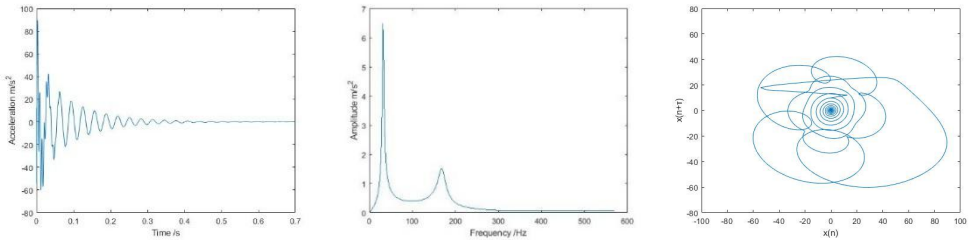

(a) Time domain; *(b) Frequency domain;* *(c) Phase Space topology;*

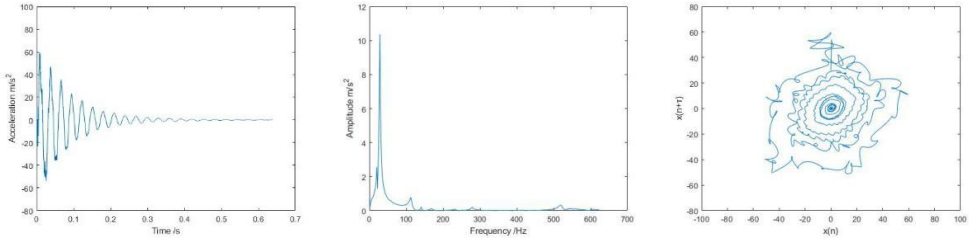

(d) Time domain; *(e) Frequency domain;* *(f) Phase Space topology;*

Figure 4-30 Simulation result (a-c) and Experiment result (d-f) of No.1 Sample.

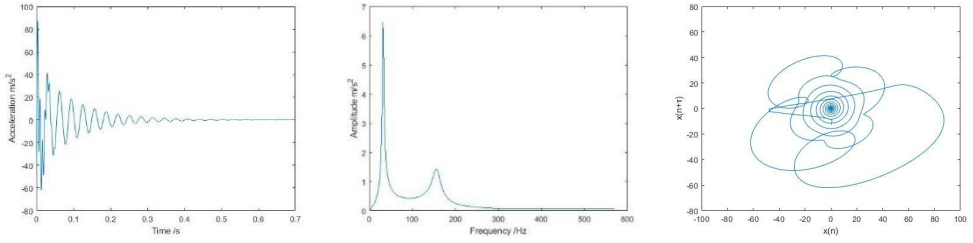

(a) Time domain; *(b) Frequency domain;* *(c) Phase Space topology;*

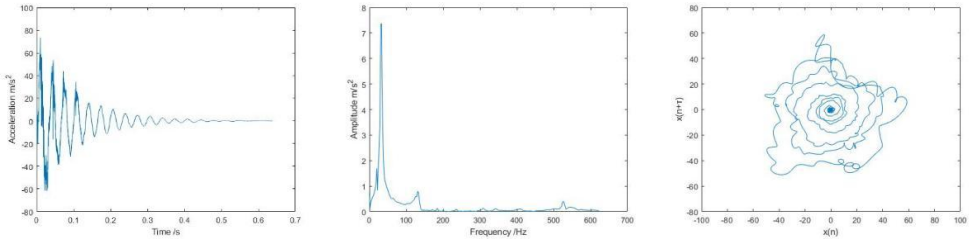

(d) Time domain; *(e) Frequency domain;* *(f) Phase Space topology;*

Figure 4-31 Simulation result (a-c) and Experiment result (d-f) of No.2 Sample.

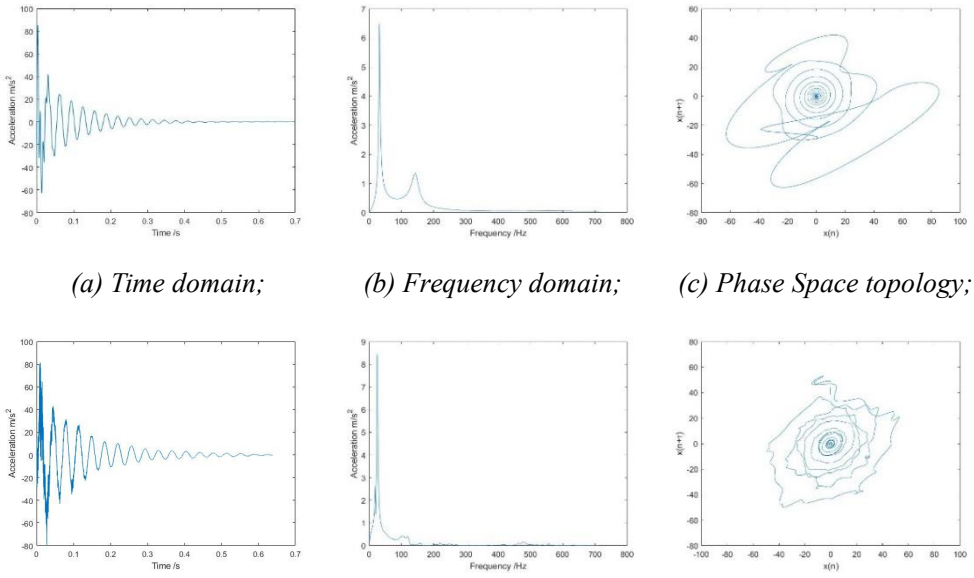

(a) Time domain; *(b) Frequency domain;* *(c) Phase Space topology;*

(d) Time domain; *(e) Frequency domain;* *(f) Phase Space topology;*

Figure 4-32 Simulation result (a-c) and Experiment result (d-f) of No.3 Sample.

Figure 4-33 compared the changing of CPST along with delamination size in both simulation and experiment. In this figure, both results in the simulation and experiment have the same changing trend with different delamination sizes in laminate. A small deviation exists between the two results, yet it is still acceptable because of the inevitable disturbance and error in experiments. The result also illustrates the possibility to improve the vibration-based method to detect and estimate delamination in composite laminated structures based on the phase space topology structures.

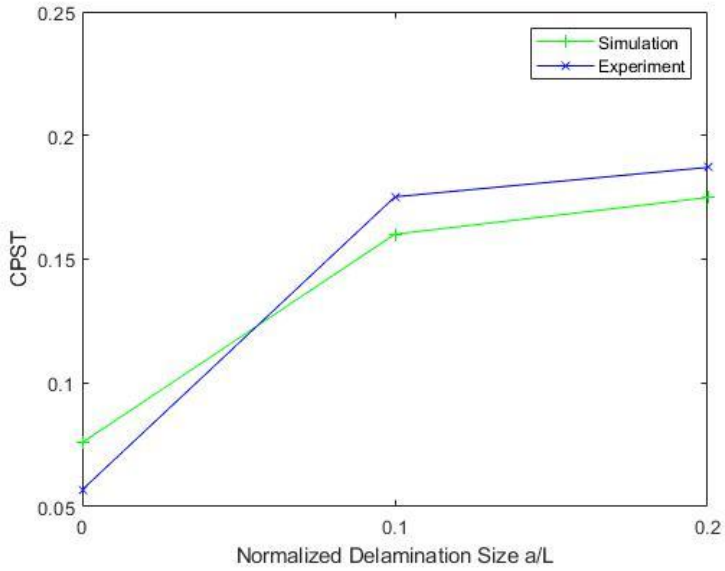

Figure 4-33 The changing trend of experiment and simulation.

4.4 Conclusions

In this chapter, the effect of delamination on the phase space topology structures of dynamic responses was investigated based on the Phase Space Reconstructed (PSR) method and the CPST feature. Based on this work, the feasibility of using the proposed method and feature for detecting and assessing delamination parameters in composite structures is demonstrated. Some conclusions can be drawn as:

1. The possibility of the improvement for the vibration-based methods based on the phase space topology analysis to detect and assess delamination in a beam and a composite laminated panel was demonstrated. The sensitivity and robustness of the proposed method based on the phase space topology were tested both by simulation and experiment as well as the feature named Change of Phase Space Topology (CPST). It should be noted that the delamination will change both the shape and the size of

phase space topology structures of the dynamic responses due to the change of the signal frequency and amplitude in the time domain.

2. Moreover, the result shows that the CPST increased along with the rising of delamination depth and size, while the natural frequency decreased due to the stiffness reduction and deformation change generated by the delamination. The proposed vibration-based method by using phase space topology structures and CPST is more sensitive than the vibration-based method using the natural frequencies of the first two modes due to that the value of CPST is related to both the natural frequency and the amplitude of signals. The robustness of the proposed method using CPST is demonstrated due to that this feature is a type of average feature which can eliminate the noise. Moreover, the changing trend of CPST with delamination depth changing fluctuates less than the natural frequency due to that it's not the properties of structures and this feature is just related to the change of the phase space structures. Therefore, this feature is easier to be analyzed.

Chapter 5 THE DELAMINATION DETECTION AND ASSESSMENT BASED ON PHASE SPACE TOPOLOGY ANALYSIS COMBINED WITH WAVELET PACKET DECOMPOSITION

This chapter improves the delamination assessment method based on the phase space topology analysis of the dynamic responses for composite structures. As shown in Chapter 4, the phase space topology structures and CPST form dynamic signals that can be used to assess delamination in composites structures. However, the sensitivity still needs to be further improved to analyze the effect of delamination since the delamination is a type of local damage, and its effect on the dynamic responses will be significant in the particular frequency ranges. However, the useful information may be covered in the initial and is difficult to be capture and analyzed, which will affect the accuracy of the delamination assessment. Moreover, as mentioned in Section 1.3, there may be errors in damage detection by using just one type of feature because the different situations may have the same feature. So it is necessary to develop more features that contain different local information of the structures to enhance the accuracy of delamination assessment based on the phase space topology analysis of dynamic responses.

Wavelet methods can divide the vibration signal into different sub-signals with different frequency ranges, which contain local information of structures in different frequency ranges. Therefore, these methods can improve the sensitivity of vibration-based methods by capturing the sub-signals, which contain useful weak information about the delamination. Some researchers have done similar work to show the possibility and advantages of the phase space topology analysis combined with wavelet methods to analyze the local information of signals [194-197]. However, the effect of delamination on the phase space topology structures of sub-signals generated by wavelet packet methods with different frequency ranges has not been investigated. Therefore, this chapter will analyze the change generated by delamination in the phase space topology structures of sub-signals decomposed by the wavelet packet method. The result will test the possibility and potential of the phase space topology analysis cooperating with wavelet packet decomposition.

5.1 Methodology

This section will introduce the wavelet packet decomposition method. Then the procedure of the proposed method combined the phase space topology structures with the wavelet packet decomposition method will be shown as well as the calculation of the new feature.

5.1.1 Wavelet Packet Decomposition Method

The wavelet packet analysis is one of the most useful wavelet methods in many applications [198-200]. This chapter used the wavelet packet method to

analyze the vibration signal from structures. For an origin signal $f(t)$, it can be constructed by the sum of 2^j components at *j* level decomposition as:

$$f(t) = \sum_{i=1}^{2^j} g_j^i(t), \tag{5-1a}$$

$$g_j^i(t) = \sum_{k=-\infty}^{\infty} c_{j,k}^i u_{j,k}^i(t), \tag{5-1b}$$

where the $u_{j,k}^i(t)$ is a wavelet packet with three indices as integers *i, j,* and *k* which are the modulation, scale, and translation parameters, respectively. For equation (5-1b), the formulation of the wavelet packet is shown as follow:

$$u_{j,k}^i(t) = 2^{j/2} u^j(2^j t - k), \tag{5-2}$$

where the $u^j(2^j t - k)$ is the mother wave when the $j = 1$. There are different types of mother waves. In this chapter, the Haar wave was used as the mother wave to decompose and analyze the vibration signal from the target. The Haar wave is simple so the signal decomposition will be easy and fast by using this wave [139, 201]. The Haar function is showed as follows:

$$u(t) = \begin{cases} 1, 0 \le t \le \frac{1}{2} \\ -1, \frac{1}{2} \le t \le 1 \cdot \\ 0, others \end{cases} \tag{5-3}$$

For equation (5-1b), there are recursive relations between the *j*th and the (*j*+1)th level components as follows:

$$c_{j,k}^{2i} = \sum_l a_{l-2k} c_{j+1,l}^i, \tag{5-4a}$$

$$c_{j,k}^{2i+1} = \sum_l b_{l-2k} c_{j+1,l}^i, \tag{5-4b}$$

where the a_{l-2k} and b_{l-2k} are coefficients determined by mother waves $u(t)$. Then the $c_{j,k}^i$ in equation (5-1b) can be solved as the following formulation:

$$c_{j,k}^{i} = \int_{-\infty}^{\infty} f(t) u_{j,k}^{i}(t) dt \,. \tag{5-5}$$

Based on equation (5-1) to (5-5), the component $g_j^i(t)$ of each level can be calculated [137, 198, 200]. The wavelet packet method can provide higher resolution both in the low-frequency range and the high-frequency range. In this chapter the scale is chosen $j = 2$, which means the modulation $i = 2^j = 4$. The diagram showed the procedure of wavelet packet decomposition as follow:

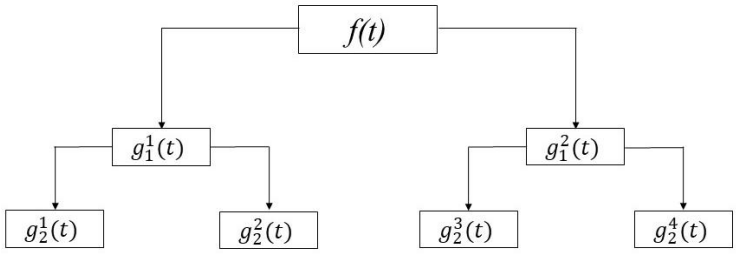

Figure 5-1 The tree-map of 2 level wavelet packet decomposition.

The signal from a composite laminated panel under impulse excitation is decomposed to level 2 with four components as shown below:

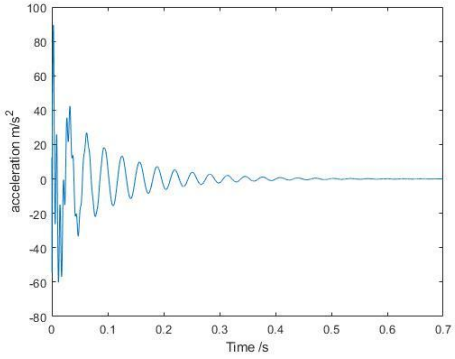

(a) original signal;

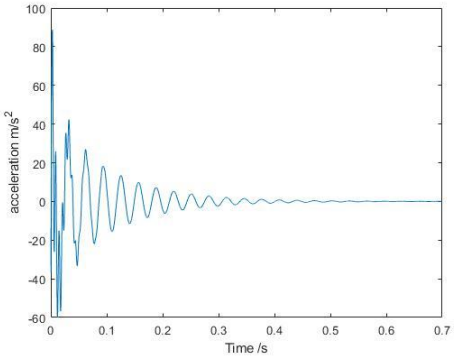

(b) g_2^1*;*

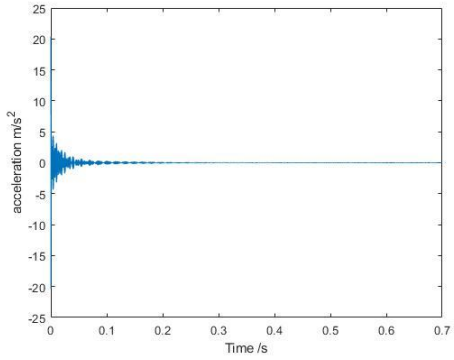

(c) g_2^2*;*

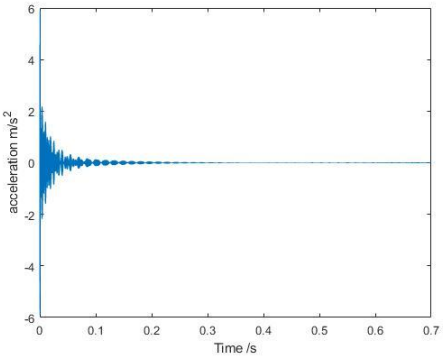

(d) g_2^3*;*

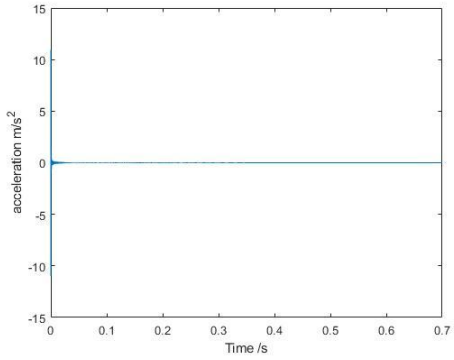

(e) g_2^4*;*

Figure 5-2 The original signal and the sub-signals after wavelet packet decomposition.

Based on Figure 5-2, the original signal was divided into sub-signal with different frequency ranges. Moreover, the sub-signals have different magnitudes which means they have different energy values. The energy

spectrum and frequency spectrum of sub-signals from structures will be affected by delamination. Therefore, it can detect delamination in structure based on analyzing the energy and frequency of sub-signals [137].

5.1.2 Phase Space Topology Analysis of Sub-signals

After decomposition of the original signal by wavelet packet method, the Phase Space topology of each sub-signal can be constructed and analyzed to analyze the local information of the delaminated structures to improve the sensitivity and accuracy of delamination assessment. In this section, the procedure of the proposed method by combining the phase space topology analysis with wavelet packet decomposition will be introduced.

The previous work indicates that the damage will shift the frequency both in the original signal [22] and the sub-signals [199]. It will also change the energy distribution for different sub-signals [137], i.e. some modes are strengthened, while other modes are weakened. The change of frequency and energy will affect the states of dynamic systems. In phase space, all possible states of a dynamic system are represented, and each possible state of the system is associated with one unique point in the phase space. The phase space topology contains useful information of variables in the dynamic system, including the frequency and energy. Therefore, the phase space could be used as a good candidate for signal change identification and structural damage detection [116, 118].

Following the PSR method in Chapter 4, the phase space topology

structures of sub-signals can be constructed and the $CPST_{ij}$ of each sub-signal can be calculated. The flow chart of the procedure is shown in Figure 5-3:

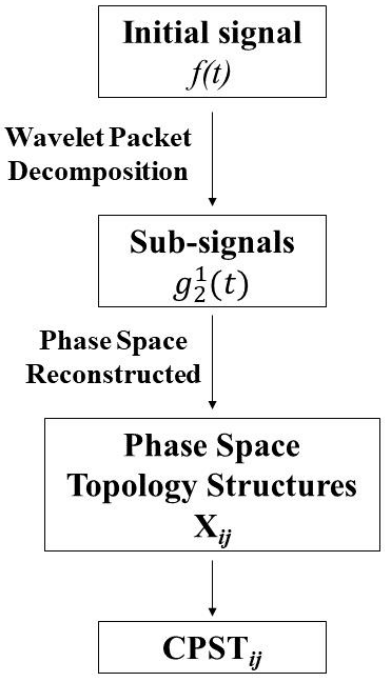

Figure 5-3 The procedure of the proposed method based on the phase space topology structures and wavelet packet decomposition.

where the time delay $\tau = 13$ for beam and $\tau = 97$ for the laminated panel in the following sections, respectively. About the embedding dimension m, the value is still 2 chosen to reconstruct the phase space topology of sub-signals with different delamination. The PSR method and calculation of CPST was shown from equations (4-1) to (4-7) in Chapter 4. Most of the previous work used the energy and energy distribution of sub-signals to assess the damage in the structures [137, 202] and ignored the shift of the frequency. For this time, the CPST ratio of each sub-signal will be used as the damage index, which is related to both the energy and the frequency of each sub-signal. The proposed feature to describe the phase space topology structures of

sub-signals generated by wavelet packet decomposition was defined as:

$$R_{ij} = \frac{CPST_{ij}}{\sum CPST_{ij}}. \tag{5-6}$$

Based on the new proposed damage index, the effect of delamination on the dynamic responses of samples can be evaluated and investigated.

5.2 Delamination Assessment for Beam Structures

To verify the possibility and advantages of the proposed method based on the phase space topology analysis and wavelet packet decomposition, a homogeneous beam with various delamination was used as the sample first. The model of a delaminated beam is shown in the following figure:

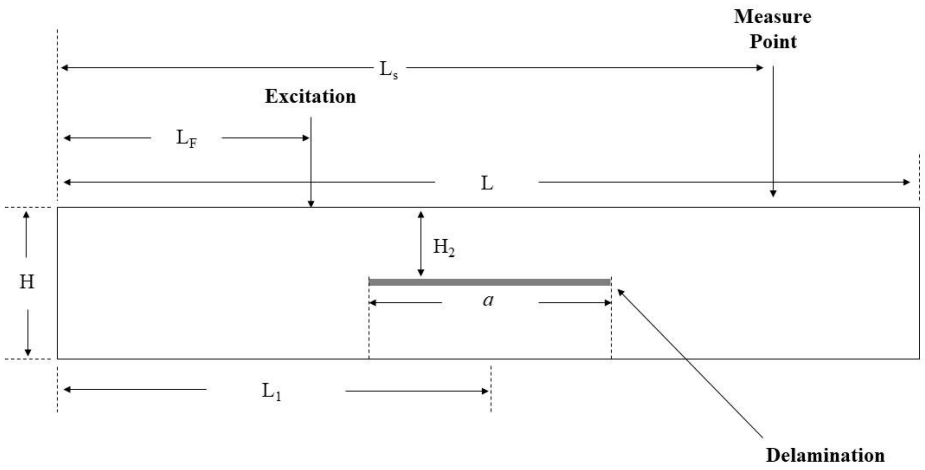

Figure 5-4 The model of delaminated beam.

As noted in Figure 5-4, the delamination size and depth are represented by a and H_2. The location of the delamination middle is represented by L_1, which is fixed as $L_1 = 0.5L$ The information of proposed sample is shown as Table 5-1:

Table 5-1 The properties of beam.

Modulus /GPa	Density /kg/m^3	Length (L) /m	Width (b) /m	Thickness (H) /m
30	1000	1	0.1	0.01

The excitation is located at $L_F = 0.2L$ and the measured point is located at $L_s = 0.73L$ for different delamination size and $L_s = 0.76L$ for different delamination depth based on the result in Chapter 3. The displacement was measure as the vibration signals to be analyzed. The conditions of the simulation are the same as Chapter 4 in Section 4.2. This sampling frequency is $f = 1000Hz$, which means the frequency range of each mode is shown in Table 5-2:

Table 5-2 Frequency range of components.

Components number	Frequency Range/Hz
$\boldsymbol{g_2^1}$	0-125
$\boldsymbol{g_2^2}$	125-250
$\boldsymbol{g_2^3}$	250-375
$\boldsymbol{g_2^4}$	375-500

5.2.1 Delamination Size Assessment

First, the delamination size was investigated. The delamination was set in the mid-plane of the beam ($H_2 = 0.5H$) and in the mid-span ($L_1 = L/2$). The result is shown in Table 5-3:

Table 5-3 The CPST of sub-signals with different delamination sizes.

Normalized Delamination size a/L	g_2^1(×10^{-8})	g_2^2(×10^{-8})	g_2^3(×10^{-8})	g_2^4(×10^{-8})
0	10.383	9.7301	2.1354	1.7732
0.05	12.763	9.4823	2.2238	1.7355
0.10	13.441	9.5491	2.2747	1.7584
0.15	17.219	9.7502	2.3967	1.8492
0.20	22.865	9.8793	2.6475	1.6946
0.25	31.174	9.7178	2.4414	2.1026
0.30	52.212	9.2964	2.5794	1.9418
0.35	80.193	8.6501	2.6751	1.7904
0.40	120.07	7.8079	2.7130	1.6133
0.45	160.85	6.7919	2.9865	1.3881
0.50	193.74	6.0513	3.6731	1.2140

Based on Table 5-3, it can be obtained that the value of CPST from different sub-signals are different because the frequencies and amplitudes of all sub-signals were affected due to the stiffness reduction and deformation changing generated by delamination. It also should be noted that the changing trend of CPSTs from different sub-signals g_j^i are different, which means the effect of delamination on the different sub-signals with various frequencies is different as mentioned in Chapter 3. The CPST of g_2^1 is larger than others in all cases, such as the result of intact cases is 10.383, while others are 9.7301, 2.1354, and 1.7732. The reason is that the energy of the original signal is mainly distributed to the g_2^1 [198]. While the change of g_j^i from the different cases is related to the natural frequency changing and energy distribution changing so it is different with various delamination sizes. The result is shown

in Figures 5-5 to 5-7:

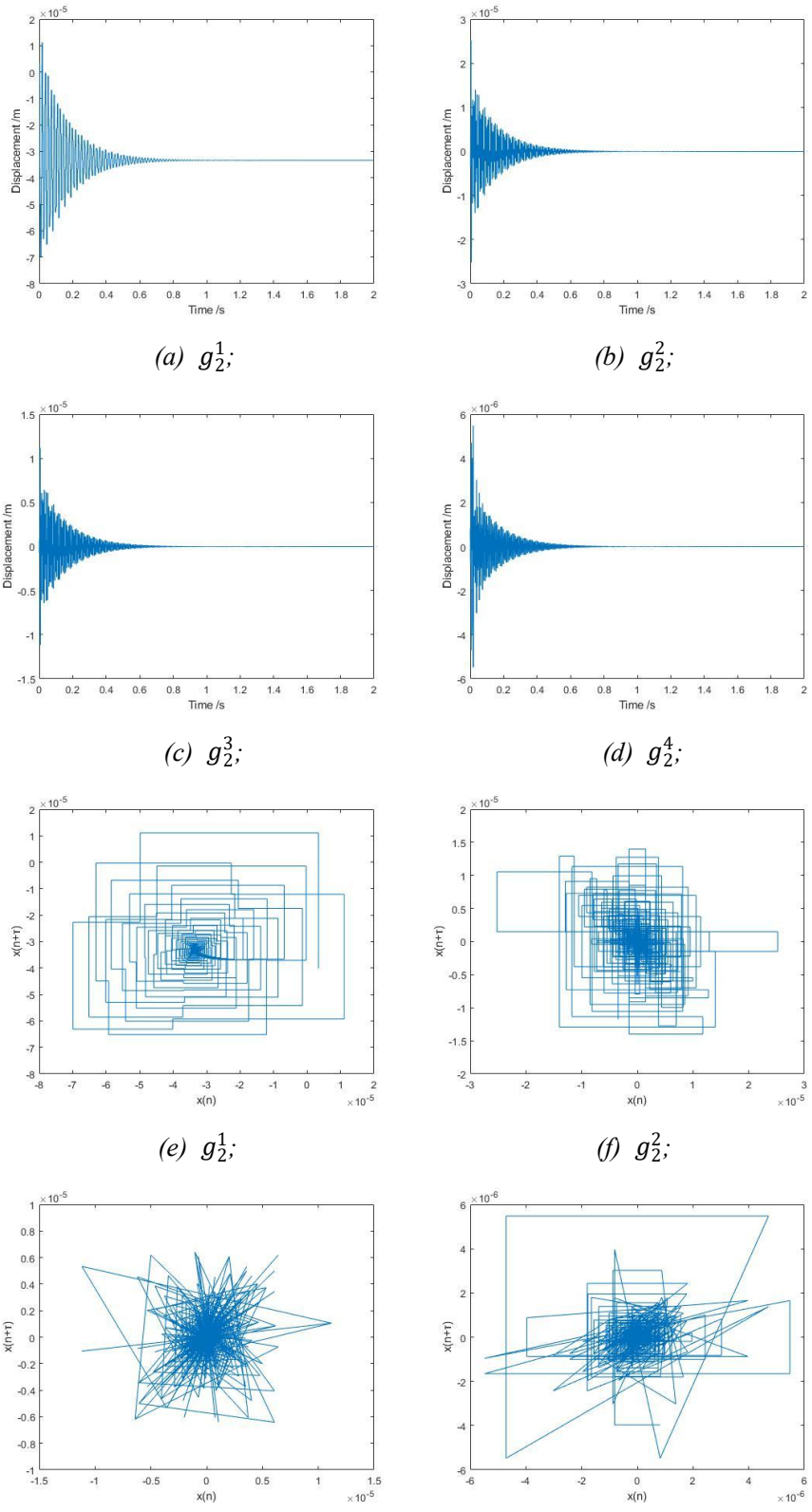

(a) g_2^1; *(b)* g_2^2;

(c) g_2^3; *(d)* g_2^4;

(e) g_2^1; *(f)* g_2^2;

(g) g_2^3; *(h)* g_2^4;

Figure 5-5 The time domain sub-signal (a-d) and phase space topology (e-h) of each sub-signals from the undamaged beam.

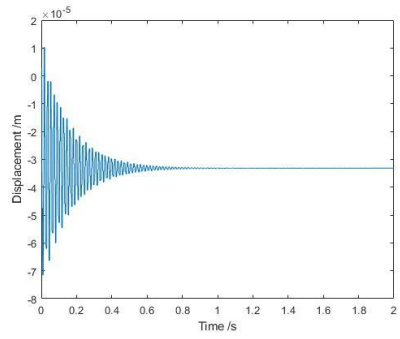

(a) g_2^1;

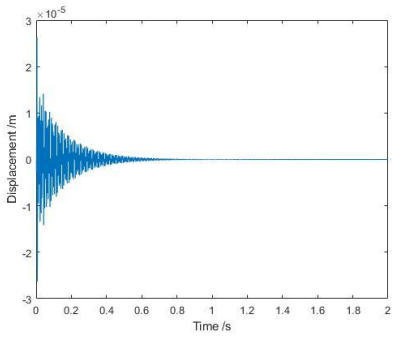

(b) g_2^2;

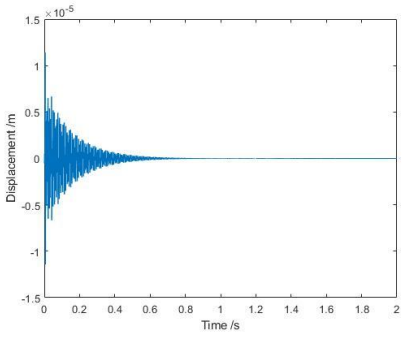

(c) g_2^3;

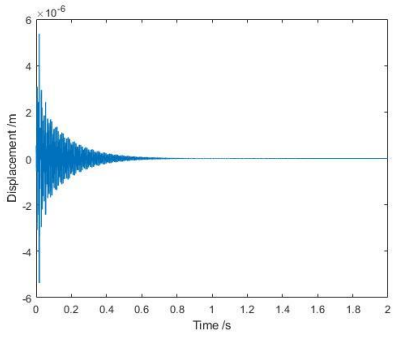

(d) g_2^4;

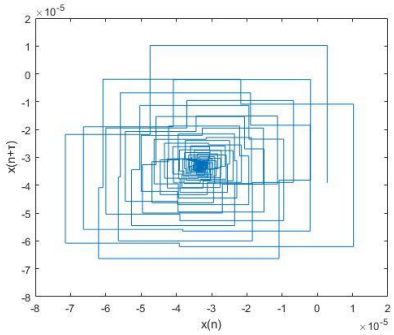

(e) g_2^1;

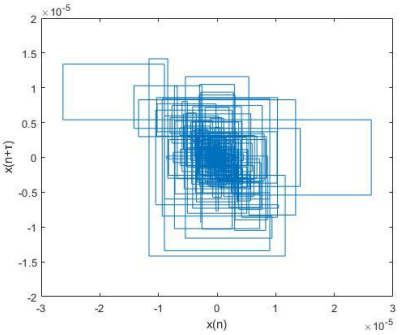

(f) g_2^2;

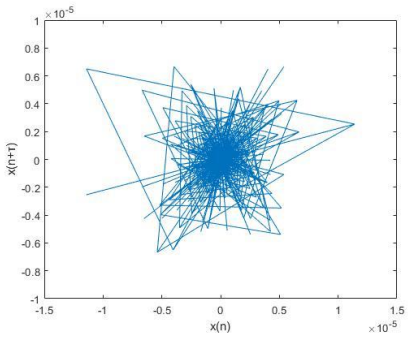

(g) g_2^3;

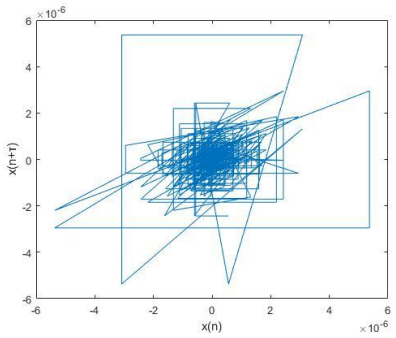

(h) g_2^4;

Figure 5-6 The time domain sub-signal (a-d) and phase space topology (e-h) of each sub-signals from the beam with delamination size $a/L = 0.1$.

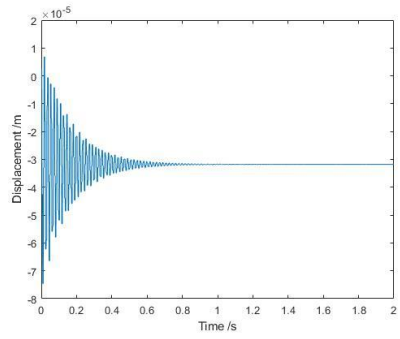

(a) g_2^1;

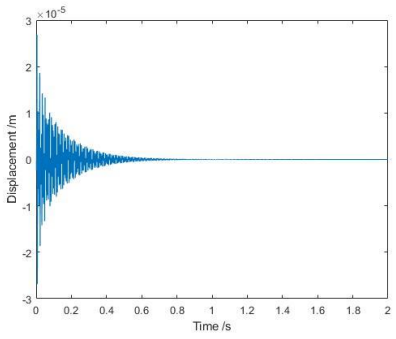

(b) g_2^2;

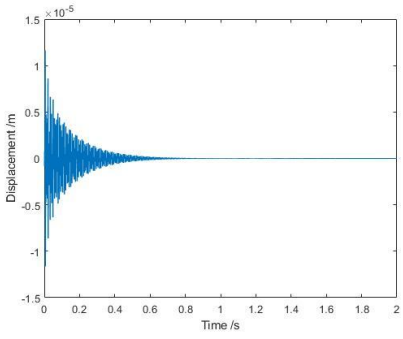

(c) g_2^3;

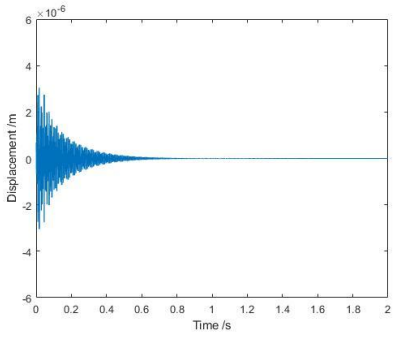

(d) g_2^4;

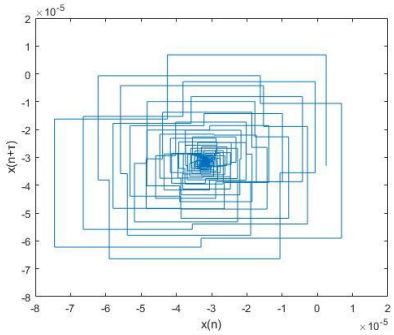

(e) g_2^1;

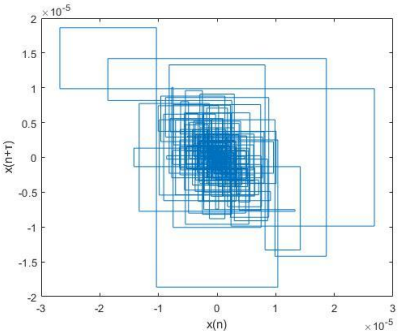

(f) g_2^2;

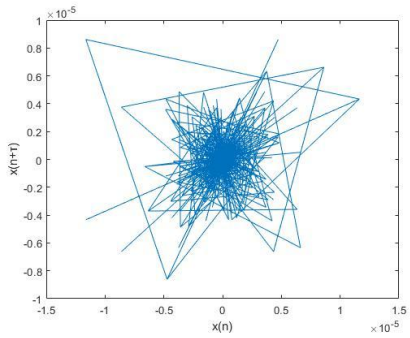

(g) g_2^3;

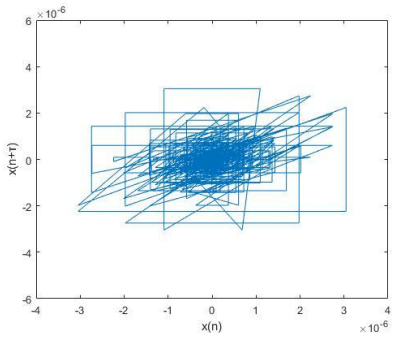

(h) g_2^4;

Figure 5-7 The time domain sub-signal (a-d) and phase space topology (e-h) of each sub-signals from the beam with delamination size $a/L = 0.2$.

Based on Figures 5-5 to 5-7, the shape of the phase space topology from all sub-signals has been changed from different situations due to the change of frequency and amplitude of signals generated by various delamination sizes in all frequency ranges of structural vibration responses. While the shape of g_2^2, g_2^3, and g_2^4 has a clear change which is due to the sub-signals with various frequencies have different sensitivity to the delamination size. It should be also noted that the size of the phase space topology structures of g_2^4 decrease clearly, which means the energy of this sub-signal decrease. The changing trend of CPST ratio is calculated by equation (5-13) and shown in Figure 5-8:

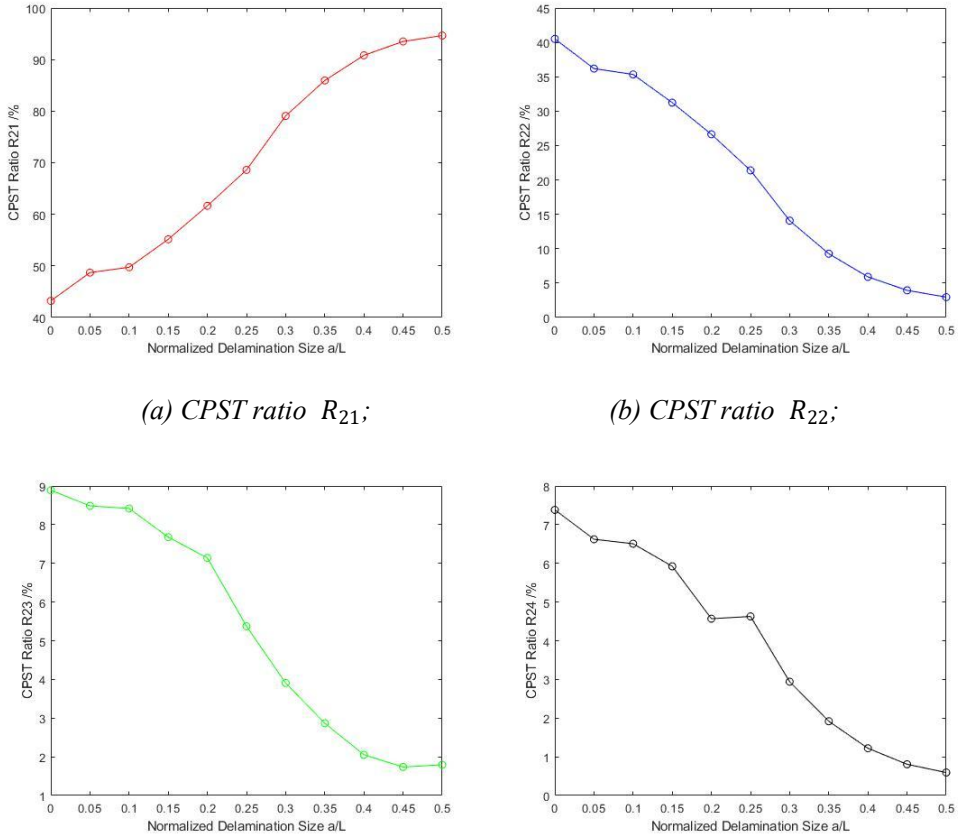

(a) CPST ratio R_{21}; *(b) CPST ratio R_{22};*

(c) CPST ratio R_{23}; *(d) CPST ratio R_{24};*

Figure 5-8 The changing trend of CPST ratio from each sub-signal from beams with different size delamination.

Figure 5-8 indicates that the CPST ratio is affected by delamination in the beam. However, the change trend and value are different from sub-signals. The CPST ratio R_{21} from sub-signal g_2^1 will increase with delamination size becoming larger, while the CPST ratio R_{22}, R_{23} and R_{24} are decreasing. There are two reasons for this phenomenon. First, the delamination will reduce the frequency which the sub-signal frequency range is fixed. Therefore, the energy will transform from the high-frequency sub-signals into the low-frequency sub-signal which will enhance the energy ratio and size of the phase space topology of the low-frequency sub-signals, while the energy and size of the phase space topology of high-frequency sub-signals will decrease. Second, the natural frequencies of sub-signals will be affected by the delamination, which will change the shape of the phase space topology from sub-signals and enhance the CPST. Therefore, the CPST ratio R_{22}, R_{23} and R_{24} will decrease with small fluctuation due to the high-frequency signals being more sensitive to the delamination as mentioned in Chapter 3, while the R_{21} will increase with delamination size increasing.

Moreover, due to the energy contribution mentioned in reference [198], it should be noted that the change of CPST ratio R_{21} and R_{22}, which are from 45% to 95% and 40% to 4%, respectively, is much larger than R_{23} and R_{24}, which are from 9% to 1.8% and 7.5% to 0.6%, respectively.

5.2.2 Delamination Depth Assessment

Then, the delamination depth to the top surface of samples was

investigated based on the proposed method. The delamination size was set as $a = 0.1L$ and in the mid-span ($L_1 = L/2$). The result is shown in Table 5-4:

Table 5-4 The CPST of sub-signals with different delamination depths.

Normalized Delamination Depth H_2/H	**g_2^1(×10^{-8})**	**g_2^2(×10^{-8})**	**g_2^3(×10^{-8})**	**g_2^4(×10^{-8})**
0	8.7557	8.4138	1.8882	1.5538
0.05	9.1773	5.1873	1.3163	0.98975
0.10	12.460	8.1481	1.9290	1.5140
0.15	12.769	8.2243	1.9385	1.5034
0.20	12.944	8.2140	1.9423	1.5232
0.25	12.879	8.0994	1.8844	1.4938
0.30	13.287	8.2019	1.9580	1.5441
0.35	13.499	8.2253	1.9602	1.5547
0.40	13.883	8.2516	1.9497	1.5576
0.45	13.899	8.1533	1.9382	1.5175
0.50	14.076	8.2569	1.9543	1.5682

Based on Table 5-4, it indicates that the value of CPST from different sub-signals are different. The CPST of g_2^1 is larger than others due to the distribution of energy from the original signal which is mainly in the low-frequency range[198]. However, the change of CPSTs generated by delamination depth is smaller than the delamination size as shown in Table 5-3. For example, the CPST of g_2^1 just increases from 8.7557 to 14.076 with delamination depth from 0 to 0.5Hz, which the CPST value of g_2^1 is from 10.383 to 193.74. This is due to the less effect of delamination depth than delamination size as observed in Chapter 3. The time domain sub-signals and

phase space topology of sub-signals are shown in Figures 5-9 to 5-11:

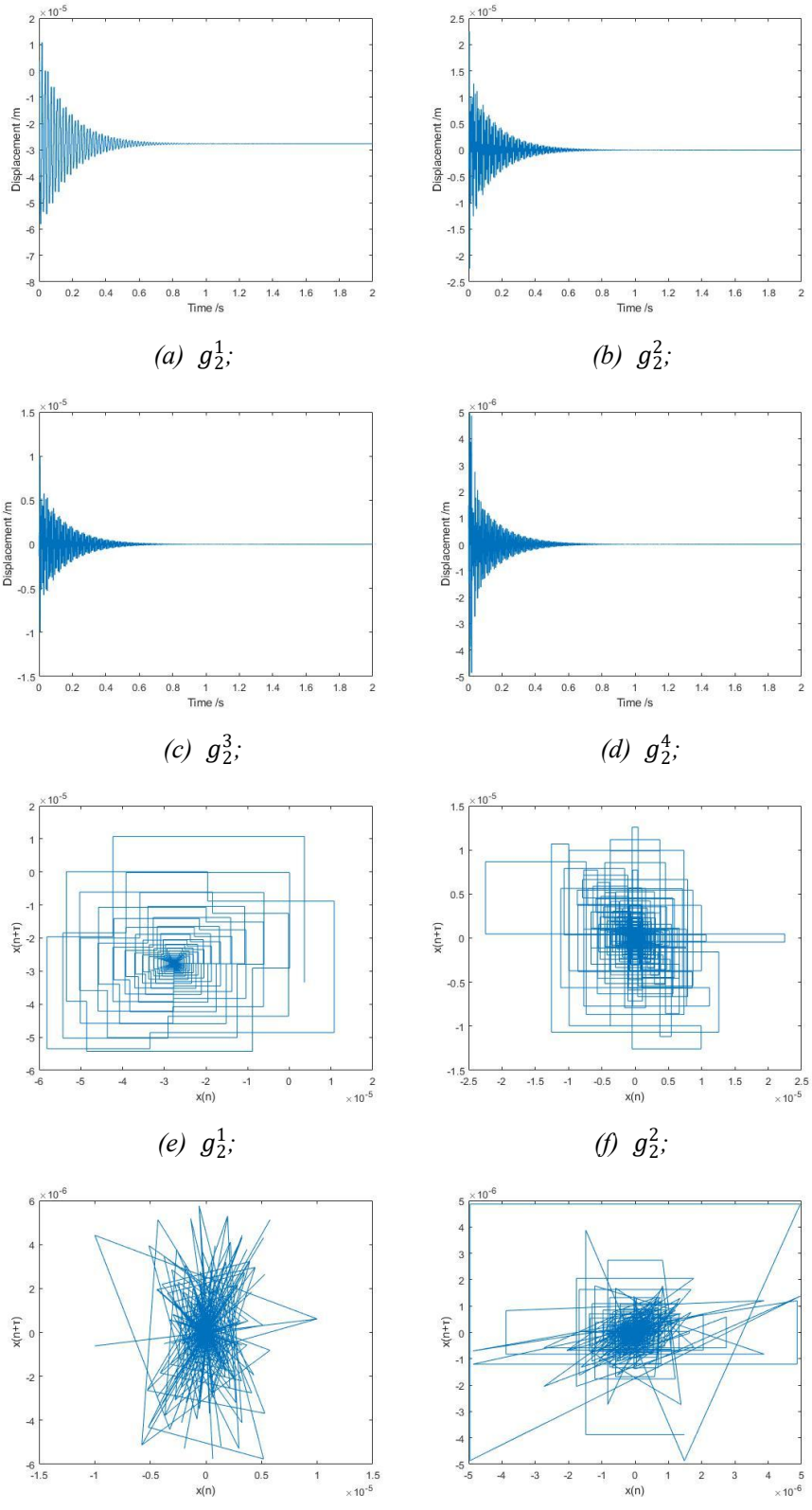

(a) g_2^1; *(b)* g_2^2;

(c) g_2^3; *(d)* g_2^4;

(e) g_2^1; *(f)* g_2^2;

(g) g_2^3; *(h)* g_2^4;

Figure 5-9 The time domain sub-signal (a-d) and phase space topology (e-h) of each sub-signals from the undamaged beam.

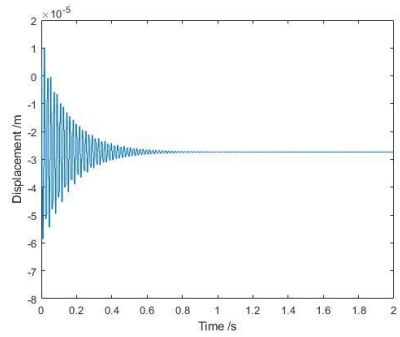

(a) g_2^1;

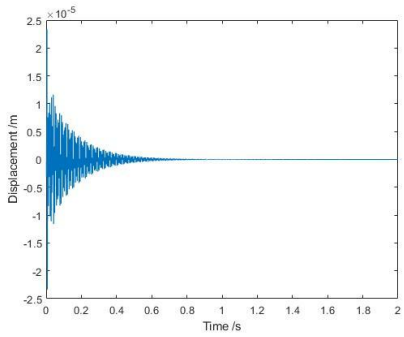

(b) g_2^2;

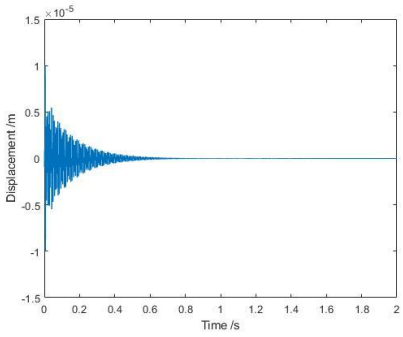

(c) g_2^3;

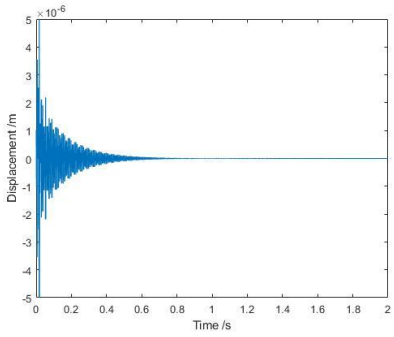

(d) g_2^4;

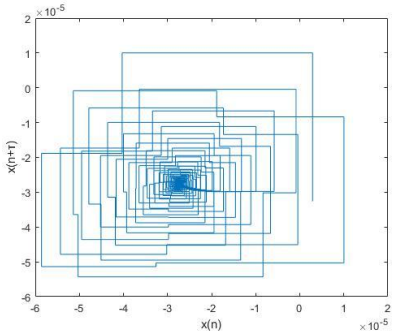

(e) g_2^1;

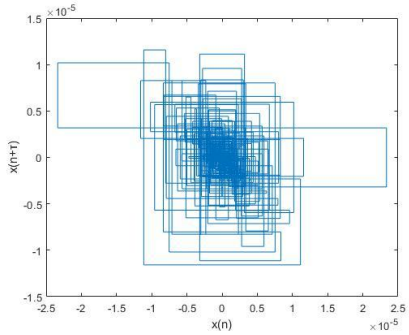

(f) g_2^2;

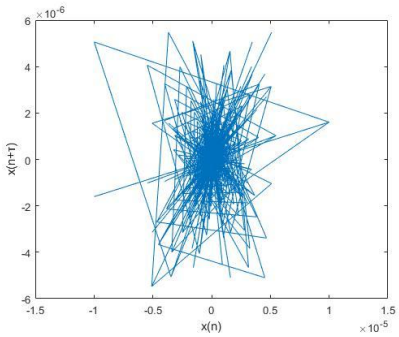

(g) g_2^3;

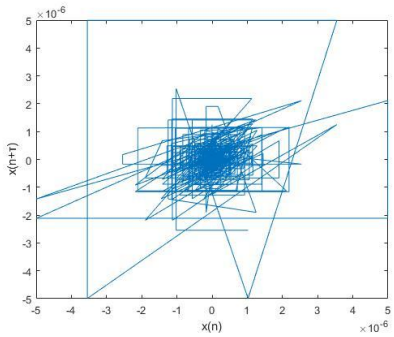

(h) g_2^4;

Figure 5-10 The time domain sub-signal (a-d) and phase space topology (e-h) of each sub-signals from the beam with delamination depth $H_2/H = 0.1$.

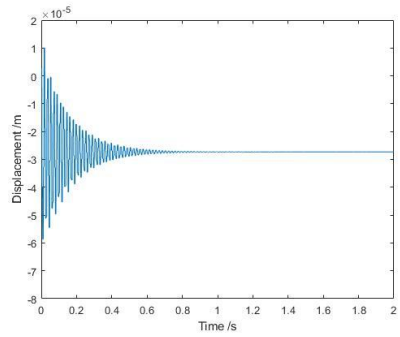

(a) g_2^1;

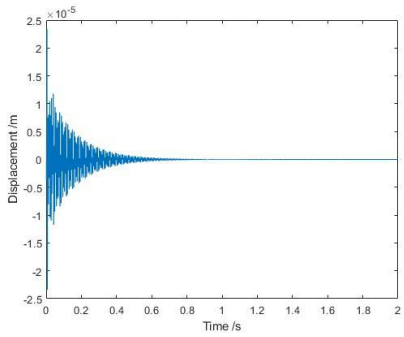

(b) g_2^2;

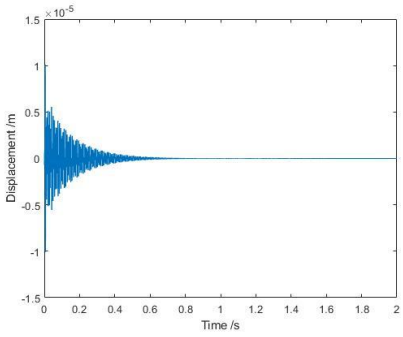

(c) g_2^3;

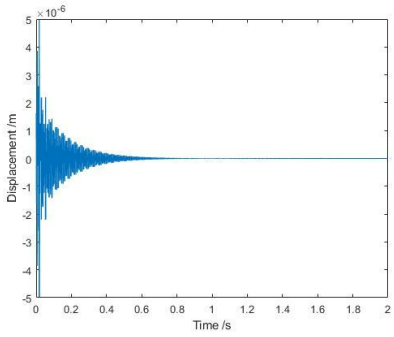

(d) g_2^4;

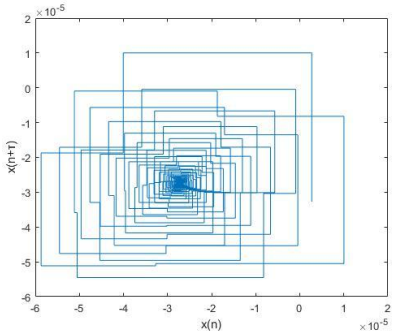

(e) g_2^1;

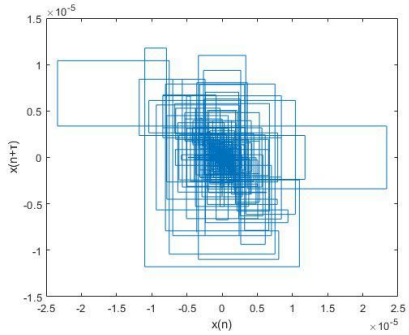

(f) g_2^2;

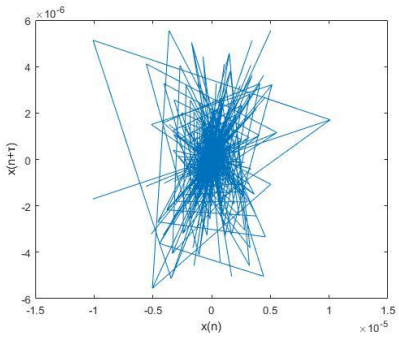

(g) g_2^3;

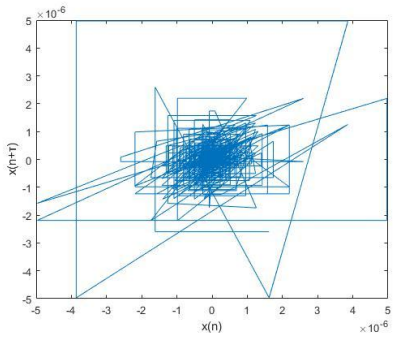

(h) g_2^4;

Figure 5-11 The time domain sub-signal (a-d) and phase space topology (e-h) of each sub-signals from the beam with delamination depth $H_2/H = 0.2$.

Based on Figures 5-9 to 5-11, the phase space topology of all sub-signals has changed with various delamination depths, while the change is not clear due to the little effect of delamination depth. Figures 5-9 and 5-10 show that there is a difference between the undamaged sample and the damaged sample, while the delamination depth affects the phase space topology small by comparing Figures 5-10 and 5-11. The changing trend of CPST ratio is calculated by equation (5-13) as shown in Figure 5-12:

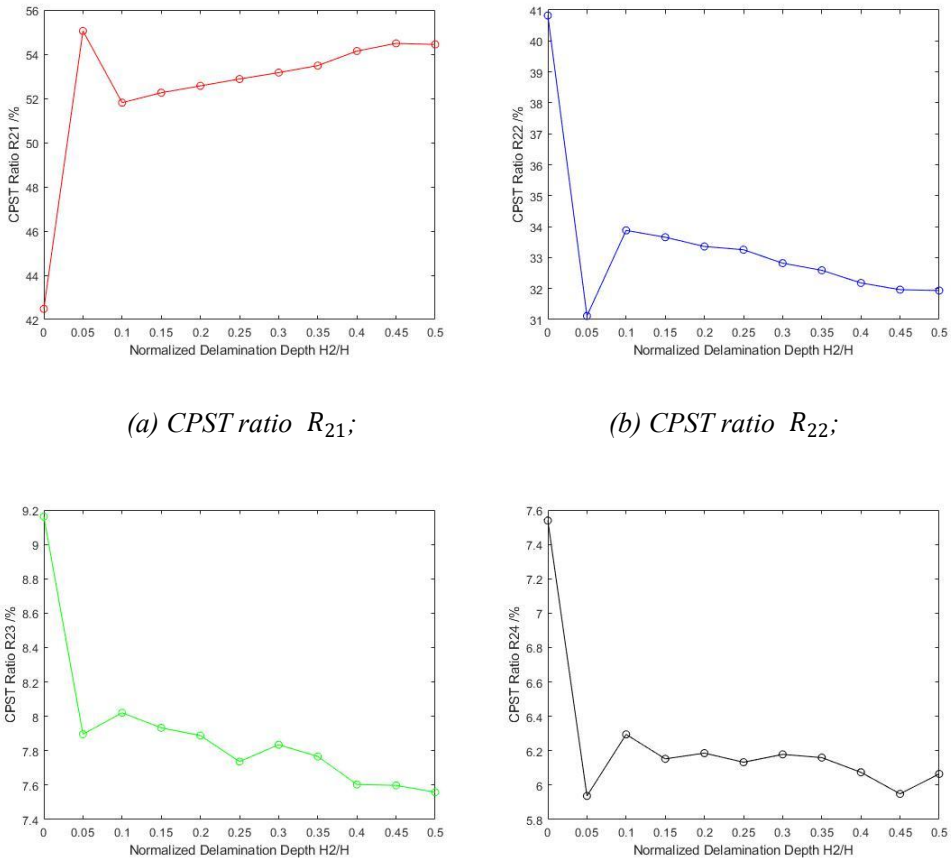

(a) CPST ratio R_{21}; *(b) CPST ratio R_{22};*

(c) CPST ratio R_{23}; *(d) CPST ratio R_{24};*

Figure 5-12 The changing trend of CPST ratio from each sub-signals from beams with different depth delamination.

Figure 5-12 shows the CPST ratio of g_2^1 is increasing with delamination

depth increasing, while other sub-signals are decreasing. This means the energy of the original signal is distributed more into sub-signal g_2^1 with delamination being deeper because of the frequency of sub-signals shifting. Moreover, there is fluctuation when the normalized delamination depth is between 0 to 0.1. The reason may be when the delamination is close to the surface, the effect of delamination on the vibration responses and characteristics fluctuates as indicated in Chapters 2 and 3. This can provide more information about the delamination compared with the result in Chapter 4. It also should be noted that the change ratio of R_{21} and R_{22} is larger with about 12% and 10% respectively, than R_{23} and R_{24}, which is 1.4% and 1.8%, due to the contribution of energy [198]. However, the change ratio is smaller than the delamination size because of the less effect of delamination depth.

5.3 Delamination Assessment for Laminated Panel

Furthermore, in this section, a model of a composite laminate with delamination damage was constructed by finite element software ABAQUS to evaluate the effectiveness of the proposed method in assessing delamination and investigate the effect of delamination in the composite plate structures. The detailed configuration of the composite laminate is shown in Figure 5-13. The rectangular laminate panel was clamped at one side creating a cantilever panel configuration and the panel was modeled using 8-node elements C3D8R. The dimensions of the panel were $320mm \times 300mm \times 3.96mm$ with 12 layers in

the laminates. The size of element resolution in the x-y section was 8mm, while for the damaged part, to improve the accuracy of calculation, the resolution was 1mm. The resolution of the elements in the x-z section was 0.33mm.

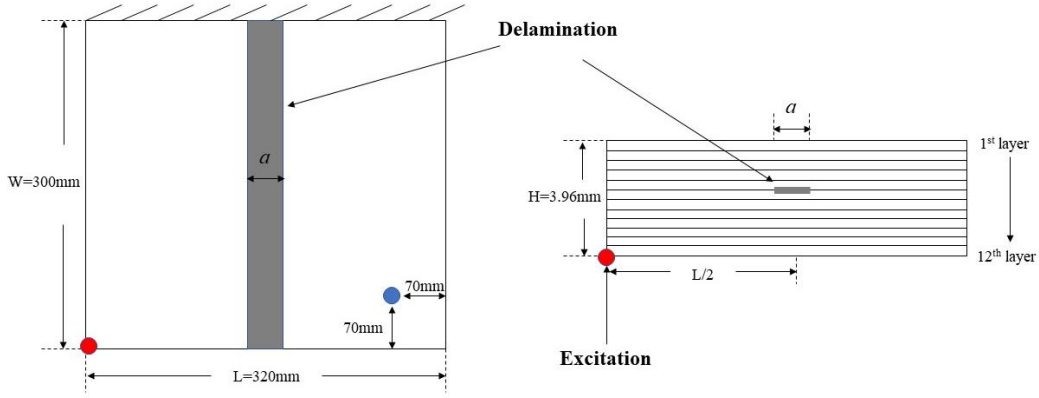

(a) Top View; *(b) Side View;*

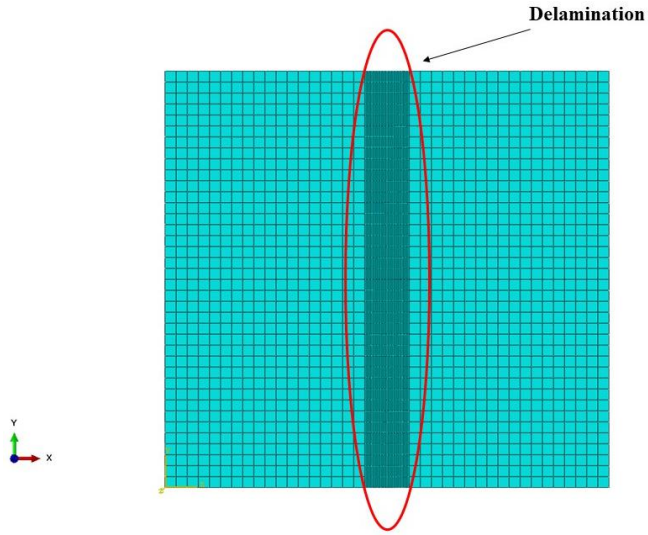

(c) Top View of ABAUQS model;

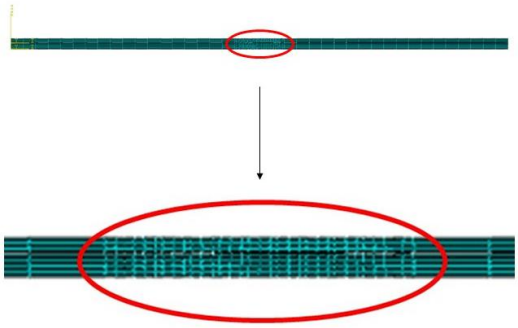

(d) Side View of ABAUQS model;

Figure 5-13 The model of a composite laminate with delamination.

The properties of laminate are described in Table 5-5, including the values for the elastic modulus (E_{ii}), shear modulus (G_{ii}), and Poisson ratio (v_{ii}) used in the simulation of a composite laminates panel.

Table 5-5 The properties of the composite laminate.

E_{11}(GPa)	E_{22}(GPa)	E_{33}(GPa)	G_{12}(GPa)	G_{13}(GPa)	G_{23}(GPa)	v_{12}	v_{13}	v_{23}
27	27	4.7	4.7	4.7	4.7	0.28	0.1	0.1

The delamination was set across the width of the panel and it was located in the middle of length as shown in Figure 5-13(a). The delamination was created by the cohesive surface interaction. The conditions of the simulation are the same as in Chapter 4, Section 4.3. The length of the delamination a showed in Figure 5-13(a) was changed to different values in the simulation. The sampling frequency is $f = 12794$ Hz. Therefore, the frequency range of wavelet packet decomposition is shown in Table 5-6:

Table 5-6 Frequency range of components.

Components number	Frequency /Hz
$\boldsymbol{g_2^1}$	0-1599.25
$\boldsymbol{g_2^2}$	1599.25-3198.5
$\boldsymbol{g_2^3}$	3198.5-4797.75
$\boldsymbol{g_2^4}$	4797.75-6397

5.3.1 Simulation

5.3.1.1 Delamination Size Assessment

In this simulation, the samples with different delamination size a were investigated. In this work, the delamination was located between the 5th and 6th layers. The CPST value was calculated to make a comparison for investigating their sensitivity to the size of delamination. The results are presented in Table 5-7:

Table 5-7 The CPST of sub-signal from laminate with different delamination size.

Delamination size *a*/mm	g_2^1	g_2^2	g_2^3	g_2^4
0	0.0782	0.0136	0.0033	4.8044×10^{-4}
16	0.1510	0.0133	0.0035	4.5077×10^{-4}
32	0.1598	0.0129	0.0038	4.0872×10^{-4}
48	0.1741	0.0120	0.0044	3.6426×10^{-4}
64	0.1793	0.0116	0.0048	3.2137×10^{-4}
80	0.1935	0.0109	0.0051	3.0565×10^{-4}
96	0.1953	0.0105	0.0056	2.5470×10^{-4}
112	0.1968	0.0102	0.0059	2.2545×10^{-4}
128	0.2321	0.0099	0.0061	2.2289×10^{-4}
144	0.2347	0.0100	0.0062	2.1870×10^{-4}
160	0.2415	0.0099	0.0065	2.7782×10^{-4}

The result in Table 5-7 shows that the CPST of g_2^1 is much larger than the

others as the same as the result of beam samples. This phenomenon indicates that the energy of the original signal is mainly distributed into sub-signal g_2^1, which means the vibration responses are concentrated in low-frequency ranges as same as the result in Section 5.2.1 and previous work [198]. It should also be noted that the CPSTs of the sub-signals from different cases are different due to the change of dynamic responses generated by various delamination sizes. The phase space topology of sub-signal is shown in Figures 5-14 to 5-16:

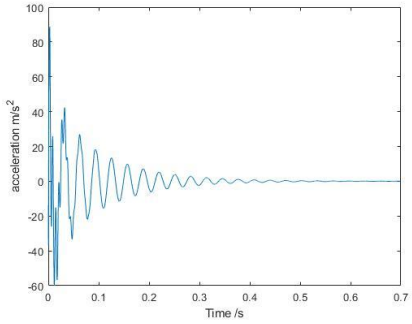

(a) g_2^1;

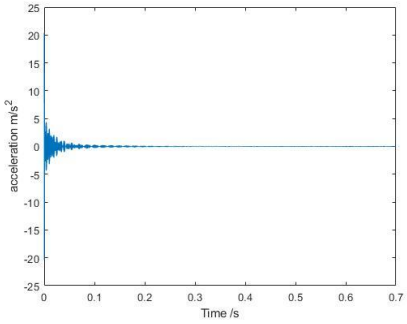

(b) g_2^2;

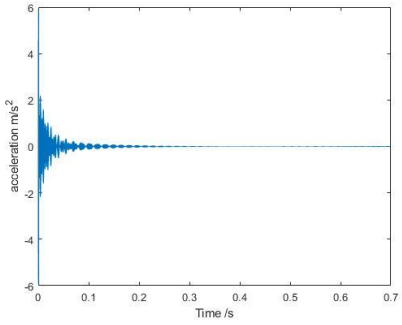

(c) g_2^3;

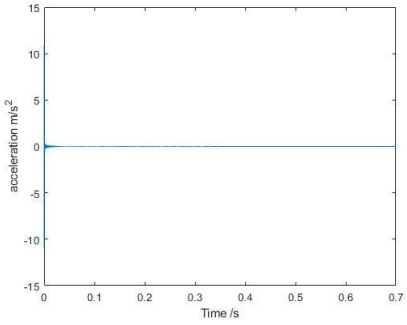

(d) g_2^4;

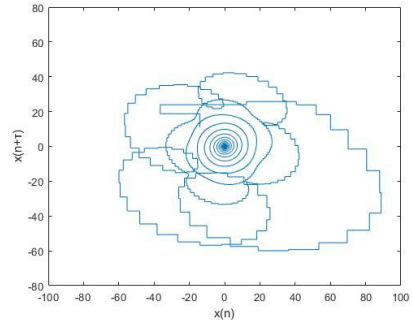

(e) g_2^1;

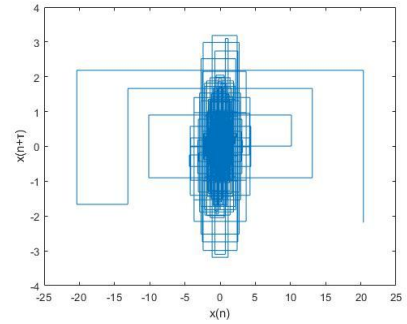

(f) g_2^2;

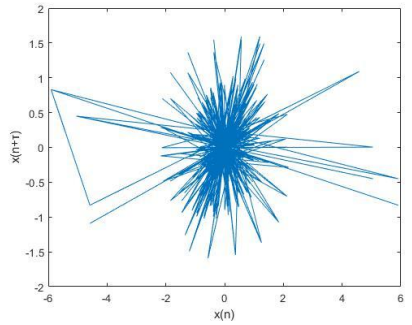

(g) g_2^3;

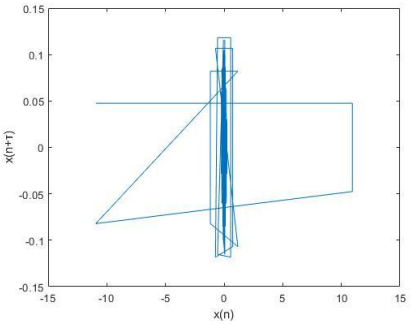

(h) g_2^4;

Figure 5-14 The time domain sub-signal (a-d) and phase space topology (e-h) of each sub-signal from undamaged laminate.

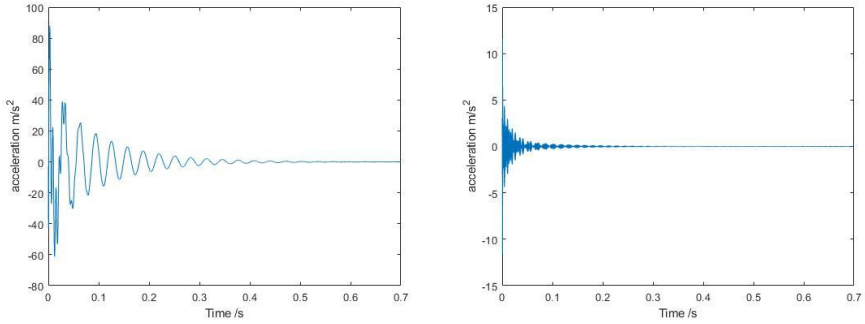

(a) g_2^1;

(b) g_2^2;

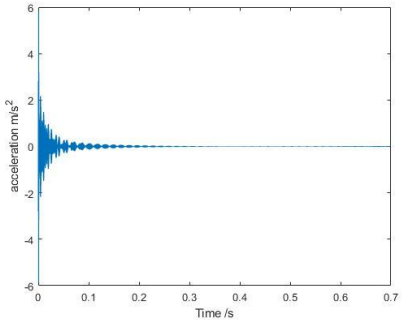

(c) g_2^3;

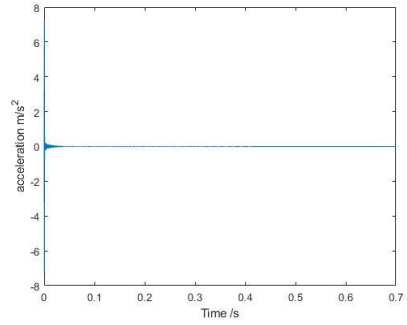

(d) g_2^4;

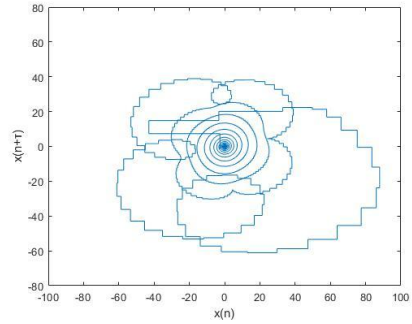

(e) g_2^1;

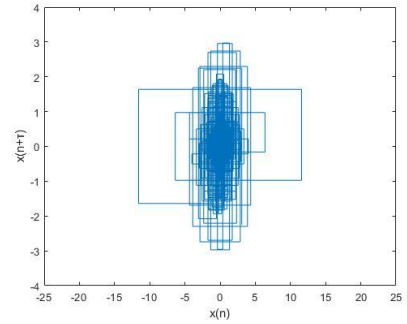

(f) g_2^2;

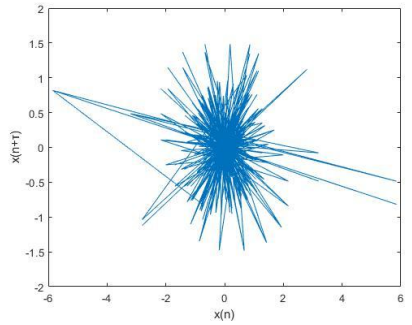

(g) g_2^3;

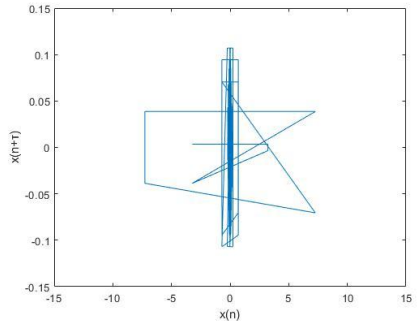

(h) g_2^4;

Figure 5-15 The time domain sub-signal (a-d) and phase space topology (e-h) of each sub-signal from laminate with a=16mm delamination.

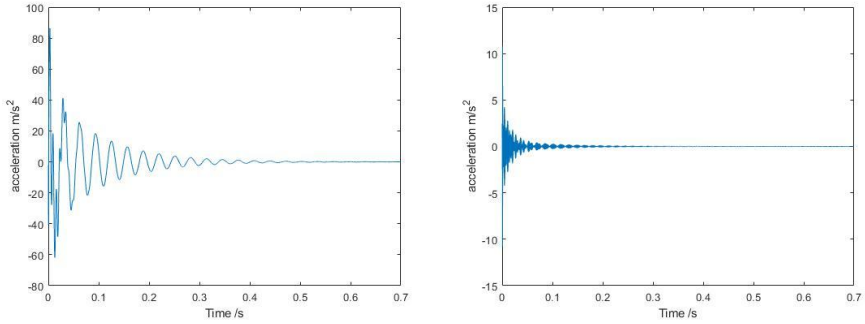

(a) g_2^1; *(b)* g_2^2;

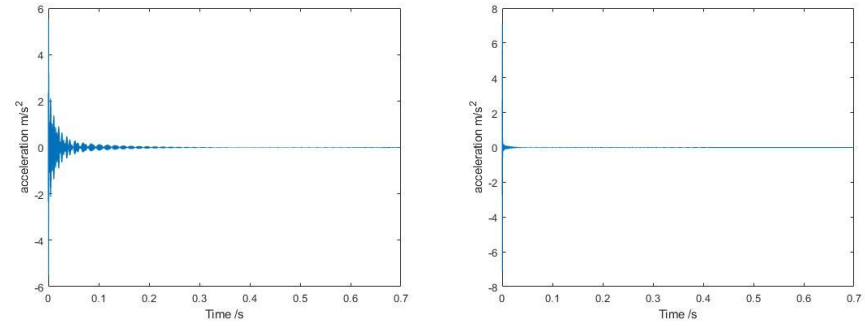

(c) g_2^3; *(d)* g_2^4;

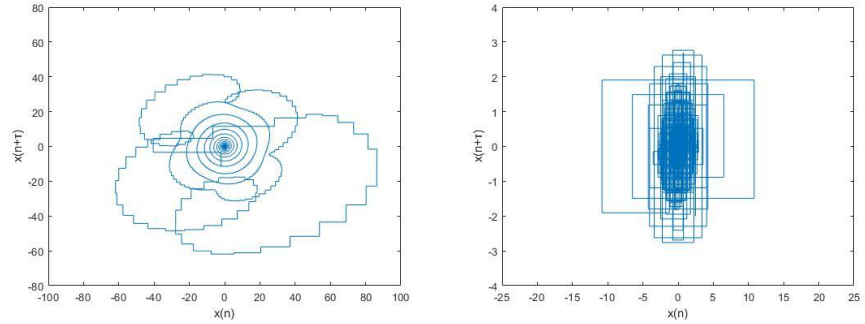

(e) g_2^1; *(f)* g_2^2;

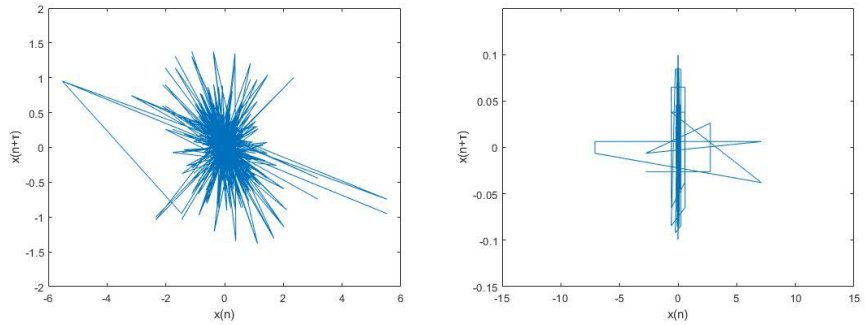

(g) g_2^3; *(h)* g_2^4;

Figure 5-16 The time domain sub-signal (a-d) and phase space topology (e-h) of each sub-signal from laminate with a=32mm delamination.

Based on Figures 5-14 to 5-16, the size of phase space topology from different sub-signals decreases with the size of delamination increases. The reason for this phenomenon is the change in the energy distribution and the frequency shifting of sub-signals. The size of the phase space topology structure is related to the amplitude of measured signals and vibration energy of the measured point in the intact part of delaminated samples, while these two factors are determined by the mode shapes of structure vibration. There will be some local modes in the delaminated part which will be distributed energy [43]. Therefore, the energy of the intact part will become smaller, which makes the phase space topology structure size smaller.

It also should be noted that the amplitude of the low-frequency sub-signal (g_2^1) is much larger than the high-frequency sub-signal (g_2^2, g_2^3 and g_2^4), which means the energy is mainly distributed into low-frequency sub-signals as mentioned in [198]. While based on (e)-(g) of Figures 5-14 to 5-16, it is clear that the phase space topology of all sub-signals from laminate with different size delamination has been changed. Both the shape and size of the phase space topology from all sub-signals are affected by delamination. The shape of the phase space topology is changed because the frequencies of sub-signals generated by the wavelet packet decomposition are changed. Figure 5-14 to 5-16 show that the shape of all phase space topology from all sub-signals are changed, which means the delamination affect all the natural frequencies. Moreover, the size is also changed due to that the energy ratio of

each mode is affected. The phase space topology of g_2^2, g_2^3, and g_2^4 become smaller with the delamination size increasing, which means the energy of these sub-signals is reduced. The ratio of CPST from each sub-signal is shown in Figure 5-17:

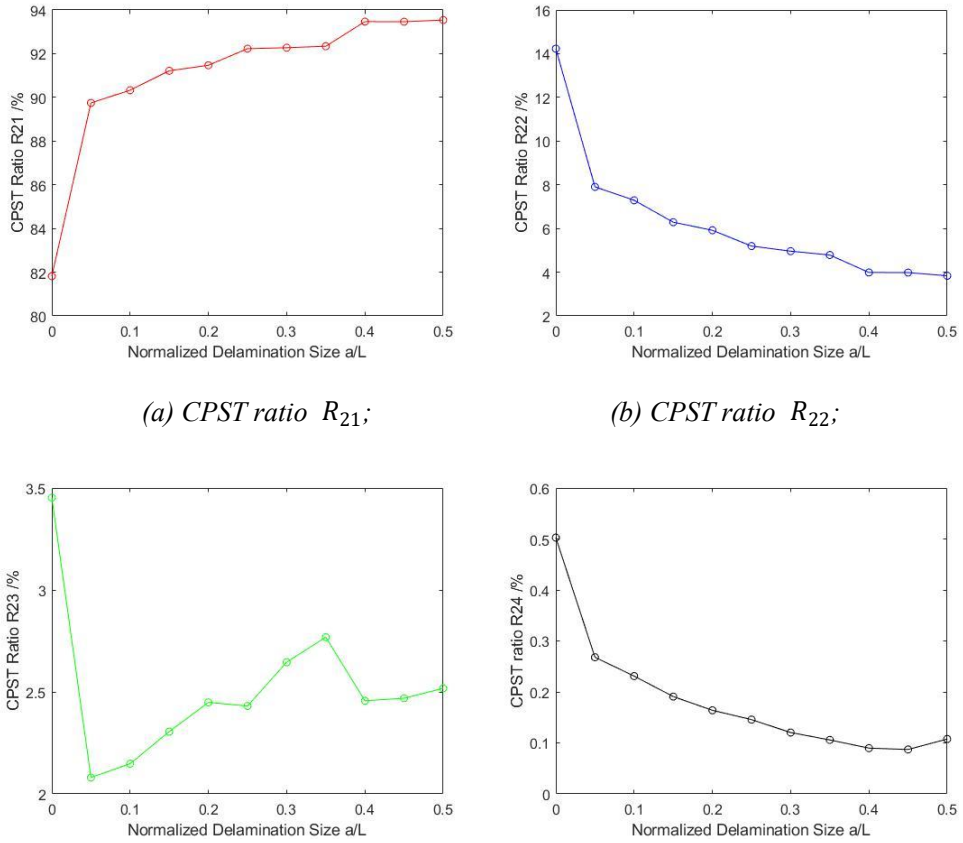

(a) CPST ratio R_{21}; *(b) CPST ratio R_{22};*

(c) CPST ratio R_{23}; *(d) CPST ratio R_{24};*

Figure 5-17 The changing trend of CPST ratio from each sub-signals from laminate with different delamination sizes.

Figure 5-17 shows that the CPST ratio of R_{21} increases with the size of delamination increasing from 82% to 94%, while the R_{22} and R_{24} decrease from 14% to 4% and 0.5% to 0.1% respectively. There are two reasons for this phenomenon. First, the energy ratio of the low-frequency sub-signal will increase with the original signal resonant frequency decreasing. Therefore, the

CPST ratio of g_2^1 will become larger while other components will decrease [45]. On the other side, the resonant frequencies of the sub-signals shift due to the delamination, which will change the modulus of structure. The reasons are mentioned in Section 4.2. A similar trend and phenomenon also can be found in previous work [137]. Moreover, it should be noted that the changing trend of R_{23} are fluctuating more compared with the result in Section 5.2.1. This means the dynamic responses of the composite plate structures are more complicated than the beam structures. However, the CPST ratio of R_{23} is small than 3.5%, so it will not affect the CPST of the original signal much. Therefore, the result in Section 4.3.1.1 has no similar phenomenon since the local information of this sub-signals with small energy and amplitude covered by the initinal signals. This result demonstrated the proposed method based on wavelet packet decomposition can improve the delamination assessment based on the phase space topology structures of dynamic responses.

Furthermore, the volume of the low-frequency range (R_{21} and R_{22}) was larger than the high-frequency range (R_{23} and R_{24}). The CPST ratio change of R_{21} and R_{22} are about 12% and 10% respectively, while the change range of R_{23} and R_{24} are from 1.5% and 0.4%. This indicates that the low-frequency sub-signals (R_{21} and R_{22}) are more sensitive to the delamination than the high-frequency sub-signals (R_{23} and R_{24}). This is because the energy of the original signal is distributed into g_2^1 and g_2^2 mainly [198].

5.3.1.2 The Analysis of the Robustness to the Noise

In the proposed method, the signals will be decomposed as several sub-signals, some of which will be with high-frequency ranges. These signals will be easier affected by the noise due to the small energy of these sub-signals. The resistance to the noise and disturbance of the proposed method was investigated in this section. The signal-noise ratio (SNR) was set 3 levels (no noise, SNR=10dB, SNR=5dB). The noise is Additive White Gaussian Noise provided by MATLAB software. Figures 5-18 to 5-20 show the phase space of each sub-signals with different noise situations.

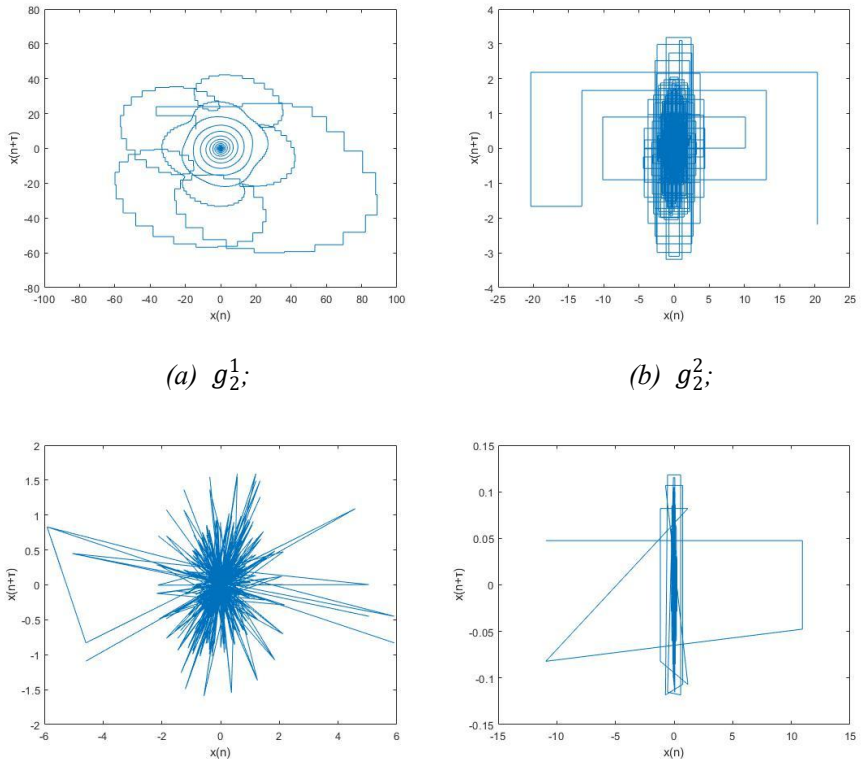

(a) g_2^1; *(b)* g_2^2;

(c) g_2^3; *(d)* g_2^4;

Figure 5-18 The phase space of sub-signals without noise.

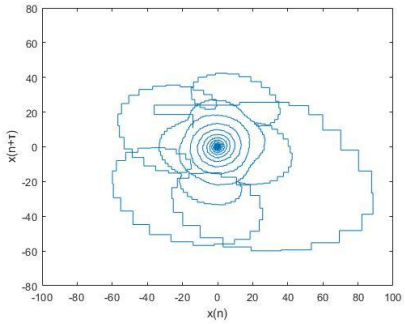

(a) g_2^1;

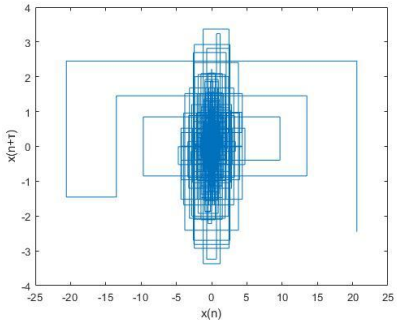

(b) g_2^2;

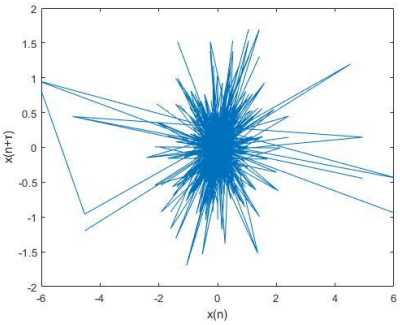

(c) g_2^3;

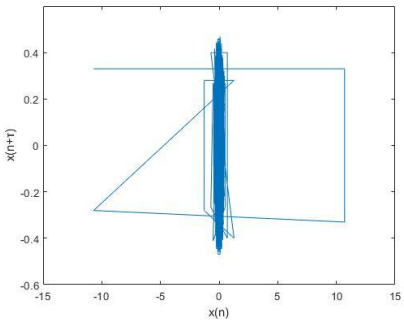

(d) g_2^4;

Figure 5-19 The phase space of sub-signals with noise (SNR=10dB).

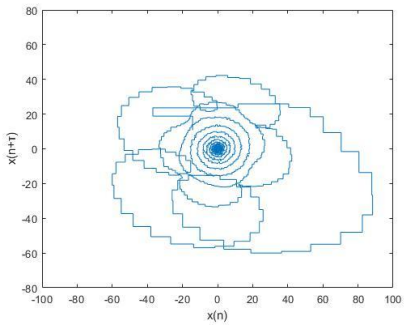

(a) g_2^1;

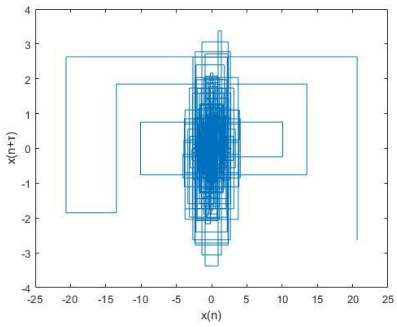

(b) g_2^2;

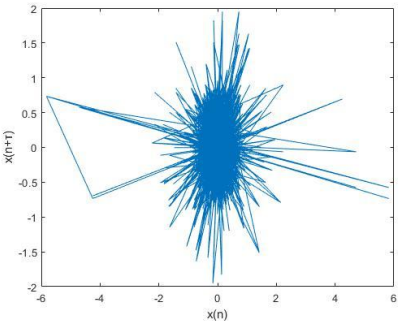

(c) g_2^3;

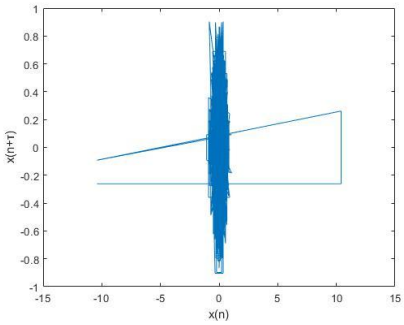

(d) g_2^4;

Figure 5-20 The phase space of sub-signals with noise (SNR=5dB).

Based on the figures above, it is clear that the noise effect on phase space of the high-frequency range (g_2^3 and g_2^4) is larger than the low-frequency range (g_2^1 and g_2^2). This illustrates that the low-frequency range sub-signals are more resistant to the noise than the high-frequency range sub-signals. This is because the energy and amplitude of high-frequency sub-signals are small which is easier to be covered by noise. Moreover, the noise mainly contributes to the high-frequency sub-signals and adds the energy of high-frequency sub-signals. However, the shape of the phase space topology structure is still similar which is just related to the frequency of the useful signal. The phase space structures of noise are different due to different frequencies so it will not change the shape of phase space structures. Therefore, the effect of the noise on the proposed method based on phase space topology analysis is small. These properties make this proposed method resistant to noise. The CPST ratio changing trend with different signal-noise ratio (SNR) was also calculated. The result is showed as follows:

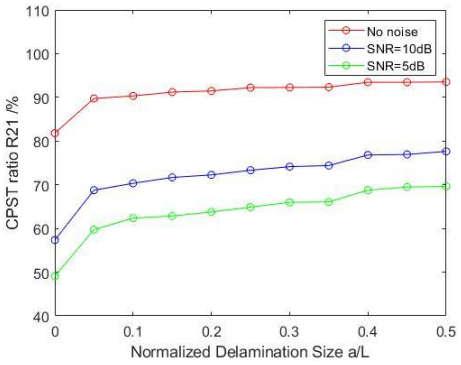

(a) CPST ratio R_{21};

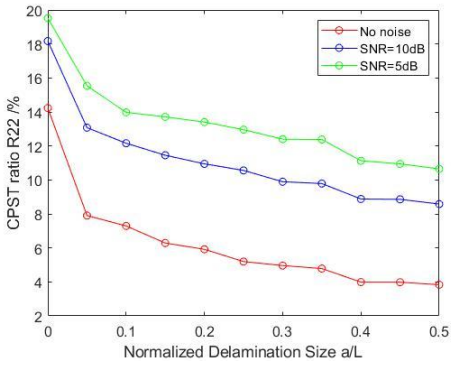

(b) CPST ratio R_{22};

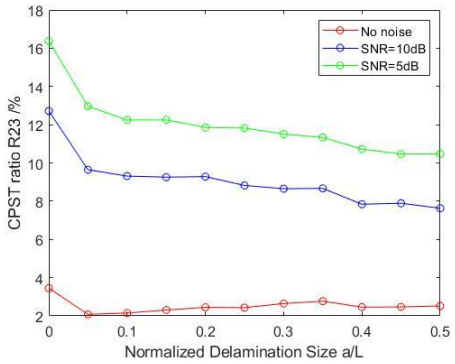

(c) CPST ratio R_{23};

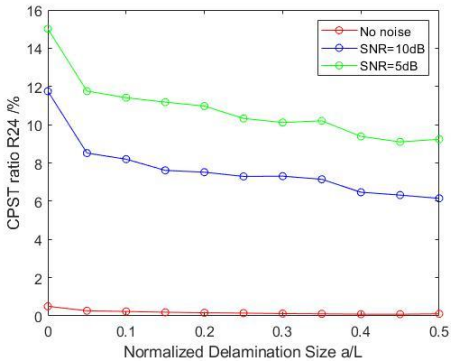

(d) CPST ratio R_{24};

Figure 5-21 The changing trend of CPST ratio from each sub-signal with different noise levels.

Based on Figure 5-21, the CPST ratio of all sub-signals is affected by noise and the effect of different sub-signals is various. The noise reduces the CPST ratio R_{21} and enhance the R_{22}, R_{23} and R_{24}. Because the energy of noise is most in high-frequency ranges. It can increase the energy ratio of high-frequency sub-signals, which makes the CPST ratio of high-frequency sub-signals larger due to more energy and larger amplitude. However, it should be noted that the changing trend affected by the noise of R_{21}, R_{22} and R_{24} is the same without the noise effect by comparing Figure 5-17 and

Figure 5-21. This is because the CPST is the average of all the data, which can eliminate the effect of noise. This result shows the robustness of the proposed method to the noise and disturbance.

5.3.2 Experiment

To verify the finite element models and validate the proposed method for delamination detection, carbon fiber reinforced epoxy (CFRP) plates with embedded delamination were manufactured to test the proposed method by experiments in this section. Figure 5-22 showed the arrangement of the experiment:

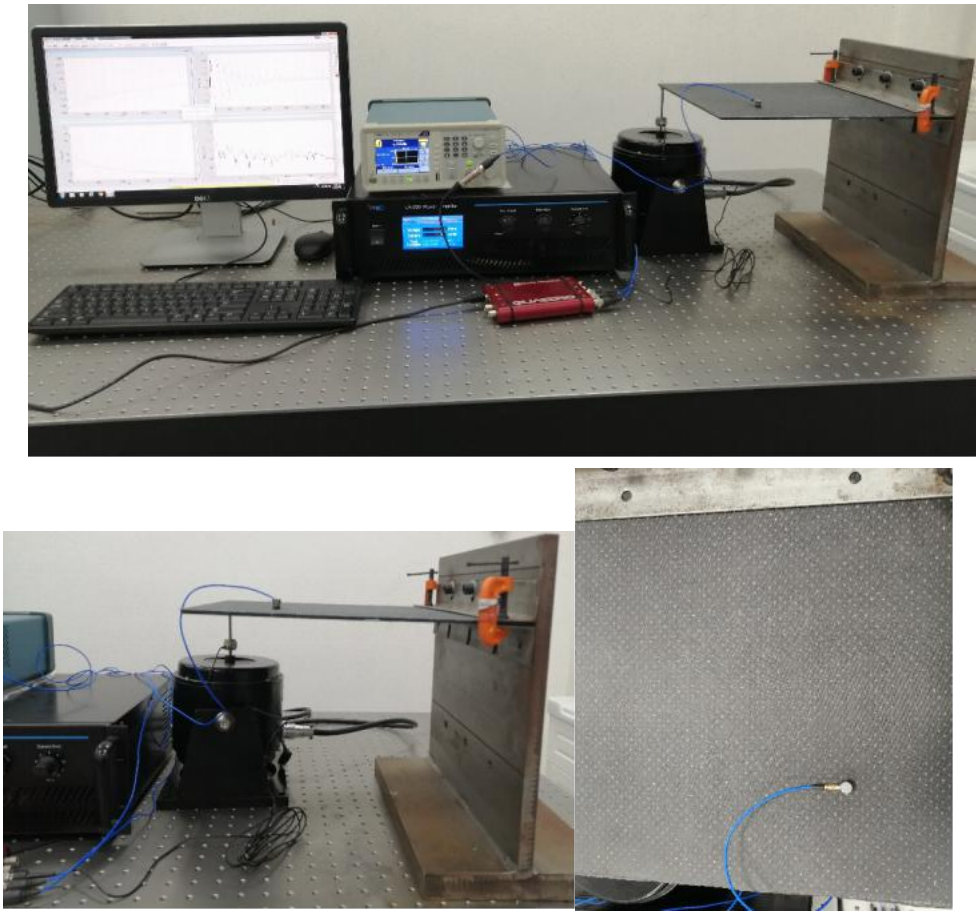

Figure 5-22 The arrangement of the experiment.

The vibration signal was measured by PCB 352C65 accelerometer and SignalCalc Ace from Data Physics on the location shown in Figure 5-13(a) by

blue point. A MS-200 shaker and LA-200 Power Amplifier with AFG1022 Arbitrary Function Generator were used to generate impulse excitation into the structure in the location shown in Figure 5-13(a) by the redpoint. For the sample, Polytetrafluoroethylene (PTFE) film was embedded into the panel to make delamination. The samples are shown in Figure 5-13:

(a) Sample No.1; *(b) Sample No.2;* *(c) Sample No.3;*

Figure 5-23 The sample for experiments.

Three samples were made for the experiment as follows: 1. The laminate panel with no damage; 2. The size of delamination is 32×300mm; 3. The size is 64×300mm. Table 5-8 shows the feature of the experiment and the simulation:

Table 5-8 The CPST of sub-signal from cases with different delamination.

Sample No.	**Situation**	g_2^1	g_2^2	g_2^3	g_2^4
1	Undamaged	0.0412	0.0107	0.0048	9×10^{-4}
2	32×300mm	0.1765	0.0147	0.0072	15×10^{-4}
3	64×300mm	0.2481	0.0145	0.0069	10×10^{-4}

Based on Table 5-8, the distribution of CPST of the experiment is the same as the simulation is shown in Table 5-7, while the CPST of g_2^1 is the largest with the lowest frequency range due to the distribution of energy. The difference between CPSTs from different samples is clear, which means the proposed method is effective in experiments. It should also be noted that there is a difference between simulation and experiment, which is generated by the noise and details in the experiment, such as disturbance and conditions limitation. Figures 5-24 to 5-26 show the phase space topology of each sub-signal from different situations:

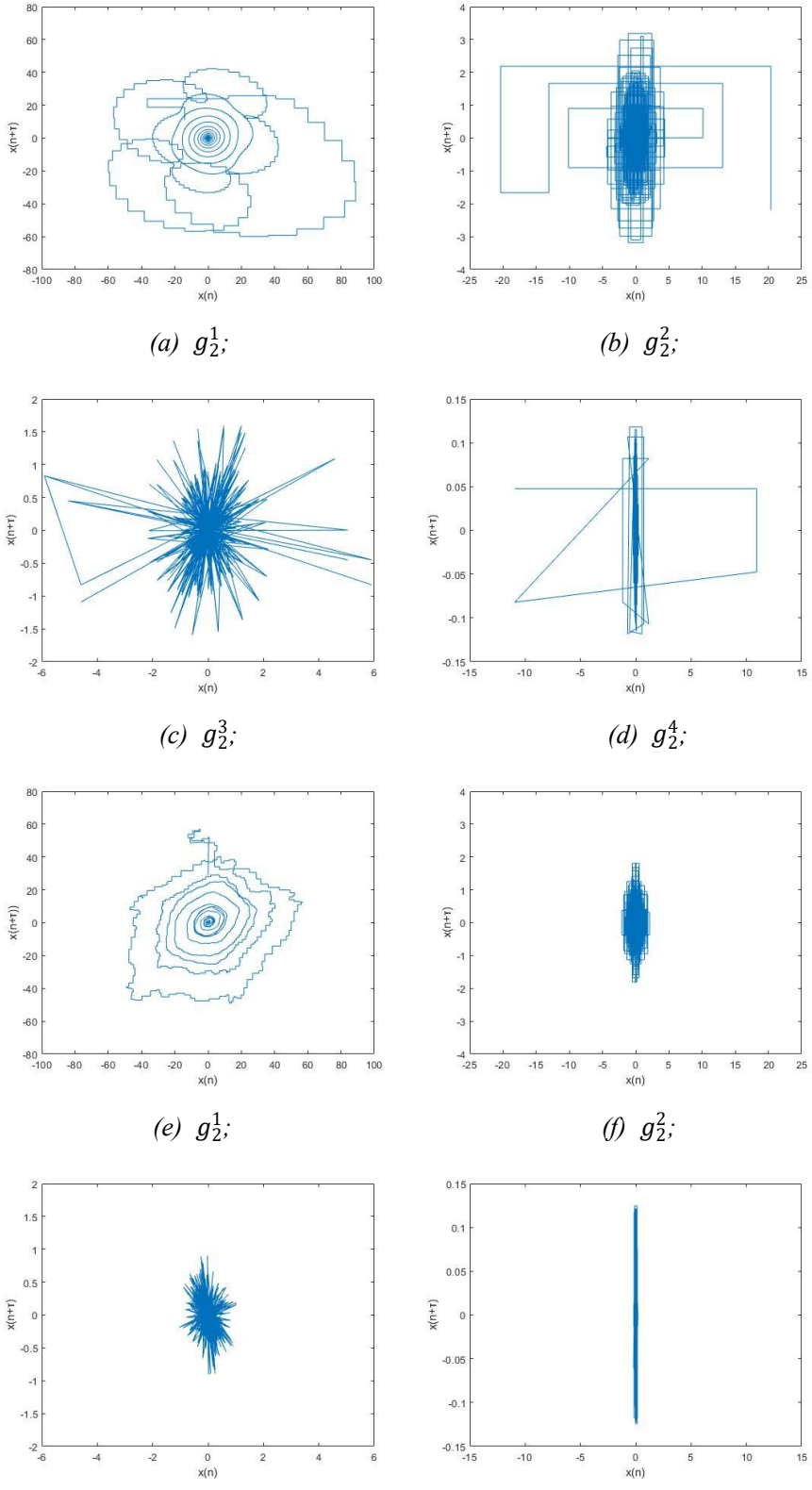

(a) g_2^1*;* *(b)* g_2^2*;*

(c) g_2^3*;* *(d)* g_2^4*;*

(e) g_2^1*;* *(f)* g_2^2*;*

(g) g_2^3*;* *(h)* g_2^4*;*

Figure 5-24 The phase space topology of each sub-signals from Sample No.1 (simulation (a-d) and experiment (e-h)).

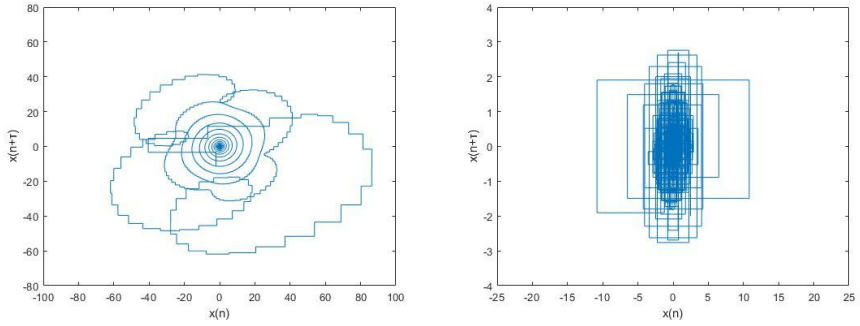

(a) g_2^1*;* *(b)* g_2^2*;*

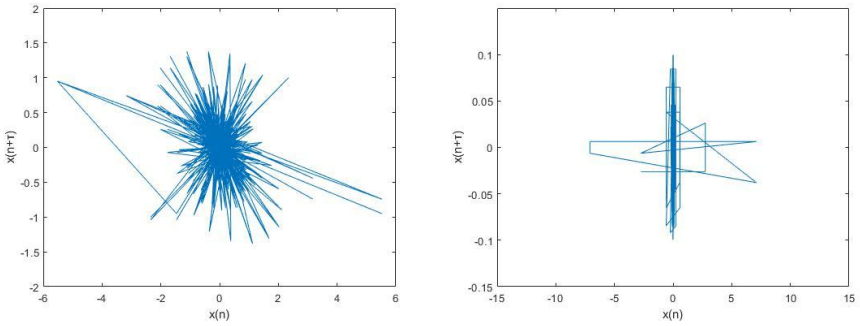

(c) g_2^3*;* *(d)* g_2^4*;*

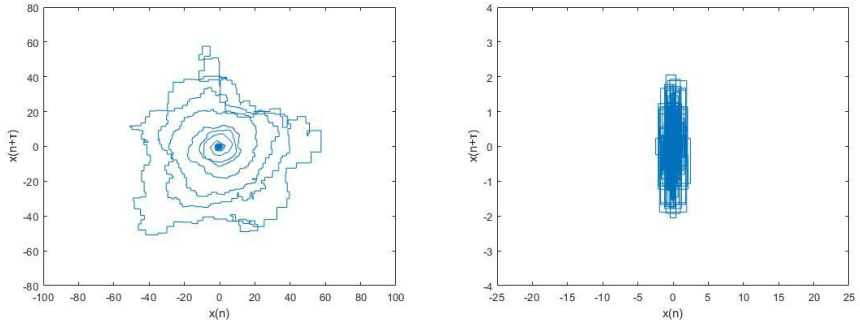

(e) g_2^1*;* *(f)* g_2^2*;*

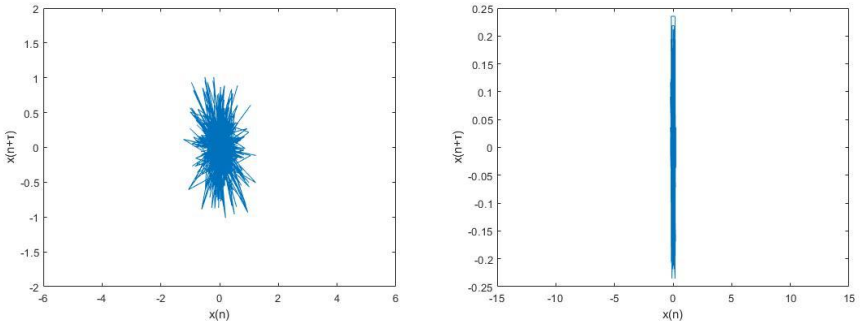

(g) g_2^3*;* *(h)* g_2^4*;*

Figure 5-25 The phase space topology of each sub-signals from Sample No.2 (simulation (a-d) and experiment (e-h)).

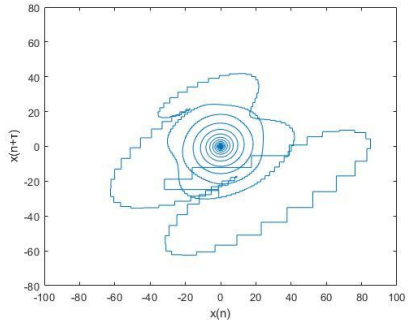

(a) g_2^1;

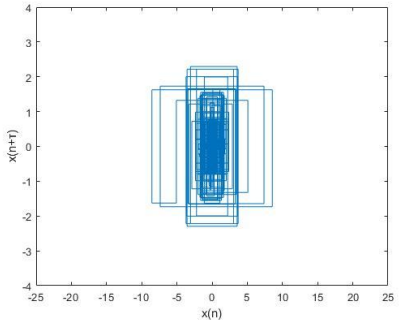

(b) g_2^2;

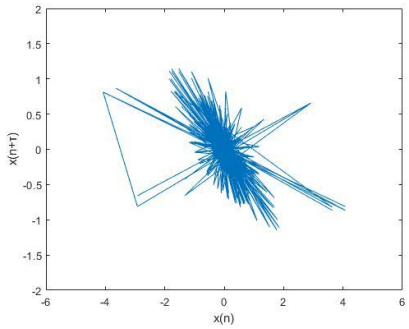

(c) g_2^3;

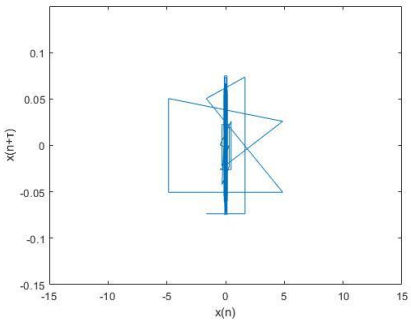

(d) g_2^4;

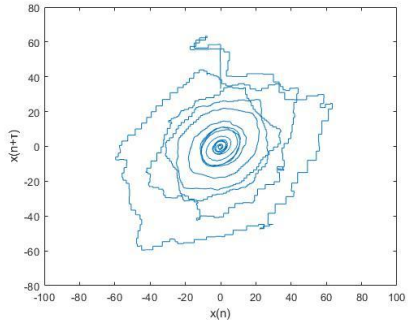

(e) g_2^1;

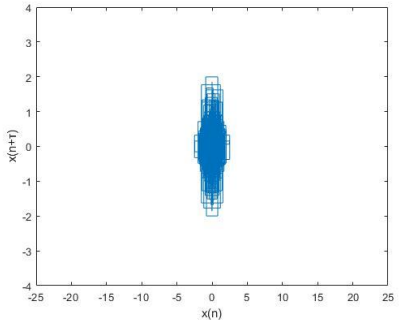

(f) g_2^2;

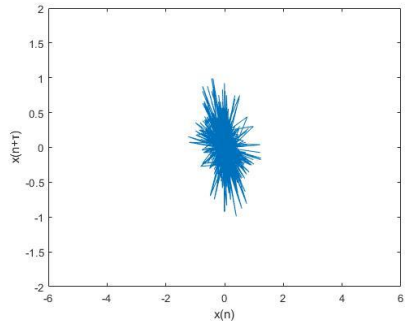

(g) g_2^3;

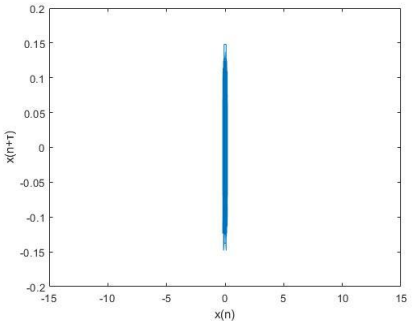

(h) g_2^4;

Figure 5-26 The phase space topology of each sub-signals from Sample No.3 (simulation (a-d) and experiment (e-h)).

Based on these phase space topology structures, the shape of sub-signals is similar both in simulation and experiment, which showed the credibility of the simulation. The size of the phase space structures of the simulation is larger than the experiment, which is due to a number of original signal data is lost in the experiment. The result of Section 5.3.2 shows that the disturbance will affect the phase space shape of each sub-signals. It also should be noted that the conditions in the experiment will have some differences from the simulation, which will generate errors. So the difference between simulation and experiment is accepted. Figure 5-27 shows the CPST ratio of each sub-signals both in simulation and experiment:

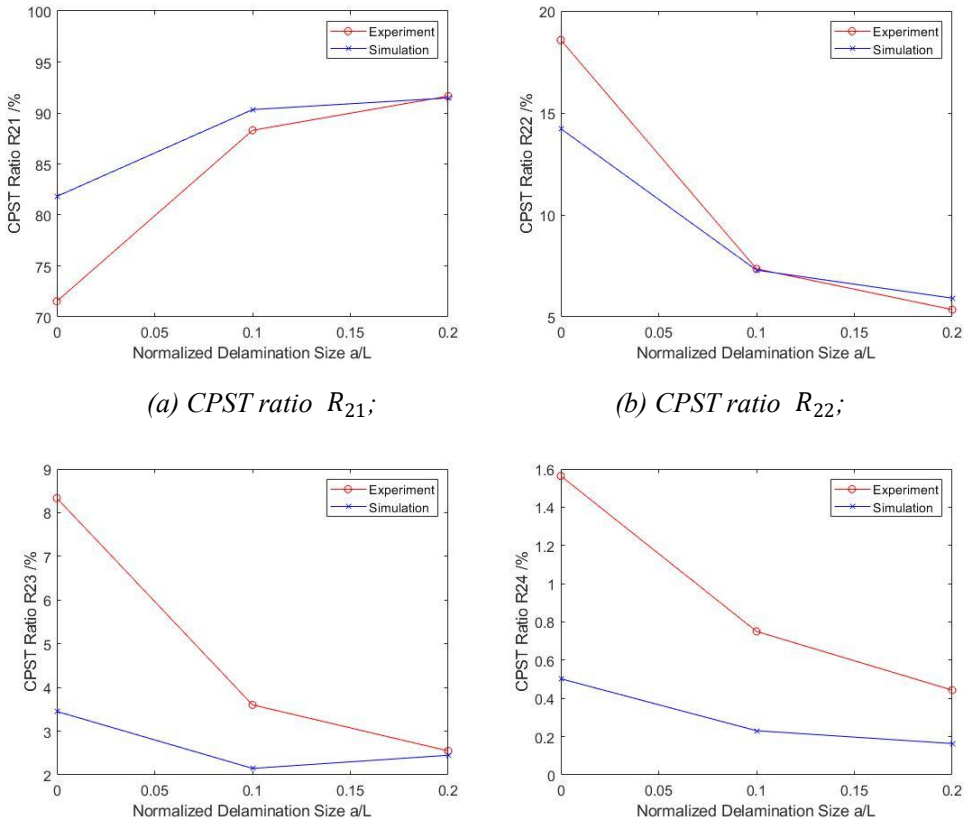

(a) CPST ratio R_{21}; *(b) CPST ratio R_{22};*

(c) CPST ratio R_{23}; *(d) CPST ratio R_{24};*

Figure 5-27 The changing trend of CPST ratio from each sub-signals from laminate with different delamination sizes.

Based on Figure 5-27, although there is some difference between experiment and simulation in value of CPST and CPST ratio, the changing trend of the CPST ratio from different sub-signals is the same both in experiment and simulation. Moreover, the change of the high-frequency range is larger than the low frequency which is also analyzed in previous sections. Considering the difference between experiment and simulation, the result is consistent, which demonstrated the credibility of the proposed method and features.

5.4 Conclusions

This work develops a method by combining the wavelet packet decomposition method combined with the phase space topology analysis method to analyze the vibration signal from a beam and a composite laminates panel to detect and analyze the delamination in these structures. The result shows the possibility and advantages of the proposed method for delamination identification and assessment in composites laminates structures. The proposed damage indexes can provide more information about the delamination, so it can improve the delamination detection and assessment in the following chapter. Based on the result of this work, some conclusion can be drawn as:

1) The result of this chapter shows that phase space topology structures of all sub-signals have clear changes with different delamination, which means the phase space topology structures of all the sub-signals in various frequency ranges generated by the wavelet packet decomposition method are affected by the delamination in composite structures. The sensitivity to

the delamination and robustness to the noise and disturb of the proposed method has been analyzed and demonstrated by using both simulation and experiment. Therefore, it is possible to use the proposed method and features based on the wavelet packet decomposition combined with the phase space topology analysis to assess delamination in the composite structures.

2) The result also shows that the change of indexes from the proposed method is different from various sub-signals generated by the wavelet packet method due to the different effects of delamination on the sub-signals. It also illustrated the phase space topology structures of sub-signals in different frequency ranges have various sensitivities to the delamination. The CPST ratio of high-frequency sub-signals will decrease with delamination size and depth increasing as the result of the amplitude and energy of high-frequency sub-signals reducing. While there is fluctuation in some sub-signals due to the CPST is related to both the energy distribution and the frequency shifting of sub-signals, while these two features have different changing trends as shown in previous works. Therefore, compared with the previous method which just can provide one damage index of the original signal, the proposed method can provide more different information from sub-signals with different frequency ranges for the delamination in structures, which can enhance the accuracy of delamination assessment.

Chapter 6 THE DELAMINATION ASSESSMENT IN COMPOSITE LAMINATE PANEL BASED ON THE ANN WITH DIFFERENT INPUT FACTORS

This chapter focuses on the development of methods by using the ANN (ANN) based on the dynamic characteristics to assess the delamination and estimate its parameters in composite structures, including location, size, and depth. As mentioned in Chapter 1, the analysis of the effect generated by delamination on the dynamic responses of composite structures is difficult due to that more parameters need to be considered and the effect of delamination on the composite structures is complicated. Therefore, it is necessary to develop new assessment methods to estimate the delamination parameters based on the dynamic responses in composite structures without analytical models to analyze the relationship between delamination and dynamic responses. The ANN (ANN) can estimate the targets without analysis of the relationship between input factors and assessment targets based on training with various cases as mentioned in Chapter 1. This method learns a set of giving data samples to predict the unknown outcomes from future datasets. Therefore, it is possible to assess delamination in composite structures based on training the ANN with a lot of cases to predict the delamination configuration based on the vibration characteristics. This chapter will test the

feasibility and advantages of the proposed methods by using ANN to assess the delamination in composite structures by using the features proposed in the previous chapters.

It should also be noted that the input factors selection is important to estimate and predict the targets by the ANNs as mentioned in previous work due to the different properties of input factors [147], including the sensitivity and accuracy of input factors. As shown in previous Chapters 1, the vibration characteristics will be the same in different cases, which will reduce the accuracy of delamination assessment based on the vibration signals. It also should be noted that some characteristics are less sensitive to delamination and they will be changed by the disturbance and noise. The ANN trained by these wrong input factors will make mistakes in target prediction and assessment. Therefore, it is necessary to investigate the effect of different input factors on the performance of delamination assessment by using the ANNs. This chapter also investigates the effect of three different features as input factors, including two proposed features in previous chapters, on the performance of delamination assessment by using the ANN to find the best input factors in this research.

6.1 Artificial Neural Network (ANN) Design

This section will give an introduction to the Artificial Neural Network (ANN). The ANNs can provide the prediction and estimation of targets based on the input factors from targets after training. There are several types of

neural network which have been used for damage assessment, such as back-propagation (BP) neural network [152, 203], convolution neural network [64, 155]. In this chapter, a Radial-based Function Neural Network (RBFNN) was used for delamination assessment. The RBFNN is used in many types of applications, including dynamic control [204, 205], dynamic system prediction [206, 207], and fault analysis [208, 209]. These researches illustrated the feasibility of RBFNN for dynamic signal analysis and damage assessment. The model for RBFNN in this work is shown as the following figure:

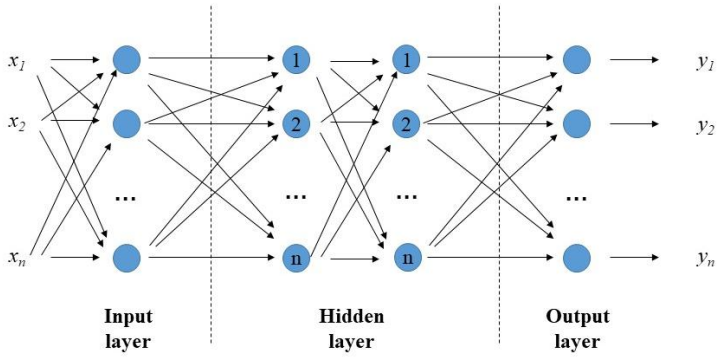

Figure 6-1 The model of ANN.

For RBFNN, there are three layers, an input layer, two hidden layers, and an output layer. As shown in Figure 6-1, the x_n is the nth input factor and the y_n is the nth output of the ANN. A single-output RBFNN with N hidden layer neurons can be described as:

$$\boldsymbol{Y} = \sum_{n=1}^{N} \omega_n \cdot radbas_n(\boldsymbol{X}), \tag{6-1}$$

where $\boldsymbol{X} = (\boldsymbol{x_1}, \boldsymbol{x_2}, \cdots, \boldsymbol{x_n})$ is the input signal with N input variables and $\boldsymbol{Y} = (\boldsymbol{y_1}, \boldsymbol{y_2}, \cdots, \boldsymbol{y_n})$ is the output factor. Here, ω_n is the connecting weights between the hidden neuron and the output layer. The transit function

$radbas_n(\boldsymbol{X})$ of the RBFNN in the hidden layer is the Gauss function as equation 6-2:

$$radbas_n(\boldsymbol{X}) = e^{(-\|\boldsymbol{X}-\boldsymbol{\mu}_n\|/\sigma_n^2)}. \quad (6\text{-}2)$$

In equation (6-2), $\boldsymbol{\mu}_n$ denotes the center vector of the *n*th hidden neuron, and $\|\boldsymbol{X}-\boldsymbol{\mu}_n\|$ is the Euclidean distance between $\boldsymbol{X}$ and $\boldsymbol{\mu}_n$. The σ_n is the radius of the *n*th hidden neuron. For this chapter, the three types of input factors are the vibration characteristics (natural frequency and amplitude of the first two modes), CPST from original vibration signal, and CPST from sub-signals generated by wavelet packet decomposition. The output factors are the location, size, and depth of delamination.

6.2 Delamination Assessment Procedure

This section will introduce the procedure of the proposed methods of delamination assessment by using RBFNN with three input factors. Based on the result of Chapters 4 and 5, the change of phase space topology (CPST) from the original dynamic signal and sub-signals generated by the wavelet packet decomposition method can be utilized as the damage index for delamination assessment. So they can be used as the input factor for ANN for delamination assessment. The natural frequency and amplitude of the first two modes in the frequency domain are also used as the input factor to investigate the effect of input factors on delamination assessment performance based on RBFNN to find the best input factors in this research

6.2.1 Fourier Transform Method

The feasibility of the natural frequency and amplitude of the first two modes in the frequency domain as the input factors for ANN to assess damage has been demonstrated in previous work [62, 210, 211]. Following these researches, the natural frequencies and amplitude generated by the Fourier Transform Method from the dynamic signals were used as input factors into ANN for delamination assessment as a comparison. The procedure is as shown in Figure 6-2:

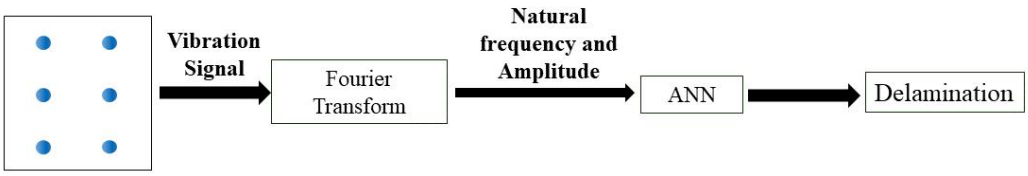

Figure 6-2 The procedure using natural frequency and amplitude with ANN.

The vibration signals measured by sensors were transformed by the Fourier transform method to get the natural frequencies and amplitude. Then the natural frequency and amplitude o can be used as the input factors for ANN to detect damage. In this chapter, the natural frequencies and amplitudes of the first two modes were used because these two modes are clear in the frequency domain transformed by the Fourier Transformed method in Chapter 4.

6.2.2 Phase Space Topology Analysis with ANN

The assessment method will be based on ANN with the phase space topology analysis. In this section, the change of Phase Space topology (CPST) was used as the delamination index which is calculated by the phase space reconstructed method introduced in Chapter 4. Therefore, the CPST of the

original signal was used directly as input factors for ANN to predict delamination. Figure 6-3 shows the procedure of delamination assessment based on the phase space method with ANN.

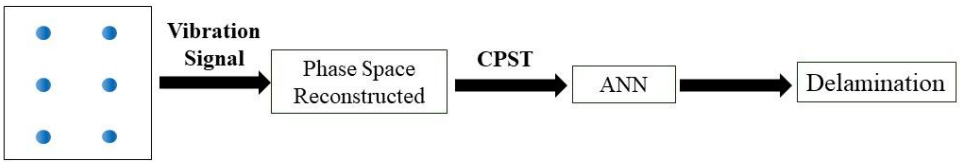

Figure 6-3 The procedure of the phase space method with ANN.

The vibration signals measured by sensors were analyzed and calculated by the phase space reconstructed method to get the CPST. The CPST from different cases were used as the input factors to train RBFNN and estimate delamination. Based on the result in Chapter 4, the CPST is more sensitive to delamination than the natural frequency of the first two modes. Therefore, it can improve the performance of the proposed method based on RBFNN for delamination assessment compared with previous vibration characteristics.

6.2.3 Phase Space Topology Analysis with Wavelet Packet Decomposition and ANN

At last, the CPSTs of sub-signals made by the wavelet packet decomposition which was introduced in Chapter 5, were used as the input factors for ANN training and delamination estimate. Figure 6-4 shows the procedure of delamination assessment based on the phase space reconstructed method combined with wavelet packet decomposition and ANN.

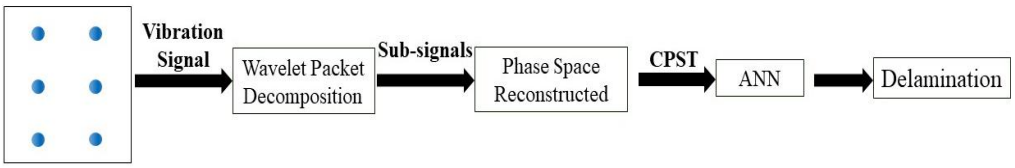

Figure 6-4 The procedure of phase space method and wavelet packet decomposition with ANN.

First, the vibration signals measured by sensors were decomposed by the wavelet packet method into several sub-signals with different frequency ranges. Then the CPSTs were calculated from different sub-signals as input factors to train ANN and detect delamination. Based on Chapter 5, the CPSTs from the sub-signals can provide more information about the delamination which can improve the performance of the proposed method based on RBFNN.

6.3 Simulation Result

To verify the possibility of the proposed method based on the ANN and investigate the effect of input factors, a beam and a composite panel with delamination were simulated in this section.

6.3.1 The Delamination Assessment for Beams

First, a homogeneous beam with various delamination was used as the sample to test the feasibility and show the effect of input factors on the performance of delamination assessment based on the ANN.

6.3.1.1 The Delaminated Beam Model

The configuration of the beam sample and the arrangement of the

experiment are shown In Figure 6-5:

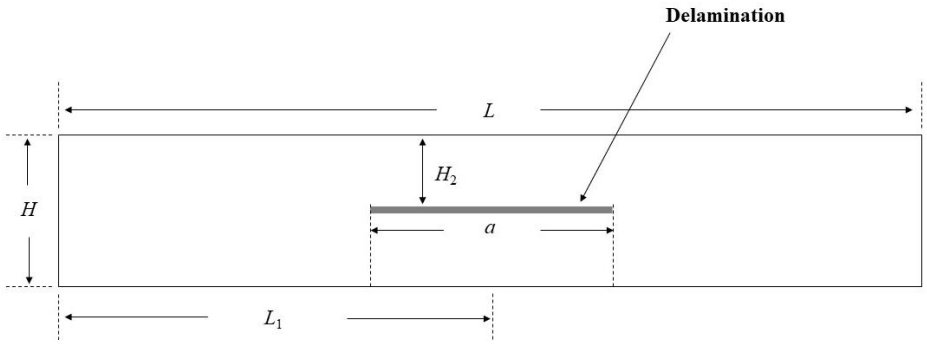

(a) model of a delaminated beam;

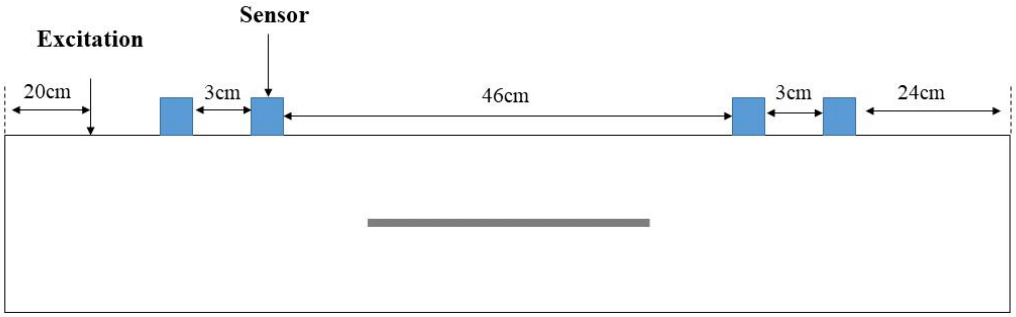

(b) Experiment arrangement;

Figure 6-5 The model of the delaminated beam.

The delamination in the beam is noted by the grey part with different configures in Figure 6-5, which is through the width of the beam. The delamination was changed with various sizes (a) and depths (H_2). The middle point location of the delamination will also be changed which is represented by L_1. This research used four sensors to measure the vibration signal as shown in Figure 6-5(b), which were located in the 4 optimal locations in Chapter 3 for various delamination parameters (i.e. sensors axial location are 0.24L, 0.27L, 0.73L, and 0.76L from the left end of the beam, while L is the total length of the beam). A rectangle pulse excitation was used to generate vibration in the beam at the location shown in Figure 6-5(b), which is the

same as Section 4.2. The parameters of the beam are shown in Table 6-1.

Table 6-1 The Parameters of Samples.

Modulus /GPa	**Density /kg/m^3**	**Length (*L*) /m**	**Width (*b*) /m**	**Thickness (*H*) /m**
30	1000	1	0.1	0.01

The beam was modeled by using 8-node elements C3D8R in ABAQUS. In ABAQUS software, cohesive surface contact interaction was used to simulate the delamination. While the number of elements is related to the delamination part which needs to use smaller elements compared with intact parts. For the undamaged case, there were 10,000 elements in the model by the size of elements is $0.1 \times 0.1 \times 0.001mm$. The sampling frequency is $f = 1{,}000Hz$ with the time periodic $T = 2s$. The total number of data is 2,000.

6.3.1.2 Result Analysis

There are 31 cases with different delamination to train the RBFNN, including an undamaged one. Three cases were used as testing samples. In this section, the natural frequency and amplitude of 1st mode were used as vibration characteristics for ANN to estimate delamination. To show the accuracy of the proposed method for delamination prediction, the total error of each case was calculated as the following formulation:

$$R = (1 - (1 - \frac{|H_{2m} - H_{2r}|}{H_{2r}}) \cdot (1 - \frac{|L_{1m} - L_{1r}|}{L_{1r}}) \cdot (1 - \frac{|a_m - a_r|}{a_r})) \times 100\% \qquad (6\text{-}1)$$

where H_{2m}, L_{1m} and a_m represent the depth, location, and size which are predicted by the proposed method, while the H_{2r}, L_{1r} and a_r are depth, location, and size of delamination, respectively. The result is shown in Tables

6-2 to 6-4:

Table 6-2 The result of Sample No.1.

Input factors	**Size (a) /cm**	**Depth (H_2) /cm**	**Location (L_1) /m**	**Error (R)**
Real Situation	**7.5000**	**0.3000**	**0.5000**	—
Natural frequency and Amplitude	7.3493	0.3483	0.5007	17.9%
CPST from original signal	7.5000	0.3000	0.5000	0
CPSTs from sub-signals	7.5400	0.3023	0.5025	1.8%

Table 6-3 The result of Sample No.2.

Input factors	**Size (a) /cm**	**Depth (H_2) /cm**	**Location (L_1) /m**	**Error (R)**
Real Situation	**8.0000**	**0.3000**	**0.3500**	—
Natural frequency and Amplitude	7.8147	0.4071	0.5027	64.6%
CPST from original signal	7.5000	0.3000	0.5000	46.4%
CPSTs from	7.5797	0.3040	0.4839	42.3%

sub-signals				

Table 6-4 The result of Sample No.3.

Input factors	**Size (a) /cm**	**Depth (H_2) /cm**	**Location (L_1) /m**	**Error (R)**
Real situation	**6.0000**	**0.4000**	**0.5000**	—
Natural frequency and Amplitude	7.4226	0.3584	0.5051	32.3%
CPST from original signal	6.3631	0.3167	0.4987	25.7%
CPSTs from sub-signals	6.6746	0.3601	0.4931	21.1%

The result indicates that the proposed method can predict the delamination in the beam and estimate its information, including size, depth, and location. However, there are still some errors in prediction and estimate by using the proposed method. The result for sample No.1 in Table 6-2 is best with 17.9%, 0%, and 1.8%. The error is small, which demonstrates the possibility and accuracy of the proposed methods for the No.1 sample especially by using CPST of original signal and CPSTs of sub-signals generated by wavelet decomposition as input factors. While the result of sample No.2 and sample No.3 has less accuracy. The reason for the error may be that the number of

training cases is not large enough, which can be improved by more cases. The error also may be generated by the structure of RBFNN, which can be improved by optimization and adding more hidden layers and neurons. The locations of sensors also should be investigated and optimized to improve the accuracy of the proposed methods based on the ANN.

On the other hand, for all cases, it should be noted that the input factor will affect the accuracy of the estimate by the proposed method. The errors of result calculated by the RBFNN based on CPSTs from sub-signals generated by wavelet packet decomposition is smallest for sample No.2 and sample No.3 with 42.3% and 21.1% respectively, which means this input factor is the best one for RBFNN to detect and predict the delamination in these two samples. This is the result of the different sensitivity and accuracy of the different features of the delamination parameters changing as shown in the previous work. The CPSTs of the sub-signals can provide more information to enhance the accuracy with high sensitivity, while the CPST of the original signals may be the same from different cases and the natural frequency and amplitude have low sensitivity to the delamination and robustness to the disturbance. Therefore, the result calculated by ANN based on the CPSTs as input factors should be best with the same conditions.

6.3.2 The Delamination Assessment for Laminate Panel

In this section, a composite laminates panel with delamination by the

simulation to investigate the possibility of the proposed method and analyze the effect of input factors on the delamination assessment based on ANN. For this purpose, a model of a composite laminate with delamination damage was constructed as shown in Figure 6-6.

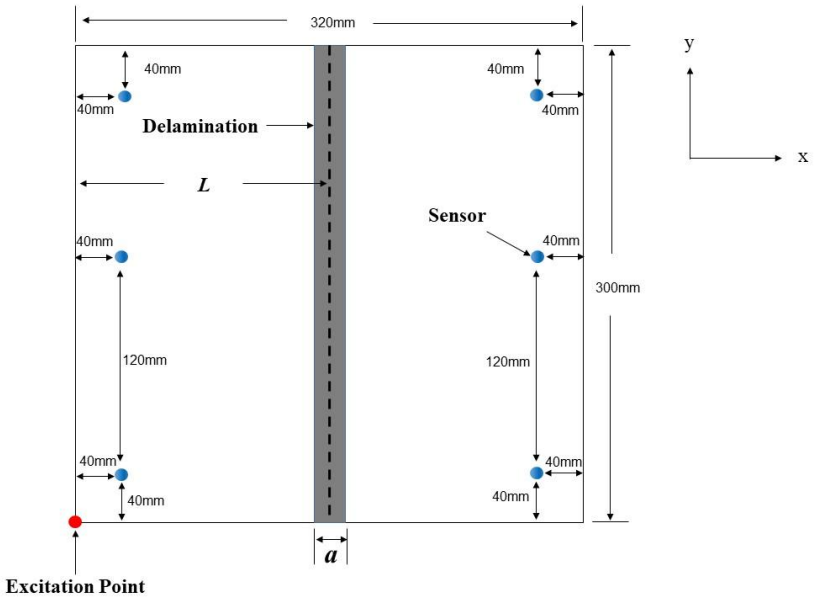

(a) Top view;

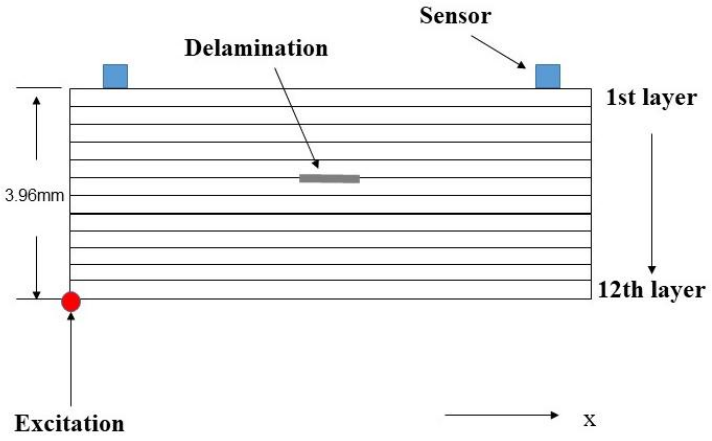

(b) Side view;

Figure 6-6 The model of a composite laminate with delamination.

As shown in Figure 6-6(a), six sensors were used to measure vibration signals. An impulse excitation is used to generate traverse vibration responses at the

locations shown by the red point in Figure 6-6. The laminate panel sample size is $320mm \times 300mm \times 3.96mm$ with 12 layers. The grey part is the delamination zone which is with various parameters, including size a, location L, and depth (layers) as shown in Figure 6-6. This rectangular laminate panel was clamped at one side creating a cantilever panel configuration and the panel was still modeled by using 8-node elements C3D8R. The properties of laminate were described in Table 6-5, describing the values for the elastic modulus (E_{ij}), shear modulus (G_{ij}), and Poisson ratio (v_{ij}) used in the simulation of a composite laminate.

Table 6-5 The properties of the composite laminate.

E_{11}(GPa)	E_{22}(GPa)	E_{33}(GPa)	G_{12}(GPa)	G_{13}(GPa)	G_{23}(GPa)	v_{12}	v_{13}	v_{23}
27	27	4.7	4.7	4.7	4.7	0.28	0.1	0.1

There are 55 cases for ANN training and 2 cases for testing with various delamination in the composite laminates panel. The following sections will show the result.

6.3.2.1 Fourier Transform Method with ANN

The test result based on vibration characteristics generated by the Fourier transform method with RBFNN was calculated in this section. The input factors were the natural frequencies and amplitude of six sensors for the 1st and 2nd modes. The result for samples in the x-y plane is shown in Figures 6-7 and 6-8:

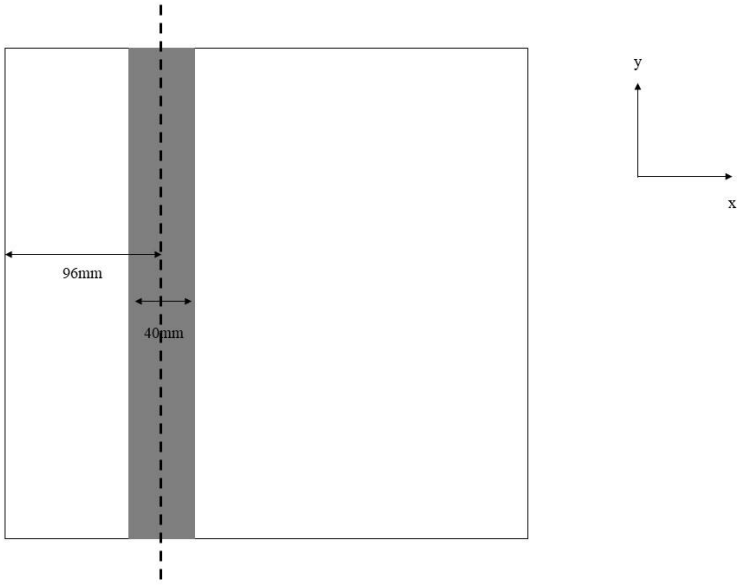

(a) Sample Model;

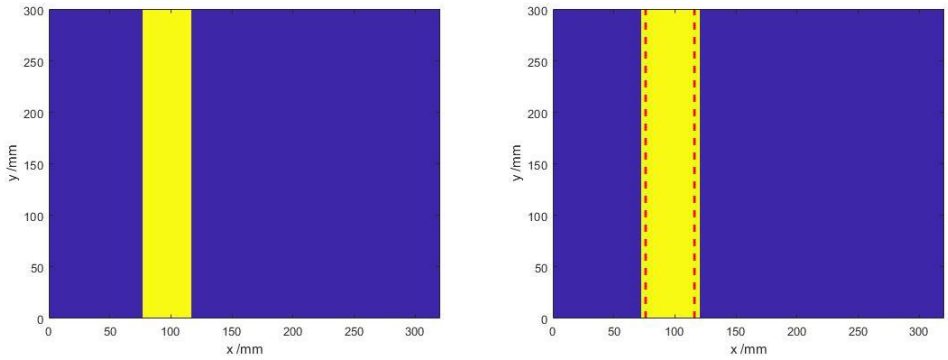

(b) Real situation; *(c) Test result;*

Figure 6-7 The top view result for sample No.1.

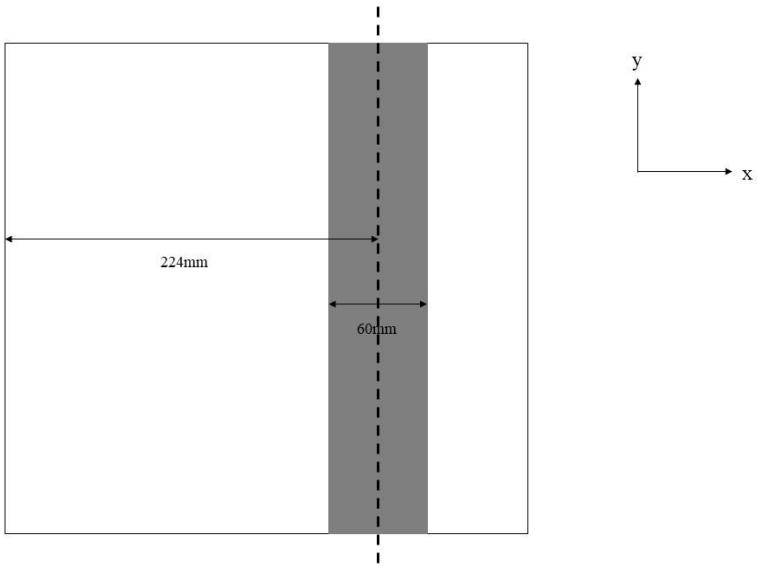

(a) Sample Model;

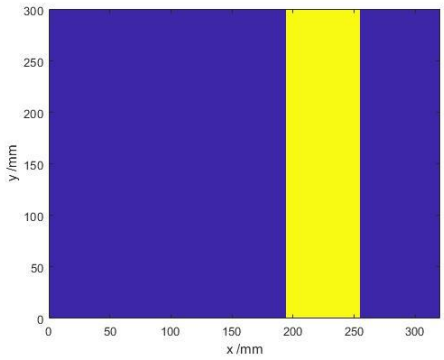

(b) Real situation;

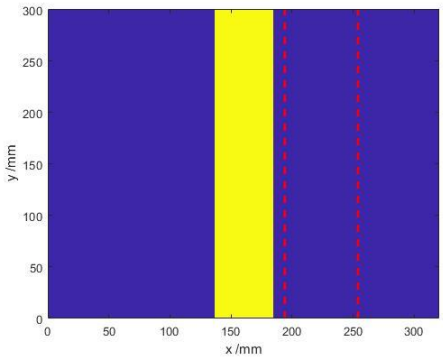

(c) Test result;

Figure 6-8 The top view result for sample No.2.

The result indicates that the RBFANN can provide information about delamination in samples based on the vibration characteristics as input factors. The delamination part was noted by grey in the sample model and yellow in the result. In Figures 6-7(c) and 6-8(c), the actual delamination zone is noted by red weak lines. It should be noted that there are errors in assessment, especially for sample No.2. The actual range of delamination is from 200mm to 250mm in the x-axis, while the estimated result by ANN based on the

natural frequency and amplitude is from 140mm to 180mm in sample No.2. The assessment result is a little different from the real situation for the delamination size. These errors may be generated by the input factors. As shown in Chapters 3 and 4, the change of the natural frequencies and amplitude of the first two modes with delamination is complicated and small when the delamination location changes. Therefore, the calculation by using ANN based on these features is inaccurate. The side view result is given below:

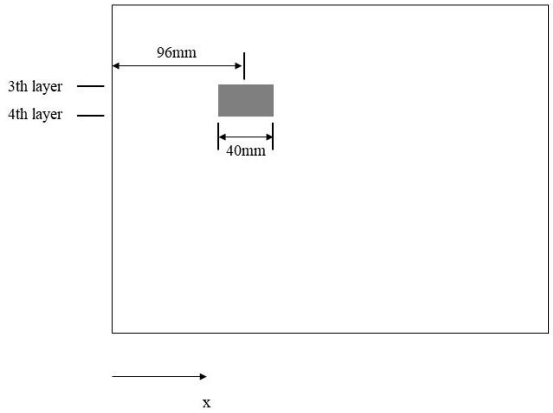

(a) Sample Model;

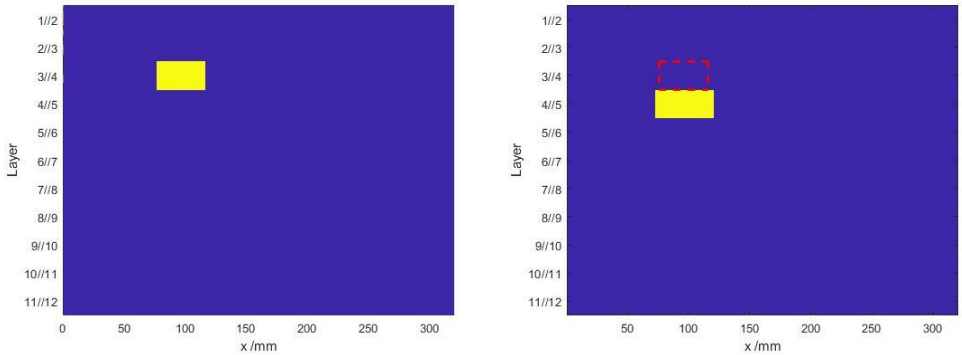

(b) Real situation; *(c) Test result;*

Figure 6-9 The side view result for sample No.1.

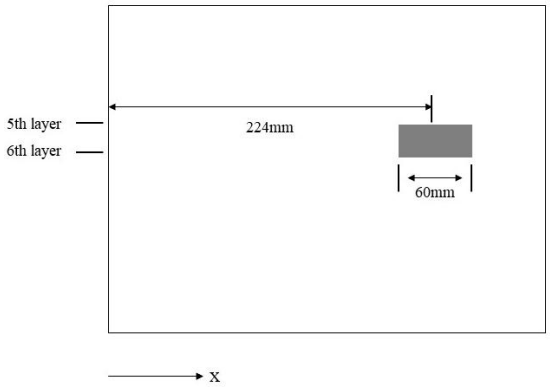

(a) Sample Model;

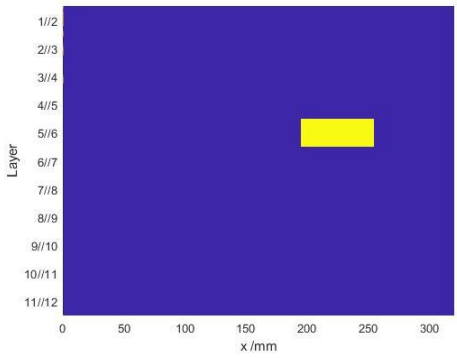

(b) Real situation;

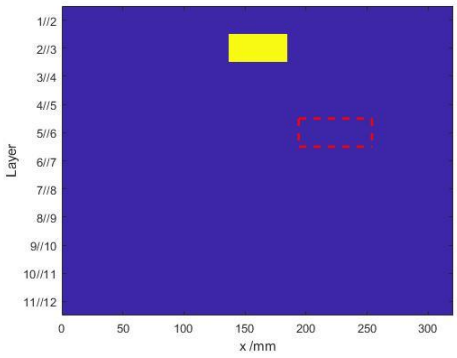

(c) Test result;

Figure 6-10 The side view result for sample No.2.

The delamination is noted by the grey part in the model figure and the yellow part in the figures. Moreover, the actual delamination zone is noted in Figure 6-9 and Figure 6-10 by red weak lines for comparison. The result in Figure 6-9 and 6-10 indicates that the RBFANN can provide information about delamination in samples. However, there are errors in assessment and prediction for both two samples. For sample No.1, the depth of delamination is between the 3rd layer and 4th layer, while the assessment result is between the 4th layer and 5th layer. For sample No.2, the delamination should be between the 5th and the 6th layers, while the result estimated is between the 2nd

and 3rd layers. The reason for the error may be that the sensitivity of the natural frequency and amplitude, is not enough for delamination depth as mentioned in Chapters 3 and 4. The result indicates that the RBFNN based on the natural frequency as input factors can predict the delamination in structures but the accuracy is not good enough.

6.3.2.2 Phase Space Topology Analysis with ANN

Second, the test result based on Phase Space reconstructed method with ANN was calculated. In this section, the CPST from the vibration signals was used as input factors into ANN. The result for samples in the x-y plane (top view) is shown as follows:

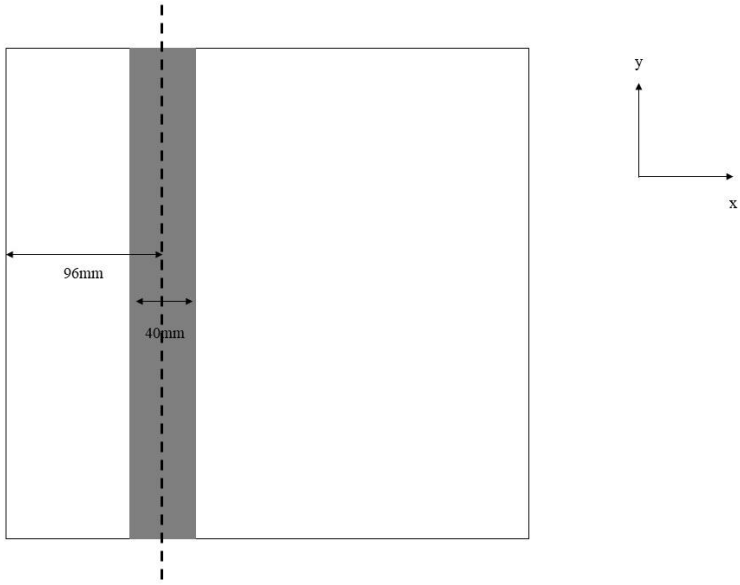

(a) Sample Model;

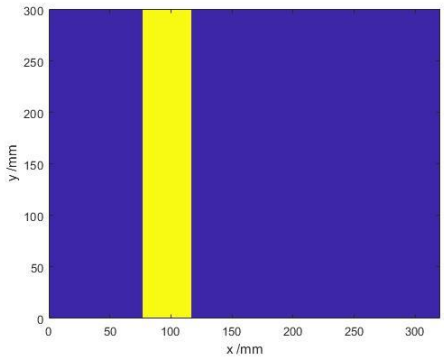

(b) Real situation;

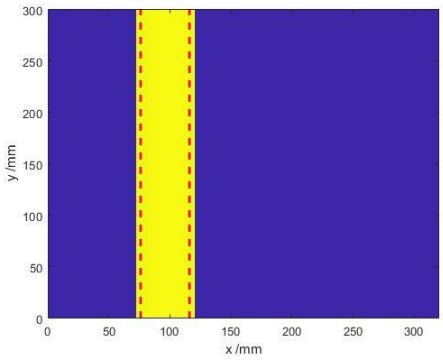

(c) Test result;

Figure 6-11 The top view result for sample No.1.

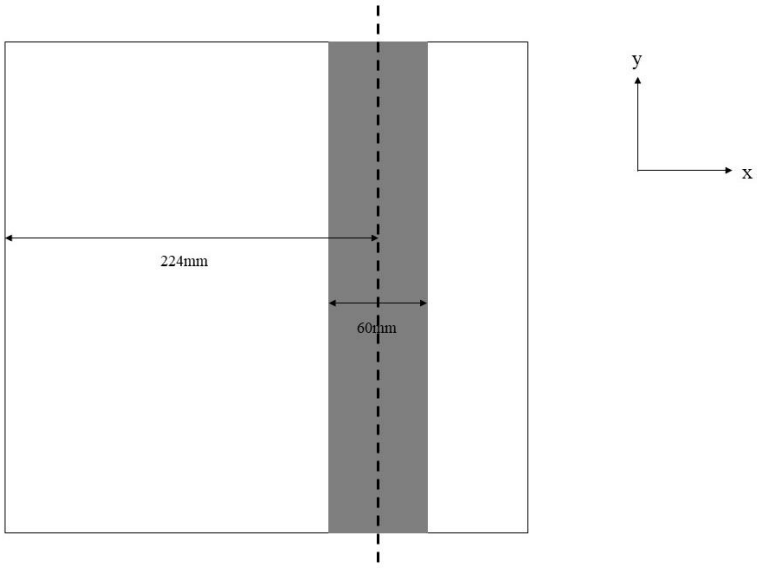

(a) Sample Model;

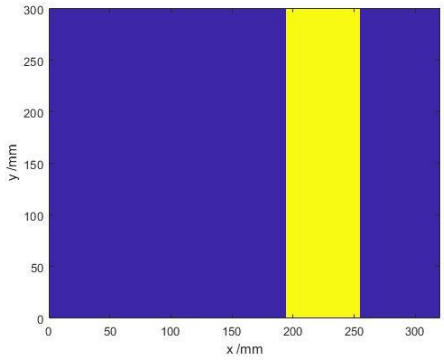

(b) Real situation;

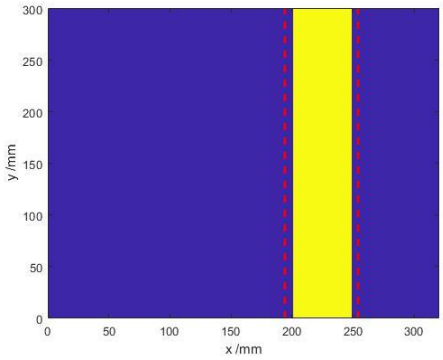

(c) Test result;

Figure 6-12 The top view result for sample No.2.

In Figure 6-11 and Figure 6-12, the delamination part was noted by grey in the sample model and yellow in the result. The red weak lines in Figure 6-11(c) and Figure 6-12(c) are used to illustrate the actual delamination part for comparison. It illustrates that the RBFNN can provide information about the location and size of delamination for samples in the x-y plane by using CPST from the original signals as input factors. However, compare Figure 6-12 with Figure 6-8, it should be noted that the performance of delamination

assessment has clear improvement and closer to the real situation, which is because the sensitivity of CPST is better than the natural frequency and amplitude. However, there is still some estimation error, especially for the size of delamination. Both these two samples have errors of about 10mm, while the result of sample No.1 is larger than the real situation and sample No.2 is smaller. The errors may be generated by the ANN which can be improved by the design optimization and the training with more cases. The result for samples in the side view is shown below which can show the information about size, depth, and location of delamination in samples:

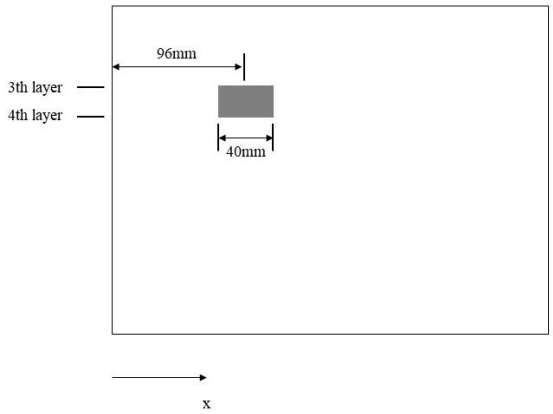

(a) Sample Model;

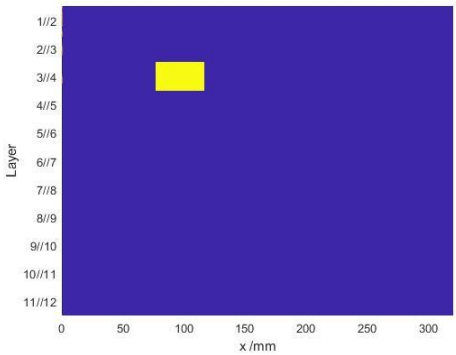

(b) Real situation;

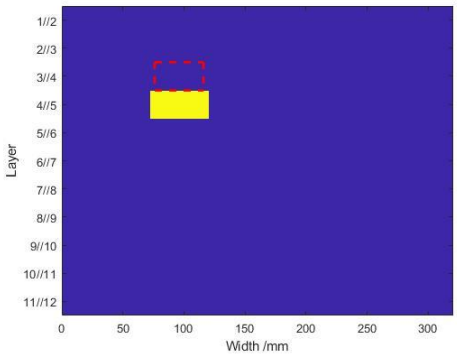

(c) Test result;

Figure 6-13 The side view result for sample No.1.

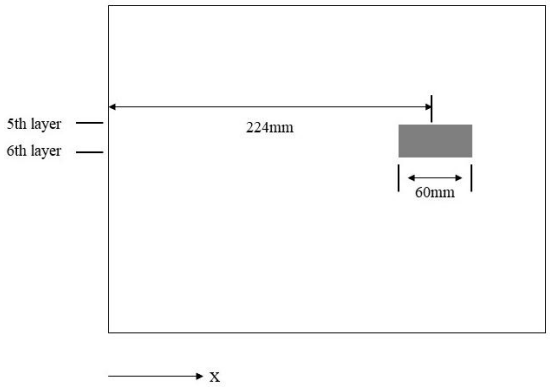

(a) Sample Model;

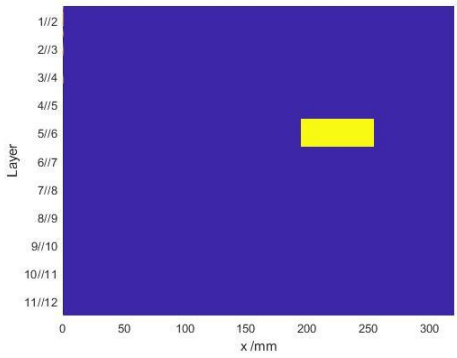

(b) Real situation;

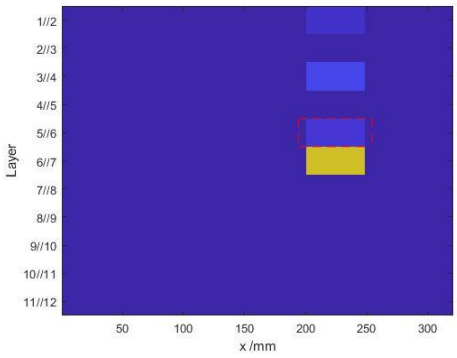

(c) Test result;

Figure 6-14 The side view result for sample No.2.

The result in Figures 6-13 and 6-14 shows that the proposed method based on CPST from the initial vibration signal can provide information about the delamination in samples. The delamination part was noted by grey in the sample model and yellow in the test result in Figure 6-13 and Figure 6-14(b). The red weak lines are used to illustrate the actual delamination zone. While, in Figure 6-14(c), the undamaged part is noted by dark blue, and the delamination part calculated was noted by other colors. The result in Figures 6-13 and 6-14 illustrates that the location estimated by ANN in the x-axis is accurate. All the parts noted by the colors except dark blue are delamination

calculated by RBFNN based on the CPST as input factors from the initial dynamic signals. While the information about the other information of delamination has a difference between the real situation and the estimation result of RBFNN, especially the delamination depth which affects the dynamic responses a little. The result of delamination depth assessed by ANN for sample No.1 is between the 4^{th} layer and 5^{th} layer, while the real situation is between the 3^{rd} layer and 4^{th} layer. The accuracy of this sample is the same as the previous work by using natural frequency and amplitude. For sample No.2, the delamination region detected by ANN based on CPST is larger than the real situation but it also covers the real situation. This error may be generated by the sensitivity of CPST to the depth of delamination which is not high enough. The improvement can be done by the design of ANN which should be optimized by more training cases and improvement of input factors to detect delamination more accurately. However, based on the result in Section 6.3.2.1 by using the natural frequency and amplitude of the first two modes as input factors, the performance of RBFNN has a clear improvement for delamination information prediction on the x-axis location.

6.3.2.3 Phase Space Topology Analysis Combined with Wavelet Packet Decomposition and ANN

At last, the test result based on phase space reconstructed with wavelet packet decomposition ANN was calculated. In this section, the CPSTs from

sub-signals generated by the wavelet packet decomposition was used as input factors into ANN. The result is shown in Figures 6-15 to 6-16:

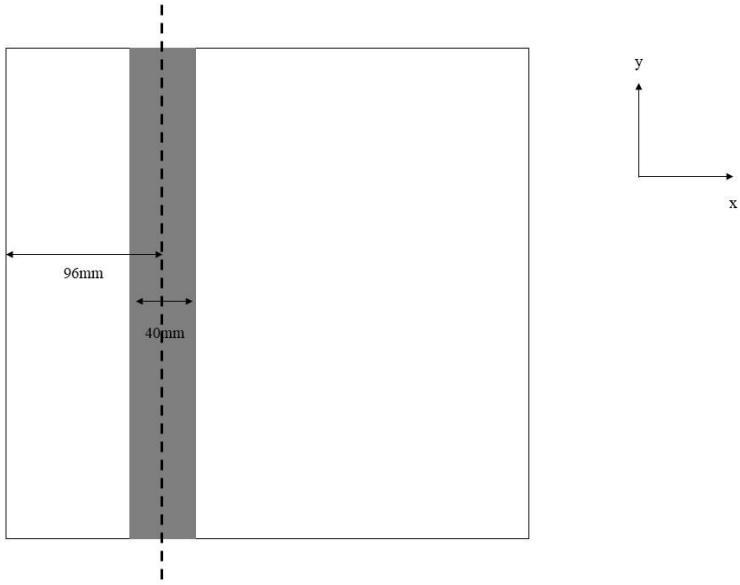

(a) Sample Model;

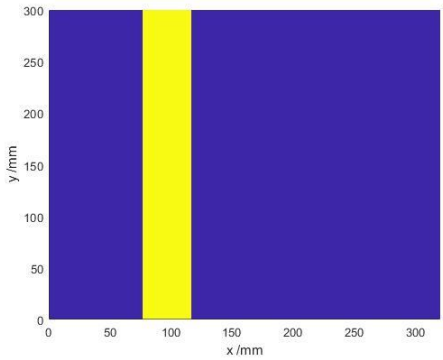

(b) Real situation;

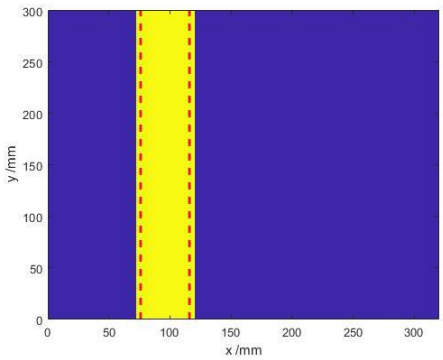

(c) Test result;

Figure 6-15 The top view result for sample No.1.

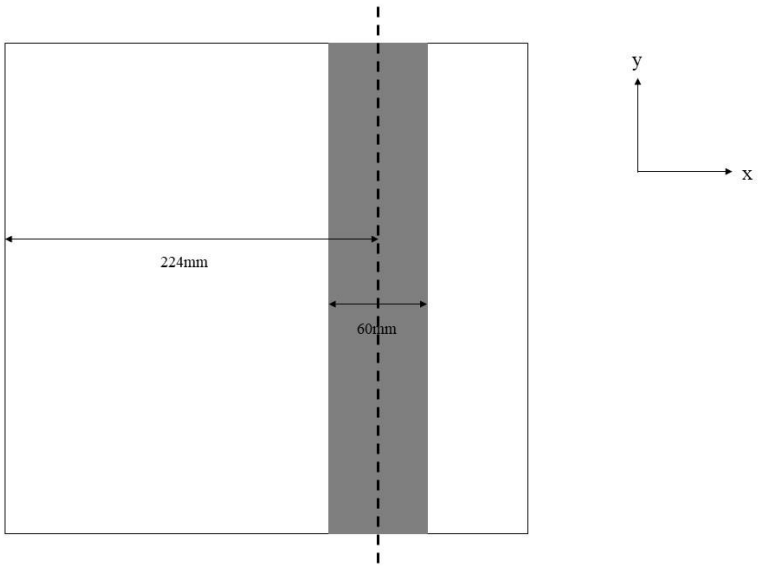

(a) Sample Model;

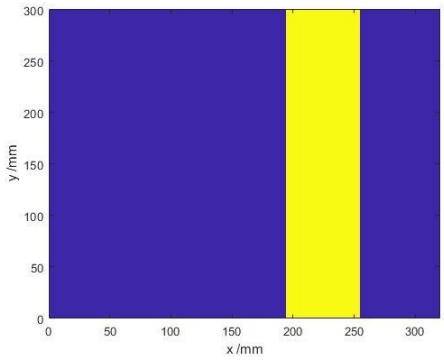

(b) Real situation;

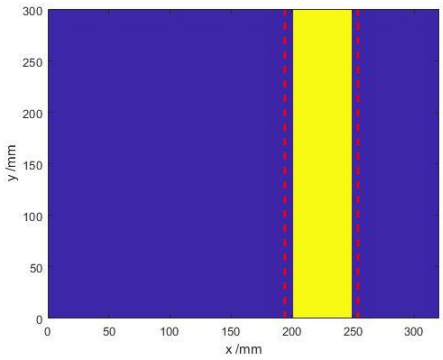

(c) Test result;

Figure 6-16 The top view result for sample No.2.

In Figure 6-15 and Figure 6-16, the delamination part was noted by grey in the sample model and yellow in the result. The actual delamination zone is noted in Figure 6-15 and Figure 6-16 by red weak lines. It indicates that the proposed method based on the CPSTs from sub-signals generated by wavelet packet decomposition can provide information about the location and size of delamination for samples in the x-y plane (top view). The result from RBFNN for location on the x-axis is relatively close to the real situation. However,

there are still some errors in estimation, especially for the size of delamination, which is about 10mm. This result is the same as the result in Section 6.3.2.3, which is that the assessment result of sample No.1 is larger than the real situation and the result of sample No.2 is smaller. The accuracy in this section is also better than in Section 6.3.2.1 due to the higher sensitivity and robustness of the CPSTs to the delamination. The errors in delamination size may also be generated by RBFNN which will require optimization and more training cases. The result for samples in the side view is shown as follows:

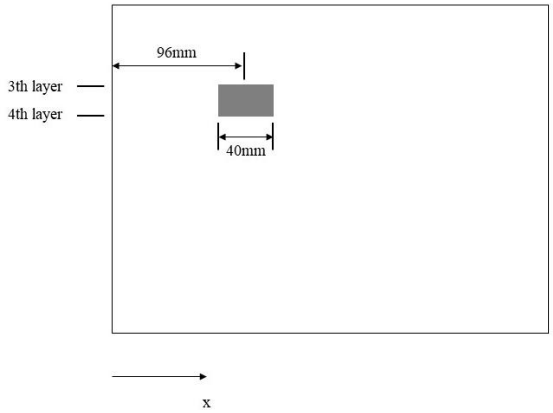

(a) Sample Model;

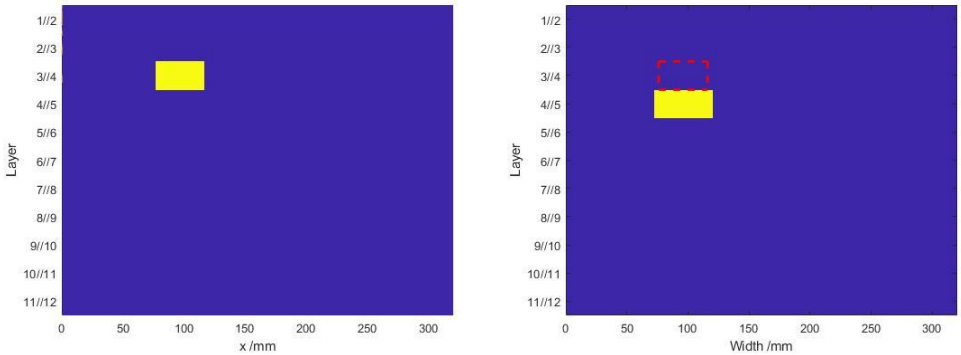

(b) Real situation; *(c) Test result;*

Figure 6-17 The side view result for sample No.1.

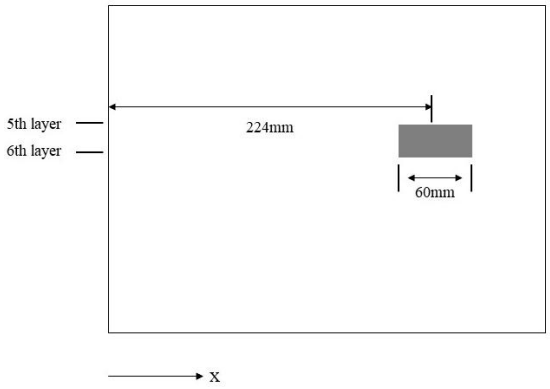

(a) Sample Model;

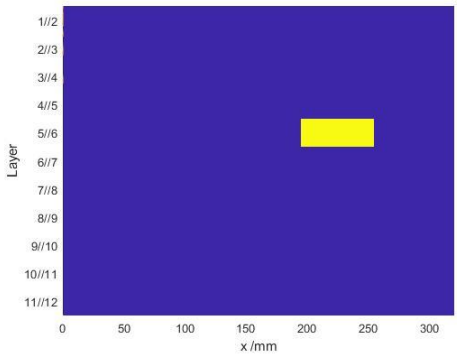

(b) Real situation;

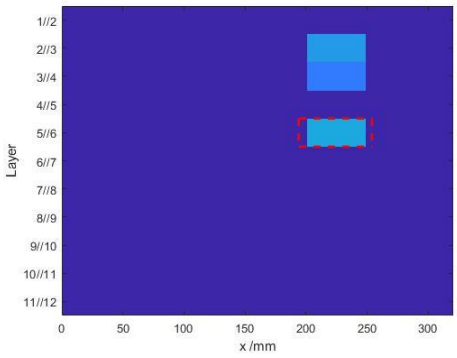

(c) Test result;

Figure 6-18 The side view result for sample No.2.

The result in Figures 6-17 and 6-18 shows that the proposed method based on CPST from the initial vibration signal can provide information about the delamination in samples. The delamination part was noted by grey in the sample model and yellow in the result. While, in Figure 6-18(c), there are several colors to show the delamination depth except dark blue which is used to show the undamaged part, which is similar to Section 6.3.2.2. The actual delamination zone is noted by red weak lines in Figure 6-17(c) and Figure 6-18(c). Based on Figure 6-17 and Figure 6-18, it should be noted that the location of delamination in the x-axis is estimated accurately by RBFNN.

However, there are some errors in the size and depth of the assessment and estimation. For sample No.1, the depth of delamination estimated by ANN based on the CPSTs from the sub-signal generated by the wavelet packet decomposition method is between the 4^{th} and 5^{th} layer, while the actual delamination is between the 3^{rd} and 4^{th} layer. The accuracy is the same as the result in Section 6.3.2.2. However, although the assessment result of sample No.2 is also inaccurate, the estimated delamination region based on the CPSTs from the sub-signals is smaller than the CPST from the original signals covering the actual delamination layers. The reduction of the estimated region in the x-z plane illustrates the improvement of the accuracy based on the ANNs. The improvement may be because the CPSTs from the sub-signals generated by wavelet packet decomposition are more sensitive to the delamination and they contain more information about the delamination. This error can be reduced by optimizing and training RBFNN with more cases, which is also the same as the previous sections.

6.3.2.4 Comparing Results of Different Input Factors

The previous sections show the possibility of the ANN with the three types of input factors to estimate the delamination parameters. However, they also indicate there are still errors in the assessment by using the ANN with different types of input factors. The possible reason for the errors may be as the following: 1) The locations and number of sensors need to be optimized,

which show significant effects on the dynamic signal measurement due to the varying sensitivity of different measurement locations as shown in Chapter 3; 2) The training for the ANN need more cases; 3) The design of the ANN needs to be improved, such as using other types of ANN and adding more layers.

It should also be noted that with the same conditions and design, the result of ANN by using different features as input factors is different. Therefore, this section will compare the result and investigate the effect of the input factors. The accuracy ratio is defined as follows:

$$L_{1c} = (1 - |L_{1r} - L_{1t}|/L_{1r}) \times 100\%, \quad (6\text{-}3)$$

$$a_c = (1 - |a_r - a_t|/a_r) \times 100\%, \quad (6\text{-}4)$$

where the L_{1r} and a_r mean the location and size of delamination in samples as shown in Figure 6-6, while L_{1t} and a_t are the predicted location and size by the proposed method. For the delamination depth, the accuracy can be set as:

$$h_c = \frac{n_r}{n_t} \times 100\%, \quad (6\text{-}5)$$

where n_r means the number of the right test result and n_t means the total number of the total result. Based on this set, the accuracy of RBFNN with vibration characteristic is zero which has no right test result due to the sensitivity of the natural frequency and amplitude to the delamination is low. Based on equation (6-3) to (6-5), the comparison of assessment result for Sample No.1 based on three types of input factor is estimated and shown as following Table 6-6:

Table 6-6 The accuracy for sample No.1.

Input Factor	Location	Size	Depth
Natural frequency and Amplitude	100%	80%	0%
CPST from initial singal	100%	80%	0%
CPSTs from sub-signals	100%	80%	0%

The result in Table 6-6 shows that the input factor does not affect the performance of the delamination assessment and prediction. For sample No.1, the accuracy of the location and size is about 100% and 80% respectively for the result based on the three proposed input factors, while the delamination depth estimate is all wrong. As mentioned in Chapter 3, the effect of delamination depth is smaller than the other two parameters, which may be the reason for the errors. The error may also be generated by the design of ANN. The design of RBFNN can be optimized with more training cases. Moreover, other types of ANN have different advantages and researchers have proved their feasibility for damage assessment [148, 155, 210, 212], which can be used to detect delamination in the composite structure. These methods can improve the accuracy of ANN for damage assessment. The comparison of the assessment result for sample No.2 is shown in Table 6-7:

Table 6-7 The accuracy for sample No.2.

Input Factor	Location	Size	Depth
Natural frequency and Amplitude	71%	80%	0%
CPST from original signals	100%	80%	25%
CPSTs from sub-signals	100%	80%	33%

The result in Table 6-7 illustrates that the accuracy of ANN by using CPST from the original signals and the CPSTs from sub-signal enhances the accuracy of prediction compared with RBFNN using natural frequency and amplitude from signals. The accuracy for all parameters is improved and enhanced, especially the delamination depth, which is 0%, 25 %, and 33% based on the different input factors. The best result is calculated by using ANN based on the CPSTs from the sub-signals because it can provide more information and details of the effect generated by delamination depth on the structures with higher sensitivity and robustness.

The result above all shows that the input factor will affect the performance of RBFNN for delamination assessment in composites laminates panel because the sensitivity, robustness, and the accuracy of the input factors for the damage are different. Therefore, it is necessary to investigate and choose the best feature as input factors to assess delamination in composite structures. Moreover, it should also be noted that all the result has some errors in delamination parameters estimate. As mentioned above, the performance of

the assessment can be improved by the design of the ANN and the training with more cases.

6.4 Conclusions

This chapter used a type of ANNs named RBFNN combined with different types of input factors from dynamic responses to estimate the delamination in beams and composites laminates panels and investigate the effect of the input factors on the delamination assessment performance. Based on this chapter, there are some conclusions as follows:

1) The proposed method based on the ANN (ANN) can assess delamination and estimate its parameters, including location, size, and depth. However, there is still some error in the testing models which can be polished by improving the structures of ANN with the design and training the ANN by more cases. It should be also noted that the accuracy of different parameters of delamination will vary due to the various effects of various delamination parameters. The errors about the delamination depth are significant due to that the effect of delamination depth is small on the features and input factors.
2) The result shown in this chapter indicates that the input factor will affect the performance of the proposed method for delamination assessment as the result of different features will have various sensitivities, different robustness to the noise, and different accuracy as mentioned in Chapters 4 and 5. Therefore, it is necessary to choose

the best input factors for delamination assessment in composite structures. The proposed method based on CPSTs from sub-signals generated by wavelet packet decomposition is the best type of input factor for now due to the high sensitivity, good robustness, and good accuracy.

This chapter proves the feasibility of the proposed method and indicates the effect of input factors for the proposed method which can be considered to improve the proposed method performance based on the ANN. The proposed methods based on ANN are also potential to detect other types of damage and recognize the type of damage for composite structures.

Chapter 7 CONCLUSIONS

7.1 Conclusions

Some conclusions can be drawn based on this research as follows:

1. The analytical model based on the Green's function method is possible to calculate the vibration characteristics and analyze the dynamic responses of delaminated beams under harmonic excitation. The result demonstrates the accuracy and credibility of the proposed model compared with previous works. It can be seen the difference between the free mode model and the constrained mode model appears when the delamination is not in the mid-plane. Moreover, it should be noted that the deformation of the delaminated beams under excitation of various frequencies will be large when the delamination is located between the peaks of deformation due to the additional axial load generated by the delamination. The result also shows that the effect of delamination on the different parts of the beams is different. Therefore, it is necessary to optimize the measurement locations for delamination assessment based on the dynamic responses of structures with considering the effect of delamination.
2. The effect of sensor locations on the measurement of the dynamic response is investigated and observed as shown in Chapter 3. So the optimization for measurement locations of beams considering the effect of delamination is necessary and significant for the delamination assessment, which can provide a strong signal with less disturbance. It should be noted

that various delamination parameters have different effects on optimization, while the effect of delamination depth is smallest both on the observability and natural frequency. The result also mentioned that the optimal locations for two types of delamination parameters will be close to the result of the parameter with a larger effect on the modal observabilities. Moreover, the optimal measurement locations for delamination depths and sizes are the same calculated based on the free mode model and the constrained mode model. Therefore, the following chapter for the delamination assessment focusing on the size and depth can use the optimal locations without considering the model type.

3. The proposed methods by using the change of the phase space topology of the dynamic responses can be used to detect and assess the delamination in structures. It also should be noted that the size and shape of phase space topology are affected by the delamination, which is related to the frequency and amplitude of the dynamic signals. The change of the phase space structures generated by the various delamination depths is small, while the change generated by the various delamination size is clear due to the different effects generated by these two parameters. The change of phase space topology (CPST), which was used to describe the change of the phase space structures as damage index, is more sensitive to the delamination than the first two modes' natural frequencies. It should be noted that the changing trend of the CPST is monotonic with delamination

depth changing, while the natural frequency will fluctuate, due to the CPST is not the properties of structures and just describing the change of the phase space structures. Therefore, it can be easier to assess delamination depth based on the change of CPST with good credibility. The robustness to the measured noise from the signal of the proposed feature is also tested and demonstrated, which is because this feature is a type of average, which can eliminate the disturbance.

4. The proposed delamination assessment method based on the phase space reconstruction combined with the wavelet decompose method can analyze the vibration signal from structures and provide more information about the delamination. It can be obtained that the phase space structures of different sub-signals have various shapes and sizes due to the different frequencies and amplitude. The phase space topology structures of sub-signals can also show the change of energy distribution of sub-signals in different frequency ranges generated by the delamination. The proposed features named CPST ratio of the sub-signals also have different changing trends with various delaminations. It can be seen that the CPST ratio of the first sub-signal with the lowest frequency will increase, while the other CPST ratio will decrease since the energy distribution is changed by the delamination. So this proposed method can provide more information about the delamination to enhance the accuracy of delamination assessment compared with the previous work using one CPST for one case.

The robustness of this proposed method was also investigated and tested, which shows that although the values of CPSTs are different, the changing trend of the CPST ratio of different sub-signals will not be affected by the noise.

5. The proposed method based on the artificial neural network (ANN) was tested to detect and estimate the delamination in structures without mechanism and theoretical analysis for composite structures. The ANN can establish nonlinear models to investigate the relationship between input factors and targets. The result shows the possibility of this proposed method. It should be noted that the delamination depth is the most difficult to be estimated due to the small effect generated by this parameter on the input factors. The result also shows that the input factors will affect the performance of the delamination assessment based on the ANN due to the various sensitivity, robustness, and accuracy of the input factors to the delamination. For now, the CPSTs from the sub-signals generated by wavelet packet decomposition is the best input factor to the ANN for delamination assessment and calculation, because it can provide more information about the delamination with high sensitivity and good robustness. This proposed method is applicable for different types of damage in various composite structures because it does not need mechanism analysis.

7.2 Future Work

Based on the conclusions of this research, some recommendations for future research are given below:

1. Previous work just analyzes the dynamic responses of delaminated beams. The potential of the Green's function method to solve the dynamic responses of other delaminated structures can be investigated, such as delaminated panels. Moreover, the potential of the Green's function methods to solve the multiple physics fields coupled response has been demonstrated in the previous work [213, 214]. Previous work has analyzed the vibration of intact beams with various coupled loads, such as thermoelastic loads, piezoelectric loads. Following these researches, the multiple-physics fields coupled vibration of delaminated beams can be solved by the Green's function methods, which is useful for functional composite structures;
2. As mentioned in Chapter 1, there are different types of damage in composite structures, including matrix crack and fiber break. Different types of damage will have various effects on the dynamic responses of different locations in the beams, which can not be ignored in the optimization for measurement locations. Therefore, it is necessary to optimize the measurement locations to improve the damage detection for other types of damage of composite structures to enhance the sensitivity and reduce the disturbance by considering the effect of damages. The

beams with other types of damage can still be analyzed to calculate the modal observability and spatial observability to optimize the measurement locations for other types of damage detection and assessment.

3. The proposed methods based on the phase space topology structures, the wavelet methods, and the artificial neural network (ANN) for damage assessment of composites structures need to be developed to detect other types of damage in composite structures. There are different types of damage in composites structures, such as fiber break and matrix crack as mentioned in Chapter 1. This research has demonstrated the feasibility of the proposed method for delamination assessment. The feasibility and accuracy of the proposed method based on the phase space topology analysis and the proposed damage index for other types of damage need to be tested and analyzed.
4. The proposed method for damage assessment based on other types of signals from structures needs to be tested and investigated. Different types of damage will have different effects on the operation of composite structures. Therefore, it is necessary to recognize the damage type. This research has demonstrated the feasibility of the proposed methods to assess the delamination in composite structures with less mechanism analysis based on the ANN. Therefore, it is possible to recognize the damage types in the composite structures by using the ANN with various

input factors.

5. There are different types of characteristics and signals, such as thermal signals, and electric signals, which are useful to detect and assess delamination mentioned in Chapter 1. The potential of the proposed method to analyze the multiple-physic field couple vibration signals to detect damage in composite structures can be investigated. Different types of signals have different advantages. These signals can be analyzed by using the proposed method based on the phase space topology analysis in this research to improve the performance of these methods for damage detection by reducing the noise and enhancing the sensitivity as mentioned in previous work. Furthermore, it should be also noted the phase space topology analysis can be also used for signals in various physics fields, such as electric signal and thermal signal as mentioned in Chapter 1. Therefore, the potential of the phase space topology for multiple physics fields coupled signals analysis can be investigated and tested for damage assessment in function composite structures.

APPENDIX

Matrix T*(i,j)* of the free mode model in Chapter 2

$T(1,1) = \varphi_{11}(L_1);\ T(1,2) = \varphi_{21}(L_1)/k_1;\ T(1,3) = \varphi_{31}(L_1)/k_1^2;\ T(1,4) = \varphi_{41}(L_1)/k_1^3;$

$T(1,5) = -\varphi_{12}(L_1);\ T(1,6) = -\varphi_{22}(L_1)/k_2;\ T(1,7) = -\varphi_{32}(L_1)/k_2^2;\ T(1,8) = -\varphi_{42}(L_1)/k_2^3;$

$T(2,1) = k_1\varphi_{41}(L_1);\ T(2,2) = \varphi_{11}(L_1);\ T(2,3) = \varphi_{21}(L_1)/k_1;\ T(2,4) = \varphi_{31}(L_1)/k_1^2;$

$T(2,5) = -k_2\varphi_{42}(L_1);\ T(2,6) = -\varphi_{12}(L_1);\ T(2,7) = -\varphi_{22}(L_1)/k_2;\ T(2,8) = \varphi_{32}(L_1)/k_2^2;$

$T(3,1) = -E_1I_1k_1^2\varphi_{31}(L_1) - b_1k_1\varphi_{41}(L_1);\ T(3,2) = -E_1I_1k_1\varphi_{41}(L_1) - b_1\varphi_{11}(L_1);$

$T(3,3) = -E_1I_1\varphi_{11}(L_1) - b_1\varphi_{21}(L_1)/k_1;\ T(3,4) = -E_1I_1\varphi_{21}(L_1)/k_1 - b_1\varphi_{31}(L_1)/k_1^2;$

$T(3,5) = E_2I_2k_2^2\varphi_{32}(L_1);\ T(3,6) = E_2I_2k_2\varphi_{42}(L_1);\ T(3,7) = E_2I_2\varphi_{12}(L_1);$

$T(3,8) = E_2I_2\varphi_{22}(L_1)/k_2;\ T(3,9) = E_3I_3k_3^2\varphi_{33}(L_1);\ T(3,10) = E_3I_3k_3\varphi_{43}(L_1);$

$T(3,11) = E_3I_3\varphi_{13}(L_1);\ T(3,12) = E_3I_3\varphi_{23}(L_1)/k_3;\ T(3,13) = b_1k_4\varphi_{44}(L_2);\ T(3,14) =$

$b_1\varphi_{14}(L_2);\ T(3,15) = b_1\varphi_{24}(L_2)/k_4;\ T(3,16) = b_1\varphi_{34}(L_2)/k_4^2;$

$T(4,1) = -E_1I_1k_1^3\varphi_{21}(L_1);\ T(4,2) = -E_1I_1k_1^2\varphi_{31}(L_1);\ T(4,3) = -E_1I_1k_1\varphi_{41}(L_1);$

$T(4,4) = -E_1I_1\varphi_{11}(L_1);\ T(4,5) = E_2I_2k_2^3\varphi_{22}(L_1);\ T(4,6) = E_2I_2k_2^2\varphi_{32}(L_1);$

$T(4,7) = E_2I_2k_2\varphi_{42}(L_1);\ T(4,8) = E_2I_2\varphi_{12}(L_1);\ T(4,9) = E_3I_3k_3^3\varphi_{23}(L_1);\ T(4,10) =$

$E_3I_3k_3^2\varphi_{33}(L_1);\ T(4,11) = E_3I_3k_3\varphi_{43}(L_1);\ T(4,12) = E_3I_3\varphi_{13}(L_1);$

$T(5,1) = \varphi_{11}(L_1);\ T(5,2) = \varphi_{21}(L_1)/k_1;\ T(5,3) = \varphi_{31}(L_1)/k_1^2;\ T(5,4) = \varphi_{41}(L_1)/k_1^3;$

$T(5,9) = -\varphi_{13}(L_1);\ T(5,10) = -\varphi_{23}(L_1)/k_3;\ T(5,11) = -\varphi_{33}(L_1)/k_3^2;\ T(5,12) = -\varphi_{43}(L_1)/k_3^3;$

$T(6,1) = k_1\varphi_{41}(L_1);\ T(6,2) = \varphi_{11}(L_1);\ T(6,3) = \varphi_{21}(L_1)/k_1\,;\ T(6,4) = \varphi_{31}(L_1)/k_1^2\,;$

$T(6,9) = -\,k_3\varphi_{43}(L_1);\ T(6,10) = -\,\varphi_{13}(L_1);\ T(6,11) = -\varphi_{23}(L_1)/k_3\,;\ T(6,12) = \varphi_{33}(L_1)/k_3^2;$

$T(7,5) = -\,\varphi_{12}(L_2);\ T(7,6) = -\varphi_{22}(L_2)/k_2\,;\ T(7,7) = -\,\varphi_{32}(L_2)/k_2^2\,;\ T(7,8) = -\varphi_{42}(L_2)/k_2^3\,;$

$T(7,13) = \varphi_{14}(L_2);\ T(7,14) = \varphi_{24}(L_2)/k_4\,;\ T(7,15) = \varphi_{34}(L_2)/k_2^2\,;\ T(7,16) = \varphi_{44}(L_2)/k_4^3\,;$

$T(8,9) = -\,\varphi_{13}(L_2);\ T(8,10) = -\varphi_{23}(L_2)/k_3\,;\ T(8,11) = -\,\varphi_{33}(L_2)/k_3^2\,;\ T(8,12) = -\varphi_{43}(L_2)/k_3^3;$

$T(8,13) = \varphi_{14}(L_2);\ T(8,14) = \varphi_{24}(L_2)/k_4\,;\ T(8,15) = \varphi_{34}(L_2)/k_4^2\,;\ T(8,16) = \varphi_{44}(L_2)/k_4^3\,;$

$T(9,5) = -\,k_2\varphi_{42}(L_2);\ T(9,6) = -\,\varphi_{12}(L_2);\ T(9,7) = -\varphi_{22}(L_2)/k_2\,;\ T(9,8) = \varphi_{32}(L_2)/k_2^2\,;$

$T(9,13) = k_4\varphi_{44}(L_2);\ T(9,14) = \varphi_{14}(L_2);\ T(9,15) = \varphi_{24}(L_2)/k_4\,;\ T(9,16) = \varphi_{34}(L_2)/k_4^2\,;$

$T(10,9) = -\,k_3\varphi_{43}(L_2);\ T(10,10) = -\,\varphi_{13}(L_2);\ T(10,11) = -\varphi_{23}(L_2)/k_3\,;\ T(10,12) =$

$\varphi_{33}(L_2)/k_3^2\,;$

$T(10,13) = k_4\varphi_{44}(L_2);\ T(10,14) = \varphi_{14}(L_2);\ T(10,15) = \varphi_{24}(L_2)/k_4\,;\ T(10,16) = \varphi_{34}(L_2)/k_4^2\,;$

$T(11,1) = -\,b_4k_1\varphi_{41}(L_1);\ T(11,2) = -b_4\varphi_{11}(L_1);\ T(11,3) = -b_4\varphi_{21}(L_1)/k_1;$

$T(11,4) = -b_4\varphi_{31}(L_1)/k_1^2;$

$T(11,5) = E_2I_2k_2^2\varphi_{32}(L_2);\ T(11,6) = E_2I_2k_2\varphi_{42}(L_2);\ T(11,7) = E_2I_2\varphi_{12}(L_2);$

$T(11,8) = E_2I_2\varphi_{22}(L_2)/k_2\,;\ T(11,9) = E_3I_3k_3^2\varphi_{33}(L_2);\ T(11,10) = E_3I_3k_3\varphi_{43}(L_2);$

$T(11,11) = E_3I_3\varphi_{13}(L_2);\ T(11,12) = E_3I_3\varphi_{23}(L_2)/k_3\,;\ T(11,13) = -\,E_4I_4k_4^2\varphi_{34}(L_2) +$

$b_4k_4\varphi_{44}(L_2);\ T(11,14) = -\,E_4I_4k_4\varphi_{44}(L_2) + b_4\varphi_{14}(L_2);\ T(11,15) = -\,E_4I_4\varphi_{14}(L_2) + b_4\varphi_{24}(L_2)/$

k_4;

$T(11,16) = -E_4I_4\varphi_{44}(L_2)/k_4 + b_4\varphi_{34}(L_2)/k_4^2$;

$T(12,5) = E_2I_2k_2^3\varphi_{22}(L_2)$; $T(12,6) = E_2I_2k_2^2\varphi_{32}(L_2)$; $T(12,7) = E_2I_2k_2\varphi_{42}(L_2)$;

$T(12,8) = E_2I_2\varphi_{12}(L_2)$; $T(12,9) = E_3I_3k_3^3\varphi_{23}(L_2)$; $T(12,10) = E_3I_3k_3^2\varphi_{33}(L_2)$;

$T(12,11) = E_3I_3k_3\varphi_{43}(L_2)$; $T(12,12) = E_3I_3\varphi_{13}(L_2)$; $T(12,13) = -E_4I_4k_4^3\varphi_{24}(L_2)$;

$T(12,14) = -E_4I_4k_4^2\varphi_{34}(L_2)$; $T(12,15) = -E_4I_4k_4\varphi_{44}(L_2)$; $T(12,16) = -E_4I_4\varphi_{14}(L_2)$;

$T(13,1) = \varphi_{11}(0)$; $T(13,2) = \varphi_{21}(0)/k_1$; $T(13,3) = \varphi_{31}(0)/k_1^2$; $T(13,4) = \varphi_{41}(0)/k_1^3$;

$T(14,1) = k_1\varphi_{41}(0)$; $T(14,2) = \varphi_{11}(0)$; $T(14,3) = \varphi_{21}(0)/k_1$; $T(14,4) = \varphi_{31}(0)/k_1^2$;

$T(15,13) = \varphi_{14}(L)$; $T(15,14) = \varphi_{24}(L)/k_4$; $T(15,15) = \varphi_{34}(L)/k_4^2$; $T(15,16) = \varphi_{44}(L)/k_4^3$;

$T(16,13) = k_4\varphi_{44}(L)$; $T(16,14) = \varphi_{14}(L)$; $T(16,15) = \varphi_{24}(L)/k_4$; $T(16,16) = \varphi_{34}(L)/k_4^2$;

Matrix S*(i,j)* of the free mode model in Chapter 2

$S(1,1) = -\frac{\varphi_{41}(l_1-\xi)H(l_1-\xi)}{k_1^3E_1I_1} + \frac{\varphi_{42}(l_1-\xi)H(l_1-\xi)}{k_2^3E_2I_2}$

$S(2,1) = -\frac{\varphi_{31}(l_1-\xi)H(l_1-\xi)}{k_1^2E_1I_1} + \frac{\varphi_{32}(l_1-\xi)H(l_1-\xi)}{k_2^2E_2I_2}$

$S(3,1) = \frac{\varphi_{21}(l_1-\xi)H(l_1-\xi)}{k_1} - \frac{\varphi_{22}(l_1-\xi)H(l_1-\xi)}{k_2} - \frac{\varphi_{23}(l_1-\xi)H(l_1-\xi)}{k_3} - b_1\bullet\left(\frac{\varphi_{34}(l_2-\xi)H(l_2-\xi)}{k_4^2E_4I_4} - \frac{\varphi_{31}(l_1-\xi)H(l_1-\xi)}{k_4^2E_1I_1}\right)$

$S(4,1) = \varphi_{11}(l_1-\xi)H(l_1-\xi) - \varphi_{12}(l_1-\xi)H(l_1-\xi) - \varphi_{13}(l_1-\xi)H(l_1-\xi)$

$S(5,1) = -\frac{\varphi_{41}(l_1-\xi)H(l_1-\xi)}{k_1^3E_1I_1} + \frac{\varphi_{43}(l_1-\xi)H(l_1-\xi)}{k_3^3E_3I_3}$

$S(6,1) = -\frac{\varphi_{31}(l_1-\xi)H(l_1-\xi)}{k_1^2E_1I_1} + \frac{\varphi_{33}(l_1-\xi)H(l_1-\xi)}{k_3^2E_3I_3}$

$$S(7,1) = -\frac{\varphi_{44}(l_2-\xi)H(l_2-\xi)}{k_4^3 E_4 I_4} + \frac{\varphi_{42}(l_2-\xi)H(l_2-\xi)}{k_2^3 E_2 I_2}$$

$$S(8,1) = -\frac{\varphi_{44}(l_2-\xi)H(l_2-\xi)}{k_4^3 E_4 I_4} + \frac{\varphi_{43}(l_2-\xi)H(l_2-\xi)}{k_3^3 E_3 I_3}$$

$$S(9,1) = -\frac{\varphi_{34}(l_2-\xi)H(l_2-\xi)}{k_4^2 E_4 I_4} + \frac{\varphi_{32}(l_2-\xi)H(l_2-\xi)}{k_2^2 E_2 I_2}$$

$$S(10,1) = -\frac{\varphi_{34}(l_2-\xi)H(l_2-\xi)}{k_4^2 E_4 I_4} + \frac{\varphi_{33}(l_2-\xi)H(l_2-\xi)}{k_3^2 E_3 I_3}$$

$$S(11,1) = \frac{\varphi_{24}(l_2-\xi)H(l_2-\xi)}{k_4} - \frac{\varphi_{22}(l_2-\xi)H(l_2-\xi)}{k_2} - \frac{\varphi_{23}(l_2-\xi)H(l_2-\xi)}{k_3} + b_4 \bullet \left(\frac{\varphi_{31}(l_1-\xi)H(l_1-\xi)}{k_1^2 E_1 I_1} - \frac{\varphi_{34}(l_2-\xi)H(l_2-\xi)}{k_4^2 E_4 I_4}\right)$$

$$S(12,1) = \varphi_{14}(l_2-\xi)H(l_2-\xi) - \varphi_{12}(l_2-\xi)H(l_2-\xi) - \varphi_{13}(l_2-\xi)H(l_2-\xi)$$

$$S(13,1) = -\frac{\varphi_{41}(0-\xi)H(0-\xi)}{k_1^3 E_1 I_1}$$

$$S(14,1) = -\frac{\varphi_{31}(0-\xi)H(0-\xi)}{k_1^2 E_1 I_1}$$

$$S(15,1) = -\frac{\varphi_{44}(L-\xi)H(L-\xi)}{k_4^3 E_4 I_4}$$

$$S(16,1) = -\frac{\varphi_{34}(L-\xi)H(L-\xi)}{k_4^2 E_4 I_4}$$

where

$$b_1 = b_4 = \frac{(H_2+H_3)E_2A_2E_3A_3}{4a(E_2A_2+E_3A_3)}$$

Matrix T*(i,j)* of the constrained mode model in Chapter 2

$$T(1,1) = \varphi_{11}(L_1);\ T(1,2) = \varphi_{21}(L_1)/k_1;\ T(1,3) = \varphi_{31}(L_1)/k_1^2;\ T(1,4) = \varphi_{41}(L_1)/k_1^3;$$

$$T(1,5) = -\varphi_{12}(L_1);\ T(1,6) = -\varphi_{22}(L_1)/k_2;\ T(1,7) = -\varphi_{32}(L_1)/k_2^2;\ T(1,8) = -\varphi_{42}(L_1)/k_2^3;$$

$$T(2,1) = k_1\varphi_{41}(L_1);\ T(2,2) = \varphi_{11}(L_1);\ T(2,3) = \varphi_{21}(L_1)/k_1;\ T(2,4) = \varphi_{31}(L_1)/k_1^2;$$

$$T(2,5) = -k_2\varphi_{42}(L_1);\ T(2,6) = -\varphi_{12}(L_1);\ T(2,7) = -\varphi_{22}(L_1)/k_2;\ T(2,8) = \varphi_{32}(L_1)/k_2^2;$$

$$T(3,1) = -E_1I_1k_1^2\varphi_{31}(L_1) - b_1k_1\varphi_{41}(L_1);\ T(3,2) = -E_1I_1k_1\varphi_{41}(L_1) - b_1\varphi_{11}(L_1);$$

$$T(3,3) = -E_1I_1\varphi_{11}(L_1) - b_1\varphi_{21}(L_1)/k_1;\ T(3,4) = -E_1I_1\varphi_{21}(L_1)/k_1 - b_1\varphi_{31}(L_1)/k_1^2;$$

$T(3,5) = (E_2I_2 + E_3I_3)k_2^2\varphi_{32}(L_1);\ T(3,6) = (E_2I_2 + E_3I_3)k_2\varphi_{42}(L_1);$

$T(3,7) = (E_2I_2 + E_3I_3)\varphi_{12}(L_1);\ T(3,8) = (E_2I_2+E_3I_3)\varphi_{22}(L_1)/k_2\,;\ T(3,9) = b_1k_4\varphi_{44}(L_2);$

$T(3,10) = b_1\varphi_{14}(L_2);\ T(3,11) = b_1\varphi_{24}(L_2)/k_4;\ T(3,12) = b_1\varphi_{34}(L_2)/k_4^2\,;$

$T(4,1) = -E_1I_1k_1^3\varphi_{21}(L_1);\ T(4,2) = -E_1I_1k_1^2\varphi_{31}(L_1);\ T(4,3) = -E_1I_1k_1\varphi_{41}(L_1);$

$T(4,4) = -E_1I_1\varphi_{11}(L_1);\ T(4,5) = (E_2I_2 + E_3I_3)k_2^3\varphi_{22}(L_1);\ T(4,6) = (E_2I_2 + E_3I_3)k_2^2\varphi_{32}(L_1);$

$T(4,7) = (E_2I_2 + E_3I_3)k_2\varphi_{42}(L_1);\ T(4,8) = (E_2I_2 + E_3I_3)\varphi_{12}(L_1);$

$T(5,5) = -\varphi_{12}(L_2);\ T(5,6) = -\varphi_{22}(L_2)/k_2\,;\ T(5,7) = -\varphi_{32}(L_2)/k_2^2\,;\ T(5,8) = -\varphi_{42}(L_2)/k_2^3\,;$

$T(5,9) = \varphi_{14}(L_2);\ T(5,10) = \varphi_{24}(L_2)/k_4\,;\ T(5,11) = \varphi_{34}(L_2)/k_2^2\,;\ T(5,12) = \varphi_{44}(L_2)/k_4^3\,;$

$T(6,5) = -k_2\varphi_{42}(L_2);\ T(6,6) = -\varphi_{12}(L_2);\ T(6,7) = -\varphi_{22}(L_2)/k_2\,;\ T(6,8) = \varphi_{32}(L_2)/k_2^2\,;$

$T(6,9) = k_4\varphi_{44}(L_2);\ T(6,10) = \varphi_{14}(L_2);\ T(6,11) = \varphi_{24}(L_2)/k_4\,;\ T(6,12) = \varphi_{34}(L_2)/k_4^2\,;$

$T(7,1) = -b_4k_1\varphi_{41}(L_1);\ T(7,2) = -b_4\varphi_{11}(L_1);\ T(7,3) = -b_4\varphi_{21}(L_1)/k_1;$

$T(7,4) = -b_4\varphi_{31}(L_1)/k_1^2\,;$

$T(7,5) = (E_2I_2 + E_3I_3)k_2^2\varphi_{32}(L_2);\ T(7,6) = (E_2I_2 + E_3I_3)k_2\varphi_{42}(L_2);$

$T(7,7) = (E_2I_2 + E_3I_3)\varphi_{12}(L_2);\ T(7,8) = (E_2I_2+E_3I_3)\varphi_{22}(L_2)/k_2\,;$

$T(7,9) = -E_4I_4k_4^2\varphi_{34}(L_2) + b_4k_4\varphi_{44}(L_2);\ T(7,10) = -E_4I_4k_4\varphi_{44}(L_2) + b_4\varphi_{14}(L_2);$

$T(7,11) = -E_4I_4\varphi_{14}(L_2) + b_4\varphi_{24}(L_2)/k_4;\ T(7,12) = -E_4I_4\varphi_{44}(L_2)/k_4+b_4\varphi_{34}(L_2)/k_4^2\,;$

$T(8,5) = (E_2I_2 + E_3I_3)k_2^3\varphi_{22}(L_2);\ T(8,6) = (E_2I_2 + E_3I_3)k_2^2\varphi_{32}(L_2);$

$T(8,7) = (E_2I_2 + E_3I_3)k_2\varphi_{42}(L_2);\ T(8,8) = (E_2I_2 + E_3I_3)\ \varphi_{12}(L_2);\ T(8,9) = -E_4I_4k_4^3\varphi_{24}(L_2);$

$T(8,10) = -E_4I_4k_4^2\varphi_{34}(L_2);\ T(8,11) = -E_4I_4k_4\varphi_{44}(L_2);\ T(8,12) = -E_4I_4\varphi_{14}(L_2);$

$T(9,1) = \varphi_{11}(0);\ T(9,2) = \varphi_{21}(0)/k_1;\ T(9,3) = \varphi_{31}(0)/k_1^2;\ T(9,4) = \varphi_{41}(0)/k_1^3;$

$T(10,1) = k_1\varphi_{41}(0);\ T(10,2) = \varphi_{11}(0);\ T(10,3) = \varphi_{21}(0)/k_1;\ T(10,4) = \varphi_{31}(0)/k_1^2;$

$T(11,9) = \varphi_{14}(L);\ T(11,10) = \varphi_{24}(L)/k_4;\ T(11,11) = \varphi_{34}(L)/k_4^2;\ T(11,12) = \varphi_{44}(L)/k_4^3;$

$T(12,9) = k_4\varphi_{44}(L);\ T(12,10) = \varphi_{14}(L);\ T(12,11) = \varphi_{24}(L)/k_4;\ T(12,12) = \varphi_{34}(L)/k_4^2;$

Matrix T*(i,j)* of the constrained mode model in Chapter 2

$S(1,1) = -\frac{\varphi_{41}(l_1-\xi)H(l_1-\xi)}{k_1^3E_1I_1} + \frac{\varphi_{42}(l_1-\xi)H(l_1-\xi)}{k_2^3E_2I_2}$

$S(2,1) = -\frac{\varphi_{31}(l_1-\xi)H(l_1-\xi)}{k_1^2E_1I_1} + \frac{\varphi_{32}(l_1-\xi)H(l_1-\xi)}{k_2^2E_2I_2}$

$S(3,1) = \frac{\varphi_{21}(l_1-\xi)H(l_1-\xi)}{k_1} - \frac{\varphi_{22}(l_1-\xi)H(l_1-\xi)}{k_2} - b_1\bullet\left(\frac{\varphi_{34}(l_2-\xi)H(l_2-\xi)}{k_4^2E_4I_4} - \frac{\varphi_{31}(l_1-\xi)H(l_1-\xi)}{k_4^2E_1I_1}\right)$

$S(4,1) = \varphi_{11}(l_1-\xi)H(l_1-\xi) - \varphi_{12}(l_1-\xi)H(l_1-\xi)$

$S(5,1) = -\frac{\varphi_{44}(l_2-\xi)H(l_2-\xi)}{k_4^3E_4I_4} + \frac{\varphi_{42}(l_2-\xi)H(l_2-\xi)}{k_2^3E_2I_2}$

$S(6,1) = -\frac{\varphi_{34}(l_2-\xi)H(l_2-\xi)}{k_4^2E_4I_4} + \frac{\varphi_{32}(l_2-\xi)H(l_2-\xi)}{k_2^2E_2I_2}$

$S(7,1) = \frac{\varphi_{21}(l_1-\xi)H(l_1-\xi)}{k_1} - \frac{\varphi_{22}(l_1-\xi)H(l_1-\xi)}{k_2} + b_4\bullet\left(\frac{\varphi_{31}(l_1-\xi)H(l_1-\xi)}{k_1^2E_1I_1} - \frac{\varphi_{34}(l_2-\xi)H(l_2-\xi)}{k_4^2E_4I_4}\right)$

$S(8,1) = \varphi_{14}(l_2-\xi)H(l_2-\xi) - \varphi_{12}(l_2-\xi)H(l_2-\xi)$

$S(9,1) = -\frac{\varphi_{41}(0-\xi)H(0-\xi)}{k_1^3E_1I_1}$

$S(10,1) = -\frac{\varphi_{31}(0-\xi)H(0-\xi)}{k_1^2E_1I_1}$

$S(11,1) = -\frac{\varphi_{44}(L-\xi)H(L-\xi)}{k_4^3E_4I_4}$

$$S(12,1) = -\frac{\varphi_{34}(L-\xi)H(L-\xi)}{k_4^2 E_4 I_4}$$

$$b_1 = b_4 = \frac{(H_2+H_3)E_2A_2E_3A_3}{4a(E_2A_2+E_3A_3)}$$

REFERENCE

1. Castanie, B., C. Bouvet, and M. Ginot, *Review of composite sandwich structure in aeronautic applications.* Composites Part C: Open Access, 2020. **1**: p. 100004.

2. Koli, D.K., G. Agnihotri, and R. Purohit, *Advanced Aluminium Matrix Composites: The Critical Need of Automotive and Aerospace Engineering Fields.* Materials Today: Proceedings, 2015. **2**(4-5): p. 3032-3041.

3. Ikutegbe, C.A. and M.M. Farid, *Application of phase change material foam composites in the built environment: A critical review.* Renewable and Sustainable Energy Reviews, 2020. **131**: p. 110008.

4. Egbo, M.K., *A fundamental review on composite materials and some of their applications in biomedical engineering.* Journal of King Saud University - Engineering Sciences, 2020.

5. Panigrahy, S. and B. Kandasubramanian, *Polymeric thermoelectric PEDOT: PSS & composites: Synthesis, progress, and applications.* European Polymer Journal, 2020. **132**: p. 109726.

6. Garg, P., et al., *Advance research progresses in aluminium matrix composites: manufacturing & applications.* Journal of Materials Research and Technology, 2019.

7. Khan, M.Z.R., S.K. Srivastava, and M.K. Gupta, *A state-of-the-art review on particulate wood polymer composites: Processing, properties and applications.* Polymer Testing, 2020. **89**: p. 106721.

8. Gialanella S, M.A., *Aerospace Alloys*. 2020.

9. González, C., et al., *Structural composites for multifunctional applications: Current challenges and future trends.* Progress in Materials Science, 2017. **89**: p. 194-251.

10. Giurgiutiu, V., *7.19 Smart Materials and Health Monitoring of Composites.* 2018: p. 364-381.

11. Miclos, S., et al., *Transverse mechanical stress and optical birefringence induced into single-mode optical fibre embedded in a smart polymer composite material.* Composite Structures, 2019. **218**: p. 15-26.

12. Paul, B.B.K.E.H., *Prototyping materials experience: Towards a shared understanding of underdeveloped smart material composites.* International Journal of Design, 2019. **13**(2): p. 18.

13. Sideris, E.A. and H.C. de Lange, *Pumps operated by solid-state electromechanical smart material actuators - A review.* Sensors and Actuators A: Physical, 2020. **307**: p. 111915.

14. Towsyfyan, H., et al., *Successes and challenges in non-destructive testing of aircraft composite structures.* Chinese Journal of Aeronautics, 2019.

15. Cepero-Mejías, F., et al., *Review of recent developments and induced damage assessment in the modelling of the machining of long fibre reinforced polymer composites.* Composite Structures, 2020. **240**: p. 112006.

16. Geng, D., et al., *Delamination formation, evaluation and suppression during drilling of composite laminates: A review.* Composite Structures, 2019. **216**: p. 168-186.

17. Lou, X., et al., *Failure analysis of composite laminate under low-velocity impact based on micromechanics of failure.* Composite Structures, 2017. **163**: p. 238-247.

18. Pakdel, H. and B. Mohammadi, *Stiffness degradation of composite laminates due to matrix cracking and induced delamination during tension-tension fatigue.* Engineering Fracture Mechanics, 2019. **216**: p. 106489.

19. Wang, Y., *Multiphysics analysis of lightning strike damage in laminated carbon/glass fiber reinforced polymer matrix composite materials: A review of problem formulation and computational modeling.* Composites Part A: Applied Science and Manufacturing, 2017. **101**: p. 543-553.

20. Schwartzentruber, J., M. Papini, and J.K. Spelt, *Characterizing and modelling delamination of carbon-fiber epoxy laminates during abrasive waterjet cutting.* Composites Part A: Applied Science and Manufacturing, 2018. **112**: p. 299-314.

21. Khan, R., et al., *Effect of stress ratio or mean stress on fatigue delamination growth in composites: Critical review.* Composite Structures, 2015. **124**: p. 214-227.

22. Della, C.N. and D. Shu, *Vibration of Delaminated Composite Laminates: A Review.* Applied Mechanics Reviews, 2007. **60**(1): p. 1.

23. Venkate Gowda, C., N. Rajanna, and N.G.S. Udupa, *Investigating the effects of delamination location and size on the vibration behaviour of laminated composite beams.* Materials Today: Proceedings, 2017. **4**(10): p. 10944-10951.

24. Shankar, G., S. Keshava Kumar, and P.K. Mahato, *Vibration analysis and control of smart composite plates with delamination and under hygrothermal environment.* Thin-Walled Structures, 2017. **116**: p. 53-68.

25. Parhi, P.K., S.K. Bhattacharyya, and P.K. Sinha, *Dynamic analysis of multiple delaminated composite twisted plates.* Aircraft Engineering and Aerospace Technology, 1999. **71**(5): p. 451-461.

26. Jafari-Talookolaei R A, K.M.H., Ahmadian M T. Ahmadian, M. Abedi, *Dynamic response of a delaminated beam due to a moving force*. 2012.

27. Kargarnovin, M.H., M.T. Ahmadian, and R.A. Jafari-Talookolaeia, *Forced vibration of delaminated Timoshenko beams subjected to a moving load.* Science and Engineering of Composite Materials, 2012. **19**(2): p. 145-157.

28. Wang J T S, L.Y.Y., Gibby J A., *Vibrations of split beams.* Journal of Sound and Vibration, 1982. **84**(4): p. 12.

29. Mujumdar P M, S.S., *Flexural vibrations of beams with delaminations.* Journal of sound and vibration, 1988. **125**(3): p. 21.

30. Shen, M.H. and J. Grady, *Free vibrations of delaminated beams.* 1991.

31. Torabi, K., M. Shariati-Nia, and M. Heidari-Rarani, *Experimental and theoretical investigation on transverse vibration of delaminated cross-ply composite beams.* International Journal of Mechanical Sciences, 2016. **115-116**: p. 1-11.

32. Ju F, L.H.P., Lee K H, *Dynamic response of delaminated composite beams with intermittent contact in delaminated segments.* Composites Engineering, 1994. **4**: p. 14.

33. Luo H , H.S., *Dynamics of delaminated beams.* International Journal of Solids and Structures, 2000. **37**(10): p. 19.

34. Jafari-Talookolaei, R.-A., M. Abedi, and M. Hajianmaleki, *Vibration characteristics of generally laminated composite curved beams with single through-the-width delamination.* Composite Structures, 2016. **138**: p. 172-183.

35. Hasan Callioglu, G.A., *Vibration analysis of delaminated composite beams using analytical and FEM models.* Indian Journal of Engineering & Materials Sciences, 2011. **18**(1): p. 8.

36. Ju F, L.H.P., Lee K H, *Dynamic response of delaminated composite beams with intermittent contact in delaminated segments.* Composites Engineering, 1994. **4**(12): p. 14.

37. Ostachowicz W, Ż.A., *Vibration of a laminated beam with a delamination including contact effects.* Shock and Vibration, 2004. **11**: p. 15.

38. Manoach, E., et al., *Dynamics of a laminated composite beam with delamination and inclusions.* The European Physical Journal Special Topics, 2013. **222**(7): p. 1649-1664.

39. Kargarnovin M H, A.M.T., Jafari-Talookolaei R A, *Forced Vibration of Delaminated Timoshenko Beams under the Action of Moving Oscillatory Mass.* Shock and Vibration, 2013. **20**(1): p. 17.

40. Jafari-Talookolaei, R.-A., M.H. Kargarnovin, and M.T. Ahmadian, *Dynamic response of a delaminated composite beam with general lay-ups based on the first-order shear deformation theory.* Composites Part B: Engineering, 2013. **55**: p. 65-78.

41. Kargarnovin, M.H., R.A. Jafari-Talookolaei, and M.T. Ahmadian, *Vibration analysis of delaminated Timoshenko beams under the motion of a constant amplitude point force traveling with uniform velocity.* International Journal of Mechanical Sciences, 2013. **70**: p. 39-49.

42. Radu A G, C.A., *Dynamic stability analysis of composite plates including delaminations using a higher order theory and transformation matrix approach.* International Journal of Solids and Structures, 2002 **39**(7): p. 17.

43. Marjanović, M. and D. Vuksanović, *Layerwise solution of free vibrations and buckling of laminated composite and sandwich plates with embedded delaminations.* Composite Structures, 2014. **108**: p. 9-20.

44. Oh, J., M. Cho, and J.-S. Kim, *Dynamic analysis of composite plate with multiple delaminations based on higher-order zigzag theory.* International Journal of Solids and Structures, 2005. **42**(23): p. 6122-6140.

45. Mondal, S. and L.S. Ramachandra, *Dynamic instability of damped composite plates with embedded delaminations.* Journal of Sound and Vibration, 2019. **455**: p. 221-240.

46. S, G., *A review of non-destructive testing methods of composite materials.* Procedia Structural Integrity, 2016. **1**: p. 8.

47. Diamanti, K. and C. Soutis, *Structural health monitoring techniques for aircraft composite structures.* Progress in Aerospace Sciences, 2010. **46**(8): p. 342-352.

48. Wei, F. and Q. Pizhong, *Vibration-based Damage Identification Methods: A Review and Comparative Study.* Structural Health Monitoring: An International Journal, 2010. **10**(1): p. 83-111.

49. Das, S., P. Saha, and S.K. Patro, *Vibration-based damage detection techniques used for health monitoring of structures: a review.* Journal of Civil Structural Health Monitoring, 2016. **6**(3): p. 477-507.

50. Tate, I.V., S. Roy, and K.R. Jagtap, *Delamination Detection of Composite Cantilever Beam Coupled With Piezoelectric Transducer Using Natural Frequency Deviation.* Procedia Engineering, 2014. **97**: p. 1293-1304.

51. Yang, C. and S.O. Oyadiji, *Detection of delamination in composite beams using frequency deviations due to concentrated mass loading.* Composite Structures, 2016. **146**: p. 1-13.

52. Zhang, Z., et al., *Vibration-based inverse algorithms for detection of delamination in composites.* Composite Structures, 2013. **102**: p. 226-236.

53. Zhang, Z., et al., *Vibration-based assessment of delaminations in FRP composite plates.* Composites Part B: Engineering, 2018. **144**: p. 254-266.

54. Zhang, Z., et al., *Vibration-based delamination detection in curved composite plates.* Composites Part A: Applied Science and Manufacturing, 2019. **119**: p. 261-274.

55. Qiao, P., et al., *Curvature mode shape-based damage detection in composite laminated plates.* Composite Structures, 2007. **80**(3): p. 409-428.

56. Cao, M.S., et al., *Multiscale shear-strain gradient for detecting delamination in composite laminates.* Applied Physics Letters, 2013. **103**(10): p. 101910.

57. Xu, W., et al., *Delamination monitoring in CFRP laminated plates under noisy conditions using complex-wavelet 2D curvature mode shapes.* Smart Materials and Structures, 2017. **26**(10): p. 104008.

58. Xu, W., et al., *A noise-robust damage indicator for characterizing singularity of mode shapes for incipient delamination identification in CFRP laminates.* Mechanical Systems and Signal Processing, 2019. **121**: p. 183-200.

59. Manoach, E., et al., *Vibration based damage detection in composite beams under temperature variations using Poincaré maps.* International Journal of Mechanical Sciences, 2012. **62**(1): p. 120-132.

60. Khan, A., et al., *Structural vibration-based classification and prediction of delamination in smart composite laminates using deep learning neural network.* Composites Part B: Engineering, 2019. **161**: p. 586-594.

61. Bayissa, W.L., N. Haritos, and S. Thelandersson, *Vibration-based structural damage identification using wavelet transform.* Mechanical Systems and Signal Processing, 2008. **22**(5): p. 1194-1215.

62. Yam, L.H., Y.J. Yan, and J.S. Jiang, *Vibration-based damage detection for composite structures using wavelet transform and neural network identification.* Composite Structures, 2003. **60**(4): p. 403-412.

63. Trendafilova, I. and E. Manoach, *Vibration-based damage detection in plates by using time series analysis.* Mechanical Systems and Signal Processing, 2008. **22**(5): p. 1092-1106.

64. Abdeljaber, O., et al., *Real-time vibration-based structural damage detection using one-dimensional convolutional neural networks.* Journal of Sound and Vibration, 2017. **388**: p. 154-170.

65. Raghavan, A. and C.E.S. Cesnik, *Review of Guided-wave Structural Health Monitoring.* The Shock and Vibration Digest, 2007. **39**(2): p. 91-114.

66. Su, Z., L. Ye, and Y. Lu, *Guided Lamb waves for identification of damage in composite structures: A review.* Journal of Sound and Vibration, 2006. **295**(3-5): p. 753-780.

67. Shoja, S., V. Berbyuk, and A. Boström, *Delamination detection in composite laminates using low frequency guided waves: Numerical simulations.* Composite Structures, 2018. **203**: p. 826-834.

68. De Luca, A., et al., *Guided wave SHM system for damage detection in complex composite structure.* Theoretical and Applied Fracture Mechanics, 2020. **105**: p. 102408.

69. Yelve, N.P., M. Mitra, and P.M. Mujumdar, *Detection of delamination in composite laminates using Lamb wave based nonlinear method.* Composite Structures, 2017. **159**: p. 257-266.

70. Soleimanpour, R. and C.-T. Ng, *Locating delaminations in laminated composite beams using nonlinear guided waves.* Engineering Structures, 2017. **131**: p. 207-219.

71. Zhao, G., et al., *Detection and monitoring of delamination in composite laminates using ultrasonic guided wave.* Composite Structures, 2019. **225**: p. 111161.

72. Yu, X., M. Ratassepp, and Z. Fan, *Damage detection in quasi-isotropic composite bends using ultrasonic feature guided waves.* Composites Science and Technology, 2017. **141**: p. 120-129.

73. Feng, B., A.L. Ribeiro, and H.G. Ramos, *A new method to detect delamination in composites using chirp-excited Lamb wave and wavelet analysis.* NDT & E International, 2018. **100**: p. 64-73.

74. Sun, G. and Z. Zhou, *Application of laser ultrasonic technique for non-contact detection of drilling-induced delamination in aeronautical composite components.* Optik, 2014. **125**(14): p. 3608-3611.

75. Duan, Y., et al., *Reliability assessment of pulsed thermography and ultrasonic testing for impact damage of CFRP panels.* NDT & E International, 2019. **102**: p. 77-83.

76. Sadeghi, M.Z., et al., *Damage detection by double-sided ultrasonic assessment in low-velocity impacted CFRP plates.* Composite Structures, 2019. **208**: p. 646-655.

77. Teng, G., et al., *A Nonlinear Method for Characterizing Discrete Defects in Thick Multilayer Composites.* Applied Sciences, 2019. **9**(6): p. 1183.

78. Hauffe, A., F. Hähnel, and K. Wolf, *Comparison of algorithms to quantify the damaged area in CFRP ultrasonic scans.* Composite Structures, 2020. **235**: p. 111791.

79. Le, M., et al., *B-scan ultrasonic testing of rivets in multilayer structures based on short-time Fourier transform analysis.* Measurement, 2018. **128**: p. 495-503.

80. Zhang, Z., et al., *Ultrasonic detection and characterization of delamination and rich resin in thick composites with waviness.* Composites Science and Technology, 2020. **189**: p. 108016.

81. Mohammadkhani, R., et al., *Improving Depth Resolution of Ultrasonic Phased Array Imaging to Inspect Aerospace Composite Structures.* Sensors (Basel), 2020. **20**(2).

82. Aldrin, J.C., et al., *Fundamentals of angled-beam ultrasonic NDE for potential characterization of hidden regions of impact damage in composites.* 2018. **1949**: p. 120005.

83. Mahmod, M.F., E.A. Bakar, and A.R. Othman, *Defect Detection of Fiberglass Composite Laminates (FGCL) with Ultrasonic A-Scan Signal Measurement.* IOP Conference Series: Materials Science and Engineering, 2016. **114**: p. 012106.

84. Duchene, P., et al., *A review of non-destructive techniques used for mechanical damage assessment in polymer composites.* Journal of Materials Science, 2018. **53**(11): p. 7915-7938.

85. Park, B., H. Sohn, and P. Liu, *Accelerated noncontact laser ultrasonic scanning for damage detection using combined binary search and compressed sensing.* Mechanical Systems and Signal Processing, 2017. **92**: p. 315-333.

86. De Rosa, I.M., C. Santulli, and F. Sarasini, *Acoustic emission for monitoring the mechanical behaviour of natural fibre composites: A literature review.* Composites Part A: Applied Science and Manufacturing, 2009. **40**(9): p. 1456-1469.

87. Schoßig, M., et al., *ESEM investigations for assessment of damage kinetics of short glass fibre reinforced thermoplastics – Results of in situ tensile tests coupled with acoustic emission analysis.* Composites Science and Technology, 2011. **71**(3): p. 257-265.

88. Noorsuhada, M.N., *An overview on fatigue damage assessment of reinforced concrete structures with the aid of acoustic emission technique.* Construction and Building Materials, 2016. **112**: p. 424-439.

89. Saeedifar, M., et al., *Delamination analysis in composite laminates by means of Acoustic Emission and bi-linear/tri-linear Cohesive Zone Modeling.* Composite Structures, 2017. **161**: p. 505-512.

90. Michalcová, L. and M. Kadlec, *Carbon/epoxy composite delamination analysis by acoustic emission method under various environmental conditions.* Engineering Failure Analysis, 2016. **69**: p. 88-96.

91. Sobhani, A., et al., *The study of buckling and post-buckling behavior of laminated composites consisting multiple delaminations using acoustic emission.* Thin-Walled Structures, 2018. **127**: p. 145-156.

92. Yu, F.-m., et al., *A novel method of identifying damage types in carbon fiber-reinforced plastic cross-ply laminates based on acoustic emission detection using a fiber-optic sensor.* Composites Science and Technology, 2016. **135**: p. 116-122.

93. Kang, J.-j., et al., *Delamination failure monitoring of plasma sprayed composite ceramic coatings in rolling contact by acoustic emission.* Engineering Failure Analysis, 2018. **86**: p. 131-141.

94. Xu, D., et al., *Achieving robust damage mode identification of adhesive composite joints for wind turbine blade using acoustic emission and machine learning.* Composite Structures, 2020. **236**: p. 111840.

95. Kong, X., et al., *Damage identification in fiber reinforced titanium matrix composites using acoustic emission.* Journal of Alloys and Compounds, 2020. **826**: p. 153928.

96. Ghadermazi, K., et al., *Delamination detection in glass–epoxy composites using step-phase thermography (SPT).* Infrared Physics & Technology, 2015. **72**: p. 204-209.

97. Shi, Q., et al., *Barker-coded modulation laser thermography for CFRP laminates delamination detection.* Infrared Physics & Technology, 2019. **98**: p. 55-61.

98. Kakei, A., et al., *Detection and characterisation of delamination damage propagation in Woven Glass Fibre Reinforced Polymer Composite using thermoelastic response mapping.* Composite Structures, 2016. **153**: p. 442-450.

99. Wang, Q., et al., *Using differential spread laser infrared thermography to detect delamination and impact damage in CFRP.* Infrared Physics & Technology, 2020. **106**: p. 103282.

100. Wandowski, T., P.H. Malinowski, and W.M. Ostachowicz, *Delamination detection in CFRP panels using EMI method with temperature compensation.* Composite Structures, 2016. **151**: p. 99-107.

101. Matsuzaki, R., K. Yamamoto, and A. Todoroki, *Delamination detection in carbon fiber reinforced plastic cross-ply laminates using crack swarm inspection: Experimental verification.* Composite Structures, 2017. **173**: p. 127-135.

102. Pegorin, F., K. Pingkarawat, and A.P. Mouritz, *Electrical-based delamination crack monitoring in composites using z-pins.* Composites Part A: Applied Science and Manufacturing, 2018. **104**: p. 120-128.

103. Han, D.-H. and L.-H. Kang, *Nondestructive evaluation of GFRP composite including multi-delamination using THz spectroscopy and imaging.* Composite Structures, 2018. **185**: p. 161-175.

104. Han, H., D. Cao, and L. Liu, *Green's functions for forced vibration analysis of bending-torsion coupled Timoshenko beam.* Applied Mathematical Modelling, 2017. **45**: p. 621-635.

105. Zhao, X., et al., *Forced vibration analysis of Timoshenko double-beam system under compressive axial load by means of Green's functions.* Journal of Sound and Vibration, 2020. **464**: p. 115001.

106. Foda M A, A.Z., *A dynamic Green function formulation for the response of a beam structure to a moving mass.* Journal of sound and vibration, 1998. **210**(3): p. 12.

107. Abu-Hilal, M., *Forced vibration of Euler–Bernoulli beams by means of dynamic Green functions.* Journal of Sound and Vibration, 2003. **267**(2): p. 191-207.

108. Kukla, S. and I. Zamojska, *Frequency analysis of axially loaded stepped beams by Green's function method.* Journal of Sound and Vibration, 2007. **300**(3-5): p. 1034-1041.

109. Li, X.Y., X. Zhao, and Y.H. Li, *Green's functions of the forced vibration of Timoshenko beams with damping effect.* Journal of Sound and Vibration, 2014. **333**(6): p. 1781-1795.

110. Zhao, X., et al., *Green's functions for the forced vibrations of cracked Euler–Bernoulli beams.* Mechanical Systems and Signal Processing, 2016. **68-69**: p. 155-175.

111. Nie, Z., H. Hao, and H. Ma, *Structural damage detection based on the reconstructed phase space for reinforced concrete slab: Experimental study.* Journal of Sound and Vibration, 2013. **332**(4): p. 1061-1078.

112. Hammami, M., et al., *Nonlinear behaviour of glass fibre reinforced composites with delamination.* Composites Part B: Engineering, 2016. **92**: p. 350-359.

113. Andreaus, U. and P. Baragatti, *Experimental damage detection of cracked beams by using nonlinear characteristics of forced response.* Mechanical Systems and Signal Processing, 2012. **31**: p. 382-404.

114. Mohamad, T.H., F. Nazari, and C. Nataraj, *A Review of Phase Space Topology Methods for Vibration-Based Fault Diagnostics in Nonlinear Systems.* Journal of Vibration Engineering & Technologies, 2019. **8**(3): p. 393-401.

115. Takens, F., *Detecting strange attractors in turbulence.* Dynamical systems and turbulence, 1981: p. 366-381.

116. M.D. Todd, J.M.N., L. M. Pecora, L. N. Virgin, , *Vibration-based damage assessment utilizing state space geometry changes local attractor variance ratio.* Smart Materials and Structures, 2001. **10**: p. 9.

117. Nichols, J.M., et al., *Use of chaotic excitation and attractor property analysis in structural health monitoring.* Phys Rev E Stat Nonlin Soft Matter Phys, 2003. **67**(1 Pt 2): p. 016209.

118. Nie, Z., H. Hao, and H. Ma, *Using vibration phase space topology changes for structural damage detection.* Structural Health Monitoring: An International Journal, 2012. **11**(5): p. 538-557.

119. Liu, G., Z. Mao, and M. Todd, *Damage detection using transient trajectories in phase-space with extended random decrement technique under non-stationary excitations.* Smart Materials and Structures, 2016. **25**(11): p. 115014.

120. Worden, K., et al., *A review of nonlinear dynamics applications to structural health monitoring.* Structural Control and Health Monitoring, 2008. **15**(4): p. 540-567.

121. Song, W., et al., *Tool Wear Detection Based on Duffing-Holmes Oscillator.* Mathematical Problems in Engineering, 2008. **2008**: p. 1-15.

122. Liu, X., et al., *Locating and imaging contact delamination based on chaotic detection of nonlinear Lamb waves.* Mechanical Systems and Signal Processing, 2018. **109**: p. 58-73.

123. Zhang, W., et al., *Detection of minor damage in structures with guided wave signals and nonlinear oscillator.* Measurement, 2018. **122**: p. 532-544.

124. Requejo, J.M., et al., *Pig ear skin temperature and feed efficiency: Using the phase space to estimate thermoregulatory effort.* Biosystems Engineering, 2018. **174**: p. 80-88.

125. Wang, D., et al., *Multi-step ahead wind speed forecasting using an improved wavelet neural network combining variational mode decomposition and phase space reconstruction.* Renewable Energy, 2017. **113**: p. 1345-1358.

126. Sun, W. and Y. Wang, *Short-term wind speed forecasting based on fast ensemble empirical mode decomposition, phase space reconstruction, sample entropy and improved back-propagation neural network.* Energy Conversion and Management, 2018. **157**: p. 1-12.

127. Sayed, K., et al., *Characterization of phase space trajectories for Brain-Computer Interface.* Biomedical Signal Processing and Control, 2017. **38**: p. 55-66.

128. Darjani, N. and H. Omranpour, *Phase space elliptic density feature for epileptic EEG signals classification using metaheuristic optimization method.* Knowledge-Based Systems, 2020. **205**: p. 106276.

129. Ryabov, V. and D. Nerukh, *Quantifying long time memory in phase space trajectories of molecular liquids.* Journal of Molecular Liquids, 2011. **159**(1): p. 99-104.

130. Agaoglou, M., et al., *The phase space mechanism for selectivity in a symmetric potential energy surface with a post-transition-state bifurcation.* Chemical Physics Letters, 2020. **754**: p. 137610.

131. Li, B. and X. Chen, *Wavelet-based numerical analysis: A review and classification.* Finite Elements in Analysis and Design, 2014. **81**: p. 14-31.

132. Peng, Z.K. and F.L. Chu, *Application of the wavelet transform in machine condition monitoring and fault diagnostics: a review with bibliography.* Mechanical Systems and Signal Processing, 2004. **18**(2): p. 199-221.

133. Chiariotti, P., M. Martarelli, and G.M. Revel, *Delamination detection by Multi-Level Wavelet Processing of Continuous Scanning Laser Doppler Vibrometry data.* Optics and Lasers in Engineering, 2017. **99**: p. 66-79.

134. Liu, Z., L. Zhang, and J. Carrasco, *Vibration analysis for large-scale wind turbine blade bearing fault detection with an empirical wavelet thresholding method.* Renewable Energy, 2020. **146**: p. 99-110.

135. Sha, G., et al., *Multiple damage detection in laminated composite beams by data fusion of Teager energy operator-wavelet transform mode shapes.* Composite Structures, 2020. **235**: p. 111798.

136. Zhou, J., Z. Li, and J. Chen, *Damage identification method based on continuous wavelet transform and mode shapes for composite laminates with cutouts.* Composite Structures, 2018. **191**: p. 12-23.

137. Yan, Y.J. and L.H. Yam, *Detection of delamination damage in composite plates using energy spectrum of structural dynamic responses decomposed by wavelet analysis.* Computers & Structures, 2004. **82**(4-5): p. 347-358.

138. Wei, Z., L.H. Yam, and L. Cheng, *Detection of internal delamination in multi-layer composites using wavelet packets combined with modal parameter analysis.* Composite Structures, 2004. **64**(3-4): p. 377-387.

139. Hein, H. and L. Feklistova, *Computationally efficient delamination detection in composite beams using Haar wavelets.* Mechanical Systems and Signal Processing, 2011. **25**(6): p. 2257-2270.

140. S. Legendre, J.G., D. Massicotte,, *Ultrasonic NDE of composite material structures using wavelet coefficients.* NDT & E International,, 2001. **34**(1): p. 7.

141. Jasiuniene, E., et al., *Ultrasonic non-destructive testing of complex titanium/carbon fibre composite joints.* Ultrasonics, 2019. **95**: p. 13-21.

142. Matz, V., et al., *Signal-to-noise ratio enhancement based on wavelet filtering in ultrasonic testing.* Ultrasonics, 2009. **49**(8): p. 752-9.

143. Hoseini, M.R., M.J. Zuo, and X. Wang, *Denoising ultrasonic pulse-echo signal using two-dimensional analytic wavelet thresholding.* Measurement, 2012. **45**(3): p. 255-267.

144. Bettayeb, F., S. Haciane, and S. Aoudia, *Improving the time resolution and signal noise ratio of ultrasonic testing of welds by the wavelet packet.* NDT & E International, 2005. **38**(6): p. 478-484.

145. Zhao, B., et al., *Experimental study on micro-damage identification in reinforced concrete beam with wavelet packet and DIC method.* Construction and Building Materials, 2019. **210**: p. 338-346.

146. Golhani, K., et al., *A review of neural networks in plant disease detection using hyperspectral data.* Information Processing in Agriculture, 2018. **5**(3): p. 354-371.

147. Hossain, M.S., et al., *Artificial neural networks for vibration based inverse parametric identifications: A review.* Applied Soft Computing, 2017. **52**: p. 203-219.

148. Gomes, G.F., et al., *The use of intelligent computational tools for damage detection and identification with an emphasis on composites – A review.* Composite Structures, 2018. **196**: p. 44-54.

149. Chakraborty, D., *Artificial neural network based delamination prediction in laminated composites.* Materials & Design, 2005. **26**(1): p. 1-7.

150. Pathirage, C.S.N., et al., *Structural damage identification based on autoencoder neural networks and deep learning.* Engineering Structures, 2018. **172**: p. 13-28.

151. Padil, K.H., N. Bakhary, and H. Hao, *The use of a non-probabilistic artificial neural network to consider uncertainties in vibration-based-damage detection.* Mechanical Systems and Signal Processing, 2017. **83**: p. 194-209.

152. Tan, Z.X., et al., *Detecting damage in steel beams using modal strain energy based damage index and Artificial Neural Network.* Engineering Failure Analysis, 2017. **79**: p. 253-262.

153. Gu, J., M. Gul, and X. Wu, *Damage detection under varying temperature using artificial neural networks.* Structural Control and Health Monitoring, 2017. **24**(11): p. e1998.

154. Chen, S., et al., *Operational Damage Identification Scheme Utilizing De-Noised Frequency Response Functions and Artificial Neural Network.* Journal of Nondestructive Evaluation, 2020. **39**(3).

155. Yao, Y., et al., *Artificial intelligence-based hull structural plate corrosion damage detection and recognition using convolutional neural network.* Applied Ocean Research, 2019. **90**: p. 101823.

156. Crivelli, D., M. Guagliano, and A. Monici, *Development of an artificial neural network processing technique for the analysis of damage evolution in pultruded composites with acoustic emission.* Composites Part B: Engineering, 2014. **56**: p. 948-959.

157. Nazarko, P. and L. Ziemianski, *Damage detection in aluminum and composite elements using neural networks for Lamb waves signal processing.* Engineering Failure Analysis, 2016. **69**: p. 97-107.

158. Dae-Cheol Seo, J.-J.L., *Damage detection of CFRP laminates using electrical resistance measurement and neural network.* Composite structures, 1999. **47**(1-4): p. 6.

159. de Oliveira, M.A. and D.J. Inman, *Performance analysis of simplified Fuzzy ARTMAP and Probabilistic Neural Networks for identifying structural damage growth.* Applied Soft Computing, 2017. **52**: p. 53-63.

160. Kim, J.W. and S. Park, *Magnetic Flux Leakage Sensing and Artificial Neural Network Pattern Recognition-Based Automated Damage Detection and Quantification for Wire Rope Non-Destructive Evaluation.* Sensors (Basel), 2018. **18**(1).

161. Wong, E.W.C. and D.K. Kim, *A simplified method to predict fatigue damage of TTR subjected to short-term VIV using artificial neural network.* Advances in Engineering Software, 2018. **126**: p. 100-109.

162. Karnik, S.R., et al., *Delamination analysis in high speed drilling of carbon fiber reinforced plastics (CFRP) using artificial neural network model.* Materials & Design, 2008. **29**(9): p. 1768-1776.

163. Zhang, W., et al., *An Artificial Neural Network-Based Algorithm for Evaluation of Fatigue Crack Propagation Considering Nonlinear Damage Accumulation.* Materials (Basel), 2016. **9**(6).

164. Della, C.N. and D. Shu, *Vibration of beams with double delaminations.* Journal of Sound and Vibration, 2005. **282**(3-5): p. 919-935.

165. Hirwani, C.K., et al., *Experimental and numerical analysis of free vibration of delaminated curved panel.* Aerospace Science and Technology, 2016. **54**: p. 353-370.

166. Weaver Jr W, T.S.P., Young D H, *Vibration problems in engineering*. 1990.

167. Michaltsos, G.T., E. Sarantithou, and D.S. Sophianopoulos, *Flexural–torsional vibration of simply supported open cross-section steel beams under moving loads.* Journal of Sound and Vibration, 2005. **280**(3-5): p. 479-494.

168. Lee, J., *Free vibration analysis of delaminated composite beams.* Computers & Structures, 2000. **74**(2): p. 9.

169. Luo H, H.S., *Dynamics of delaminated beams.* International Journal of Solids and Structures, 2000. **37**(10): p. 20.

170. Della, C.N. and D. Shu, *Vibration of delaminated multilayer beams.* Composites Part B: Engineering, 2005. **37**(2-3): p. 227-236.

171. Bambang Surono, R.S., I Made Miasa, *Natural Frequency and Mode Shape of Rectangle Delamination: Experiment and Simulation*, in *12th South East Asian Technical University Consortium (SEATUC)*, IEEE, Editor. 2018.

172. Muhammad Imran, R.K., Saeed Badshah, *Experimental, Numerical and Finite Element Vibration Analysis of Delaminated Composite Plate.* Scientia Iranica, 2019.

173. Bedon, C., *Issues on the Vibration Analysis of In-Service Laminated Glass Structures: Analytical, Experimental and Numerical Investigations on Delaminated Beams.* Applied Sciences, 2019. **9**(18): p. 3928.

174. Engr. Muhammad Imran, S.B., Rafiullah Khan, *Experimental investigation of the influence of stacking sequence and delamination size on the natural frequencies of delaminated composite plate.* Pakistan Journal of Scientific & Industrial Research Series A: Physical Sciences, , 2019. **62**(3).

175. Chang, T.P. and J.Y. Liang, *Vibration of postbuckled delaminated beam-plates.* International Journal of Solids and Structures, 1998. **35**(12): p. 1199-1217.

176. Della, C.N., *Free vibration analysis of composite beams with overlapping delaminations under axial compressive loading.* Composite Structures, 2015. **133**: p. 1168-1176.

177. Pan, J., et al., *A novel method of vibration modes selection for improving accuracy of frequency-based damage detection.* Composites Part B: Engineering, 2019. **159**: p. 437-446.

178. Zorić, N.D., et al., *Optimal vibration control of smart composite beams with optimal size and location of piezoelectric sensing and actuation.* Journal of Intelligent Material Systems and Structures, 2012. **24**(4): p. 499-526.

179. Gupta, V., M. Sharma, and N. Thakur, *Optimization Criteria for Optimal Placement of Piezoelectric Sensors and Actuators on a Smart Structure: A Technical Review.* Journal of Intelligent Material Systems and Structures, 2010. **21**(12): p. 1227-1243.

180. Dunant Halim, S.O.R.M., *An optimization approach to optimal placement of collocated piezoelectric actuators and sensors on a thin plate.* Mechatronics, 2003. **13**(1): p. 21.

181. Halim, D., G. Barrault, and B.S. Cazzolato, *Active control experiments on a panel structure using a spatially weighted objective method with multiple sensors.* Journal of Sound and Vibration, 2008. **315**(1-2): p. 1-21.

182. Nestorović, T. and M. Trajkov, *Optimal actuator and sensor placement based on balanced reduced models.* Mechanical Systems and Signal Processing, 2013. **36**(2): p. 271-289.

183. Bruant, I., L. Gallimard, and S. Nikoukar, *Optimal piezoelectric actuator and sensor location for active vibration control, using genetic algorithm.* Journal of Sound and Vibration, 2010. **329**(10): p. 1615-1635.

184. Daraji, A.H., J.M. Hale, and J. Ye, *New Methodology for Optimal Placement of Piezoelectric Sensor/Actuator Pairs for Active Vibration Control of Flexible Structures.* Journal of Vibration and Acoustics, 2018. **140**(1).

185. Zorić, N.D., et al., *Active vibration control of smart composite plates using optimized self-tuning fuzzy logic controller with optimization of placement, sizing and orientation of PFRC actuators.* Journal of Sound and Vibration, 2019. **456**: p. 173-198.

186. Nestorović, T., K. Hassw, and A. Oveisi, *Software-in-the-loop optimization of actuator and sensor placement for a smart piezoelectric funnel-shaped inlet of a magnetic resonance imaging tomograph.* Mechanical Systems and Signal Processing, 2021. **147**: p. 107097.

187. Hu, J. and Z. Kang, *Topological design of piezoelectric actuator layer for linear quadratic regulator control of thin-shell structures under transient excitation.* Smart Materials and Structures, 2019. **28**(9): p. 095029.

188. Dunant, H., *Vibration analysis and control of smart Structures*. 2002, University of Newcastle.

189. Jane K C, C.C.C., *Postbuckling deformation and vibration of a delaminated beam-plate with arbitrary delamination location.* Mechanics research communications, 1998. **25**(3): p. 15.

190. Nichols, J.M., *Structural health monitoring of offshore structures using ambient excitation.* Applied Ocean Research, 2003. **25**(3): p. 101-114.

191. Ganesh, S., K.S. Kumar, and P.K. Mahato, *Free Vibration Analysis of Delaminated Composite Plates Using Finite Element Method.* Procedia Engineering, 2016. **144**: p. 1067-1075.

192. Sayyad, A.S. and Y.M. Ghugal, *On the free vibration analysis of laminated composite and sandwich plates: A review of recent literature with some numerical results.* Composite Structures, 2015. **129**: p. 177-201.

193. Mujumdar P M, S.S., *Flexural vibrations of beams with delaminations.* Journal of sound and vibration, 1988. **125**(3): p. 20.

194. Jiang, Y., H. Zhu, and Z. Li, *A new compound faults detection method for rolling bearings based on empirical wavelet transform and chaotic oscillator.* Chaos, Solitons & Fractals, 2016. **89**: p. 8-19.

195. Li, H., et al., *Analysis of dynamic of two-phase flow in small channel based on phase space reconstruction combined with data reduction sub-frequency band wavelet.* Chinese Journal of Chemical Engineering, 2015. **23**(6): p. 1017-1026.

196. Lee, S.H., et al., *Classification of normal and epileptic seizure EEG signals using wavelet transform, phase-space reconstruction, and Euclidean distance.* Comput Methods Programs Biomed, 2014. **116**(1): p. 10-25.

197. Zeng, W., et al., *Classification of gait patterns between patients with Parkinson's disease and healthy controls using phase space reconstruction (PSR), empirical mode decomposition (EMD) and neural networks.* Neural Netw, 2019. **111**: p. 64-76.

198. Han, J.-G., W.-X. Ren, and Z.-S. Sun, *Wavelet packet based damage identification of beam structures.* International Journal of Solids and Structures, 2005. **42**(26): p. 6610-6627.

199. Law, S.S., et al., *Structural damage detection from wavelet packet sensitivity.* Engineering Structures, 2005. **27**(9): p. 1339-1348.

200. Pan, Y., et al., *Structural health monitoring and assessment using wavelet packet energy spectrum.* Safety Science, 2019. **120**: p. 652-665.

201. J.Falkowski, R.S.S.B., *The Haar wavelet transform: its status and achievements.* Computers & Electrical Engineering, 2003. **29**(1): p. 20.

202. Esmaeel, R.A. and F. Taheri, *Delamination detection in laminated composite beams using the empirical mode decomposition energy damage index.* Composite Structures, 2012. **94**(5): p. 1515-1523.

203. Shu, J., et al., *The application of a damage detection method using Artificial Neural Network and train-induced vibrations on a simplified railway bridge model.* Engineering Structures, 2013. **52**: p. 408-421.

204. Fei, J. and H. Ding, *Adaptive sliding mode control of dynamic system using RBF neural network.* Nonlinear Dynamics, 2012. **70**(2): p. 1563-1573.

205. Shi, X., et al., *Design of adaptive backstepping dynamic surface control method with RBF neural network for uncertain nonlinear system.* Neurocomputing, 2019. **330**: p. 490-503.

206. Rubio, J.d.J., et al., *Uniform stable radial basis function neural network for the prediction in two mechatronic processes.* Neurocomputing, 2017. **227**: p. 122-130.

207. Khosravi, A., et al., *Prediction of wind speed and wind direction using artificial neural network, support vector regression and adaptive neuro-fuzzy inference system.* Sustainable Energy Technologies and Assessments, 2018. **25**: p. 146-160.

208. Ke, M., et al., *A Self-Adaptive RBF Neural Network Classifier for Transformer Fault Analysis.* IEEE Transactions on Power Systems, 2010. **25**(3): p. 1350-1360.

209. Vallabhaneni, V. and D. Maity, *Application of Radial Basis Neural Network on Damage Assessment of Structures.* Procedia Engineering, 2011. **14**: p. 3104-3110.

210. Avci, O., et al., *Wireless and real-time structural damage detection: A novel decentralized method for wireless sensor networks.* Journal of Sound and Vibration, 2018. **424**: p. 158-172.

211. Geng, X., et al., *Research on FBG-Based CFRP Structural Damage Identification Using BP Neural Network.* Photonic Sensors, 2018. **8**(2): p. 168-175.

212. Yan, B., et al., *Beam Structure Damage Identification Based on BP Neural Network and Support Vector Machine.* Mathematical Problems in Engineering, 2014. **2014**: p. 1-8.

213. Zhao, X., E.C. Yang, and Y.H. Li, *Analytical solutions for the coupled thermoelastic vibrations of Timoshenko beams by means of Green's functions.* International Journal of Mechanical Sciences, 2015. **100**: p. 50-67.

214. Zhao, X., et al., *Coupled thermo-electro-elastic forced vibrations of piezoelectric laminated beams by means of Green's functions.* International Journal of Mechanical Sciences, 2019. **156**: p. 355-369.

PUBLICATION DURING PHD STUDY

1. Li X, Halim D, Xiaoling Liu, Chris Rudd. Delamination Detection in Composite Laminates using a Vibration-Based Chaotic Oscillator Method[C]//INTER-NOISE and NOISE-CON Congress and Conference Proceedings. Institute of Noise Control Engineering, 2018, 258(4): 3531-3539.
2. Xuan LI, Dunant Halim, Xiaoling Liu. Forced Vibration Analysis of a Fibre-Reinforced Polymer Laminated Beam using the Green Function Method[C]. INTER-NOISE and NOISE-CON Congress and Conference Proceedings. Seoul, 2020
3. Xuan LI, Dunant Halim, Xiaoling Liu. Vibration Sensor Placement for Delamination Detection in a Beam Structure based on the Vibration-based Chaotic Oscillator Method[C]. INTER-NOISE and NOISE-CON Congress and Conference Proceedings. Seoul, 2020